# On Variational Problems and Gradient Flows in Image Processing

Der Fakultät der Naturwissenschaften
der Universität Duisburg-Essen
(Standort Duisburg)

zur Erlangung des akademischen Grades eines

Doktors der Naturwissenschaften

eingereichte Dissertation von

Marc Droske

aus Mechernich

Datum der Einreichung: 9. März 2005

# Contents

# 3   Morphological registration

# 4   $\Gamma$-Convergence of perturbed registration energies

# 5   Mumford-Shah based registration

# 6 Willmore flow on level sets and graph surfaces

# 7 Narrow band methods for geometric evolution problems

# Notations

| | |
|---|---|
| $\mathcal{M}$ | denotes always a hypersurface |
| $\mathcal{M}_c[u]$ | Level set of $u$ for $c \in \mathbb{R}$, i. e., $\{u = c\} := \{x \in \Omega : u(x) = c\}$ |
| $\mathscr{M}[u]$ | Morphology of an image $I$, i. e., $\{\mathcal{M}_c[u] : c \in \mathbb{R}\}$ |
| $P[u]$ | Projection onto tangent space $T\mathcal{M}$, i. e., $P[u] = \mathbb{1} - \frac{\nabla u}{\|\nabla u\|} \otimes \frac{\nabla u}{\|\nabla u\|}$. |
| $n_I$ | Gauss-map of the morphology of $u$. $n_u = \frac{\nabla u}{\|\nabla u\|}$. |
| $D\phi$ | Jacobian $(\frac{\partial \phi_i}{\partial x_j})_{ij}$ of the function $\phi$ |
| $\phi_{i,j}$ | $j$-th partial derivative of $i$-th component of $\phi$, $\frac{\phi_i}{\partial x_j}$ |
| $\det A$ | determinant of the matrix $A$ |
| $\operatorname{Cof} A$ | cofactor matrix of a matrix $A \in \mathbb{R}^{n,n}$. For $A$ invertible $\operatorname{Cof} A = \det A \cdot A^{-T}$ |
| $\mu = \mu^n$ | $n$-dimensional Lebesgue measure |
| $\mathscr{H}^n$ | $n$-dimensional Hausdorff measure |
| $\mathrm{d}A$ | area element |
| $\operatorname{card} A$ | number of elements of the set $A$ |
| $B_r(x)$ | open ball or radius $r$ around $x$ |
| $B_r(A)$ | tubular neighborhood of the set $A$ with radius $r$, i. e., $\bigcup_{x \in A} B_r(x)$ |
| $u \cdot v$ | Euclidian scalar product $u_i v_i$ of the vectors $u$ and $v$ |
| $\|u\|$ | Euclidian norm $\sqrt{u \cdot u}$ of $u$ |
| $u \otimes v$ | tensor product $uv^T$ |
| $A : B$ | matrix inner product $A_{ij} B_{ij}$ of the matrices $A = (A_{ij})$ and $B = (B_{ij})$ |
| $\|A\|$ | Frobenius norm $\sqrt{A : A}$ of the matrix $A$ |
| $\mathcal{I}_h$ | interpolation operator $H^{1,2} \to \mathcal{V}_h$ |
| $\operatorname{grad} E$ | gradient of the functional $E$ with respect to the canonical metric |
| $\operatorname{grad}_g E$ | gradient of $E$ with respect to the metric $g$ |
| $\mathscr{L}(\mathscr{X}, \mathscr{Y})$ | space of bounded linear operators between Banach spaces $\mathscr{X}$ and $\mathscr{Y}$ |
| $\nabla_{\mathcal{M}} f$ | gradient on the surface w.r.t. a metric |
| | or in the level set context the tangential gradient, |
| | i. e. projection of the gradient onto the tangent space |
| $\operatorname{div} v$ | divergence of the vector field $v : \Omega \to \mathbb{R}^d$, $v_{i,i}$ |
| $\mathbf{div} T$ | divergence $(\partial_j T_{ij})$ of the tensor field $T : \Omega \to \mathbb{R}^{m,n}$ |
| $\Delta_{\mathcal{M}} f$ | Laplace-Beltrami operator |
| $BV(\Omega)$ | space of functions of bounded variation |
| $SBV(\Omega)$ | space of special functions of bounded variation ($\mu_c = 0$) |
| $\mathbb{M}^d$ | $d \times d$ matrices with entries in $\mathbb{R}$ |
| $\operatorname{int} A$ | interior of the set $A$ |
| $\overline{A}$ | closure of the set $A$ |
| $\langle \cdot, \cdot \rangle$ | dual pairing |

| | |
|---|---|
| $\partial A$ | boundary of the set $A$ |
| $\mathscr{C}^m(\Omega)$ | $m$-times continuously differentiable functions $\Omega \to \mathbb{R}$ |
| $\mathscr{C}^m(\Omega; \mathbb{R}^d)$ | $= \left\{ \phi = (\phi_i) : \Omega \to \mathbb{R}^d \ : \ \phi_i \in \mathscr{C}^m(\Omega) \text{ for all } i = 1, \ldots, d \right\}$ |
| $L^p(\Omega; \mathbb{R}^d)$ | $= \left\{ \phi = (\phi_i) : \Omega \to \mathbb{R}^d \ : \ \phi_i \in L^p(\Omega) \text{ for all } i = 1, \ldots, d \right\}$ |
| $S^n$ | $n$-dimensional unit sphere |
| $\mathscr{A}$ | space of admissible functions in the context of energy minimization |
| $\Gamma - \lim E_\alpha$ | $\Gamma$-limit of the sequence of functionals $E_\alpha$. |
| $v^\perp$ | clockwise rotation of a vector $v \in \mathbb{R}^2$ by $\pi/2$ |
| ap lim sup | approximate $\limsup$ (cf. p. 23) |
| ap lim inf | approximate $\liminf$ (cf. p. 23) |
| $S_u$ | set of points where ap lim inf $\neq$ ap lim sup |
| $\ker F$ | kernel of an operator $F : \mathscr{X} \to \mathscr{Y}$, i. e., $\{F = 0\}$ |
| range $F$ | range of an operator $F : \mathscr{X} \to \mathscr{Y}$, i. e., $\{F(x) \ : \ x \in \mathscr{X}\}$ |
| $\mathscr{L}$ | space of level set ensembles |

# Chapter 1

# Introduction

FINDING a point–to–point correspondence between a pair of images is a fundamental problem in image processing. The process of determining a mapping between two images, or in other words, of finding a deformation of one image, such that it is as "similar" as possible to a given second image is referred to as image registration or image matching.

Image registration has become a very challenging task and has quickly lead to a large interdisciplinary field of research. Various mathematical, algorithmical, information theoretical and medical studies were stimulated by the rapid development of tomography. With the early success of X-ray based *computed tomography* (CT) and its enormous impact on diagnostics and surgery planning much effort has been invested into further radiological research. CT data offered the first type of images to be processed and visualized volumetrically and opened the way to three dimensional anatomical data processing. However, CT images mainly show bone structures and suffer from lack of detail in the remaining parts. A popular approach to enrich the information is to map the acquired data onto a reference image, for which detailed information of anatomical and functional structures is available through some pre-processing. This reference information can then be mapped back onto the particular patient. This is where the need for image registration comes into play and subsequently the demand for efficient handling and processing of large datasets has grown immensely. *Magnetic resonance tomography* (MRT) was the next milestone in the history of radiology. Since it is based on the spin of hydrogen atoms, which are present throughout the tissue, MRT allows the generation of images with very detailed and sharp tissue structures. In some cases, for a deeper understanding of the particular clinical case, it was essential to have access to several different imaging modalities at the same time, i. e., sources of data like CT or MRT. The number of different modalities and variations of existing technology has been growing steadily and current research in new approaches like *diffuse tomography* indicate significant further potential. Subtle tumor infiltration, for example, may require special FLAIR sequences on MRT. Furthermore, acquisition devices have improved significantly with respect to the accuracy of the sampling. It is already possible to produce CT images of $1024^2$ pixels in resolution per slice, and for MRT resolutions of $256^2$ or $512^2$ have become standard.

Due to the complexity and immense structural variety of natural images, the task of image registration poses a multitude of theoretical as well as algorithmical challenges. In this chapter we first give a short overview on practical problems, especially in clinical applications, where image registration plays an important role. Due to the wide spectrum of different tasks, models, applications as well as computational approaches, this overview is not meant to be comprehensive. The methods also differ in the assumptions on the theoretical model and date properties. A variety of techniques rely on structural assumptions on the underlying registration problem, i. e., some kind of *a-priori* information on the type of deformation, intensity invariance of the images or other prerequisites. We refer to [120, 35] for a more detailed overview on registration methods.

This thesis is devoted to mathematical and algorithmical aspects of non-rigid registration and its connection to other fields in image processing, especially image restoration, feature extraction and continuation techniques of features that are also used in the framework of image inpainting.

We will propose numerical methods to solve such computationally demanding problems efficient and robustly.

The thesis is organized as follows: In the next section of the introduction, an overview on registration will be given. For a comprehensive understanding of image similarity we will first revise fundamental concepts in mathematical image processing and motivate the combination of different image processing tasks into a single model. In Section 1.3 we will introduce a simple unimodal registration approach, that will serve as a model problem to devise and verify robust numerical algorithms. It turns out that the task of image matching is generically ill-posed, and that consequently regularization is of fundamental importance. Different approaches of regularization with an emphasis on the application for image registration will be outlined in Section 1.4. In Section 1.5 we will introduce some basic notations and results from mathematical morphology that will play an important rôle to devise a class of similarity measures that is based on the shapes of the objects of the underlying input images.

In Chapter 2 we will construct a robust and efficient optimization algorithm that is essentially built upon the concept of a generalized gradient descent with a regularizing metric. Furthermore multiscale and multilevel techniques will be incorporated and discussed.

However, in the applications the task of registration of data from different imaging machinery is much more important. In Chapter 3 we will devise a morphological registration algorithm, that is based on the geometric information in the images. This information is essentially contrast-invariant. In that chapter we will incorporate an additional regularization and apply techniques from nonlinear elasticity to address the question of existence. Here, we will also discuss a weaker notion of boundary conditions, that will turn out to be more convenient for registration problems with large displacement fields.

Regularization will give rise to the question of how the regularized problem and the original problem are related. Even though the solutions of the regularized problem will in general differ from the original, one may study the behaviour of the solutions when the regularization tends to $0$. In Chapter 4 we will use the concept of $\Gamma$-convergence to two types of regularizations: nonlinear *Tikhonov-regularization* and *multiscale* strategies.

Chapter 5 will be devoted to a registration approach that complements to the morphological alignment of images: based upon variational free discontinuity problems, image registration can be significantly enhanced and stabilized by incorporating an energy that penalizes a disalignment of image discontinuities. We will present a level set algorithm which is based on shape optimization techniques and compare it to a phase-field approximation of the free discontinuity problem.

As will be described in Section 1.1 the *Willmore energy* is of fundamental importance for contrast invariant inpainting of images and higher order regularization of contours. In Chapter 6 we will derive a level set formulation for the $L^2$-gradient flow of the Willmore energy (*Willmore flow*) and consider a semi-implicit Finite Element scheme for the numerical computation.

The *Willmore flow* is a geometric flow of fourth order and hence computationally demanding. In Chapter 7 a narrow band approach is proposed for the solution of higher order flows with semi-implicit time stepping schemes. We will apply the algorithmical framework to the inpainting of two-dimensional surfaces in three-dimensional medical datasets.

In subsequent sections, we review different approaches presented in the literature and describe mathematical models for the registration problem.

## 1.1 An overview on registration

### 1.1.1 Registration problems in variational form

So far, we have only vaguely defined the registration problem. How do we judge whether images are similar and furthermore is there a way to measure the distance between images? Does it apply universally to all classes of images? The common aim of most registration methods is first to define a way of measuring the similarity or analogously the disparity between images, which are mathematically understood as functions from an image domain $\Omega \subset \mathbb{R}^d$ into $\mathbb{R}^d$ and in $L^\infty(\Omega)$.

Figure 1.1: *An overview of MRT (magnetic resonance), CT (computed tomography), PD (positron density) and MR-FLAIR images. The two images on the left, and the images on the right show axial resp. sagittal slices of the human spine. The others show axial slices of a human brain. ([†]kindly provided by Neurosurgical clinic, Bonn. [‡]image courtesy Max-Planck institute of cognitive neurosciences, Leipzig)*

Furthermore, let us denote by $\mathcal{V} \subset \left\{ \phi : \Omega \to \mathbb{R}^d \right\}$ a space of deformations which we consider as possible candidates for suitable mappings from one image domain to another and by $\mathscr{I}$ a suitable space of images, which is yet left to be specified.

We are left to define a disparity function $\mathbb{D} : \mathscr{I} \times \mathscr{I} \times \mathcal{V} \to \mathbb{R}_0^+$ and henceforth formulate the registration problem as follows: find $\phi \in \mathcal{V}$, such that for given $u_T$ and $u_R$, $\phi$ is a solution of the following minimization problem

$$\mathbb{D}[u_T, u_R, \phi] = \inf_{\psi \in \mathcal{V}} \mathbb{D}[u_T, u_R, \psi]. \tag{1.1}$$

Equivalently this can be understood as maximizing the similarity of $u_T \circ \phi$ and $u_R$, which may be defined by $-\mathbb{D}[u_T, u_R, \phi]$.

Even though most registration problems can be written in such a *variational* form, some techniques are driven by image dependent "forces" [195] and cast directly into the form of an instationary PDE. Throughout this thesis, we will only consider registration problems of the form (1.1).

## 1.1.2 Image analysis and similarity

Natural images in general contain a whole range of characteristics. The most fundamental problem of the task of registration, also referred to as *image matching*, is the question of how to formalize the similarity of images. If we do not want to restrict ourselves to a particular class of images (e. g. photographs of buildings, CT images of human skulls, scans of typed texts) one is confronted with all the types of structures which a bounded function from a particular domain to a bounded interval may represent: images contain flat regions, edges, corners, textures, self-similarities, sensoring artefacts, occlusions, curves, straight lines etc. And even before tackling the problem of registration, in the analysis of a single image, like object classification (*segmentation*), the problem of analyzing images by abstraction is important. It eventually boils down to analyzing the human perception of vision.

MOREL ET AL. have picked up fundamental works which are known as *Gestalt*[1]-theory. It connects many of the geometrical ideas (edges, curvature, length, continuation) that are important in the mathematical modeling for many image processing tasks. Contrast plays a vital rôle in the perception of images. The notion of morphology and its geometrical interpretation, decouples the analysis of contrast and the analysis of shapes. The basis of morphological analysis of images is the decomposition of the graph of the image intensity function into a family of level sets. As we will describe in detail in Section 1.5, this family provides the entire topographic description of the image. The level sets give rise to the study of shapes. For images which are described by intensity functions of bounded variation, the boundaries of sets of the form $\{u \geq 0\}$ are rectifiable and have a well-defined normal $\mathcal{H}^{d-1}$ everywhere. For sufficiently smooth isophotes, these sets can be understood as smooth submanifolds and hence be analyzed by differential geometric techniques. Since the geometry is characterized by differential geometric entities like tangent spaces, first and second fundamental forms (and hence notions of curvature), and corresponding differential operators, morphological methods lead in a very natural way to geometric partial differential equations.

A large conceptual area of image processing is based on statistical and information theoretic approaches (Bayesian analysis, *Gabor*-filters [116], etc.). However, the connection to geometry is rather implicit and yet not completely understood.

Let us also mention that images can be decomposed uniquely into a structural part $u$ and an oscillatory $v$ part. RUDIN&OSHER&FATEMI (ROF) proposed to minimize $\|u\|_{BV} + \lambda\|v\|_{L^2}^2$ subject to $I = u + v$ [177, 178]. The term $v$ then consists of texture and noise. As analyzed by MEYER [152], the norm of $v$ is still small in the Besov space $\dot{B}_{\infty}^{-1,\infty}$. The model of MUMFORD&SHAH is by nature related to the ROF-model, since discontinuity sets are already built into the underlying function space $SBV$ and away from these the original function ought to be approximated by a smooth function in the $L^2$ sense [163]. These approaches are *"almost"* morphological, in the sense that they identify discontinuities as jumps if they are large enough in magnitude. If we consider continuous contrast transformations, discontinuities will still be present after the contrast change and are hence also a morphological invariant. In Chapter 5 we will apply those concepts to image registration. In general, modern image analysis simultaneously treats discontinuities, geometries (along edges as well as in smooth areas) and textures. For image registration, textures are far too oscillatory to be aligned. In the following we will interpret textures as noise and aim at alignment of the main morphological features of images.

### 1.1.3  Image registration in clinical routine

Due to the complexity of anatomical and spatial structures, and the increasing understanding of functional relationships in clinical research areas such as neurosurgery, preoperative diagnostics can be significantly enhanced by having access to a multitude of preoperative imaging modalities. Even during the surgery itself, so called frameless navigational devices can enhance the insight and security by giving visual online information that is related to anatomical and functional structures. Typically the three dimensional position of the instruments is tracked on-the-fly and set into correlation to marker points and structures, which have been preoperatively defined on computer aided surgery planning tools. The tracking of the surgical instruments is usually undertaken by optical markers (e. g. LEDs, which are linked to an active infrared array) [24].

In the planning stage, anatomical structures in images have to be identified. This process, that is called *segmentation*, helps the surgeon to obtain a three dimensional visualization of such structures during the phase of planning and also during the surgery itself, instead of inspecting sequences of single image slices manually. If online registration of the patient to the preoperatively acquired data takes place, distance maps of those segments allow fast localization of the instruments in relation to these structures. One can think of, for example, the segmentation of vital organs and vessels, such that an alarm can be triggered if the instruments approach them too closely and risk the life of the patient. Functional modalities allow to keep track of the position of eloquent cortical regions (e. g. visual, speech cortex, sensomotoric structures).

---

[1]Gestalt (ger): shape

During planning and especially during navigation, it is a severe restriction to havo to choose one particular imaging modality for the navigation system. For example, for the resection of skull base tumors, which frequently infiltrate the skull, it would be desirable to have access to CT sequences to visualize the bone structures as well as MR sequences to visualize the subtle tumor structures. The anatomical precision of the registration is of crucial importance during pre-operative planning as well as intraoperative referencing. During surgery the body position of the patient usually changes and thus has to be tracked by the navigation system.

Especially due to the impact of the operation itself, e. g., opening of the skull, the position of the organs and structures may change drastically. For instance, due to the change of pressure within the skull, the position of the brain is strongly influenced by gravitation once the skull is opened, whereas the sturdy bone structures stay in position. This phenomenon is called *brain-shift*. As a consequence, non-rigid registrations has to take place during surgery, to keep the navigation precise. To be of any use at all, these computations have to be done almost on-the-fly, in order not to interrupt the time-critical surgery process. Intraoperative imaging is often CT-based. Unimodal registration to the preoperative CT sequence would give access to different modalities which have to be matched with high precision in the planning phase.

### 1.1.4 Requirements on the deformation

Spatial misalignment of image features may have several different reasons. In medical image registration, there are several different scenarios:

(i) **intra-individual**—In clinical routine, the validation of therapies and treatments often require the reacquisition of CT or MR data in order to observe the state of the patient in intervals which range from several days to months or even years. In case of ambiguities these are enhanced by biopsies. It is unrealistic to assume that alignment could be achieved by simple rigid transformation. Non-rigidity of the tissue and different positioning may then lead to locally varying deformations. Furthermore diseases may lead to strong morphological changes. Sometimes, the neurosurgeon may decide to observe the state of the patient via follow-up MRI or CT sequences instead of immediate surgical resection. This may be the case for example for WHO[2] low grade tumors where the surgical risk of sole observation has to be weighted against the risk of neurological deficits to intervention.

Even in the same modality, the intensity levels may change, due to the infiltration of tumors on surrounding tissue. During the growth process, the borderline marks the region of high activity (mitotic activity[3]), whereas the necrotic core of the tumor is growing as well, which is due to the change of vascular nutrition within the tumor, the border and the surrounding tissue. Here the analysis of temporal changes is of enormous importance for the clinician. These considerations make clear, that morphological analysis of these structures are more important, than the contrast information, which is given by the image intensities. Furthermore this process is highly non-uniform and varies locally and hence, the transformation to capture the change over time cannot be assumed to be a purely rigid transformation.

(ii) **inter-individual**—The revolutionary advances in the development of imaging modalities has enabled clinical researchers to perform precise studies of the immense *variability* of human anatomy. As described in the excellent review by MILLER, TROUVÉ & YOUNES [156] and the overview article of GRENANDER & MILLER [120], this field, usually referred to as *computational anatomy*, aims at automatic detection of anatomical features, given as geometric entities, the evaluation and the comparison of those features as well as statistical codification of intra-individual variabilities in order to gather probabilistic information for the testing of disease states. As stated by D'ARCY THOMPSON in 1917, "in a very large part of morphology, our essential task lies in the comparison of related forms rather than

---

[2]World Health Organization. WHO grades range from I (benignant, low risk) to IV (malignant, immediate risk by further infiltration).
[3]cell activity

the precise definition of each; and the deformation of a complicated figure may be a phe-
nomenon easy of comprehension, though the figure itself may have left to be unanalyzed
and undefined."

This means that we aim at finding deformations which capture the difference from one
morphology to another. In the case of computational anatomy, the variation of a particular
patient to a given and well-understood reference anatomy allows one to devise automated
methods to detect pathologies by measuring morphological defects. Of course, those de-
fects can once more be very local in nature and require a fine space of deformations. Rigid
deformation spaces only allow for a very coarse registration, where the fine and subtle
anatomical variabilities still have to be studied by visual perception, depending strongly
on the experience of the clinician.

### 1.1.5   Morphing

Image morphing is aimed at finding a smooth transition between two separate but similar im-
ages. A simple alpha-blending is obviously smooth, but no morphing of the shapes in the images
takes place. It is more desirable to find a mapping, which transforms one image into the other.
This allows one to interpolate the spatial offset $\phi_\alpha = \mathbb{1} + \alpha u$ for $\alpha \in [0, 1]$. Here, one particularly
assumes that the images can be mapped to each other one-to-one as well.

## 1.2   The interdependency of image processing tasks

In this section we give a short overview on three other important fields of mathematical image
processing, namely *segmentation*, *feature extraction*, *image restoration/denoising* and *inpainting*.
The latter is also known as *image interpolation* (cf. the work of CASELLES, MOREL & SBERT
[45]) and *disocclusion* as by MASNOU & MOREL [148]. Most of these image processing tasks are
usually studied on their own and extended to other areas of application, as, for example, sur-
face processing. Compared to the early advances in these fields, most of those areas are already
quite well-developed, even though there is still room for improvements. Especially the task of
*segmentation*, the recognition of objects in images, has turned out to be very tough. Natural
images are often too complex and thus reveal a wide range of ambiguities. Even for the human
eye the precise demarcation of a certain region may be a difficult task. The appropriate defini-
tion of a *segment* often depends on the context: while in some applications, the boundaries of
segments can be characterized by strong "edges", this may not be true for medical applications.
As described in [99, 98] some additional information may be crucial. This may be knowledge
about functional, histological or pathological properties of certain regions. Unfortunately these
properties are not always captured well by typical imaging machinery as MRT or CT and further
imaging modalities as fMRT (functional MRT) become necessary, which indicates that at this
point image registration has to come into play.

> *We assert that paying respect to given interdependencies and devising combined ap-*
> *proaches will lead to significant advances, which may not be possible by further devel-*
> *opments that are restricted to a single discipline.*

In the following sections we will give a short introduction to developments and ideas in
the above mentioned fields of image processing and describe the links between those areas.
Throughout this thesis we will understand *segmentation* in a general sense, which covers both
the detection of regions and the extraction of features. We list and draw connections between
fundamental ideas and approaches in the field of image processing, however this should be
understood as an illustrative overview rather than a complete overview over the broad field of
ideas that can be found in the literature.

### 1.2.1   Image restoration and feature extraction

By physical considerations, natural images are always corrupted by noise. Nowadays this noise
is often hardly visible in images produced by *state-of-the-art* imaging technology as tomography

devices, digital cameras or scanners. However, this is mostly due to the fact that the generated images are already being denoised directly after acquisition and before they are transferred to a different medium. Early filters for image denoising were both homogeneous and isotropic. The probably most basic example of a filter is a discrete convolution in the neighborhood of the pixels, corresponding to a weighted sum of the surrounding intensities, i. e., a *low-pass-filter*. In an axiomatic way, ALVAREZ, GUICHARD, LIONS & MOREL [3] showed that the heat equation

$$u_t = \Delta u \quad \text{in } \mathbb{R} \times \Omega, \qquad u(0) = u_0 \quad \text{in } \{0\} \times \Omega \tag{1.2}$$

uniquely describes a *scale-space* coarsing, which fulfills a set of "natural" assumptions as *causility*, and in particular *linearity* and *isometry invariance* and thus gave rise to respect the rôle of PDEs in image processing as already proposed by KOENDERINK [137]. In the context of *morphological image processing* [149, 146, 145, 144] a large class of morphological filters, namely any contrast invariant and monotone operator can be written as a so called *sup-inf* operator.

The linear diffusion of Eq. (1.2) does obviously not take into account any structural information from the input image; it blurs out noise as well as prominent image features, such as edges the same way. PERONA&MALIK's pioneering idea [172] consists in introducing a dependence of the diffusion coefficient on some local properties of the image itself. The weighting function $g(s) = 1/(1 + \frac{s^2}{\lambda^2})$ ensures for a given $\lambda > 0$, that the diffusion coefficient is small where edges are indicated by high-gradients:

$$u_t = \text{div}(g(\|\nabla u\|^2)\nabla u) \quad \text{in } \mathbb{R} \times \Omega, \qquad u(0) = u_0 \quad \text{in } \{0\} \times \Omega. \tag{1.3}$$

It is nowadays well-known that this equation is not well-posed, since it allows backward diffusion iff $\|\nabla u\| > \lambda$ (cf. for example the books of WEICKERT [203] or AUBERT & KORNPROBST [12]). As proposed by CATTÉ, LIONS, MOREL & COLL [46] the evolution problem becomes well-defined by approximating $g(\|\nabla u\|)$ by $g(\|\nabla u_\sigma\|)$, where $u_\sigma$ corresponds to a prefiltered version of the image $u$ by linear diffusion of time $\frac{\sigma^2}{2}$. On account of the boundedness of $\|\nabla u_\sigma\|$ and the application of Schauder's fix point theorem it can be shown that the problem has a unique solution. In this setting $g(\|\nabla u_\sigma\|)$ acts as a prior for the existence of edges and steers the diffusion process. Hence, the quality of the restoration depends on the quality of this prior. WEICKERT has generalized (1.3) to anisotropic diffusion replacing $g(\|\nabla u_\sigma\|)$ by a tensor $D = D(J_\rho(u_\sigma))$ depending on the regularized structure tensor $J_\rho(u_\sigma)$. The parameter $\rho$ indicates a component-wise linear smoothing of $u_\sigma \otimes u_\sigma$ of time $\frac{\rho^2}{2}$. The idea is to smooth particularly *along* edges and prohibit by construction of $D$ an undesired smoothing *across* dominant edges. Here, $J_\rho(u_\sigma)$ is an indicator of the local image structure.

However, the quality of this prior depends also on the quality of the image itself. If precise information about the edges and feature directions would be available then $g$ resp. $D$ could be constructed in an exact way and yield a good restoration. Conversely, a good restoration would allow a robust and exact estimation of edges and feature directions. However, the evolution of the regularized equation (1.3) or the anisotropic diffusion pays respect to this: the diffusion coefficient resp. diffusion tensor ideally depends on the current function $u(t)$ during the evolution, which is expected to be an improved version of $u_0$.

In their pioneering paper, MUMFORD & SHAH [163] proposed the minimization of the following energy functional:

$$E_{MS}(u, \Gamma) = \int_\Omega (u - u_0)^2 dx + \frac{\mu}{2} \int_{\Omega \setminus \Gamma} \|\nabla u\|^2 \, d\mu + \nu \mathcal{H}^{d-1}(\Gamma) \tag{1.4}$$

where $u_0$ is the initial image defined on an open bounded set $\Omega \subset \mathbb{R}^d$. Here $\alpha, \beta$ are positive weights. The idea is to find an approximation $u$ of $u_0$ in the least-squares sense. Furthermore $u$ ought to be smooth, but only apart from a yet to be found discontinuity set of $u$, which is denoted by $\Gamma$ (set of potential edges). Hence the second integral imposes smoothness on $\Omega \setminus \Gamma$. Furthermore one incorporates the length of $\Gamma$ in the $d - 1$-dimensional Hausdorff-measure into the energy. Here, this contour can be considered as an analogon of $g$: it prohibits smoothing across features given by $\Gamma$. However, rather than being chosen *a priori*, it is an optimization variable and minimization of (1.4) means to simultaneously find $\Gamma$ and $u$, such that $\Gamma$ is an

approriate "feature set" of $u$, $u$ is a good approximation of $u_0$ in the $L^2$ sense and the length of $\Gamma$ is not too large. Thus it pays respect to the fact, that $u$ and $\Gamma$ depend on each other.

Moreover we want to mention geometric flows as *mean curvature motion* of the level lines of an image, which corresponds *geometric diffusion* of the level lines understood as submanifolds. We will describe this equation in more detail in Chapter 2, however we want to mention that PAUWELS, FIDDELAERS & VAN GOOL [171] and also SAPIRO [182] suggested to incorporate edge information of the image to steer the diffusion process in a similar way as in (1.3). PREUSSER & RUMPF then extended this idea to fully anisotropic mean curvature flow, which respects prominent feature directions of the level sets or surfaces. Here the *Weingarten map* plays the same rôle as the structure tensor for images. Once more the quality of the reconstruction depends on the quality of the prior and vice versa.

### 1.2.2   Registration and feature extraction

It is evident that the richness of available information about the local image structure influences the quality and robustness of feature extraction. Since images are corrupted by noise, simple edge detectors are often based on a certain threshold parameter to avoid over-identification. As an example consider the identification of edges by thresholding the gradient magnitude. Thresholding however is a highly unstable process: small perturbations of the image can lead to an entirely different set of detected edges. This indicates a high degree of ambiguity when the measured indicator is close to the threshold. In the case of multichannel data, this ambiguity is somewhat reduced. Let us suppose, that we have an exact registration of an MR and a CT image of the same patient available. In that case, ambiguous edges in the MR image, e. g., along the boundary of a bone structure might be clearly detectable in the other image. Hence, in the same fashion as feature detection in color images, the detection of features in the MR-CT pair is much more robust. Another way of feature detection is *segmentation*. Segmentation by *active contours* or *snakes* [135, 77, 42, 182] is done by evolving an initial curve or surface towards the boundary of an object. It is most often also based on some kind of feature detector, which allows to devise *external forces* which attract the contour towards dominant edges. In contrast to pure feature extraction, also forces depending on the curve itself (*internal forces*) play an important rôle, for instance controlling the length or the curvature of the contour. Once such internal contributions are incorporated, the segmentation process is no longer purely local. By the same kind of arguments as above the availibility of different modalities significantly facilitates the segmentation process. Segmentation can also be performed by minimizing the Mumford-Shah functional by an optimization over a space of contour sets. These contour sets are a finite union of Jordan curves. For multichannel data the fidelity term $(u - u_0)$ and the smoothness term $\|\nabla u\|^2$ could now be measured in several images, and again render the process of finding the contour $\Gamma$ more robust.

Conversely, imagine two images that are not yet registered, but that a precise segmentation of a particular object is available. As we will see later, the alignment of such segments is not hard to achieve. What remains is to perform a registration which already receives valuable hints about the position of certain features.

### 1.2.3   Registration and image restoration

The link between registration and image restoration already becomes clear by the considerations from above. However, every registration technique naturally depends on the two images, given as a reference and a template. As we will point out in subsequent sections, the task of registration is in general *ill-posed*. Without regularization these registation problems lack stability, uniqueness and existence properties. Hence, the situation becomes even much worse if the data is strongly corrupted by noise and hence the application of an image restoration method is essential. As described above, however a proper registration facilitates the process of feature preserving smoothing of both images.
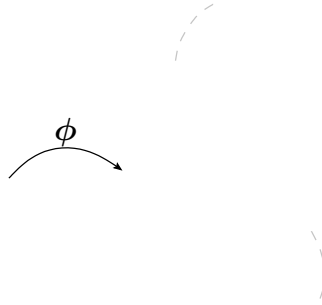
Figure 1.2: *Missing information in image registration tasks. In the CT image the right, some part of the skull is missing. A prior inpainting will prevent the registration from unpredictable results. Alternatively the matching region might be adjusted automatically and the missing structure be reconstructed on account of the knowledge of the reference shape on the left.*

### 1.2.4 The rôle of inpainting

The problem of image inpainting (also referred to as disocclusion) refers to the reconstruction of hidden domains by taking into account information from the surrounding border.

In the early work [45] CASELLES, MOREL & SBERT have introduced the *absolute minimal Lipschitz extension model* (AMLE) derived from fundamental axioms, like translation invariance, rotation invariance, comparison principle, stability and regularity. MASNOU & MOREL [148] have proposed a variational approach based on the geometry on the level lines, by taking into account geometric quantities as length and curvature and minimizing

$$e_{\text{EA}}[\mathcal{M}] = \int_{\mathcal{M}} (\alpha + \beta h^2) \, \mathrm{d}A. \tag{1.5}$$

This model of *Euler's elastica* has been formulated by treating the level lines parametically. Later, BERTALMIO, BERTOZZI & SAPIRO have applied models borrowed from fluid dynamics to inpainting problems [25].

Level set methods allow to evolve all level lines simultaneously, which has been exploited for example by BALLESTER ET AL. who have coupled the interpolation of normal fields to the interpolation of the level lines [15] or CHAN & SHEN who formulated a level set approach for the *Euler's elastica* model [52, 49]. They used a finite difference upwind scheme for the discretization of the resulting fourth order flow. ESEDOGLU & SHEN [109] have combined the MUMFORD-SHAH functional with fourth order inpainting techniques, using a conjecture of DI GIORGI to approximate the geometric flow that minimizes the *Euler's elastica* energy by a fourth order phase field model. Many of those approaches have in common that they, minimize an energy which incorporates the *Willmore energy*

$$e_W[\mathcal{M}] = \int_{\mathcal{M}} h^2 \, \mathrm{d}A.$$

We also refer to the works [178, 56, 50, 26, 199, 17, 162] for related approaches on inpainting.

For segmentation the *Willmore energy* provides a meaningful *internal* energy in regions, where no significant edge indicator is available. In those regions, the shape of the curve should be extended as smoothly as possible, a task which can be interpreted as a weak form of inpainting.

Sometimes information is also missing in images which are the input for a registration problem. Instead of simply masking out a particular region, it is more favorable to inpaint the missing information before the registration process. Once the registration is known the process of in-
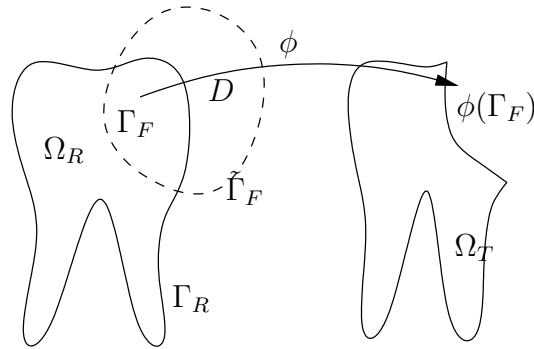
Figure 1.3: *Model-based restoration: The contour $\Gamma_R$ is partially matched on the corresponding contour $\Gamma_T$. The aim is to identify the area region $D$ in which the image of $\phi(\Gamma_R)$ does not relate to the contours of $\Omega_T$ automatically. In this region the image $u_T$ that corresponds to the edges given by $\Gamma_T$ may be restored by knowledge of the image structure of the reference $u_R$ in the preimage $\phi^{-1}(D)$.*

painting can be adjusted by exploiting morphological information from the other image, i. e., to adjust the geometry of the isophotes.

### 1.2.5  Further directions

In some image registration problems, certain structures may be corrupted or not be visible in one of the images and the boundary of these regions may not even known. In such a situation, the inpainting region has to be found automatically during the registration process, which aligns features and regions of high similarity only in the complement of that region (see Figure 1.3). Since the contour can only be detected in the exterior of the inpainting region, the Willmore energy represents a suitable regularization for the edge contour *within* the inpainting region. It ensures that the contour is smoothly extended into the inpainting domain. This process may be followed by a *model-based restoration*, which corresponds to the reconstruction of the isophotes by knowledge of the reference morphology as described at the end of Section 1.2.4 .

An immense speed-up of image processing tasks can be achieved by special implementations on modern graphics hardware. Level set algorithms for segmentation [180, 141] on graphics processing units (GPUs) can be performed in *real-time* even in volumetric data sets with simultaneous visualization of the segment. In [105, 104] a unimodal registration algorithm has been implemented on DirectX 9[4]-compatible graphics hardware with a speed up factor of 10 and higher.

### 1.2.6  Remarks

Unfortunately the problems described above do in general depend nonlinearly on each other, for instance, the Perona-Malik evolution depends non-linearly on the feature indicators. Acquired features with respect to a given registration depend nonlinearly on the input images for the matching problem etc. The coupling of different problems requires either some sort of iteration outer iteration or directly modelling a problem which comprises the desired subproblems and eventually leads to a nonlinear problem as a whole.

In Chapter 5 we will combine image restoration, feature extraction and image registration into a single model.

---

[4]Registered trademark of Microsoft Corp.

## 1.3 Unimodal registration

The simplest choice for measuring image similarity is to consider $L^p$ norms. It is in general not appropriate to assume Sobolev-regularity of images. Obviously these norms are not strong enough to capture geometrical characteristics. However, they are an important prototype to devise regularization approaches and numerical algorithms.

In the following, we will first use a simple similarity measure and concentrate on robust and efficient multiscale approaches for the solution of problems with large displacement and subsequently carry over to purely geometrical ideas.

Let us consider the following prototype problem. We now assume that the pair of images to be registered has been acquired by the same sensor and in a comparable environment. Then we can assert that if a certain physical property leads to a particular acquired image intensity in one image, it would lead to the same intensity in the other image. However, in general we obviously cannot assume the converse, namely that image intensities indicate uniquely which physical property has been measured.

Let us for now assume that the imagespace is $\mathscr{I} := \mathscr{C}^1(\Omega)$ Hence, calling $u_T \in \mathscr{I}$ the *template* and $u_R \in \mathscr{I}$ the *reference*, we aim at finding a deformation $\phi \in \mathcal{V} := L^2(\Omega)^n$, such that

$$u_T \circ \phi \approx_{\mathbb{D}} u_R \quad \text{in the sense that} \quad \mathbb{D}[u_T, u_R, \phi] := E[\phi] := \frac{1}{2} \int_\Omega |u_T \circ \phi - u_R|^2 \, \mathrm{d}\mu \to \min!$$

Obviously, the corresponding minimization problem is without further restriction to the imagespace or the space of admissible deformations not uniquely solvable and thus does not satisfy Hadamard's conditions of *well-posedness*. These conditions are the following:

(i) For all admissible data there exists a solution.

(ii) For all admissible data the solution is unique.

(iii) The solution depends continuously on the data.

As an illustrative example let us consider a displacement which keeps all level sets of $u_T$ fixed, i. e., $\{u_T = c\} = \{u_T \circ \Lambda = c\}$ for all $c \in \mathbb{R}$, then obviously for all $\phi \in \mathcal{V}$ we have $E[\phi] = E[\Lambda \circ \phi]$. There is a continuum of such deformations $\phi$ in a suitable set $\mathcal{V} = \{\phi \in W^{1,2}(\Omega; \mathbb{R}^n) : \phi(\Omega) = \Omega\}$ since $u_T \in \mathscr{C}^1(\Omega)$.

For $\psi \in \mathscr{C}_0^\infty(\Omega; \mathbb{R}^n)$ we can directly derive

$$\langle E'[\phi]; \psi \rangle_{\mathcal{V}' \times \mathcal{V}} = \int_\Omega (u_T \circ \phi - u_R) \nabla u_T \circ \phi \cdot \psi \, \mathrm{d}\mu \tag{1.6}$$

where $\langle \cdot, \cdot \rangle_{\mathcal{V}' \times \mathcal{V}}$ denotes the dual pairing in $\mathcal{V}' \times \mathcal{V}$. Hence we obtain the usual $L^2$-representation of the Fréchet-derivative of $E$ as the representation of $E'$ in the $L^2$ scalar product,

$$\mathrm{grad}_{L^2(\Omega)^d} E[\phi] = (u_T \circ \phi - u_R) \nabla u_T \circ \phi$$

if the right hand side of (1.6) is defined. A first, naive, approach to find the solution of the minimization problem would be to consider the $L^2$-gradient flow

$$\begin{aligned} \partial_t \phi &= -\mathrm{grad}_{L^2(\Omega)^d} E[\phi] & \text{in } \mathbb{R}^+ \times \Omega, \\ \phi(0) &= \phi_0 & \text{on } \{0\} \times \Omega. \end{aligned} \tag{1.7}$$

Due to the ill-posedness unregularized gradient flows don not work well in practice.

## 1.4 Regularization

As it has been pointed out in the exposition of the previous section, registration problems are typically ill-posed. This is roughly speaking due to the "high-level of non-uniqueness" and the irregular space of minimizers of the disparity measure. Suitable regularization methods are of crucial importance to methodologically and computationally overcome the problem of ill-posedness.

Regularization has two main aspects.

(i) **Choice criterion**—As we have pointed out previously, the unregularized variational registration problem (1.1) which is based solely on maximizing similarity, in general admits meaningless solutions. This is due to the fact that the stated variational problem only takes into account the properties of the deformed template and not the properties of the deformation itself and can hence be regarded as highly under-determined. Regularization imposes further restrictions on the solution. More precisely it chooses a solution from the set of minimizers, which is optimal with respect to a further measure on the solution itself. For instance, in the theory of regularization of linear inverse problems (cf. e. g. [108]), Tikhonov regularization strategies yield in the limit[5] the computation of the *Moore-Penrose* inverse of operators which are by itself not invertible and ill-posed. In a variational setting, a large amount of local minima are ruled out by regularization strategies. On the other hand regularizations do not, in general, ensure the existence of a unique minimum.

(ii) **Stability**—Although the unregularized problem is typically solvable by admitting minimizers, the high degree of ill-posedness and non-uniqueness results in numerical problems. In the discrete viewpoint, ill-posedness translates into a prohibitively high condition number. In a variational setting, local minima can be accumulated so densely in the set of solutions as to render the task of global optimization almost impossible.

In this thesis we have considered three complementary types of regularizations. Before we describe those approaches in detail, we first give a short overview and motivate their incorporation and combination in case of the registration problem.

### 1.4.1   Tikhonov regularization

#### Linear inverse problems

Let us first consider linear inverse problems of finding a solution $x$ in the Banachspace $\mathscr{X}$ such that

$$Fx = y \tag{1.8}$$

with $F : \mathscr{X} \to \mathscr{Y}$.

We call $x \in \mathscr{X}$ a *least-squares solution* of (1.8), iff $\|Fx - y\| = \inf \{ \|Fz - y\| \, : \, z \in \mathscr{X} \}$. Furthermore, we call $x$ a *best-approximate* solution of (1.8) iff it is a *least-squares solution* and

$$\|x\|_{\mathscr{X}} = \inf \{ \|z\|_{\mathscr{X}} \, : \, z \text{ is } \textit{least-squares solution} \text{ of (1.8)} \} \, .$$

Such *best-approximate* solutions are closely related to the *Moore-Penrose* inverse of $F$: If we define

$$\tilde{F} := F\big|_{\ker(F)^{\perp}} : \ker(F)^{\perp} \to \operatorname{range}(F),$$

then the *Moore-Penrose* inverse $F^{\dagger}$ of $F \in \mathscr{L}(\mathscr{X}, \mathscr{Y})$ is defined as the unique linear extension of $\tilde{F}^{-1}$ to $\mathcal{D}(F^{\dagger}) := \operatorname{range} F \oplus (\operatorname{range} F)^{\perp}$ with $\ker F^{\dagger} = \operatorname{range}(F)^{\perp}$ (see for instance the book of ENGL, HANKE & NEUBAUER [108, Def. 2.2] for a detailed treatise of the regularization methods for inverse problems). Then for $y \in \mathcal{D}(F^{\dagger})$ the problem $Fx = y$ has a unique *best-approximate* solution $x^{\dagger} := F^{\dagger} y$ ([108, Thm. 2.5.]).

For ill-posed problems in which only perturbed data $y^{\delta}$ is given instead of $y$, $F^{\dagger}$ is not a useful approximation of $F^{\dagger} y$, due to the fact that $F^{\dagger}$ is an unbounded operator. Classical *Tikhonov regularization* consists of the minimization of

$$\|Fx - y\|_{\mathscr{Y}}^{2} + \alpha \|x\|_{\mathscr{X}}^{2}$$

with a regularization parameter $\alpha > 0$.

It can be shown, that for suitably chosen regularization strategies (assuming decreasing amount of noise level $\delta$ in the data) and for reducing $\alpha \to 0$, the minimizers $x_{\alpha}$ converge to the Moore-Penrose $F^{\dagger} y$ in $\mathscr{X}$.

---

[5]The limit of solutions for the regularized problems for diminishing scaling of the regularization, with if necessary the extraction of a subsequence.

**Nonlinear problems**

Similar concepts can be carried over to the nonlinear case, even though so far, the theory of Tikhonov regularization is by far not so well developed as in the linear case. Here, we want to solve

$$F(x) = y, \tag{1.9}$$

where $F$ is a nonlinear operator between Banach spaces $\mathscr{X}$ and $\mathscr{Y}$. See the work of SCHERZER & WEICKERT [185] for relations of diffusion filtering and regularization techniques. More general than in the linear case where we looked for *best-approximate* solutions, one may look for solutions to (1.9) which are optimal with respect to a regularization energy $E_{\mathrm{reg}}$.

Consider the minimization problem (1.1) and an energy $E_{\mathrm{reg}}[\phi]$, which itself fulfills lower semicontinuity and growth conditions to ensure the existence of a minimizer. Regularization energies are usually chosen such that a finite energy implies some kind of regularity. Then one considers the competitive combination of energies and formulates the minimization problem

$$E[\phi] + \alpha E_{\mathrm{reg}}[\phi] \to \min! \tag{1.10}$$

where $\alpha > 0$. There is obviously a trade-off between minimizing the disparity and keeping the transformation smooth by keeping $E_{\mathrm{reg}}$ small. For high values of $\alpha$ the regularization dominates and will eventually prohibit precise alignment with respect to the similarity measure. When $E_{\mathrm{reg}}$ is given as a Dirichlet energy, minimization takes place in $H^{1,2}(\Omega)^n$, and since for now $\mathscr{I} = \mathscr{C}^1(\Omega; \mathbb{R}^n)$, we see that the overall integrand satisfies Caratheodory's conditions and coercivity, and hence we obtain a minimizer in $H^{1,2}(\Omega)^n$.

In Chapter 4 we will show (for a slightly reformulated minimization problem) that the sequence of minimizers $\phi_\alpha$ will allow the choice of a subsequence which converges to a minimizer of $E[\phi]$ and is optimal with respect to the regularization $E_{\mathrm{reg}}$ and thus yield a similar interpretation as the *Moore-Penrose* inverse of a linear operator, which selects an optimal solution with respect to the norm in $\mathscr{X}$.

In this thesis we are particularly interested in non-quadratic regularization energies, which apart from regularity ensure also injectivity of the solution, which is impossible to ensure by quadratic energies. In particular we will consider hyperelastic energies, and apply the framework of the direct methods in the calculus of variations for vectorial energies with polyconvex integrands. Furthermore these energies allow to prove existence also for imagespaces, where Caratheodory's condition is violated on a "small" set. We will consider the convergence of sequences of minimizers by observing that the regularized energies $\Gamma$-converge to the unregularized energy.

From a practical point of view, especially in intra-individual registration the reason for a deformation over a longer period is often at least to a large extent due to elastic deformations. In case of deformations resulting from diseases, such as growth of malignant tumors, this is not necessarily the case. However, due to the complexity of the nature of tumor growth or other morphological changes in pathology, those growth processes are difficult to model and to simulate. Nevertheless the hyperelastic energy helps to rule out meaningless solutions and maintains smoothness and injectivity which are still reasonable assumptions. We will describe this in more detail in Chapter 3.

### 1.4.2   Regularized gradient flows

A completely different point of view is given by a regularization of update directions that are required in gradient descent methods. In practice, to be able to solve the regularized problem (1.10), $\alpha > 0$ cannot be arbitrarily small. The ill-posedness would become too large, and hence cause problems due to a too high amount of local minima. On the other hand, if $\alpha$ is too large, the regularization energy will become very dominant and thus the minimization of the regularized problem will yield solutions which are far from maximizing the similarity measure of the images.

The choice criterion induced by a regularized metric is given by the idea, that those solutions should be ruled out, which cannot be reached by smooth paths from one initial deformation
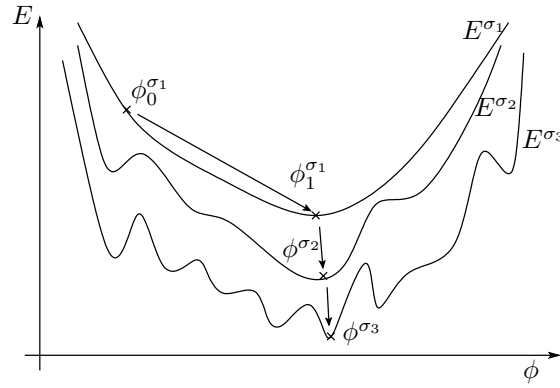
Figure 1.4: Multiscale minimization: Starting with an initial guess $\phi_0^{\sigma_1}$ the minimum $\phi_1^{\sigma_1}$ of the coarse representation of the energy $E^{\sigma_1}$ is not difficult. Taking this minimium as the starting point for the next scale is an immense aid to find the global minimum on the finest scale $E^{\sigma_3}$.

(typically the identity) to the target deformation. This idea is closely related to the works of CHRISTENSEN, GRENANDER, MILLER, TROUVÉ, YOUNES [106, 120, 58, 59, 57, 155, 156, 155] and coworkers who have considered smooth paths by local diffeomorphisms. These paths are geodesics with respect to a metric given by a differential operator integrated over time.

A regularized metric can also be interpreted as a different scalar product on the Hilbert space of deformations (cf. CLARENZ, DROSKE & RUMPF [71]). Such metrics may also exploit information about the images and respect image features, especially feature directions. Furthermore the metric can be Riemannian, i. e., depend on the particular deformation itself. In this thesis we will present a fully geometric interpretation of the NAGEL-ENKELMANN model [164] for feature based regularization of infinitesimal flow fields and embed this into the framework of metrics.

The gradient with respect to a general metric is then given by Riesz'-representation theorem:

$$g(\mathrm{grad}_g E[\phi], \psi) = \langle E'[\phi]; \psi \rangle_{\mathcal{V}' \times \mathcal{V}} \qquad \forall \psi \in \mathcal{V}.$$

In combination with Tikhonov regularization, the regularized gradient flows provide a very convenient framework for stabilizing the energy minimization by direct methods.

In Chapter 2 we give examples of suitable metrics for image matching, which have a regularizing impact on the gradient direction. Furthermore we compare the metric point of view with iterative Tikhonov regularizations, Levenberg-Marquart methods, devise efficient numerical algorithms and present results.

### 1.4.3  Multiscale methods

Tikhonov regularization and regularized gradients impose smoothness on the deformation and the flow itself. They however do not address the point of locality. Gradients depend on local quantities of the image. If the spatial difference in the images to be matched is very large the gradient may be meaningless even after regularization by a metric. Simply consider a pair of non-overlapping shapes with a constant background.

The incorporation of multiscale methods mainly aims at providing coarser energy landscapes and at improving the regularity of the energy functional itself. In general, multiscale methods provide smoothing filters, that yield a coarsening, usually by removing undesired information such as noise. If we apply such filters to the data that will be incorporated into the registration energy, we naturally obtain a much coarser energy-landscape. The most basic scale space is generated by linear diffusion which corresponds to Gaussian filtering, i. e., the convolution with a Gaussian kernel. Information is transported with infinite speed, i. e., the Green's function has infinite support, which means that information is blurred *globally* for arbitrary small scale parameters. In the context of energy minimization it has the convenient effect, that minor local minima are destroyed. Furthermore it broadens the regime of deformations which will by the gradient flow lead to the same local or global minimum. As we will describe later in more
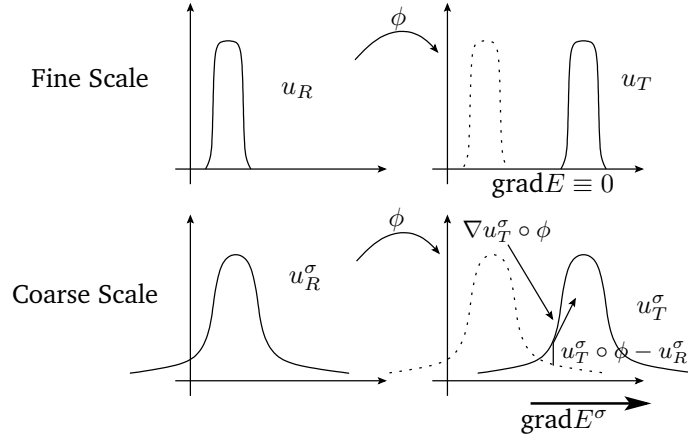
Figure 1.5: In the case of non-overlapping shapes the gradient flow will lead to degenerate solutions. After smoothing the input images the two objects will start to "see" each other.

detail, we start first with on coarse scale to avoid a high amount of local minima. Then the scale is successively reduced in order to resolve finer details in the images until the level of noise is reached.

## 1.5 The geometry of images: Morphological methods

### 1.5.1 Preliminaries

We will need an approriate notion of level sets of functions, which are not necessarily continuous. The following definition can be found for instance in [111].

**Definition 1.5.1 (Approximate limits).** *For a Borel function $u : \Omega \to \mathbb{R}$, we define the approximate* $\limsup$, *as follows*

$$\text{ap} \limsup_{y \to x} u(y) := \inf \left\{ t \in \mathbb{R} \ : \ \lim_{r \to 0} \frac{\mu(B_r(x) \cap \{u > t\})}{\mu(B_r(x))} = 0 \right\}$$

*Similarly the approximate* $\liminf$ *of $u$ is given by*

$$\text{ap} \liminf_{y \to x} u(y) := \sup \left\{ t \in \mathbb{R} \ : \ \lim_{r \to 0} \frac{\mu(B_r(x) \cap \{u < t\})}{\mu(B_r(x))} = 0 \right\}$$

*and $u$ is approximately continuous at $x$, iff* $\text{ap} \limsup u(x) = \text{ap} \liminf u(x)$ *in which case we call this value* $\text{ap} \lim u(x)$.

**Remark 1.5.2.** *If* $\liminf u$ *(*$\limsup u$*) exists then* $\text{ap} \liminf u$ *(*$\text{ap} \limsup u$*) exists and* $\liminf u = \text{ap} \liminf u$ *(*$\limsup u = \text{ap} \limsup u$*).*

**Definition 1.5.3 (Morphology).** *For a given image $u \in L^\infty(\Omega)$ we define*

$$\mathcal{M}_c[u] = \{x \in \Omega \ : \ \text{ap} \liminf u(x) = c\} \qquad \mathscr{M}[u] = \{\mathcal{M}_c[u] \ : \ c \in \mathbb{R}\}$$

*and call $\mathscr{M}[u]$ the morphology of the image $u$. We say two images $u, v$ are congruent iff* $\mathscr{M}[u] = \mathscr{M}[v]$.

By definition of $\mathscr{M}[u]$ the morphology is invariant under arbitrary contrast transformations $g : \mathbb{R} \to \mathbb{R}$, i. e.,

$$\mathscr{M}[u] = \mathscr{M}[g \circ u].$$

Another notion of the morphology has been originally introduced by MATHERON [149] and also taken into account by CASELLES, COLL & MOREL [43]. They considered the so called upper topographic map which is defined as the union of $\mathcal{X}_c u = \{u \geq c\}$. By construction they are related by $\partial \mathcal{X}_c u \setminus \partial \Omega = \mathcal{M}_c[u]$.

Hence, any method which only depends on the morphology of the given images is contrast invariant. The goal of morphological methods is to devise methods—given for example as filters or other methods where the data is at least partially given by images—which only take into account the geometrical information of shapes within the images.

### 1.5.2 Differential geometry on implicit surfaces

Let us first translate differential geometric operators and entitities into the level set context. Embedded manifolds $\mathcal{M}$ are endowed with a mapping $x : \mathcal{M} \to \mathbb{R}^{d+1}$, where $d = \dim \mathcal{M}$, which induces the first fundamental form $g$ by transferring to the scalar product in $\mathbb{R}^{d+1}$, i. e., $g(v, w) := \langle Dx(v), Dx(w) \rangle$. The *Weingarten map* $S : T_p\mathcal{M} \to T_p\mathcal{M}$ is then given by

$$S := Dx^{-1} \circ Dn,$$

where $n$ corresponds to the normal field of $x(\mathcal{M})$. In classical differential geometry, gradients of functions $f \in \mathscr{C}^1(\mathcal{M})$ on manifolds are given $g(\mathrm{grad}_\mathcal{M} f, v) := v(f)$, for all $v \in T_p\mathcal{M}$, by Riesz-representation [97, 132]. In the level set context, functions are primarily given in the Euclidian frame.

By the implicit function theorem, we immediately obtain the following

**Lemma 1.5.4.** *Let $\phi : \mathcal{M} \to \mathcal{N}$ be a differentiable map, $\dim \mathcal{M} \geq \dim \mathcal{N}$, $c \in \mathcal{N}$ and $df(x)$ have rank $\dim \mathcal{N}$ for all $x \in \mathcal{M}$ with $\phi(x) = c$. Then $\mathcal{M}_c = \{x \in \mathcal{M} : \phi(x) = c\}$ is a differentiable submanifold of $\mathcal{M}$ with dimension $\dim \mathcal{M} - \dim \mathcal{N}$.*

In order, to eliminate the normal component of the Euclidian gradient, the correct analogon of gradients and divergence is given by considering only the tangential component. Let us now define the gradient and divergence on level sets (cf. [92, 118]).

**Definition 1.5.5 (Projection onto tangent space).** *For a level set function $\phi : \Omega \to \mathbb{R}$ and $\mathcal{M} = \mathcal{M}_c[\phi] = \{\phi = c\}$ we denote by*

$$P[\mathcal{M}] := P[\phi] := \left( \mathbb{1} - \frac{\nabla \phi}{\|\nabla \phi\|} \otimes \frac{\nabla \phi}{\|\nabla \phi\|} \right) \tag{1.11}$$

*the projection onto the tangent bundle $T\mathcal{M}$.*

**Definition 1.5.6 (Tangential gradient).** *The tangential gradient of a function $u \in \mathscr{C}^1(\Omega)$ with respect to a manifold $\mathcal{M}$ is given by (using the summation convention)*

$$\nabla_\mathcal{M} u = \nabla u - (n \cdot \nabla u)n = (\mathbb{1} - n \otimes n)\nabla u = P[\mathcal{M}]\nabla u = (u_{,i} - n_i n_j u_{,j})_i.$$

*See also the book of GILBARG & TRUDINGER [118, pp. 389].*

**Definition 1.5.7 (Tangential divergence).** *The tangential divergence of a smooth tangential vectorfield $v \in \mathcal{TM}$ is given by*

$$\mathrm{div}_\mathcal{M} v = \mathrm{div} v - (Dv\, n) \cdot n = v_{i,i} - n_i n_j v_{i,j}.$$

**Lemma 1.5.8 (Laplace-Beltrami operator).** *For a smooth function $u \in \mathscr{C}^1(\Omega)$ the Laplace-Beltrami operator with respect to the manifold $\mathcal{M}$ is given by*

$$\Delta_\mathcal{M} u := \mathrm{div}_\mathcal{M} \nabla_\mathcal{M} u = \Delta u - h \partial_n u - \partial_n^2 u. \tag{1.12}$$

*where $h$ denotes the mean curvature of $\mathcal{M}$.*

*Proof.* We calculate straightforwardly by using the previous definitions

$$
\begin{aligned}
\mathrm{div}_{\mathcal{M}} \nabla_{\mathcal{M}} &= \mathrm{div}\big((\mathbb{1} - n \otimes n)\nabla u\big) - \Big(D\big((\mathbb{1} - n \otimes n)\nabla u\big)n\Big) \cdot n \\
&= \mathrm{div}\nabla u - \big(\nabla(\nabla u \cdot n) \cdot n\big) - (\nabla u \cdot n)\mathrm{div}n \\
&\quad -(D^2 u\, n \cdot n) + \Big(\nabla(n \otimes n \cdot \nabla u)n \cdot n\Big) \\
&= \Delta u - \partial_n^2 u - (\nabla(\nabla u \cdot n)) \cdot n - (\nabla u \cdot n)\mathrm{div}n \\
&\quad +(\nabla u \cdot n)(\nabla n\, n) \cdot n + \Big((n \otimes n)\nabla(\nabla u \cdot n)\Big) \cdot n \\
&= \Delta u - \partial_n^2 u - (\nabla u \cdot n)\mathrm{div}_{\mathcal{M}}n \\
&= \Delta u - \partial_n^2 u - h\partial_n u
\end{aligned}
$$

Here we have used the fact that $\Big(((n \otimes n)\nabla(\nabla u \cdot n)) \cdot n\Big) = \big(\nabla(\nabla u \cdot n) \cdot n\big).$  $\qquad\square$

**Lemma 1.5.9 (Shape operator).** *Let* $\mathcal{M} = \mathcal{M}_c[u]$, *then the matrix representation of the Weingarten map on the tangent bundle* $T\mathcal{M}$ *is given by*

$$
\mathcal{S} = \frac{1}{\|\nabla u\|} P[\mathcal{M}] D^2 u P[\mathcal{M}].
$$

*Proof.* The matrix representation of the Weingarten map is given by $dx_i(\nabla_{\mathcal{M}} n_k))_{i,j}$, where $x = \mathbb{1}$. Let us first consider the the variation of the normalization,

$$
\frac{d}{d\epsilon}\frac{v + \epsilon w}{\|v + \epsilon w\|}\Big|_{\epsilon=0} = \frac{w}{\|v\|} - \frac{v \cdot v}{\|v\|^3}w = \left(\mathbb{1} - \frac{v \otimes v}{\|v\|^2}\right)w. \tag{1.13}
$$

We first evaluate the tangential gradient of the normal field:

$$
\begin{aligned}
\nabla_{\mathcal{M}} n &= P[u]\nabla\frac{\nabla u}{\|\nabla u\|} = \frac{D^2 u\|\nabla u\| - \nabla u \nabla\|\nabla u\|}{\|\nabla u\|^2} = P[u]\left(\frac{1}{\|\nabla u\|}D^2 u - \frac{(\nabla u \otimes \nabla u)D^2 u}{\|\nabla u\|^3}\right) \\
&= \frac{1}{\|\nabla u\|}P^2[u]D^2 u = \frac{1}{\|\nabla u\|}P[u]D^2[u].
\end{aligned}
$$

After restriction of $\nabla_{\mathcal{M}} n$ to the tangent space by projection, we obtain the desired result. $\square$

The following formula provides a curvilinear generalization of Fubini's theorem, and allows us to aggregate integrals, which are defined on level sets of a function $\phi : \Omega \subset \mathbb{R}^d \to \mathbb{R}$. The general version can be found in the book of EVANS & GARIEPY [111, Sec. 3.4.2].

**Proposition 1.5.10 (Coarea formula (level sets)).** *Let* $\phi : \Omega \to \mathbb{R}$ *be Lipschitz and* $f : \Omega \to \mathbb{R}$ *be a measurable function. Then*

$$
\int_{\Omega} f\|\nabla\phi\|\,\mathrm{d}\mu = \int_{\mathbb{R}}\int_{\Omega \cap \{\phi=c\}} f\,dA\,\mathrm{d}c.
$$

# Chapter 2

# Generalized gradient flows

BEFORE we move on to more sophisticated similarity measures, let us in this chapter first address the conceptual framework for the minimization of highly nonlinear minimization problems. As motivated in the introduction, we eventually aim to find a registration model, which is based on *geometric entities*. Nevertheless, we will remain within the variational framework throughout the thesis. The registration models under considerations will always be based on an energy which is supposed to be minimized in a stable and efficient way. For the sake of clarity, we will treat the minimization process and the modeling of different disparity measures, continuously as well as numerically, separately. The following methodological framework is versatile and turns out to be very convenient for a wide range of variational problems.

In this chapter, we will first discuss generalized gradient flows, or to be more precise, gradient flows which are endowed with a regularizing metric on the space of deformations. The regularizing effect is crucial also for the numerical setting. It induces regularity on the deformation during the flow, due to the fact that update directions are prevented from being irregular, and hence it allows to choose larger step sizes. Moreover, we will stabilize and globalize the minimization process through a multiscale approach.

The idea of finding a continuous formulation, which just through the definition of scalar products and corresponding Hilbert spaces induces regularity of the flow is not new. We will show relations to classical methods, which are widely used in the *inverse problems* community. The metric point of view however, is very convenient and allows to incorporate feature dependencies in a natural way.

In the third section of this chapter, we will address the efficient numerical solution of the continuous formulations.

## 2.1 Continuous formulation of generalized gradient flows

Let us recall the gradient flow (1.7). In a more general setting, gradients are defined by the representation of the Fréchet derivative in a metric $g$, i. e.,

$$g(\text{grad}_g E[\phi], \psi) = \langle E'[\phi]; \psi \rangle \qquad \forall \psi \in \mathscr{C}_0^\infty(\Omega; \mathbb{R}^d). \tag{2.1}$$

Now we consider the $g$-gradient flow of the minimization problem, i. e.,

$$\begin{aligned} \partial_t \phi &= -\text{grad}_g E[\phi] & \text{in } \mathbb{R}^+ \times \Omega, \\ \phi(0) &= \phi_0 & \text{on } \{0\} \times \Omega, \end{aligned} \tag{2.2}$$

which for the example (1.6) leads to the problem of finding $\phi : \mathbb{R}_0^+ \to \mathcal{V}$, such that

$$g(\partial_t \phi, \psi) + \langle E'[\phi]; \psi \rangle = 0 \qquad \forall \psi \in \mathscr{C}_0^\infty(\Omega; \mathbb{R}^d) \tag{2.3}$$

such that $\phi$ fulfills the initial condition.

**Notation 2.1.1.** *For a given metric $g$, we consider its representation $A_g : \mathcal{V} \to \mathcal{V}'$ in the duality pairing $(\mathcal{V}', \mathcal{V})$:*

$$g(\boldsymbol{\phi}, \boldsymbol{\psi}) = \langle A_g \boldsymbol{\phi}; \psi \rangle_{\mathcal{V}' \times \mathcal{V}}.$$

With this notation the $g$-gradient flow can also be written as

$$\partial_t \boldsymbol{\phi} = -A_g^{-1} E'[\boldsymbol{\phi}] \tag{2.4}$$

**Theorem 2.1.2.** *Suppose $\mathcal{V}$ is a Banach space and there exists a Banach space $\mathcal{W} \supset \mathcal{V}$, such that $\mathcal{W} \hookrightarrow \mathcal{V}'$ (continuous embedding) . Let $A_g$ be a linear isomorphism from $\mathcal{V}$ onto $\mathcal{W}$. Suppose $E' :$ is Lipschitz continuous mapping from $\mathcal{V}$ to $\mathcal{W}$.*

*Then there exists a unique solution of the evolution problem of finding for initial data $\phi_0 \in \mathcal{V}$ a solution $\phi : \mathbb{R}_0^+ \to \mathcal{V}$, such that*

$$\begin{aligned} \partial_t \boldsymbol{\phi} &= -A_g^{-1} E'[\boldsymbol{\phi}] \\ \boldsymbol{\phi}(0) &= \boldsymbol{\phi}_0. \end{aligned}$$

*Proof.* Follows directly by application of the Picard-Lindelöf Theorem for Banach spaces. $\square$

**Remark 2.1.3.** *For every metric $g$, the corresponding isomorphism $A_g$ is selfadjoint, positive definite. Hence, we obtain an important property with in the context of energy minimization, namely that descent directions are preserved, i. e.,*

$$\left\langle E'[\boldsymbol{\phi}]; grad_g E[\boldsymbol{\phi}] \right\rangle = g(grad_g E[\boldsymbol{\phi}], grad_g E[\boldsymbol{\phi}]) \geq 0.$$

## 2.1.1  Examples

Let us consider some possible examples for the choice of the metric.

(i) *$L^2$ metric*—The standard choice is given by the intrinsic scalar product of $L^2$, namely $g(\boldsymbol{\phi}, \boldsymbol{\psi}) = (\boldsymbol{\phi}, \boldsymbol{\psi})_{L^2}$. Higher order terms are neglected.

(ii) *$H^{1,2}$ metric*—A gradient flow formulation in $H^{1,2}(\Omega; \mathbb{R}^d)$ corresponds to the metric $g(\boldsymbol{\phi}, \boldsymbol{\psi}) = (\boldsymbol{\phi}, \boldsymbol{\psi})_{H^{1,2}} = (\boldsymbol{\phi}, \boldsymbol{\psi})_{L^2} + (D\boldsymbol{\phi}, D\boldsymbol{\psi})_{L^2}$, which obviously reacts upon strong gradients of its arguments. Here the weighting of $(\nabla\boldsymbol{\phi}, \nabla\boldsymbol{\psi})_{L^2}$ is fixed.

(iii) *Weighted $H^{1,2}$ metric*—If we now consider for given $\sigma > 0$, the metric

$$g^\sigma(\boldsymbol{\phi}, \boldsymbol{\psi}) = (\boldsymbol{\phi}, \boldsymbol{\psi})_{L^2} + \frac{\sigma^2}{2}(\nabla\boldsymbol{\phi}, \nabla\boldsymbol{\psi})_{L^2} \tag{2.5}$$

we get $A_g = \mathbb{1} - \frac{\sigma^2}{2}\Delta$, and hence obtain

$$grad_{g^\sigma} E[\boldsymbol{\phi}] = \left( \mathbb{1} - \frac{\sigma^2}{2}\Delta \right)^{-1} grad_{L^2} E[\boldsymbol{\phi}].$$

As corresponding spaces, we now take into account $\mathcal{V} = H^{1,2}(\Omega; \mathbb{R}^d)$ and $\mathcal{W} = L^2(\Omega; \mathbb{R}^d)$. The isomorphism property and thus the Lipschitz continuity of $A_{g^\sigma}^{-1}$ are well-known in this case, since $A_{g^\sigma}^{-1} u$ is determined as the solution $v \in H^{1,2}(\Omega; \mathbb{R}^d)$ of the problem

$$v + \tau\Delta v = u \text{ in } \Omega \qquad \partial_\nu v = 0 \text{ on } \Omega,$$

with $\tau = \sigma^2/2$ which is nothing else but a semi-implicit time step of the heat equation or equivalently as the minimization of the energy

$$I(v) = \frac{1}{2} \int_\Omega \left\{ (u - v)^2 + \frac{\sigma^2}{2} \|\nabla v\|^2 \right\} \, \mathrm{d}\mu.$$

We can interpret the incorporation of this metric as a smoothing of gradients with a diffusion filter with filter width $\sigma$.

(iv) *Weighted $H^{2,2}$ metric*—$g(\phi, \psi) = (\phi, \psi)_{L^2} + \frac{\sigma^2}{2}(\nabla\phi, \nabla\psi)_{L^2} + \frac{\sigma^4}{4}(\Delta\phi, \Delta\psi)_{L^2}$, and we obtain $A_g = \mathbb{1} - \frac{\sigma^2}{2}\Delta - \frac{\sigma^4}{4}\Delta^2$, where we now take into account the spaces $\mathcal{V} = H^{2,2}(\Omega)^n$ and $\mathcal{W} = L^2(\Omega)^n$. A related idea to higher order approach is due to MODERSITZKI & FISCHER who introduced a regularization that is based on the componentwise Laplacian of the deformation, which they called *curvature regularization* [158].

(v) *Rigidity enhancing metric*—For a given deformation field at time $t$, it is known that $\phi(t, \cdot)$ is *rigid*, iff

$$D\phi(t)\, D\phi(t)^T = \mathbb{1}. \tag{2.6}$$

For $\phi(t) = \mathbb{1} + \mathbf{d}(t)$ we see that

$$(\mathbb{1} + D\mathbf{d}(t))\,(\mathbb{1} + D\mathbf{d}(t))^T = \mathbb{1} + D\mathbf{d}(t) + D\mathbf{d}(t)^T + D\mathbf{d}(t)\, D\mathbf{d}(t)^T$$
$$= \mathbb{1} + D\mathbf{d}(t) + D\mathbf{d}(t)^T + o(\|D\mathbf{d}(t)\|^2)$$

and thus aim to penalize the deviation $D\mathbf{d} + D\mathbf{d}^T$ from $0$. Now, we want at finding a metric, such that the corresponding gradient directions $\mathrm{grad}_g E[\phi]$ are close to being *infinitesimally rigid*, i. e., pointwise $\mathrm{grad}_g E[\phi] + (\mathrm{grad}_g E[\phi])^T \approx 0$. Therefore it makes sense to define the following metric

$$g(\phi, \psi) = (\phi, \psi)_{L^2} + \mu \int_\Omega \epsilon(\phi) : \epsilon(\psi)\, \mathrm{d}\mu$$

where we define, taking into account the summation convention, $A : B = A_{ij} B_{ij}$ and as usual, the symmetrized deformation gradient (here used in an infinitesimal sense) $\epsilon(\phi) := \frac{1}{2}(D\phi + D\phi^T)$, which by Korn's inequality [60] yields $H^{1,2}$-ellipticity. We thus choose again $\mathcal{V} = H^{1,2}(\Omega)^n$ and $\mathcal{W} = L^2(\Omega)^n$. With the same kind of argument, one can motivate the incorporation of $\frac{\lambda}{2}(\mathrm{div}\phi, \mathrm{div}\psi)$, since $\mathrm{tr}(D\phi) = \mathrm{div}\phi$ and thus expresses changes of area or volume that can be penalized by the Lamé-constant $\lambda$. The Euler-Lagrange equation of the functional

$$\int_\Omega \epsilon(\phi) : \epsilon(\psi)\, \mathrm{d}\mu + \int_\Omega \frac{\lambda}{2}(\mathrm{div}\phi, \mathrm{div}\psi)\, \mathrm{d}\mu$$

corresponds to the Lamé-Navier equation.

## 2.2 Gradient flows on level set functions

Let us now study the evolution of the level sets by gradient flows. One possible approach is to first consider the manifolds given by the level sets separately, define a geometric motion, for instance as arising as a gradient flow of a geometric energy, or by directly formulating a geometric motion equation and reconstruct a new image intensity function from the evolved set of shapes. This approach allows the modeling to take place entirely with respect only to the shape or more precisely on purely differential geometric quantities. Instead of solving the motion equations separately, one may derive a velocity from the purely geometric model and formulate the problem via the level set equation, which for a given normal velocity of the level lines, describes the evolution of the corresponding level set function in time. A prominent example is given by the mean curvature flow. It is well known, that the steepest descent of the area functional corresponds to the evolution of the manifold in normal direction weighted by the negative mean curvature. By noting that for an intensity function $\phi$, the mean curvature is given by the divergence of the normal, one can insert this velocity into the level set equation and yield the level set formulation of the mean curvature flow.

Let us first consider an energy density $f$ on the manifold $\mathcal{M}$, i. e.,

$$e[\mathcal{M}] = \int_\mathcal{M} f\, \mathrm{d}A.$$

The $L^2$-surface metric on a manifold $\mathcal{M}$ is given by

$$g_{L^2(\mathcal{M})}(u,v) = \int_{\mathcal{M}} uv \, \mathrm{d}A.$$

We will later use $u$ and $v$ for scalar weights of normal variations $x_\epsilon = x + \epsilon u(x)n(x)$ of the surface $\mathcal{M}$. The gradient flow with respect to $g_{L^2(\mathcal{M})}$ is given by

$$\partial_t x = -\mathrm{grad}_{L^2(\mathcal{M})} e[\mathcal{M}] \quad \text{or equivalently} \quad (\partial_t x, \vartheta)_{L^2(\mathcal{M})} = -\langle e'[\mathcal{M}]; \vartheta \rangle \quad \forall \vartheta \in \mathscr{C}^\infty(\mathcal{M}).$$

### 2.2.1  Integration of the energies

Our aim is to evolve all level sets $\mathcal{M}_c$ of a given level set function $\phi$ simultaneously. To this end, we have to construct a global energy, which is defined over the entire domain $\Omega$. This can be achieved by an application of the co-area formula (see Prop. 1.5.10 and [111]). It allows to integrate over all level sets to define the global energy, i. e.,

$$E[\phi] := \int_{\mathbb{R}} e[\mathcal{M}_c]\mathrm{d}c = \int_{\Omega} \|\nabla\phi\| \, f \, \mathrm{d}\mu.$$

Here, we set $e[\mathcal{M}_c] = 0$ if $\mathcal{M}_c = \emptyset$.

### 2.2.2  Defining a metric on the space of level set functions

In order to realize a gradient flow, we have to build a metric on the whole ensemble of level sets $\mathscr{M}[\phi]$.

**Metrics on level set functions**

Let us revisit the level set equation

$$\begin{array}{rcll} \partial_t \phi + v\|\nabla\phi\| & = & 0 & \text{in } (0,T) \times \Omega, \\ \phi(0) & = & \phi_0 & \text{in } \Omega. \end{array} \tag{2.7}$$

It allows to establish a link between the tangent vector $s := \partial_t \phi$ and the normal velocity, which is given by $v$, namely $s = -v\|\nabla\phi\|$. Here we endow the space $\mathscr{L}$ of of level set ensembles which are represented by level set functions with a trivial structure and interprete $\partial_t \phi$ as a tangent vector.

These considerations motivate us to define the following metric on $\mathscr{L}$, again using the co-area formula. We take into account the metrics on the manifolds $\mathcal{M}_c$, which measure the scalar variations of the level set function. We obtain these by the level set formula, i. e., $v = -\partial_t \phi/\|\nabla\phi\|$ and write

$$\begin{aligned} g_\phi(s_1, s_2) & := & \int_{\mathbb{R}} \int_{\mathcal{M}_c} v_1 v_2 \, \mathrm{d}A \, \mathrm{d}c \\ & = & \int_{\Omega} \frac{s_1}{\|\nabla\phi\|} \frac{s_2}{\|\nabla\phi\|} \|\nabla\phi\| \, \mathrm{d}\mu = \int_{\Omega} s_1 s_2 \, \|\nabla\phi\|^{-1} \, \mathrm{d}\mu. \end{aligned}$$

Hence, having an appropriate geometric metric at hand, we are able to consider the gradient flow of the aggregated energy $E$. The simultaneous gradient flow of the $\mathscr{M}[\phi]$ is now given by

$$\partial_t \phi = -\mathrm{grad}_{g_\phi} E[\phi] \quad \text{which means } g_\phi(\partial_t \phi, \vartheta) = -\langle E'[\phi], \vartheta \rangle \quad \forall \vartheta \in \mathscr{C}_0^\infty(\Omega).$$

Hence, we are now in position to define

**Definition 2.2.1 (Aggregated geometric flow).** *For a given energy defined on manifolds $\mathcal{M}$, the corresponding gradient flow of the level set ensembles is given by*

$$\partial_t \phi = \int_{\Omega} \partial_t \phi \, \vartheta \, \|\nabla\phi\|^{-1} \, \mathrm{d}\mu = -\langle E'[\phi], \vartheta \rangle. \tag{2.8}$$

*for all functions $\vartheta \in \mathscr{C}_0^\infty(\Omega)$.*

**Example: steepest descent of the area functional**

Let us consider the area-functional $e[\mathcal{M}] = \text{area}(\mathcal{M})$. It follows immediately by the co-area formula that the aggregated energy and its first variation are given by

$$E[\phi] = \int_\Omega \|\nabla\phi\| \, \mathrm{d}\mu, \qquad \langle E'[\phi]; \vartheta \rangle = \int_\Omega \frac{\nabla\phi \cdot \nabla\vartheta}{\|\nabla\phi\|} \, \mathrm{d}\mu \quad \forall \vartheta \in \mathscr{C}_0^\infty(\Omega),$$

and we obtain the weak formulation of the evolution equation

$$\int_\Omega \partial_t \phi \vartheta \|\nabla\phi\|^{-1} \, \mathrm{d}\mu = - \int_\Omega \frac{\nabla\phi}{\|\nabla\phi\|} \cdot \nabla\vartheta \, \mathrm{d}\mu.$$

Indeed, this is the weak formulation of mean curvature motion in level set form [112]. Applying integration by parts and the fundamental lemma, we arrive at the classical level set formulation of the mean curvature flow:

$$\partial_t \phi - \text{div}\left( \frac{\nabla\phi}{\|\nabla\phi\|} \right) \|\nabla\phi\| = 0. \tag{2.9}$$

## 2.3 Metrics steered by image features

So far we have only considered metrics which are homogeneous in space. Let us now give a short review on an image dependent regularization technique which is typically used in the context of the determination of an *optical-flow* field [130, 2, 127, 5, 94, 173, 153, 175]. Consider a "movie" $u : [0, T] \times \Omega \to \mathbb{R}$, and let us adopt for now the usual assumption that the intensity along paths, that describe the movement of an object, does not change in time (known as *brightness-constancy* assumption). Furthermore, let us assume that $\Omega \subset \mathbb{R}^2$ within this section. Then for all such paths $x(t)$, we obtain $\partial_t u(t, x(t)) = 0$, which for $v = \dot{x}(t)$ then leads to the under-determined so called *optical-flow* equation

$$\nabla u \cdot v + \partial_t u = 0.$$

A typical approach for the solution to this system for $v$ is an unconstrained optimization problem of the form [127, 205]

$$E_{\text{of}}[v] = \int_\Omega f(\nabla u \cdot v + \partial_t u) + E_{\text{reg}}[v]$$

where $f$ is convex and $\partial_t u$ and $\nabla u$ are precomputed—in practice by some robust estimator. NAGEL&ENKELMANN[164] (see also [204]) have proposed the following, image dependent regularization for two-dimensional images and small $\lambda > 0$

$$E_{\text{NA}}[v] = \int_\Omega \frac{\nabla u^\perp \otimes \nabla u^\perp + \lambda^2 \mathbb{1}}{\|\nabla u\|^2 + 2\lambda^2} \nabla v : \nabla v \, \mathrm{d}\mu$$

with $A : B = \text{tr}(A^T B)$. Let us consider a small modification, namely

$$E_{\text{reg}}[v] = \int_\Omega \frac{\nabla u^\perp \otimes \nabla u^\perp + \lambda^2 \mathbb{1}}{\|\nabla u\|^2 + \lambda^2} \nabla v : \nabla v \, \mathrm{d}\mu.$$

We can rewrite the energy as

$$\begin{aligned} E_{\text{reg}}[v] &= \int_\Omega \frac{P\|\nabla u\|^2 + \lambda^2 \mathbb{1}}{\|\nabla u\|^2 + \lambda^2} \nabla v : \nabla v \, \mathrm{d}\mu \\ &= \int_\Omega \left(1 - \gamma(\|\nabla u\|)\right) \nabla v : \nabla v + \gamma(\|\nabla u\|) P \nabla v : \nabla v \, \mathrm{d}\mu \end{aligned}$$

with $\gamma(s) = 1 - 1/(1 + s^2/\lambda^2)$ and the notation $P = P[u] := \left(\mathbb{1} - \frac{\nabla u}{\|\nabla u\|} \otimes \frac{\nabla u}{\|\nabla u\|}\right)$. In two dimensions we obviously have $P = \frac{\nabla u^\perp \otimes \nabla u^\perp}{\|\nabla u\|^2}$. The geometric interpretation is thus the following: depending on the edge-indicator function $\gamma(\|\nabla u\|)$, which yields small values for flat gradients in smooth regions and is close to $1$ on edges, the energy is a convex-combination of a homogenous penalization of gradients in $v$ in smooth regions and a purely anisotropic penalization near edges, which is reflected by the projection $P$ on the tangent space of the level lines of $u$.

Alternatively, we propose to consider regularization energies on level sets $\mathcal{M}_c$ of $u$ and obtain by the co-area formula (1.5.10)

$$
\begin{aligned}
e[\mathcal{M}, v] &= \int_{\mathcal{M}} \gamma(\|\nabla u\|)\|\nabla_{\mathcal{M}} v\|^2 \, \mathrm{d}A \\
\Rightarrow \quad E_{\mathrm{reg}}[v] &= \int_{\mathbb{R}} e[\mathcal{M}_c, v]\mathrm{d}c = \int_{\Omega} \gamma(\|\nabla u\|)\|\nabla_{\mathcal{M}} v\|^2\|\nabla u\| \, \mathrm{d}\mu.
\end{aligned}
$$

The Fréchet-derivative of $E_{\mathrm{reg}}$ with respect to $v$ is given by

$$
\left\langle E'_{\mathrm{reg}}[v]; w \right\rangle = \int_{\Omega} \gamma P[u]\nabla v : \nabla w \|\nabla u\| \, \mathrm{d}\mu.
$$

Applying integration by parts, we see that the gradient corresponds to

$$
\mathrm{grad} E_{\mathrm{reg}} = -\mathrm{div}_{\mathcal{M}}\left(\gamma(\|\nabla u\|)\nabla_{\mathcal{M}} v\right) \qquad \text{in } \Omega.
$$

From the above considerations, we are motivated to define the following metric

$$
g_\gamma(\phi, \psi) = (\|\nabla u_R\|\phi, \psi)_{L^2} + \int_{\Omega} \gamma P[u_T \circ \phi]\nabla\phi : \nabla\psi \|\nabla u_R\| \, \mathrm{d}\mu.
$$

It is symmetric and positive definite. Let us remark, that the previous derivation can also be done, by first defining the metrics on the level sets of $u$ and then integrating those metrics by the co-area formula over all level sets. For the unimodal matching energy, this approach corresponds to a regularization within the set of invariant descent directions.

## 2.4   Relations to other formulations

### 2.4.1   Nonlinear Landweber iteration

Nonlinear inverse problems are often formulated in the following form: Given two Hilbert spaces $\mathscr{X}$ and $\mathscr{Y}$, and a mapping $F : \mathscr{X} \to \mathscr{Y}$ and some $y^\delta \in \mathscr{Y}$, find $x \in \mathscr{X}$, such that according to MOROZOV's discrepancy principle

$$
\|F(x) - y^\delta\|_{\mathscr{X}} \leq \delta
$$

is fulfilled. Here, $\delta$ indicates the noise level of the data. For a comprehensive treatment of the regularization of inverse problems we again refer to [108].

For the unimodal registration problem this translates the following way: Choose $\mathscr{X} = L^2(\Omega; \mathbb{R}^d)$ and $\mathscr{Y} = L^2(\Omega)$ and further set $F(\phi) = u_T \circ \phi - u_R$ for given images $u_T$ and $u_R$.

In a Hilbert space formulation, the energy is given by the scalar product. For the registration problem we have

$$
E[\phi] = \|F(\phi) - y^\delta\|_{\mathscr{Y}}^2.
$$

Derivation yields for Fréchet-differentiable $F$

$$
\langle E'[\phi]; \psi \rangle = (F(\phi) - y^\delta, F'(\phi)\psi)_{\mathscr{Y}} = (F'(\phi)^*(F(\phi) - y^\delta), \psi)_{\mathscr{X}}.
$$

We observe that the gradient is hence given by $\mathrm{grad}_{\mathscr{X}} E[\phi] = F'(\phi)^*(F(\phi) - y^\delta)$. Here $A^* : \mathscr{Y}' \to \mathscr{X}'$ denotes the adjoint of $A$ with respect to the given scalar product and the nonlinear *Landweber iteration*

$$
\phi^{k+1} = \phi^k - F'(\phi^k)^*(F(\phi^k) - y^\delta)
$$

is nothing else, than a discrete time stepping of the gradient flow. By this reasoning, if we endow $\mathscr{X}$ with a metric $g$, the adjoint $F'(\phi)^*$ implicitly incorporates inverse $A_g^{-1}$ of the representation $A_g$ of $g$.

### 2.4.2 Iterative Tikhonov regularization

Iterative Tikhonov regularization have been applied to image registration by HENN&WITSCH [125]. The idea is the following. Given $\phi^k$, find $\phi^{k+1}$ as the solution of the following minimization problem

$$\phi^{k+1} := \underset{\phi \in \mathscr{X}}{\arg\min}\, E[\phi] + \alpha_k \|\phi - \phi^k\|_g^2 \tag{2.10}$$

where $\alpha_k$ is a decreasing sequence of weights and where we have defined $\|\cdot\|_g := \sqrt{g(\cdot,\cdot)}$. As pointed out in [73], the Euler-Lagrange equation $\alpha_k g(\phi - \phi^k, w) + \langle E'[\phi]; w\rangle$ corresponds to an implicit time step of length $\alpha_k^{-1}$ of the regularized gradient flow, i. e,

$$\alpha_k(\phi^{k+1} - \phi^k) + \operatorname{grad}_g E[\phi^{k+1}] = 0$$

One obtains an explicit time step by considering a linearization of the energy integrand around $\phi$.

### 2.4.3 Regularized Levenberg-Marquart type methods

For twice Fréchet-differentiable $F : \mathscr{X} \to \mathscr{Y}$, let us consider first and second derivatives of $E = \|\cdot\|_{\mathscr{Y}}^2$

$$\langle E'[\phi]; v\rangle = \Big(F(\phi) - y^\delta, F'(\phi)v\Big)_{\mathscr{Y}} \tag{2.11}$$

$$\langle E''[\phi]; v, w\rangle = \Big(F'(\phi)v, F'(\phi)w\Big)_{\mathscr{Y}} + \Big((F(\phi) - y^\delta), F''(\phi)(v, w)\Big)_{\mathscr{Y}} \tag{2.12}$$

For a pure Newton type method, one iteratively has to solve

$$\operatorname{grad}F(\phi^n)(\phi^{n+1} - \phi^n) = y^\delta - F(\phi^n).$$

via

$$\operatorname{Hess} F(\phi^k)(\phi^{k+1} - \phi^k) = -\operatorname{grad}F[\phi^k].$$

   The *Hessian* is due to the second part of (2.12) difficult to invert and the ill-posedness of the problem results in a large condition number of the discretized Hessian. If we drop the second, non-symmetric part of the second derivative, we arrive at the *Gauss-Newton* method, which is still difficult to solve. The idea of the *Levenberg-Marquart* method is to iteratively determine the updates $v^{k+1} = \phi^{k+1} - \phi^k$ by minimizing

$$\frac{1}{2}\left\|F(\phi^k) + F'(\phi^k)v - y^\delta\right\|_{\mathscr{Y}}^2 + \frac{1}{2}\Big(Av^{k+1}, v^{k+1}\Big)_{\mathscr{X}} \tag{2.13}$$

which leads to the *Euler-Lagrange* equation

$$\Big(F(\phi^k) + F'(\phi^k)v^{k+1} - y^\delta, F'(\phi^k)w\Big)_{\mathscr{Y}} + \Big(A \cdot v^{k+1}, w\Big)_{\mathscr{X}} = 0 \qquad \forall w \in \mathscr{Y}$$

where $A : \mathscr{X} \to \mathscr{X}$ is a self-adjoint endomorphism. This rewrites into

$$\Big(F'(\phi^k)^*(F(\phi^k) - y^\delta), w\Big)_{\mathscr{Y}} + \Big(F'(\phi^k)v^{k+1}, F'(\phi^k)w\Big)_{\mathscr{Y}} + \Big(A \cdot v^{k+1}, w\Big)_{\mathscr{X}} = 0 \qquad \forall w \in \mathscr{Y}.$$

If we introduce the metric interpretation and define $A$ by $g(v, w) =: (Av, w)_{\mathscr{X}}$ and

$$g_{\mathrm{LM}}^\phi(v, w) := g(v, w) + \Big(F'(\phi^k)v, F'(\phi^k)w\Big)_{\mathscr{Y}} \qquad \forall v, w \in \mathscr{X}$$

we observe, since $F'(\phi^k)^*(F(\phi^k) - y^\delta)$ corresponds to the derivative of $E[\phi^k]$, that

$$v^{k+1} = \text{grad}_{g^{\phi^k}_{\text{LM}}} E[\phi^k]. \tag{2.14}$$

For the unimodal matching problem, the Levenberg-Marquart metric $g_{\text{LM}}$ is on account of

$$
\begin{aligned}
\left( F'(\phi^k)v, F'(\phi^k)w \right)_{\mathscr{Y}} &= \int_\Omega \left( F'(\phi^k)v \right) \left( F'(\phi^k)v \right) \mathrm{d}\mu \\
&= \int_\Omega \left( (\nabla u_T \circ \phi^k) \cdot v \right) \left( (\nabla u_T \circ \phi^k) \cdot w \right) \mathrm{d}\mu \\
&= \int_\Omega \left( \nabla u_T \circ \phi^k \otimes \nabla u_T \circ \phi^k \right) v \cdot w \, \mathrm{d}\mu
\end{aligned}
$$

given by

$$g^{\phi^k}_{\text{LM}}(v, w) = g(v, w) + \int_\Omega \left( \nabla u_T \circ \phi^k \otimes \nabla u_T \circ \phi^k \right) v \cdot w \, \mathrm{d}\mu.$$

**Theorem 2.4.1.** *If the Fréchet-derivative $F' \in \mathscr{L}(\mathscr{X}, \mathscr{Y})$ exists, and further, $g$ is metric on $\mathscr{X}$, such that $g(u, u) \geq c_g \|u\|^2_{\mathscr{X}}$ for some $c_g > 0$. Then (2.14) is well-defined.*

*Proof.* This is a straightforward application of the Lax-Milgram Lemma [1], since $\langle E'[\phi]; w \rangle =: f(w)$ is a bounded-linear form. The coercivity of $g^{\phi}_{\text{LM}}$ follows by

$$g^{\phi}_{\text{LM}}(u, u) \geq g(u, u) \geq c_g \|u\|^2_{\mathscr{X}}$$

The continuity follows from the properties of $F$. □

### Trust-Region methods

Levenberg-Marquart type methods (cf. HENN [124], HANKE [123]. See BURGER [37] for Levenberg-Marquart level set methods) of the form (2.13) are usually enhanced with a *Trust-Region* strategy: We recall that $\| \cdot \|_g := \sqrt{g(\cdot, \cdot)}$ and minimize

$$\frac{1}{2} \left\| F(\phi^k) + F'(\phi^k)v^{k+1} - y^\delta \right\|^2_{\mathscr{Y}} + \frac{1}{2} \|v^{k+1}\|^2_g \quad \text{subject to } \|v^{k+1}\|_g \leq \eta^k.$$

The so called *trust-region radius* $\eta_k$ is incorporated to control the accuracy of the linear approximation, i. e., we want to ensure that

$$F(\phi^k + v^{k+1}) \approx F(\phi^k) + F'(\phi^k)v \text{ for all } \|v\|_g \leq \eta^k$$

and furthermore ensure that the energy should be decreasing in every iteration.

Now for $v^{k+1} := \text{grad}^{\phi}_{g_{\text{LM}}} E[\phi^k]$, we observe that for $w = v^{k+1}$

$$\left\langle E'[\phi^k]; v^{k+1} \right\rangle = -\|v^{k+1}\|^2_g - \left( F'(\phi^k)v^{k+1}, F'(\phi^k)v^{k+1} \right)_{\mathscr{Y}} \leq 0.$$

Hence we can infer the following

**Lemma 2.4.2.** *Under the conditions of Thm. 2.4.1 $\phi$ is either a stationary point or there exists $\eta > 0$, such that*

$$E[\phi - \tau grad_{g^{\phi}_{\text{LM}}} E] < E[\phi] \quad \forall 0 < \tau \leq \eta.$$

A typical strategy for trust region control is Armijo's rule 2.6.5, which is also used for gradient methods and non-linear conjugate gradient methods, in other words, the trust-region radius $\eta^k$ has to be chosen small enough, to ensure such that

$$\frac{E[\phi^k + v^{k+1}] - E[\phi^k]}{\left\langle E'[\phi^k]; v^{k+1} \right\rangle_{\mathscr{X}' \times \mathscr{X}}} \leq \alpha. \tag{2.15}$$

If this condition is violated, one successively reduces $\eta^k$. Conversely, one aims to choose $\eta^k$ as large as possible within a predefined set of candidates, e. g., $\left\{\eta_0^l : l \in \mathbb{Z}\right\}$ for $\eta_0 > 0$. At this point the truly Riemannian character of the metric comes into play. We see that $g_{\mathrm{LM}}^\phi$ now varies for different deformations $\phi$. To ensure the condition (2.15) $g_{\mathrm{LM}}^\phi$ has to be adjusted with different weights in front of $g$, which then play the rôle of the Lagrange parameter.

## 2.5   Combination with a multiscale approach

Due to the complex structure of natural images, the energy landscape of the registration problem (1.1) engenders a large amount of local minima. This obviously poses serious problems in terms of energy minimization via a gradient flow or a nonlinear conjugate gradient method. They only converge robustly, if a unique minimum is given for a convex energy. One reason for the non-convexity is the dependence of the energy on the image data which is typically corrupted by noise. Such perturbations can only be modeled statistically and eliminate even local convexity of the energy. But as described in Section 1.3 the energy is ill-posed and possesses a possibly very irregular set of minimizers which can be reached by a gradient flow for different initial deformations, even if the gradient flow is regularized by a regularized metric. Local variations of the image only capture the local alignment of the images and hence may produce unexpected degenerate solutions even for simple images. Let us consider the following example:

When the energy is non-convex, global optimization is a difficult task. In this section we will propose to generate a family of perturbations of the energy $(E^\sigma)_{\sigma>0}$, such that the family $(E^\sigma))_{\sigma>0}$ consists of simplified versions of the original energy $E$. In the same spirit as in the *scale-space* theory of images [3], we aim at reducing the complexity or variability with increasing $\sigma$. In Chapter 4 we will discuss this in the framework of $\Gamma$-convergence in more detail.
Recall the definition of the unimodal registration energy

$$E_m[\phi] = \frac{1}{2} \int_\Omega |u_T \circ \phi - u_R|^2 \, \mathrm{d}\mu$$

and let us consider *scale-space operator* $\mathcal{S}^\sigma : \mathscr{I} \to \mathscr{I}$, which maps a given initial image $u$ to a coarser image $u^\sigma$ of scale $\sigma$. We define the coarsened registration energy by measuring the disparity of the coarsened versions of the intensity functions, i. e.,

$$E_m^\sigma[\phi] := \frac{1}{2} \int_\Omega |u_T^\sigma \circ \phi - u_R^\sigma|^2 \, \mathrm{d}\mu. \tag{2.16}$$

So far, we have not addressed the qualitative effect on coarsened images with respect to an increasing scale $\sigma$. Scale-space theory [203, 3] has been built upon a variety of axioms to define which requirements should be fulfilled for a meaningful *scale-space* operator (see for instance the fundamental work of ALVAREZ, GUICHARD, LIONS & MOREL [3], or the nice overview in the book of WEICKERT [203] for details).
Let us review some well-known examples of scale-space operators.

(i) *Linear diffusion*—The simplest choice of defining a scale on an image space is to apply the linear diffusion equation

$$
\begin{aligned}
u_t &= \Delta u &&\text{in } (0, T] \times \Omega \\
u(0) &= u_0 &&\text{in } \{0\} \times \Omega
\end{aligned}
$$

on a given initial image, which corresponds to the $L^2$ gradient flow of the Dirichlet integral $\int_\Omega \|\nabla u\| \, \mathrm{d}\mu$. It is well-known that diffusion until time $t$ can be obtained by the convolution with a Gaussian with standard deviation $\sqrt{2t}$. In order to obtain an interpretation of a *filter width* we define $\mathcal{S}_{\mathrm{lin}}^\sigma I$ as the solution of the diffusion equation at time $\frac{\sigma^2}{2}$.

(ii) *Perona-Malik-diffusion*—Linear diffusion obviously does not take into account any structural information from the input image, but rather blurs out noise as well as prominent

image features, such as edges the same way. PERONA&MALIK's pioneering idea [172] consists of introducing dependence of the diffusion coefficient on some local properties of the image itself. The weighting function $g(s) = 1/(1 + \frac{s^2}{\lambda^2})$ ensures for a given $\lambda > 0$, that the diffusion coefficient is small where edges are indicated by high-gradients:

$$u_t = \mathrm{div}(g(\|\nabla u\|^2)\nabla u) \quad \text{in } (0, T] \times \Omega.$$

(iii) *Mean curvature motion (curve shortening flow) and its variants*—the geometric equivalent of linear diffusion on images is given by the $L^2$-gradient flow of the area functional $e[\mathcal{M}] = \int_{\mathcal{M}} \mathrm{d}A$. This flow is given by $\partial_t x = \Delta_{\mathcal{M}} x$ on $\mathcal{M}$ for an immersion $X : \mathcal{M} \to \mathbb{R}^d$. Since $\Delta_{\mathcal{M}} x = -\mathrm{tr}(S)n = -hn$, where $h$ is the sum of the principal curvatures, the so called *mean curvature*, the flow is driven by the mean curvature of the immersed surface.

As shown in Section 2.2 (see the weak formulation in Eq. 2.9) the mean curvature flow for level set ensembles with *Neumann* boundary conditions is given by

$$u_t - \mathrm{div}\left(\frac{\nabla u}{\|\nabla u\|}\right)\|\nabla u\| = 0 \quad \text{in } (0, T] \times \Omega \qquad \partial_n u = 0 \quad \text{on } (0, T] \times \partial\Omega.$$

Well-posedness, existence of viscosity solutions [112], inclusion principles and convergence and stability of numerical schemes [88] are well-known. Many results are obtained by the fact, that the maximum principle of the second order geometric parabolic PDE can be transferred from non-geometric PDE theory and hence classical results can be applied. Similarly as in the case of linear diffusion, information and noise are destroyed homogeneously, however during the evolution of mean curvature flow, the diffusion only takes place geometrically with respect to the shape of level lines of the image. See [183] for a detailed treatise on geometric flows in the level set context. Hence, as we will consider in subsequent chapters, the scale-space which is generated by mean curvature motion is the simplest example of an adequate morphological coarsening. In the same spirit as PERONA & MALIK improved the linear image scale-space, SAPIRO [183] proposed to incorporate an image dependent weight into the geometric diffusion equation, i. e., $\partial_t x = \mathrm{div}_{\mathcal{M}}(g\nabla_{\mathcal{M}} x)$ where $g$ plays again the rôle of an edge indicator but now in the geometrical sense. CLARENZ ET AL. [69] extended this idea even further by locally analyzing the Weingarten map of the surface, which can be understood as the geometric equivalent of the *structure tensor* which has been used for feature aligned anisotropic diffusion by WEICKERT [203]. Later, PREUSSER&RUMPF [174] have devised level set formulations of this parametric approach and PREUSSER [173] has proven the existence of viscosity solutions of the resulting second order anisotropic mean curvature flow.

In the case of linear diffusion, the support of the Green's function is infinite, hence the image information is blurred over the entire image domain for arbitrary small times and induces a much more global effect on the measurement of the mismatch $|u_T \circ \phi - u_R|$ when the two images are not correctly aligned. This transfers to the derivative of this functional as well, hence the gradient is not only concentrated on the small subset of $\Omega$ of actual disparity.

## 2.6  Discretization

### 2.6.1  Finite Element discretization in space

In this section we will focus on the discretization of the previously described continuous formulations. Algorithms for registration problems are in practical applications often required for large three dimensional data sets. Modern image acquisition technology produces images of resolutions up to $1024^3$ pixels. As pointed out previously we will avoid to establish regularity by artificially restricting the discrete function space for the deformation to coarser, lower dimensional representations. Restricting the function space to a low dimensional space of B-Spline functions automatically induces regularity, but the computational and implementational effort is higher and furthermore the continuous interpretation is not intuitive. Natural images show

a high level of details and hence very local variations of the deformation are important to be captured by the registration algorithm as well.

Instead, we have set up a continuous model with different sources of regularization and we aim to carry these regularizations over to the discrete case as closely as possible. We will define nested sequences of finite elements spaces in order to eventually apply multilevel and multigrid techniques. Multilevel approaches are very effective ingredients to avoid redundancy and unnecessary computations on fine representations. Instead, large scale approximations are computed on coarse representations which are successively prolongated to finer representations where finally only the difference to the fine details of the solution is computed.

We will now first describe the spatial discretization by finite elements, multilevel hierarchies of finite element spaces and formulate a multilevel algorithm for the energy minimization problem.

**Notation 2.6.1 (nested Finite Element hierarchy).** *Let $\mathcal{V}^1, \ldots, \mathcal{V}^{l_{\max}}$ be a sequence of finite dimensional subspaces of $H^{1,2}(\Omega)$. We call this sequence nested, iff*

$$\mathcal{V}^1 \subset \mathcal{V}^2 \subset \ldots \subset \mathcal{V}^{l_{\max}}.$$

*Let $(\psi_i^l)_i$ be a basis of $\mathcal{V}^l$ for all $l = 1, \ldots, l_{\max}$. For all $1 \le k < l \le l_{\max}$ we denote the prolongation operator from $\mathcal{V}^k$ to $\mathcal{V}^l$—usually obtained by interpolation—by $P_k^l$ and the restriction operator from $\mathcal{V}^l$ to $\mathcal{V}^k$ by $R_l^k$.*

Nested Finite Element (FE) spaces can be constructed in several ways. FE spaces are built upon a triangulation $\mathcal{T}$ of open simplices or other polygonal elements, which approximates the domain $\Omega$ (for simplicity we assume that $\Omega = \Omega_h$, where $\Omega_h$ denotes the discrete approximation of the domain $\Omega$), i. e.,

$$\bar{\Omega}_h = \bigcup_{T \in \mathcal{T}} \bar{T} \qquad T_1 \cap T_2 = \emptyset \quad \forall T_1, T_2 \in \mathcal{T}, T_1 \neq T_2. \tag{2.17}$$

On these elements, one typically defines local polynomial function spaces and aggregates the local spaces to a global one by taking into account continuity conditions. Hence, nested sequences of spaces can be achieved by enriching the local polynomial spaces by increasing the order ($p$-approach), or alternatively by generating a nested sequence of triangulations with decreasing cell size, with a fixed local basis ($h$-approach) or a combination of the two ($h$-$p$-methods).

In image processing, the images are almost always given on rectangular domains. Hence, it is very convenient to define uniform structured grids, by subdividing the domain into smaller rectangles as well and recursively refine by subdivision of cells into smaller cells with the same aspect ratio. Throughout this thesis we will assume, for the sake of simplicity, that $\Omega = (0, 1)^d$.

**Definition 2.6.2 (Quad-Tree and Oct-Tree grids).** *Let $l_{\max} \in \mathbb{N}$, $1 \le l \le l_{\max}$. Then we define triangulations $\mathcal{T}^l$ at level $l$ and the entire hierarchy $\mathcal{T}$ by*

$$\mathcal{T}^l = \left\{ E_\alpha^l = (0, 2^{-l})^d + h_l \alpha \, : \, \alpha_i \in \{0, \ldots, 2^l - 1\} \right\} \qquad \mathcal{T} = \bigcup_{l=1}^{l_{\max}} \mathcal{T}^l$$

*and we say $\mathcal{T}$ is a Quad-Tree grid for ($d = 2$) or an Oct-Tree grid ($d = 3$) of depth $l_{\max}$. We define the discretization parameter $h_l := 2^{-l}$, i. e., the edge-length of the elements on level $l$. We denote by $\mathcal{N}^l$ and $\mathcal{N}(E^l)$ the set of nodes of $\mathcal{T}^l$ resp. $E^l = E_\alpha^l$ which are defined by*

$$\mathcal{N}(E_\alpha^l) = \{(\alpha + \beta)h_l \, : \, \beta_i \in \{0, 1\}\} \quad \text{and} \quad \mathcal{N}(\mathcal{T}^l) = \bigcup_{E^l \in \mathcal{T}^l} \mathcal{N}(E^l).$$

*By $x_\alpha^l$ we denote the node at position $x_\alpha^l = h_l \alpha$.*

It is easy to check the following properties

(i) *Partitioning*—For all $1 \le l \le l_{\max}$, $\mathcal{T}^l$ is a partition of $\Omega$, i. e., (2.17) is fulfilled.

(ii) *Nestedness*— For $1 \leq l < l_{\max}$, every element $E^l \in \mathscr{T}^l$ is partitioned uniformly into $2^n$ subelements on level $l+1$

$$\bar{E}^l = \bigcup_{E^{l+1} \in \mathcal{C}(E^l)} \bar{E}^{l+1} \quad \text{where} \quad \mathcal{C}(E^l_\alpha) := \left\{ E^{l+1}_\beta \, : \, \beta_i \in \{2\alpha_i, 2\alpha_i + 1\} \right\}.$$

We refer to $\mathcal{C}(E^l)$ as the set of *children* of $E^l$.

(iii) *Regularity*—For fixed $1 \leq l \leq l_{\max}$ and all $E^l_\alpha, E^l_\beta \in \mathscr{T}^l$, the intersection $\bar{E}^l_\alpha \cap \bar{E}^l_\beta$ is either $\emptyset$, a common vertex, a common edge or a common face.

We will now define the finite element space, that has been used for all the results that are presented in this thesis. However, the formulation of the algorithm does not depend on this particular choice of space. We define

$$\mathcal{V}^l := \left\{ u \in H^{1,2}(\Omega) \, : \, u\big|_{E^l} \text{ bilinear resp. trilinear} \, \forall E^l \in \mathscr{T}^l \right\}.$$

The simplest and most natural choice of a basis is given by a so called *nodal basis*, where the basis functions are so called *hat-functions*, i. e.,

$$(\psi^l_\alpha)_\alpha \quad \text{s.t.} \quad \psi^l_\alpha(x^l_\beta) = \delta_{\alpha\beta} \quad \forall \alpha, \beta \in \mathcal{N}(\mathscr{T}^l).$$

Here we have identified indices $\beta$ with nodes $x_\beta$. Depending on the context, when no ambiguity can arise, we will also index basis functions and nodes by $i \in \{1, \dots, \mathrm{card}\mathcal{N}(\mathscr{T}^l)\} := I^l$. For $\mathcal{U}^l \in \mathcal{V}^l$, we denote by $\bar{\mathcal{U}}^l \in \mathbb{R}^{\mathrm{card}I^l}$ the vector of coefficients, which is uniquely determined by $\mathcal{U}^l = \sum \bar{\mathcal{U}}^l_i \psi^l$ and we may drop the superscript $l$ when no confusion might arise.

Due to the construction of the grids, which can be interpreted as successive uniform refinement of an initial macro triangulation, we are limited to resolutions of the type $(2^l + 1)^n$. This is not a very severe drawback in many practical applications, since medical imaging devices produce resolutions of this dyadic resolution. However, the significant merit of this structure is the computational ease of implementing multilevel approaches. By the nestedness of the grid, we automatically obtain a nested hierarchy of finite element spaces in the sense of (2.6.1). Furthermore, as we will describe in further detail in Section 2.6.4 we are in the position to embed an efficient multigrid solver for the solution of the large linear systems that have to be solved in the core of the regularized gradient flow algorithm.

## 2.6.2   Discretization of the regularized gradient flows

Since the space of deformations is vectorial, we will use the space $(\mathcal{V}^l)^n =: \mathcal{V}^n$ for fixed $l$ and use upper case symbols for elements of $\mathcal{V}^n$. We approximate the partial derivative $\partial_t \phi$ in (2.3) by the difference quotient $\frac{\phi^{n+1} - \phi^n}{\tau}$, where $\tau$ denotes the time step and $\phi^n := \phi(n\tau)$. Then (2.3) translates into

$$g\left( \frac{\Phi^{n+1} - \Phi^n}{\tau}, \Psi \right) + \langle E'[\Phi^n]; \Psi \rangle = 0 \quad \forall \Psi \in \mathcal{V}^n. \tag{2.18}$$

**Notation 2.6.3.** *For a given metric $g$ we define $\mathbf{G}_{ij} := g(\Psi_j, \Psi_i) \quad \forall i, j \in I$. Due to the properties of a metric, $\mathbf{G}$ is obviously symmetric and positive definite.*

Testing with all basis functions $\Psi_i$ and using the representation of $\Phi^{(n+1)}$ in the basis, we obtain the following discrete system:

$$\mathbf{G}(\bar{\Phi}^{n+1} - \bar{\Phi}^n) + \tau \bar{E}'[\Phi^n] = 0 \quad \text{where } \bar{E}'[\phi]_i = \langle E'[\Phi^n]; \Psi_i \rangle \, \forall i \in I \tag{2.19}$$

which is uniquely solvable on account of the positive definiteness of $\mathbf{G}$. Let us now formulate the full problem where we split $E$ into a part $E_{\mathrm{imp}}$ which we will treat implicitly in time and a part $E_{\mathrm{exp}}$ which is treated explicitly.

**Problem 2.6.4 (Discrete regularized gradient flow).** *Let $E = E_{\mathrm{imp}} - E_{\mathrm{exp}}$ be Fréchet-differentiable in $H^{1,2}(\Omega)^n$, and $g$ a metric on $H^{1,2}(\Omega)^n$, and $\mathbf{G}$ be defined by Notation 2.6.3. Given $\Phi^0 \in \mathcal{V}^h$, find a sequence $(\Phi^n) \in \mathcal{V}^h$, such that*

$$\mathbf{G}(\bar{\Phi}^{n+1} - \bar{\Phi}^n) + \tau \bar{E}'_{\mathrm{imp}}[\Phi^{n+1}] = \tau \bar{E}'_{\mathrm{exp}}[\Phi^n].$$

(a) Deformed templates on levels 4 to 8 in comparison to the reference on the right.



(b) Stationary deformations on grid levels 5 to 8.
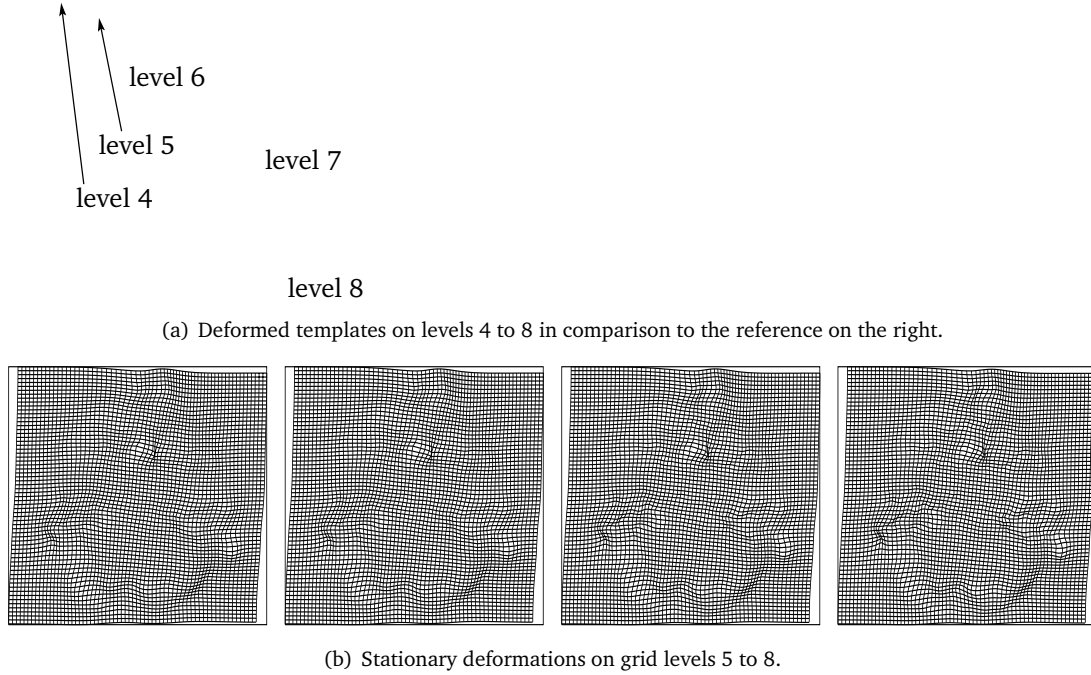
Figure 2.1: *Multiscale matching: The template image is a mirrored version of the reference image. In the top row we show the sequence of matching results on the grid refinement levels 4 through 8 corresponding to different scales. Most of the significant features can already be matched on coarse scales.*

### 2.6.3   Coupling resolution to scales

In this section we will assume that the scale space operator is generated by the heat equation. A diffusion of time $t$ is equivalent to Gaussian convolution

$$u(t) = G_\sigma * u_0.$$

The Gaussian kernel $G_\sigma$ has a "standard deviation" of $\sigma = \sqrt{2t}$ hence we obtain an interpretation of a filter width. This suggests to couple the resolution of the discretization with the linear scale parameter, and control the grid resolution such that $h$ always fulfills

$$h \leq \alpha\sigma \qquad \text{for a fixed } \alpha > 0. \tag{2.20}$$

Hence, we will first define a sequence of scales and on each of those scales check the approximation condition (2.20).

### 2.6.4   Multigrid approximation of the discrete metric

The incorporation of the metric into the gradient flow results in the inversion of a differential operator. For the computation of the gradient with respect to the weighted $H^{1,2}$-metric it is required to perform an implicit timestep of the heat-equation in every iteration of the gradient descent method. Since we have already proposed a cascadic multilevel approach for the energy minimization, we algorithmically already have a framework for hierarchical grid handling at hand. Multigrid methods as introduced by HACKBUSCH [121] are proven to be very efficient solvers for the solution of large sparse systems, as long as the discrete operator fulfills some suitable smoothing properties. To be more precise, multigrid solvers rely on iterative smoothers for the residuals of the discrete system. In the case of elliptic operators, the smoothing properties of Jacobi and SSOR iterations or incomplete Cholesky decompositions are well-known.
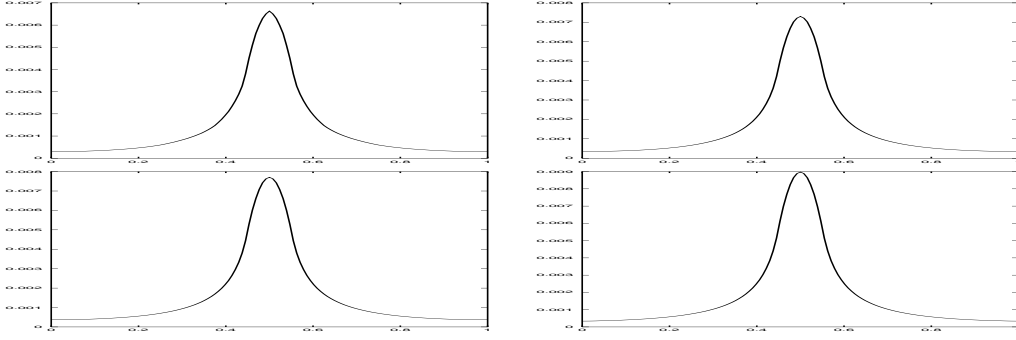
Figure 2.2: *Profiles through a three dimensional data set after the application of one multigrid cycle for the solution of the discrete heat equation with corresponding filter width $\sigma = 0.1$ and a discrete centered Dirac distribution as initial image. We applied 1 through 3 pre- and post-smoothing steps. These correspond to the actually applied kernels in a multigrid smoothing cycle. The bottom right image shows the profile corresponding to the exact discrete solution. One can clearly observe, that the overall shape varies only very slightly when the number of smoothing steps is changed.*

When it comes to energy minimization, where the discretization of the admissible space of solutions is high-dimensional, efficient solvers and approximations of the inverse metric that are computable in a fast way are essential. Additionally, it is desirable to ensure efficiency also with respect to memory usage, since the highly resolved two-dimensional or three-dimensional images themselves already have to be stored permanently in memory .

To recapitulate the multigrid method, we first define for a given matrix $A \in \mathbb{R}^{N,N}$ (where $N = |I^{l_{\max}}|$, which in our applications corresponds to the discrete form of the metric, i. e., $A_{ij} = g(\Phi_i, \Psi_j)$) the following coarse grid operators on $\mathcal{V}^l$

$$A_l := R^l_{l_{\max}} A P^{l_{\max}}_l, \qquad 1 \le l \le l_{\max}$$

and further we denote by $\mathscr{S}_l : \mathcal{V}^l \to \mathcal{V}^l$ a smoother on level $l$, e. g., an SSOR iteration. To solve the linear system $A_{l_{\max}} x_{l_{\max}} = b_{l_{\max}}$, the multigrid solver is then formulated recursively by

$$\mathbf{MG}_l x_l := \mathscr{S}^{\nu_2}_l (x_l + P^l_{l-1} \mathbf{MG}^\alpha_{l-1} R^{l-1}_l (b_l - A_l \mathscr{S}^{\nu_1}_l x_l)) \quad 1 < l \le l_{\max}$$

and $\mathbf{MG}_0$ is an exact solver on the finest grid. $\nu_1$ and $\nu_2$ denote the number of pre- and post-smoothing steps of each iteration and for $\alpha = 1$ we obtain a V-cycle and for $\alpha \ge 2$ we obtain a W-cycle. Then we iterate

$$x^{k+1}_{l_{\max}} \leftarrow \mathbf{MG}^\alpha_{l_{\max}} x^k_{l_{\max}} \qquad \text{until} \qquad \|A_{l_{\max}} x^{k+1}_{l_{\max}} - b_{l_{\max}}\| \le \epsilon.$$

For the regularized gradient flow the exact solution of the smoothing of the descent direction is often not crucial. Much more important are the smoothing properties for the regularization of the flow and furthermore the support of the discrete Green's function, or in other words the spatial filter-width of the discrete filter. Standard iterative solvers for sparse systems, which make use of the matrix structure typically require $O(N)$ iterations, since they connect the degrees of freedom as encoded in the matrix structure only in a neighborhood of each degree of freedom. For finite elements this depends on the overlapping of the basis functions and for finite difference schemes on the extent of the discrete stencil of the differential operator. In every iteration of the multigrid method, due to the restrictions and prolongations of the residuals, the iterative smoothers on each grid only have to connect the degrees of freedom in a neighborhood which corresponds to the difference of resolution from one grid level to the next.

For the multiscale approach, we considered a continuous scale space which is given by applying a scale-space operator $\mathcal{S}^\sigma$. In the final algorithm we will need to compute the solutions of the respective PDE that generates the scale-space for a decreasing sequence $\sigma_j$. Instead of solving a discrete time stepping of the PDE for *increasing* $\sigma$ in a preprocessing step and storing $u^{\sigma_j}_T$ and $u^{\sigma_j}_R$ in memory, the fast multigrid solver allows us to generate $u^{\sigma_j}_T$ on-the-fly without much computational effort.

### 2.6.5 Minimization by regularized gradient methods

Regularized gradient flows fit nicely into the framework of classical gradient methods. In fact, we can use line-search strategies, which are well-established for gradient methods. The $g$-regularized gradient flow can be considered as a *pre-conditioning* of the nonlinear-cg method, since the regularized gradient directions are by the properties of the metric still descent directions. Furthermore, the regularizing effect of the metric often compensates numerical errors by differentiation and line-search strategies in practice indicate that far larger gradient steps can be performed. We consider the following line search strategies.

**Definition 2.6.5 (Armijo-Goldstein's line-search strategy).** *For $\phi$, let $\delta \in H^{1,2}(\Omega; \mathbb{R}^d)$ be given, such that $\langle E'[\phi]; \delta \rangle < 0$. Furthermore let $\alpha \in (0,1)$ and $\beta \in (0,1)$ be fixed. Armijo's line search strategy consists of finding*

$$\tau := \max \left\{ \beta^l \; : \; l \in \mathbb{Z} \text{ and } E[\phi + \beta^l \delta] \leq E[\phi] + \alpha \beta^l \langle E'[\phi]; \delta \rangle \right\}.$$

This strategy can lead to overshooting of the step size. Although it is always ensured that the energy is decreasing in every step, the Armijo-Goldstein condition allows one to increase the timestep in the zone where the energy is increasing again. The following strategy takes into account derivatives of the energy at the deformed position:

**Definition 2.6.6 (Wolfe-Powell Line-Search strategy (strict version)).** *For $\phi$, let $\delta \in H^{1,2}(\Omega; \mathbb{R}^d)$ be given, such that $\langle E'[\phi]; \delta \rangle < 0$. Furthermore let $\alpha \in (0, \frac{1}{2})$ and $\beta \in [\alpha, 1)$ be fixed. The Wolfe-Powell line search strategy consists of finding $\tau > 0$, such that*

$$\begin{aligned} E[\phi + \tau \delta] &\leq& E[\phi] + \alpha \tau \langle E'[\phi]; \delta \rangle \text{ and} & \qquad (2.21) \\ |\langle E'[\phi + \tau \delta]; \delta \rangle| &\leq& -\beta \langle E'[\phi]; \delta \rangle. & \qquad (2.22) \end{aligned}$$

Since $0 < \beta < 1$, we ensure to choose a step-size such that the derivative is smaller than the derivative of the point where the descent direction is computed. Thus we ensure that the step-size is not too small and furthermore we avoid a regime where the energy increases steeply.

With those line search strategies at hand, we can consider a $g$-preconditioned nonlinear cg-method, which is a variant of the original method of FLETCHER & REEVES in the Banach space $\mathscr{X}$:

### 2.6.6 Algorithm: $g$-preconditioned nonlinear conjugate gradient

**Step 0** choose initial $\phi^k \in \mathscr{X}$, $0 < \epsilon \ll 1$.

**Step 1** set $\delta^0 := \text{grad}_g E[\phi^k]$.

**Step 2: inner loop**

    **Step 2.1** search step size $\tau^k$ according to strategy or 2.6.6.

    **Step 2.2** update $\phi^{k+1} := \phi^k + \tau^k \delta^k$.

    **Step 2.3** set $\beta^k := \dfrac{\|\text{grad}_g E[\phi^{k+1}]\|_g^2}{\|\text{grad}_g E[\phi^k]\|_g^2}$.

    **Step 2.4** update $\delta^{k+1} := \beta^k \delta^k - \text{grad}_g E[\phi^{k+1}]$.

    **Step 2.5** check stopping criterion $\|\text{grad}_g E[\phi^k]\|_g \leq \epsilon$.

We will propose an algorithm which marries the multiscale, multilevel and multigrid approaches that have previously been described in detail.

### 2.6.7   The full cascadic multiscale algorithm

In the previous sections we have collected all the required tools for the overall minimization:

 (i) *Regularized metric*—The metric on the space of deformations plays the rôle of penalizing irregular gradient directions. The representation of the derivative in the metric hence becomes regularized.

 (ii) *Multiscale approach*—Select a decreasing sequence of scales $\sigma_i$ and setup the energy with smoothed data.

(iii) *Coupling resolution to scales*—The resolution is chosen according to approximation properties of smoothed data. Hence for decreasing scales, the resolution is successively refined.

(iv) *nonlinear g-cg method*—modification of the nonlinear cg method by choosing the regularized negative gradient as new descent direction in every step.

 (v) *Multigrid approximation of the metric and $\mathcal{S}^\sigma$*—Solve the computation of the $g$-gradient with a multigrid solver.

Let us first describe the gradient flow version of the multiscale descent.

**Cascadic discrete multilevel algorithm for regularized gradient flow**

**Step 0**  Set the level to $l = l_0 < l_{\max}$, $\sigma_i = \sigma_0$, $i = 1$

**Step 1**  Initialize $\phi_{l_0,0} := \mathbb{1} \in \mathcal{V}^{l_0}$.

**Step 2 repeat**

> **Step 2.1**  determine level $l_k := \min\{l \ : \ h \leq \beta \sigma_k\}$
>
> **Step 2.2**  compute data on scale $\sigma_k$: $u^{\sigma_k}_{R,l} := \mathcal{S}^{\sigma_k} R^l_{l_{\max}} u_R$ and $u^{\sigma_k}_{T,l} := \mathcal{S}^{\sigma_k} R^l_{l_{\max}} u_T$
>
> **Step 2.3**  prolongate solution on current level $\phi^0_{l_i,i} := P^{l_i}_{l_{i-1}} \phi_{l_{i-1},i}$
>
> **repeat**
>
> > **Step 2.4.1**  compute descent direction $\boldsymbol{\delta}^k_{l_i,i} = \mathrm{grad}_g E[\phi^k_{l,i}]$
> >
> > **Step 2.4.2**  determine step size by line search strategy: chose such that
> > $$E[\phi^k_{l_i,i} + \tau^k_{l_i,i} \boldsymbol{\delta}^k_{l_i,i}] - E[\phi^k_{l_i,i}] \leq \alpha \tau^k_{l_i,i} \langle E'[\phi^k_{l_i,i}]; \boldsymbol{\delta}^k_{l_i,i}\rangle$$
> >
> > **Step 2.4.3**  update $\phi^{k+1}_{l_i,i} := \phi^k_{l_i,i} + \tau^{k+1}_{l_i,i} \boldsymbol{\delta}^k_{l_i,i}$
> >
> > **Step 2.4.4**  $k \leftarrow k + 1$.
> >
> **until**  $\|\mathrm{grad}_g E^{\sigma_i}[\phi^k_{l,i}]\|_g \leq \epsilon$
>
> **Step 2.4**  $i \leftarrow i + 1$.

**until**  $i >$ total number of scales

The inner loop in Step 2.4.1 corresponds to the regularized gradient flow on a fixed level $l_i$ and for a fixed scale $\sigma_i$ with a line search strategy. We obtain the multilevel nonlinear cg method, by replacing this loop with Algorithm 2.6.6, where we take the computed stationary point of the previous scale as initial value.

## 2.7   Results and Discussion

Let us now discuss some numerical results for some test cases with an emphasis on the efficiency and the robustness of the algorithm and consider the unimodal registration as a prototype for ill-posed registration problems. In real applications the deformations which yield a proper match between the input images often consist of a global, smooth and almost rigid part which mainly results from a different positioning and orientation and an additional, more local component, which results from the effective differences in morphology. The reason for such local displacements are for instance inter-individual variabilities, intra-individual growth processes or changes due to diseases. In all the examples the metric $g^\sigma$ was used where $\sigma = 5h_{l_{\max}}$.

| Process | Duration |
|---|---|
| V-cycle (single component) | 3.3s |
| computation of $E[u]$ and grad $E[u]$ | 5.25s |
| computation of $\langle E'[u], \phi \rangle$ | 5.38s |
| computation of $E[u]$ | 1.23s |
| time–step control | 1-3s |

Table 2.1: *Approximate computing times for the key ingredients of each gradient descent step in our algorithm on a reference PC (Pentium IV, 1.7 Ghz, 1Gb RAM) applied on 3D images with $129^3$ voxels.*

| Scale ($k$) | Filter width ($\epsilon_k$) | Steps ($n_k$) | Gridlevel ($l(k)$) | Time |
|---|---|---|---|---|
| 0 | .250 | 5 | 5 | <1s |
| 1 | .177 | 3 | 5 | <1s |
| 2 | .125 | 3 | 5 | <1s |
| 3 | .088 | 4 | 6 | 9s |
| 4 | .062 | 3 | 6 | 7s |
| 5 | .044 | 4 | 7 | 67s |
| 6 | .031 | 6 | 7 | 95s |
| 7 | .022 | 6 | 7 | 96s |
| 8 | .016 | 5 | 7 | 82s |
| 9 | .0 | 5 | 7 | 83s |

Table 2.2: *Iteration counts on different scales due to the adaptive stopping criteria and the corresponding absolute timings for the computation on the correspondingly chosen grid levels. Here we assume $\alpha = \frac{1}{4}, \gamma = \frac{1}{2}$.*

**Large local displacements**

As a first three-dimensional text example, let us consider the MR-dataset at the top of Figure 2.3. It shows an axial slice through a human skull which has been opened on one side due to a surgery. As can be seen in the axial slices of 2.3 and the saggital slices in 2.4 the application of the multiscale matching algorithm yields almost a perfect match of the deformed template $u_T \circ \phi$ with $u_R$. The deformation as shown in 2.3 (c) is smooth. However, one can observe an overfolding which leads to a loss of injectivity in those regions where large local displacements occur. We will introduce an additional regularization energy which will rule out such overfoldings in Chapter 5. The whole computation of the three-dimensional data set of resolution $129^3$ voxels took only approximately 4 minutes on a standard desktop PC with an Intel Pentium IV CPU running at 1.7Ghz. The durations of the key components of the algorithm are shown in Table 2.1. Thanks to the coupling of the resolution to the scale, the matching algorithm needed only 5 gradient descent steps on the finest scale. As can be seen in Table 2.2 the number of iterations on each scale is approximately constant.

**Small local displacements**

Apart from minor morphological differences, the anatomical structure of the two hemispheres of a healthy brain is almost identical, hence we a reflection by the saggital plane provides us with a feasible and meaningful test problem (cf. Figure 2.1). Naturally the reflection itself is a global minimizer of the matching energy, however in this particular test example, we are only interested in the matching of the hemispheres in the reference with their corresponding counterpart from the other side of the initial template image. Finding the reflection by minimization is almost prohibited by the regularization energy and the nature of the regularized gradient flow.

**Robustness with respect to noise**

The next test example aims to test the matching algorithm with respect to robustness against noise. Due to the multiscale approach and the regularization of the descent directions, we expect the gradient flow to behave reasonably stable for such perturbations. We generated a test pair of data by applying a twist to the same MRT data set as in the previous examples and artificially corrupted the images with $20\%$ *Salt-and-Pepper* noise, i. e., $20\%$ of the pixels were replaced by either a black or a white pixel. The original images and the noisy input data are shown in Figure 2.5. It turns out that the algorithm is very robust: the initial twist of the deformation is reproduced almost exactly.

**Large global displacements**

As another test scenario we have considered two geometrically simple input images, which differ by a strong rotation twist by a maximal angle of $\pi/3$. The input images are shown in Figure 2.6 (a) and (b). The matching result $u_T \circ \phi$ is shown in part (d) of the figure. We can conclude, that the matching algorithm is also able to cope with strong global mismatches of the input images, and to reproduce deformations which are smooth and do not reveal any numerical artefacts.

(a) reference $u_R$, axial slice through the original MR-dataset

(b) template $u_T$ (reflection of the reference)

(c) deformation applied to uniform grid

(d) matching result $u_T \circ \phi$
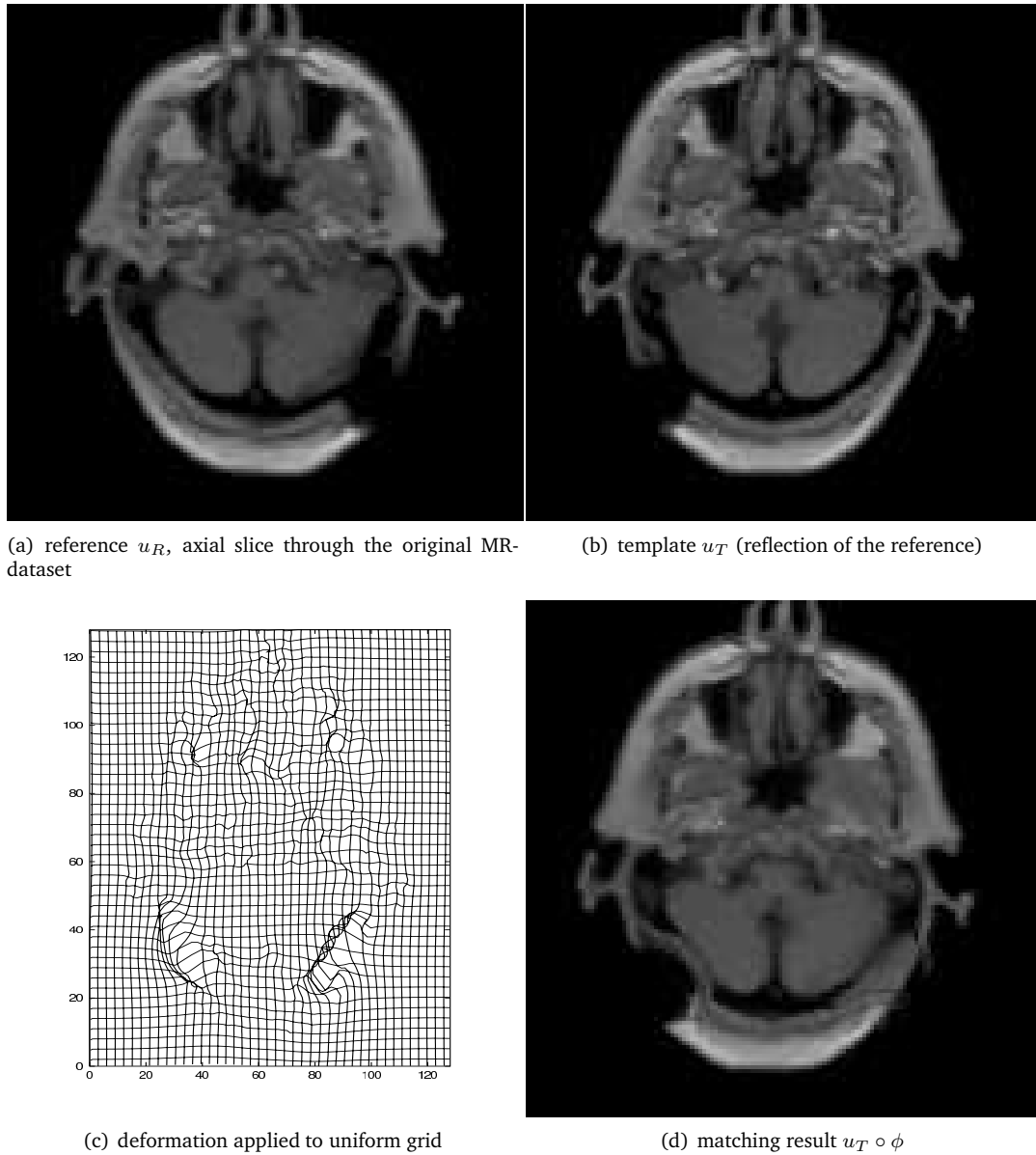
Figure 2.3: *Artificial 3D–matching example with large local magnitude of the deformation. To test the matching algorithm, the template is generated by a reflection of the reference with respect to the central symmetry plane.*

(a) reference $u_R$, saggital slice through the original MR-dataset



(b) template image



(c) deformation applied to uniform grid



(d) matching result $u_T \circ \phi$
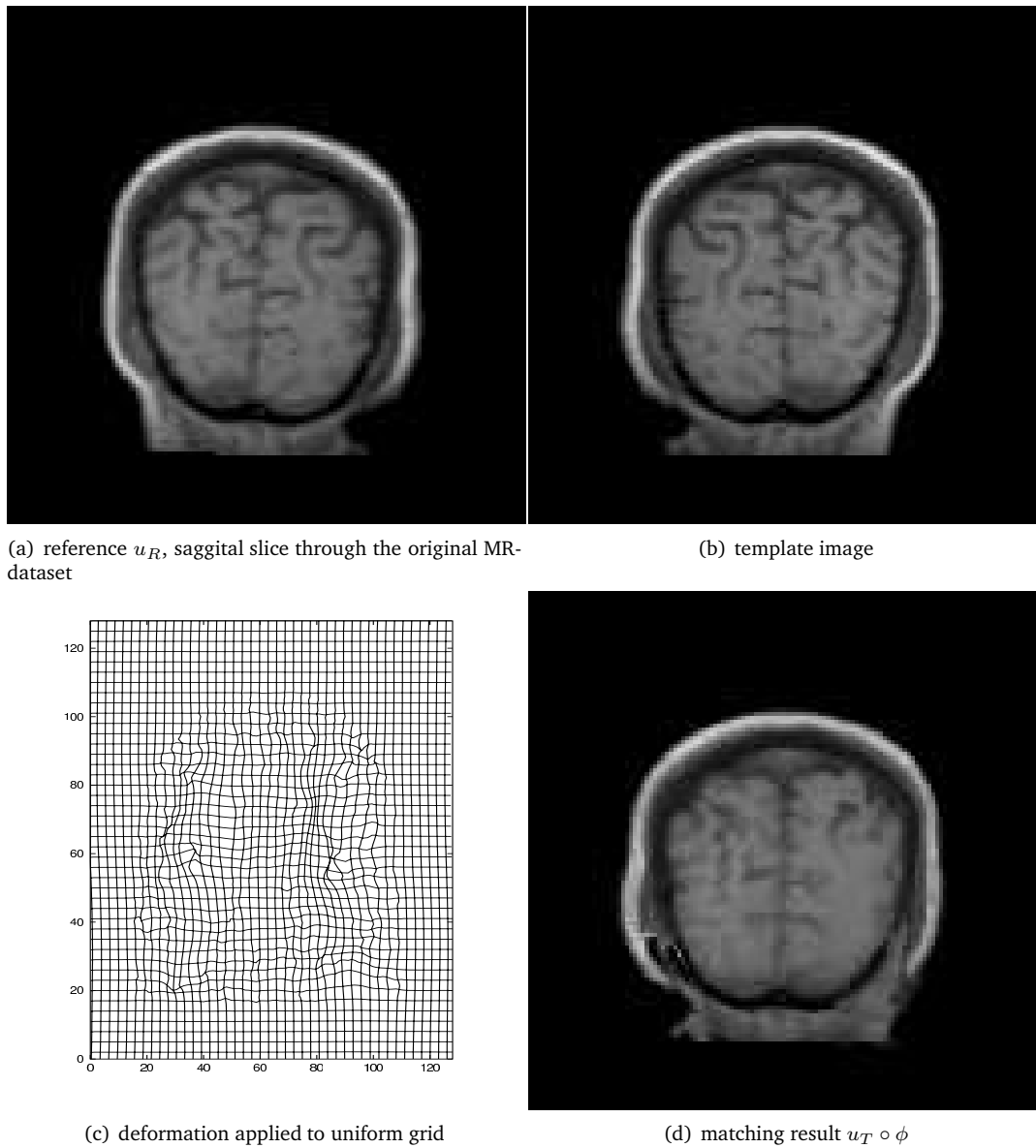
Figure 2.4: *Corresponding saggital (vertical rear view) slices of the matching example in Figure 2.3.*

(a) reference (original) $u_R^*$

(b) template (original) $u_T^*$

(c) noisy reference $u_R$

(d) noisy template $u_T$

(e) deformation $\phi$ applied to a uniform grid

(f) final match $u_T^* \circ \phi$
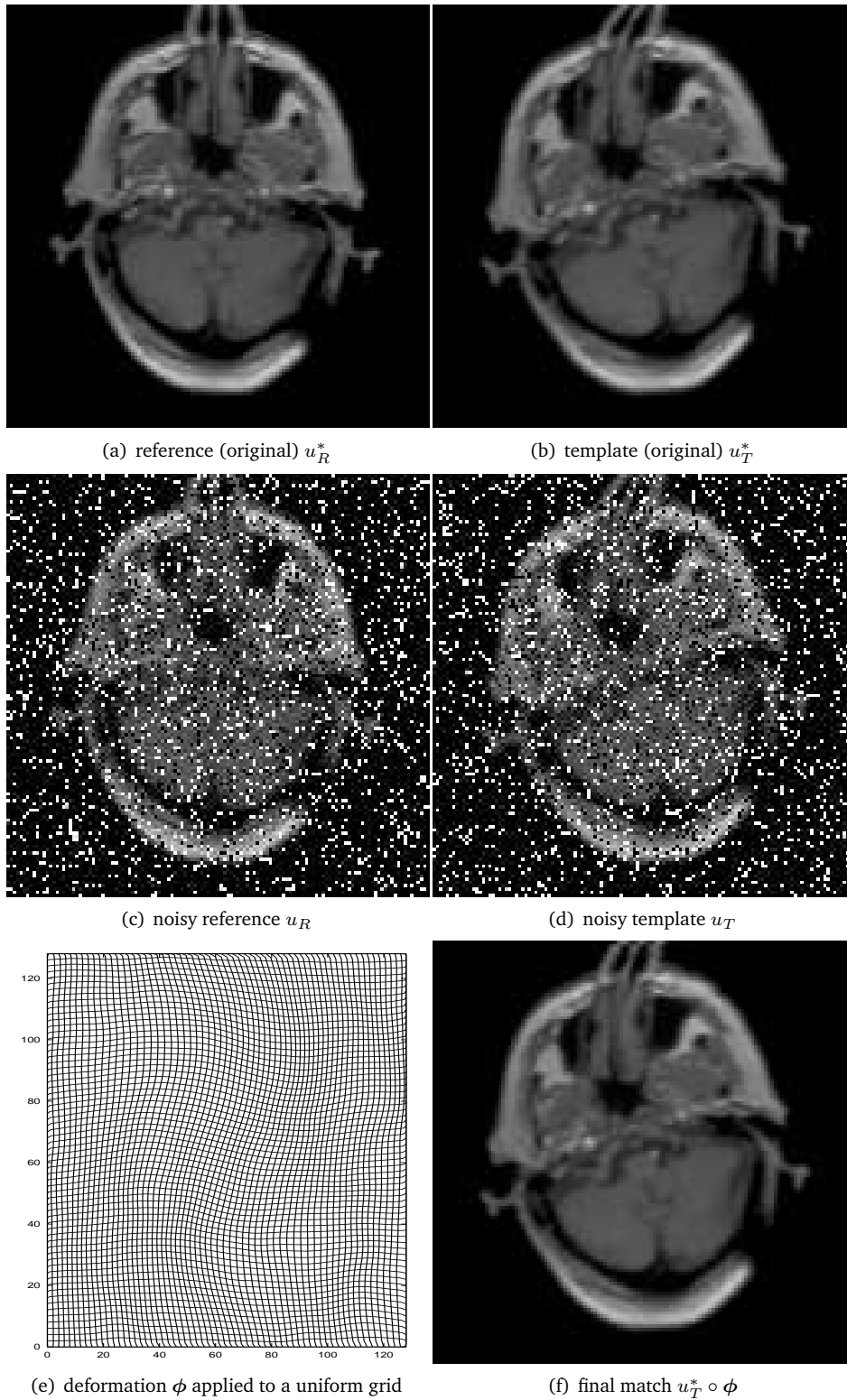
Figure 2.5: *Robustness of the multiscale matching algorithm with respect to noise. The 3D matching problem was set up by artificially corrupting the initial reference (a) and template (b) images by 20% "salt and pepper" noise. The noisy variants (c) and (d) were taken as the input to the matching algorithm. The final deformation and the deformed original template are shown in image (e) and (f) respectively.*

(a) reference $u_R$



(b) template $u_T$



(c) deformation $\phi$ applied to a uniform grid



(d) matching result $u_T \circ \phi$
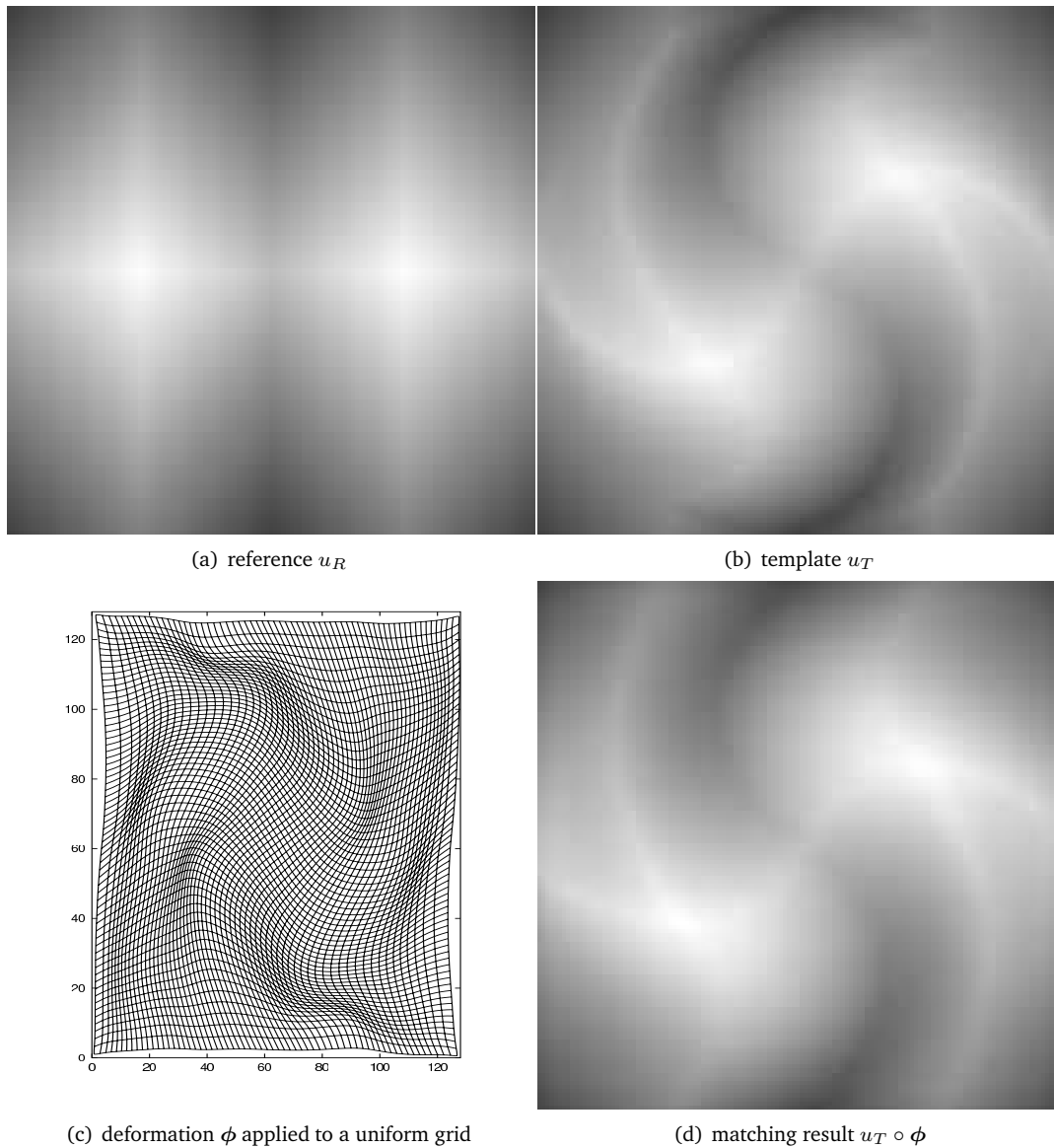
Figure 2.6: *The images show the 3D–matching results of a synthetically generated problem (rotational twist by $\frac{\pi}{3}$) with resulting rather large deformations. The images show slices through a central plane of the 3D dataset of resolution $129^3$.*

# Chapter 3

# Morphological registration

MORPHOLOGICAL shape analysis will be the fundamental ingredient in the construction of a framework for general cost functionals to measure disparity between the geometries in the images. It is easily possible to construct image pairs which contain completely different shapes, but are arbitrary close in the $L^2$ sense. The final aim is the registration of multimodal pairs of images by means of the underlying geometry. More precisely, it is based on the alignment of tangent spaces via the alignment of the normals.

This chapter is organized as follows. First the general formulation of the alignment of morphologies will be described in Section 3.1. The problem is ill-posed and requires a suitable regularization. In Section 3.2 we will propose to use a nonlinear hyperelastic regularization, because it allows the control of singularity sets and renders an existence proof for images which may reveal degenerate normals possible. We give a brief overview on the required ingredients of the direct methods in the calculus of variations. For image registration, injectivity of the deformation is an important requirement, otherwise the interpretation of the deformation as a correspondence between specific points in one image to specific points in the other becomes meaningless. We will apply injectivity techniques from nonlinear elasticity to ensure that the minimizer of the variational problem is injective, and, under additional assumptions on the space of admissible deformations, is even a homeomorphism.

We want to apply the multiscale approach combined with the regularized gradient flow of the previous chapter that has worked well to rule out convergence to local minima. The variations of the energy are presented in Section 3.3. Finally, the implementation will be described in Section 3.4 and results are presented and discussed in Section 3.5.

## 3.1 General approach based on congruence

As pointed out in the introduction, the morphology $\mathscr{M}[u]$, completely describes the topographical shape information of the image $u$. Now we aim at penalizing the deviation from congruence, or in other words to measure the morphological defect which indicates a difference in shapes. One can characterize the morphology by the Gauss-maps of the image:

**Lemma 3.1.1.** *Let $u, v \in \mathscr{C}^1(\Omega)$ and $\nabla u$ resp. $\nabla v$ be different from $0$ almost everywhere. Then*

$$\mathscr{M}[u] = \mathscr{M}[v] \quad \Leftrightarrow \quad n_u = \pm n_v \text{ a. e. on } \Omega, \text{ where } n_u : \Omega \to S^{n-1}, x \mapsto \frac{\nabla u(x)}{\|\nabla u(x)\|}$$

*where $\nabla u(x) \neq 0$ and $n_u = 0$ otherwise.*

Hence, we will have a perfect match of the morphology, i. e., $\mathscr{M}[u_R] = \mathscr{M}[u_T \circ \phi]$ iff the Gauss-map of the deformed image coincides with the Gauss-map of the reference image. Let us denote by $n_R^\phi$ the transformation of the normal with respect to the deformation $\phi$, which by the condition $n_R^\phi \cdot D\phi \, v = 0$ and the transformation rule for the exterior vector product

Figure 3.1: *The idea behind morphological registration: Alignment of the morphologies. A level set $\mathscr{M}_c[R]$ of $u_R$ is mapped into the domain of $u_T$. In order to align the level set to the iso-value $c_1$ of $u_R$, the normal $n_R$ is transformed from $x$ to $n_R^\phi$ at the deformed position $\phi(x)$ and compared with the normal $n_T$ of $u_T$. Although only one particular level set is drawn in each of the images, the aim is to align the entire morphology.*

$D\phi\, u \wedge D\phi\, v = \operatorname{Cof} D\phi(u \wedge v)$ for all $u, v \in T_p\mathcal{M}_{u_R(p)}[u_R]$ is given by

$$n_R^\phi = \frac{\operatorname{Cof} D\phi\, n_R}{\|\operatorname{Cof} D\phi\, n_R\|} = \frac{\operatorname{Cof} D\phi\, \nabla u_R}{\|\operatorname{Cof} D\phi\, \nabla u_R\|} \tag{3.1}$$

wherever this makes sense. The matching of the morphologies can be rephrased in terms of an alignment of the Gauss maps, i. e., find $\phi : \Omega \to \mathbb{R}^d$, such that $n_T \circ \phi \parallel n_R^\phi$ (see Figure 3.1). Let us now consider a function $\omega^* : S^{n-1} \times S^{n-1} \to \mathbb{R}_0^+$, which measures the misalignment of two directions in $S^{n-1}$. After integration, we arrive at a morphological registration energy of the following general form:

$$E_{\mathscr{M}}[\phi] = \int_\Omega \omega^*(n_T \circ \phi, n_R^\phi)\, \mathrm{d}\mu = \int_\Omega \omega(n_T \circ \phi, n_R, \operatorname{Cof} D\phi)\, \mathrm{d}\mu, \tag{3.2}$$

where $\omega : S^{d-1} \times S^{d-1} \times \mathbb{M}^3 \to \mathbb{R}, (u, v, A) \mapsto \omega^*(u, Av)$. We will denote the set where normals degenerate by

$$\mathscr{D}[u] := \{x \in \Omega \,:\, \nabla u = 0\}. \tag{3.3}$$

Naturally, it would be a far too severe restriction to assume that $\mathscr{D}[u_R] = \mathscr{D}[u_T] = \emptyset$. Therefore, let us first extend the integrand $\omega$ of the energy to $\mathbb{R}^d \times \mathbb{R}^d$ homogeneously, i. e., for $A \in \mathbb{M}^d$ we set

$$\omega_0(u, v, A) := \begin{cases} \omega(\frac{u}{\|u\|}, \frac{v}{\|v\|}, A), & u \neq 0 \text{ and } v \neq 0, \\ 0, & \text{otherwise.} \end{cases} \tag{3.4}$$

for $A \in \mathbb{M}^d$. We are now in the place to define rewrite the energy now depending on the image gradients:

$$\boxed{E_{\mathscr{M}}[\phi] = \int_\Omega \omega_0(\nabla u_T \circ \phi, \nabla u_R, \operatorname{Cof} D\phi)\, \mathrm{d}\mu} \tag{3.5}$$

The observation that the integrand depends on derivatives of $\phi$ via the cofactor matrix allows us to embed the theoretical treatment into the framework of the calculus of variations with polyconvex integrands introduced by BALL [13]. This will be described later and is the subject of the subsequent sections.

Let us consider some examples.

*(i)* We might start with a first choice of the form, $\omega^*(u,v) = \gamma(\sphericalangle(u,v))$, where $\gamma$ is an increasing function with $\gamma(0) = 0$ and $\sphericalangle(u,v)$ denotes the angle between $u$ and $v$. One possible example is given by

$$\omega(u,v,A) = \frac{1}{2}\left\| u - \frac{Av}{\|Av\|}\right\|^2 \quad\Rightarrow\quad E_{\mathscr{M}}[\phi] = \frac{1}{2}\int_\Omega \|n_T \circ \phi - n_R\|^2 \,\mathrm{d}\mu \tag{3.6}$$

Clearly, the energy is invariant under monotone contrast transformations $\beta : \mathbb{R} \to \mathbb{R}$ of the images.

*(ii)* The integrand in (3.6) does not fulfill the condition that for given $\phi$ it should solely depend on the morphologies $\mathscr{M}[u_T]$ and $\mathscr{M}[u_R]$, for which clearly $\mathscr{M}[u_T] = \mathscr{M}[\beta \circ u_T]$ also for *non-monotone* contrast changes $\beta : \mathbb{R} \to \mathbb{R}$. This leads us to postulate the symmetry condition

$$\omega(u,v,A) = \omega(-u,v,A) = \omega(u,-v,A) \quad \forall u,v \in \mathbb{R}^d, A \in \mathbb{R}^{d,d}. \tag{3.7}$$

In most practical multimodal registration problems, the violation of this symmetry condition would be somewhat artificial and lead to unpredictable results.

A natural choice of matching functionals is obtained by defining $\omega$ such that it depends on the scalar product of $n_R^\phi$ and $n_T$, for instance we might consider to measure the length of the projection of $n_R^\phi$ onto the tangent space $T\mathscr{M}[u_T] \perp n_T \circ \phi$, i. e., $(\mathbb{1} - n_T \circ \phi \otimes n_T \circ \phi) \cdot n_R^\phi$, which yields

$$\omega(u,v,A) = \hat{\omega}\left( (\mathbb{1} - u \otimes u) \cdot \frac{Av}{\|Av\|}\right) \tag{3.8}$$

with a *convex* and *even* function $\hat{\omega}$. Since $(-u) \otimes (-u) = (-u)(-u)^T = uu^T = u \otimes u$ and $\omega\left( (\mathbb{1} - u \otimes u) \cdot \frac{A(-v)}{\|A(-v)\|}\right) = \omega\left( (\mathbb{1} - u \otimes u) \cdot \frac{Av}{\|Av\|}\right)$ (3.7) is fulfilled. Due to the renormalization of $Av$ we see that $\omega$ is not convex with respect to $A$. Later we will become more precise on the control of $\operatorname{Cof} D\phi$ in the context of regularization.

## 3.2   Nonlinear hyperelastic polyconvex regularization

We give a brief review about the direct methods in the calculus of variations in the vectorial case. We will combine the morphological registration energy with a suitable regularization to gain control over the volume of the deformed singularity set and apply the classical machinery from non linear elasticity to prove existence of the combined energy.

Let us denote the space of admissible functions by $\mathscr{A}$. The general recipe for existence proofs relies on the following ingredients:

*(i)* *Estimate from below*. There exists $\beta \in \mathbb{R}$ such that for all $\phi \in \mathscr{A}$ we have $E[\phi] > \beta$.

*(ii)* *Compactness*. For every sequence $(\phi^k)$, $\phi^k \in \mathscr{A}$ that fulfills $E[\phi^k] < C$, the sequence has a subsequence which converges w.r.t. the given topology and the limit is in $\mathscr{A}$.

*(iii)* *Lower-semicontinuity*. For every converging sequence $\phi^k \to \phi$ w.r.t. the given topology the energy fulfills

$$E[\phi] \le \liminf_{k \to \infty} E[\phi^k].$$

Then the proof of existence is easy. By the first condition *(i)* one chooses an infimizing sequence, such that $\inf_{\psi \in \mathscr{A}} E[\psi] = \liminf_{k \to \infty} E[\phi^k]$, which by *(ii)* has a subsequence converging to some $\phi \in \mathscr{A}$. We denote the subsequence again by $(\phi^k)$. Finally, on account of the last condition *(iii)*, we deduce

$$E[\phi] \le \liminf_{k \to \infty} E[\phi^k] = \inf_{\psi \in \mathscr{A}} E[\psi].$$
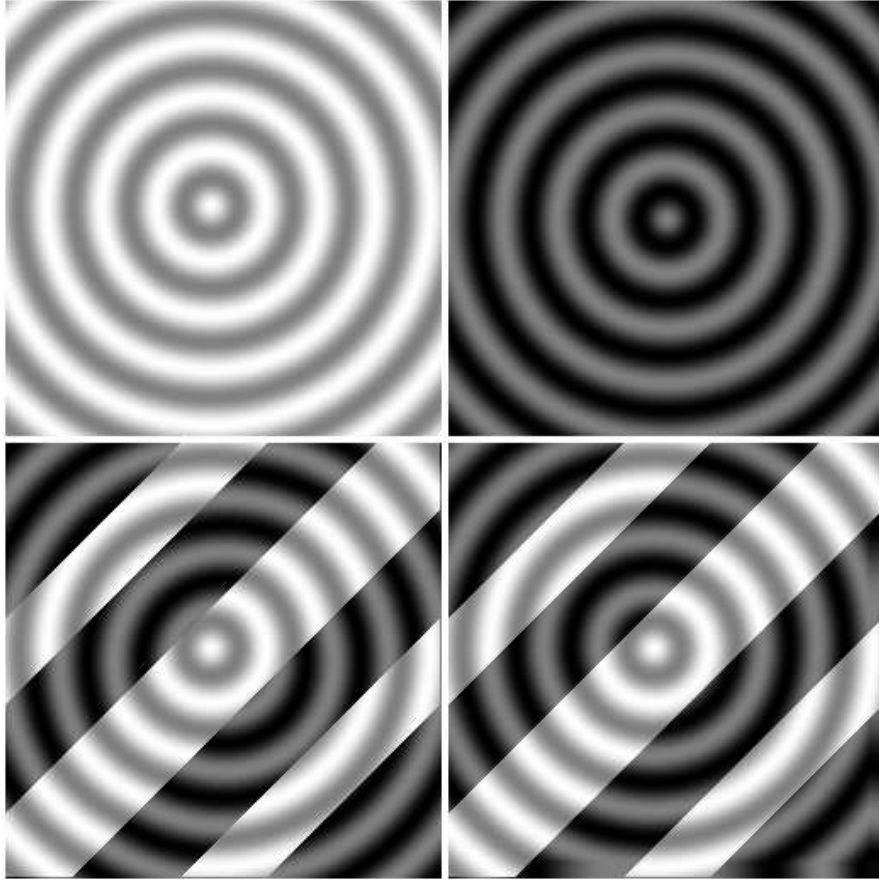
Figure 3.2: Morphological matching of images with exactly the same morphology but completely different contrast. The UPPER ROW shows the input images. Additionally the initial misfit (BOTTOM LEFT) and the final match (BOTTOM RIGHT) are shown.

The crucial point lies in the choice of the combination the topology, the compactness conditions and the conditions which ensure lower-semicontinuity. The compactness usually relies on some kind of weakened topology, e. g., weak convergence in $H^{1,p}$. In the scalar case, lower semicontinuity of energies of the form $E[\phi] = \int_\Omega f(x, \phi, D\phi)$ relies on Carathéodory's condition with respect to $x$ and $\phi$ and convexity in $D\phi$, in fact lower-semicontinuity implies convexity. In the vectorial case, such a convexity condition would be far to restrictive. However, existence can be obtained by more general notions of convexity.

### 3.2.1   General notions of convexity, Hyperelasticity and existence theory

The most general notion of convexity is quasiconvexity as introduced by MORREY [161].

**Definition 3.2.1 (Quasiconvexity).** *Let $f : \mathbb{R}^{m,n} \to \mathbb{R}$ be a locally integrable Borel function. Then*

$$f \; quasiconvex \; :\Leftrightarrow f(A) \leq \frac{1}{\mu(D)} \int_D f(A + D\phi)\, \mathrm{d}\mu \tag{3.9}$$

*for every bounded domain $D \subset \mathbb{R}^d$, every $A \in \mathbb{R}^{m,n}$ and for every $\phi \in W_0^{1,\infty}(D; \mathbb{R}^m)$.*

Under suitable *growth conditions*, quasiconvexity implies weak lower semicontinuity and *vice versa* [79]. For variational methods in nonlinear elasticity, quasiconvexity is however of no use, since these growth conditions are too prohibitive.

The following convexity condition is due to BALL[13] and is tailored to the existence theory in elasticity.
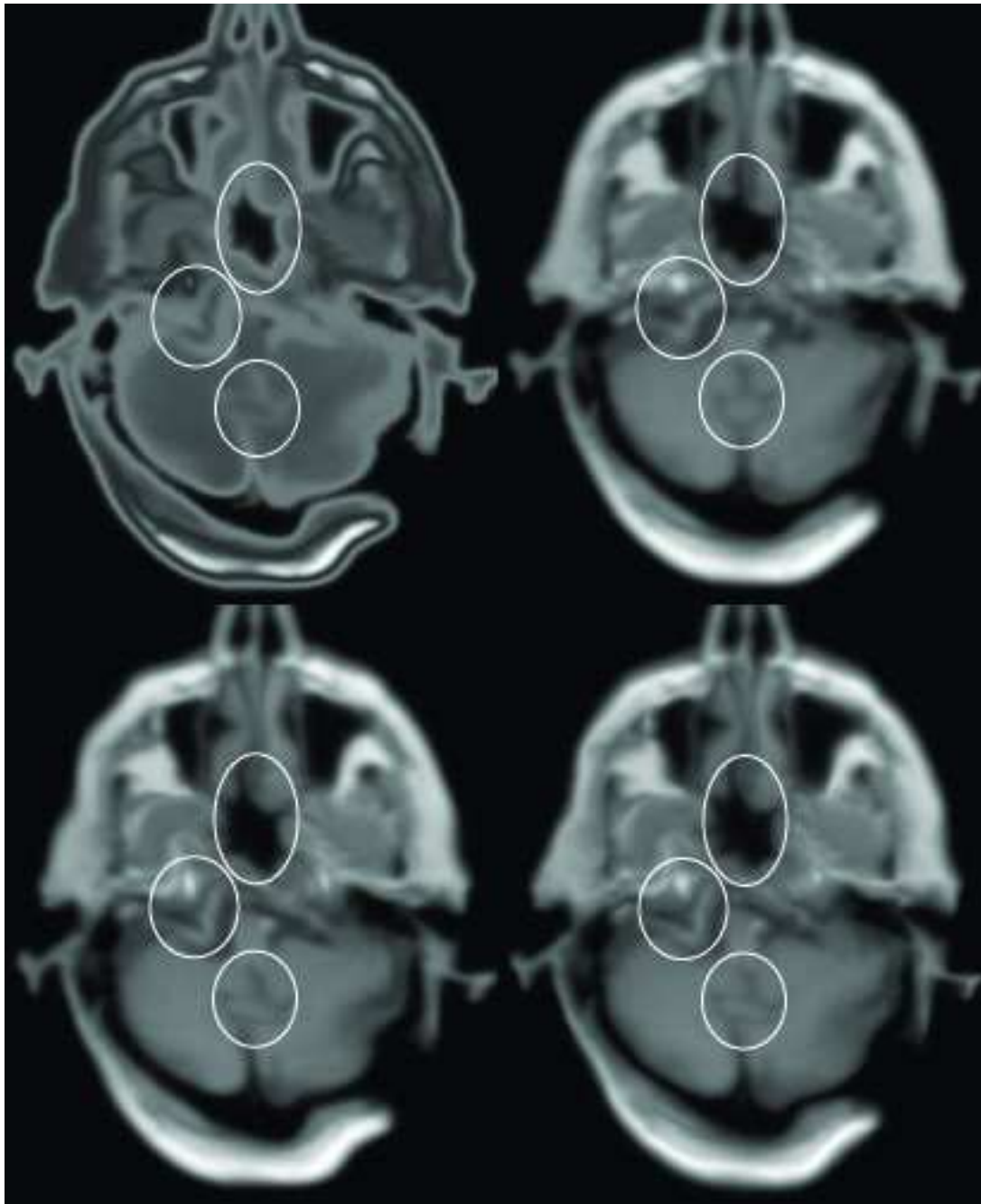
Figure 3.3: *Test example.* TOP LEFT*: reference image $u_R = \beta \circ u_T \circ \psi$, generated from the template image by applying an artificial volume preserving distortion $\psi$ and a non-monotone contrast transformation $\beta$.* TOP RIGHT*: template image $u_T$.* BOTTOM LEFT*: reference image $u_T \circ \psi$ before contrast transformation. Bottom right: registration result $u_T \circ \phi$, template image applied to the computed deformation $\phi$. All images have a resolution of $257^2$. Areas of special interest are marked by white circles. See Figure 3.4 for the corresponding deformation.*
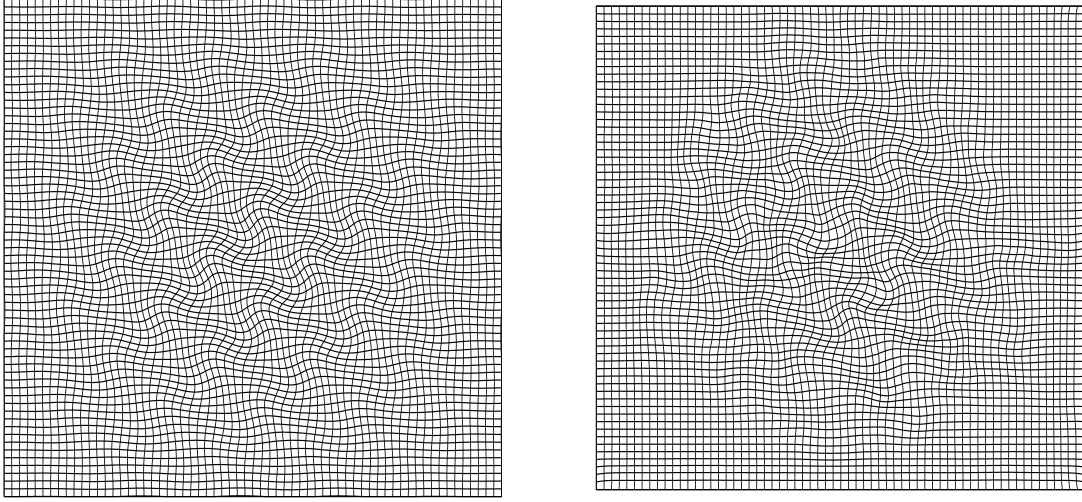
Figure 3.4: *Exact deformation $\psi$ (*LEFT*) and computed deformation $\phi$ (*RIGHT*) for the example in Figure 3.3.*

**Definition 3.2.2 (Polyconvexity).** *We define for $2 \leq s \leq \min(n, m)$ the adjugate $\mathrm{adj}\, A$ of a matrix $A \in \mathbb{R}^{n,m}$ by the matrix of all its $s \times s$-minors. Furthermore, we set*

$$\tau(n, m) = \sum_{s=1}^{\min(n,m)} \sigma(s) \qquad \sigma(s) = \binom{m}{s}\binom{n}{s}.$$

*A function $W : \mathbb{R}^{n,m} \to \bar{\mathbb{R}}$ is said to be polyconvex if there exists a convex function $g : \mathbb{R}^{\tau(n,m)} \to \mathbb{R}$, such that*

$$f(F) = g(T(F)), \tag{3.10}$$

*where $T : \mathbb{R}^{n,m} \to \mathbb{R}^{\tau(n,m)}$ is defined by*

$$T(F) := (F, \mathrm{adj}_2 F, \ldots, \mathrm{adj}_{\min(n,m)} F).$$

*For $n = m = 3$ we will write*

$$\mathbb{W}(F, \mathrm{Cof}\, F, \det F) = g(T(F))$$

**Remark 3.2.3.** *In two dimensions the cofactor matrix is given by* $\mathrm{Cof}\, A = \begin{pmatrix} a_{22} & -a_{21} \\ -a_{12} & a_{11} \end{pmatrix}$. *In three dimensions we write (with cyclic indices)* $(\mathrm{Cof}\, A)_{ij} = a_{i+1,j+1} a_{i+2,j+2} - a_{i+1,j+2} a_{i+2,j+1}$.

It can directly be seen that polyconvexity is implied by convexity, and that polyconvexity only differs from convexity in the vectorial case, i. e., $m > 1$ and $n > 1$.

Polyconvexity implies quasiconvexity [79, Ch. 4, Thm. 1.1], which itself under suitable growth conditions implies weak lower semicontinuity of energies with quasiconvex integrands. However, in general the converse is not true. In this *smaller class of applicable functions* with respect to convexity, it turns out that the growth and *coercivity conditions* are more mild than they have to be for quasiconvex functions.

**Regularization via hyperelastic energies**

We are interested in the application of the existence theory for nonlinear elastic problems. *Hyperelasticity* means, that the *Piola-Kirchhoff* stress tensor can be written in terms of the Fréchet-derivative of an energy with a *stored energy function $\hat{W}$*:

$$E_{\mathrm{reg}}[\phi] = \int_\Omega W(D\phi)\,\mathrm{d}\mu = \int_\Omega \hat{\mathbb{W}}(D\phi, \mathrm{Cof}\, D\phi, \det D\phi)\,\mathrm{d}\mu \tag{3.11}$$
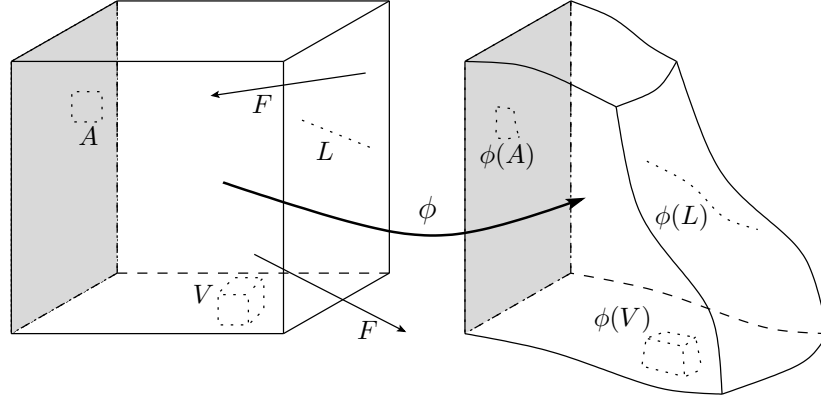
Figure 3.5: *Length, area and volume deformation: for infinitesimal test volumes of dimension one (L), two (A) and three (V) the infinitesimal deformation of length, area and volume is given by $\|D\phi\|$, $\|\mathrm{Cof}\,D\phi\|$ resp. $\det D\phi$.*

where $\hat{\mathbb{W}} : \mathbb{R}^{m,n} \times \mathbb{R}^{m,n} \times \mathbb{R}$ is convex and $\lim W(D\phi) = +\infty$ for $\det D\phi \to 0+$ or $+\infty$, e. g.,

$$E_{\mathrm{reg}}[\phi] = \int_\Omega \|D\phi\|^p + \|\mathrm{Cof}\,D\phi\|^q + \Gamma(\det D\phi)\,\mathrm{d}\mu. \tag{3.12}$$

with a suitable choice for $\Gamma$. Materials which are modeled with such kind of energies are called *Mooney-Rivlin*-materials. For our registration problems, these energies allow us to control the *length-*, *area-* and *volume-* deformation separately (see Figure 3.6). In particular, the properties of $\Gamma$ ensure that a set of finite volume will not be mapped to a set of arbitrary small or large volume. Such a mechanism to prevent the blow up of singularity sets under the deformation will turn out to be the key ingredient of the existence proof for the regularized matching problem.

We combine the matching energy and the regularization into a total energy (see Figure 3.2) for a first result)

$$E[\phi] := E_{\mathscr{M}}[\phi] + \alpha E_{\mathrm{reg}}[\phi]. \tag{3.13}$$

**Restrictions on the integrand of the registration energy**

In essence, the hyperelastic regularization energy ensures the desired *compactness* property. On account of the growth conditions of the *stored energy* function $W$, one may deduce from the boundedness of the energy the control of the invariants of the Jacobian. Due to polyconvexity, the chosen regularization is also weakly lower semi-continuous. If we combine the regularization with the matching energy, we have to ensure that the overall energy is still lower semicontinuous. Due to the fact, that $E_{\mathscr{M}}$ is positive, the compactness property is still fulfilled. The choice of the integrand (3.4) depends on the cofactor matrix of the Jacobian. Hence, we require the $\omega_0$ to be convex in the argument $A$.

Unfortunately one can show that any function $f : \mathbb{M} \to \mathbb{R}$ which is 0-homogeneous and *convex* has to be constant, which would restrict our choice to trivial and useless matching energies. Indeed, first note that for any convex function we have

$$f(E - s(C - D)) \le f(E) - s(f(C) - f(D)). \tag{$*$}$$

Now let us assume, $A, B \in \mathbb{M}^d$ such that $\infty > f(A) - f(B) = \delta > 0$ and define $A_{\alpha,r} := rA + \alpha(A - B)$ with $r > 0$ and $\alpha > 0$. We define $s := \frac{\alpha}{r}$ and use $(*)$:

$$f(A_{\alpha,r}) = f(rA + s(A - B)) \ge f(rA) + s\big(f(rA) - f(rB)\big)$$
$$= f(A) + \frac{\alpha}{r}(f(A) - f(B)) = f(A) + \frac{\alpha\delta}{r} \xrightarrow{r \to 0} +\infty.$$

We deduce $f(A - B) = +\infty$, which contradicts the assumption on $f$. As long as $\hat{\omega}$ in (3.8) is not constant the matching energy in (3.8) will not be lower semicontinuous.

Therefore this particular choice is not appropriate to apply existence proof techniques of the direct methods of the calculus of variations. As an alternative we drop the normalization $\|\mathrm{Cof}\, Aw\|$ and consider

$$\omega(u, v, A) = \|(\mathbb{1} - v \otimes v) Aw)\|^{\gamma} \quad \text{for } 1 \leq \gamma \leq q \tag{3.14}$$

which is *convex* w.r.t. $A$ and results in the following registration energy

$$E_{\mathscr{M}}[\phi] = \int_{\Omega} \left\| (\mathbb{1} - (n_T \circ \phi) \otimes n_T \circ \phi) \cdot \mathrm{Cof}\, D\phi\, n_R \right\|^{\gamma} \mathrm{d}\mu.$$

With this kind of integrand, we have still ensured that $\omega_0(v, w, A) = 0$ iff $v \parallel Aw$. The value $\|\mathrm{Cof}\, D\phi n_R\|$ corresponds to the change of the area element on the level set $\mathcal{M}_c[u_R]$ (see also [103]).

**Global invertibility**

In nonlinear elasticity *global invertibility* is an important requirement, since the loss of injectivity would be highly "unphysical". The phenomenon of *cavitation*, which means that the deformed object is torn apart, may be more realistic [14]. However, for the purpose of a suitable regularization for image registration, this loss of continuity is obviously undesirable.

The theory is based on the following fundamental theorem.

**Theorem 3.2.4.** *Let $\Omega \subset \mathbb{R}^d$ be open, bounded and connected,* $\mathrm{int}\, \bar{\Omega} = \Omega$, $\psi \in \mathscr{C}^0(\bar{\Omega}; \mathbb{R}^d)$ *injective. If $\phi \in \mathscr{C}^0(\bar{\Omega}; \mathbb{R}^d) \cap \mathscr{C}^1(\Omega; \mathbb{R}^d)$ satisfies*

$$\det D\phi > 0 \quad \text{in } \Omega \qquad \phi\big|_{\partial\Omega} = \psi\big|_{\partial\Omega},$$

*then $\phi : \bar{\Omega} \to \phi(\bar{\Omega})$ is a homeomorphism, and $\phi$ is a diffeomorphism in $\Omega$.*

The proof is based on the topological degree (see [60, ch.5]). Hence the condition that $\phi$ coincides with an injective function on the boundary cannot be dropped. The following extension is due to BALL [14]

**Theorem 3.2.5.** *Let $\Omega \subset \mathbb{R}^d$ be a non-empty bounded connected strongly Lipschitz open set. Let $\phi_0 : \bar{\Omega} \to \mathbb{R}^d$ be in $\mathscr{C}(\bar{\Omega}; \mathbb{R}^d)$ and one-to-one in $\Omega$, $p > d$ and let $\phi \in W^{1,p}(\Omega)$ take values in $\mathbb{R}^d$ and satisfy $\phi\big|_{\partial\Omega} = \phi_0\big|_{\partial\Omega}$. Furthermore let $\det D\phi(x) > 0$ for $\mu$-almost every $x$ in $\Omega$. Let $\phi_0(\Omega)$ satisfy the cone-condition and suppose that for some $q > d$,*

$$\int_{\Omega} \|D\phi^{-1}\|^q \det D\phi \, \mathrm{d}\mu < \infty.$$

*Then $\phi$ is a homeomorphism of $\Omega$ onto $\phi_0(\Omega)$, and the inverse function $x(\phi)$ belongs to $W^{1,p}(\phi_0(\Omega))^d$. The matrix of weak derivatives of $x(\cdot)$ is given by*

$$Dx(y) = D\phi^{-1}(x(y)) \text{ almost everywhere in } \phi_0(\Omega).$$

*If, further, $\phi_0(\Omega)$ is strongly Lipschitz, then $\phi$ is a homeomorphism of $\bar{\Omega}$ onto $\phi_0(\bar{\Omega})$.*

Since, we control the growth of the inverse of $\phi$ by $\mathrm{Cof}\, D\phi$ and $\det D\phi$ and the fact that $D\phi^{-T} \det D\phi = \mathrm{Cof}\, D\phi$, one immediately obtains the following corollary [14]:

**Corollary 3.2.6.** *Under the hypotheses above, there exists $\phi \in \mathscr{A}$ which minimizes $E_{\mathrm{reg}}$ on $\mathcal{A}$, $\phi$ is a homeomorphism of $\Omega$ onto $\phi_0(\Omega)$ and the inverse function $x(\phi)$ belongs to $W^{1,\sigma}(\phi_0(\Omega))$, where $\sigma = q(1 + s)/(q + s)$. If, further, $\phi_0(\Omega)$ is strongly Lipschitz, then $\phi$ is a homeomorphism of $\bar{\Omega}$ onto $\phi(\Omega_0)$.*

Hence, if we fix the deformation along the boundary we can ensure that the minimizing deformation is a *homeomorphism*. This fact has been exploited in [103].
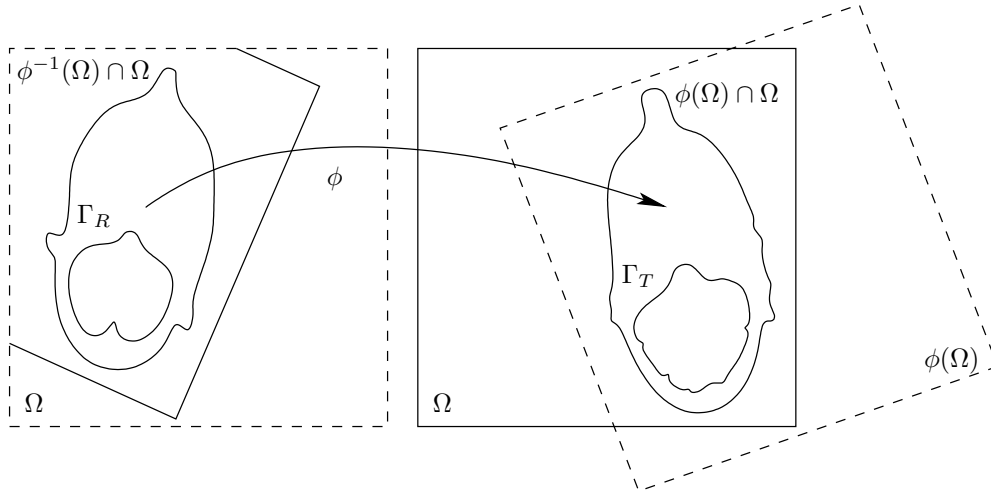
Figure 3.6: *For large deformations, it might be more appropriate to allow free boundary conditions instead of fixing $\phi$ to be the identity on $\partial\Omega$. The disparity of the images is only measured on the subset of $\Omega$ which is again mapped under $\phi$ into $\Omega$, namely $\phi^{-1}(\Omega) \cap \Omega$.*

### Free boundaries and alignment of feature sets

Dirichlet conditions on $\partial\Omega$ have a significant disadvantage, in the case when large transformations are necessary. The hyperelastic regularization energy by construction penalizes deformations, which result in strong distortions. In some cases, however, strong distortions are unavoidably close to the boundary in order to transform one part of the image into a distant part of the other image. The matching energy is always balanced against the regularization energy, so if the weight which controls the intensity of the regularization remains unchanged, the total energy will prevent a proper match. However, it is undesirable to reduce this weight, since the regularization rules out irregular minimizers.

One might relax the boundary condition by allowing the boundary to move freely, in particular allowing that $\phi(\Omega) \not\subset \Omega$. Since $u_T$ is only defined on $\Omega$, the disparity cannot be measured in $\phi(\Omega) \cap \Omega^C$. Hence, we might adjust the domain of integration to cut out the set that is not mapped onto $\Omega$ and integrate only over $\phi^{-1}(\Omega) \cap \Omega$. However, this would lead to trivial undesired minimizers: any deformation in the kernel of the regularization, i. e., translations, which map $\Omega$ entirely out of $\Omega$ will have zero energy (cf. Figure 3.5). This will also lead to a loss of compactness.

In order to penalize such deformations, we consider an additional energy contribution. Let us assume that we have two feature sets $\Gamma_R$, $\Gamma_T \subset \Omega$, which correspond to each other. Furthermore, we assume that $\Gamma_R$ and $\Gamma_T$ are of class $\mathscr{C}^{0,1}$. We define an energy, which measures the distance of the transformed feature set $\phi(\Gamma_R)$ to the feature set $\Gamma_T$ and consider:

$$E_{\mathrm{dist}}[\phi] := \int_{\phi(\Gamma_R)} \mathrm{dist}(\cdot, \Gamma_T)^2 \, \mathrm{d}\mu \tag{3.15}$$

The next lemma assures that the control of the $H^{1,p}$-norm and the control of $E_{\mathrm{dist}}$ implies the boundedness of the $L^p$-norm of the deformations.

**Lemma 3.2.7.** *Let $\Omega \subset \mathbb{R}^d$ open, bounded and connected with Lipschitz boundary. Let $\Gamma_1$, $\Gamma_2$ be two $n-1$-dimensional Lipschitz surfaces, such that*

$$C_\Gamma := \mathrm{diam}\,\Gamma_2 := \sup_{x_1 \in \Gamma_2, x_2 \in \Gamma_2} |x_1 - x_2| < +\infty.$$

*Then there exists $C = C(\Gamma_1, \Gamma_2)$, such that for all $\phi \in W^{1,p}(\Omega; \mathbb{R}^d)$ with $1 < p < \infty$, $p > 3$ the following inequality holds:*

$$\|\phi\|_{L^p(\Omega)} \leq C\Big(\|\mathrm{dist}_{\Gamma_2}(\phi(\cdot))\|_{L^p(\Gamma_1)} + \|D\phi\|_{L^p(\Omega)} + 1\Big)$$

*Proof.* First we note $W^{1,p}(\Omega)$ is compactly embedded in $\mathscr{C}^0(\Omega;\mathbb{R}^d)$ and that for fixed $\tilde{x}_2$ in $\Gamma_2$ and all $x_1 \in \Gamma_2$ we have $|\phi(x)| \leq |\phi(x) - x_2| + |x_2| \leq |\phi(x) - x_1| + |x_1 - x_2| + |\tilde{x}_2| \leq |\phi(x) - x_1| + \operatorname{diam}\Gamma_2 + |x_2|$, i. e., $|\phi(x)| \leq C_\Gamma + C$ and hence $\|\phi\|_{L^p\Gamma_1} \leq C\left(\|\operatorname{dist}_{\Gamma_2}(\phi(\cdot))\|_{L^p(\Gamma_1)} + 1\right)$. Now we show that there is a constant again denoted by $C$, such that

$$\|\phi\|_{L^p(\Omega)} \leq C\left(\|\phi\|_{L^p(\Gamma_1)} + \|D\phi\|_{L^p(\Omega)} + 1\right)$$

by a Poincaré-type argument [1]. Assume that the inequality does not hold. Then there exists a sequence $(\phi_k)_k$, $k \in \mathbb{N}$ such that

$$\|D\phi_k\|_{L^p(\Omega)} + \|\phi_k\|_{L^p(\Gamma_1)} + 1 \leq \frac{1}{k}\|\phi_k\|_{L^p(\Omega)} \tag{3.16}$$

from which we deduce $\|\phi_k\|_{L^p(\Omega)} \to +\infty$. For $K > 0$ arbitrary, we have

$$\delta_k := K\|\phi_k\|_{L^p(\Omega)}^{-1} \to 0 \text{ for } k \to \infty.$$

We define $\psi_k := \delta_k \phi_k$, i. e., $\|\psi_k\|_{L^p(\Omega)} = \delta_k\|\phi_k\| = K$, and (3.16) now yields

$$\|D\psi_k\|_{L^p(\Omega)} + \|\psi_k\|_{L^p(\Gamma_1)} + \delta_k \leq \frac{1}{k}\|\psi_k\|_{L^p(\Omega)} = \frac{K}{k} \to 0 \text{ for } k \to +\infty.$$

Hence, the $\psi_k$ are bounded in $H^{1,p}(\Omega)$ and thus allows the choice of a subsequence $\psi_k \rightharpoonup \psi$ weakly in $H^{1,p}(\Omega)$. Due to the above inequality and the weak convergence of the subsequence, we deduce $D\psi_k \to 0$ strongly in $L^p(\Omega)$, hence $D\psi_k \to 0$. Due to the connectedness of $\Omega$, $\psi$ is constant almost everywhere. Hence, due to Sobolev's embedding $\psi_k \to \psi$ strongly. We see that $\|\psi_k\|_{L^p(\Gamma_1)} \to 0$ and hence, due to the continuity of the trace onto $\Gamma_1$ we obtain $\psi \equiv 0$. On the other hand, we have $\psi_k \to 0$ strongly in $L^p(\Omega)$ due to Rellich's embedding theorem, thus

$$K = \|D\psi_k\|_{L^p(\Omega)} \to 0$$

which is a contradiction and concludes the proof.                                               $\square$

### Avoiding fold-over for free boundaries

CIARLET & NEČAS proposed [62] to add a further constraint on the admissible set to ensure injectivity of the resulting deformation by forbidding deformations which start to fold over beyond points where self-contact occurs. In contrast to Theorem 3.2.5 which relies on the existence of an injective deformation $\phi_0$ on $\Omega$ and which by degree-theoretical arguments transfers the injectivity of $\phi_0$ onto $\phi$, the constraint

$$\int_\Omega \det D\phi \, d\mu \leq \operatorname{vol}\phi(\Omega)$$

allows to prescribe Dirichlet conditions on a subset of the boundary. In [62], the authors have also treated the problem, where $\phi(\Omega)$ has to be in the interior of an obstacle $B$ which is a closed, possibly unbounded subset of $\mathbb{R}^d$. Here, we confine ourselves to the case $B = \mathbb{R}^d$, since in typical registration applications such an obstacle condition does not have to be incorporated.

We now cite the existence theorem of BALL [13] and the extension by Theorem 5 in [62].

**Theorem 3.2.8 (Existence).** *Let the boundary $\Gamma = \partial\Omega$ be Lipschitz, $\mathscr{H}^{d-1}(\Gamma_0) > 0$, and a stored energy function $W : \mathbb{M}_+^3 \to \mathbb{R}$ be given, which satisfies the following assumptions:*

 (i) *Polyconvexity—There exists a convex function $\mathbb{W} : \mathbb{M}^3 \times \mathbb{M}^3 \times (0, +\infty) \to \mathbb{R}$ such that*

$$W(F) = \mathbb{W}(F, \operatorname{Cof} F, \det F) \text{ for all } F \in \mathbb{M}_+^3.$$

 (ii) *Coercivity—There exist constants $a > 0$, $b \in \mathbb{R}$, $p > 0$, $q \geq \frac{p}{p-1}$, $r > 1$, such that*

$$W(F) \geq a(\|F\|^p + \|\operatorname{Cof} F\|^q + (\det F)^r) + b \text{ for all } F \in \mathbb{M}_+^3.$$

*We define*

$$\mathscr{A} := \{\, \phi \in W^{1,p}(\Omega; \mathbb{R}^3);\ \mathrm{Cof}\, D\phi \in L^q(\Omega; \mathbb{M}^3),\ \det D\phi \in L^r(\Omega), \tag{3.17}$$

$$\det D\phi > 0 \text{ a.e. in } \Omega \,\}$$

*Let the density $f$ of the applied body force be such that the linear form $\psi \in W^{1,p}(\Omega) \mapsto \int_{\Omega} f \cdot \psi \, \mathrm{d}\mu$ is continuous and let $\phi_0 \in W^{1,p}(\Omega)$ be given in such a way that the set*

$$\mathscr{A}_0 := \{\, \phi \in \mathscr{A} \,:\, \phi = \phi_0 \text{ on } \Gamma_0 \} \tag{3.18}$$

*is not empty. Assume that $\inf_{\phi \in \mathscr{A}_0} E[\phi] < +\infty$ where the energy $E$ is defined by (3.13). Then the problem of finding a minimizing deformation $\phi \in \mathscr{A}$, i. e., $E[\phi] = \inf_{\psi \in \mathscr{A}} E[\psi]$ has at least one solution (BALL '77).*

*If further, the admissible set $\mathscr{A}_0$ is replaced by*

$$\mathscr{A}_0^{\#} := \left\{ \phi \in \mathscr{A}_0 \,:\, \int_{\Omega} \det D\phi \, \mathrm{d}\mu \le \mathrm{vol}\, \phi(\Omega) \right\}$$

*and $W$ furthermore fulfills $W(F) \to +\infty$ as $\det F \to 0+$, then by CIARLET&NEČAS '87 the minimum problem again has at least one solution $\phi \in \mathscr{A}_0^{\#}$, which is now injective almost everywhere in the sense that*

$$\mathrm{card}\, \phi^{-1}(y) = 1 \text{ for almost all } y \in \phi(\Omega). \tag{3.19}$$

## 3.2.2 Existence

### Existence for unimodal registration

Before this framework was applied to morphological registration, *hyperelastic regularization* has been used by RUMPF [179] to prove the existence of a homeomorphic minimizer of the unimodal registration energy provided that the space of admissible deformations is chosen such that the deformations are fixed on the boundary. Images are allowed to have discontinuities as long as the measure of $\delta$-neighborhoods of the discontinuity set converges to zero for $\delta \to 0$.

### Existence for multimodal registration

In this section we will address the question of existence for the morphological registration energy combined with the hyperelastic regularization energy of (3.11)

$$E[\phi] := E_{\mathscr{M}}[\phi] + \alpha_{\mathrm{reg}} E_{\mathrm{reg}}[\phi] + \alpha_{\mathrm{dist}} E_{\mathrm{dist}}[\phi]. \tag{3.20}$$

Existence of a homeomorphism $\phi$ with $\phi = \mathbb{1}$ on $\partial\Omega$ has been proved in [103]. In this section we will follow the strategy presented therein and modify the existence result in order to allow free boundaries of the transformed domain. In this case, the homeomorphism property is lost, however it is still *injective* $\mu$-almost everywhere.

**Definition 3.2.9.** *Let us now define the space of images. We set*

$$\mathscr{I} := \mathscr{I}(\Omega) := \left\{ u \in C^1(\bar{\Omega}) \,:\, \exists \mathscr{D}[u] \subset \Omega \text{ such that } \nabla u \neq 0 \text{ on } \Omega \setminus \mathscr{D}_u \text{ and } \mu(B_\epsilon(\mathscr{D}[u])) \xrightarrow{\epsilon \to 0} 0 \right\}.$$

*For convenience we define $\mathscr{D}_T := \mathscr{D}_{u_T}$ and $\mathscr{D}_R := \mathscr{D}_{u_R}$. Let us consider the space of admissible deformations*

$$\mathscr{A}^{\#} := \left\{ \phi \in \mathscr{A} \,:\, \int_{\Omega} \det \nabla \phi \, \mathrm{d}\mu \le \mathrm{vol}\, \phi(\Omega) \right\} \tag{3.21}$$

*where $\mathscr{A}$ was defined in (3.17).*

**Theorem 3.2.10 (Existence of minimizing deformations).** *Suppose $d = 3$, $u_T, u_R \in \mathscr{I}(\Omega)$, and consider the total energy $E$ defined in (3.20) for deformations $\phi$ in the set of admissible deformations $\mathscr{A}^{\#}$ from (3.21) where $p, q > 3$ and $r > 1$.*

*(i) Polyconvexity. Suppose $W : \mathbb{M}^3 \times \mathbb{M}^3 \times \mathbb{R}^+ \to \mathbb{R}$ is convex.*

*(ii) Growth condition. Let there exist constants $\beta, \gamma, s \in \mathbb{R}$, $\beta > 0$, and $s > \frac{2q}{q-3}$ such that*

$$W(F) \;\geq\; \beta \left( \|F\|_2^p + \|\mathrm{Cof}\, F\|_2^q + (\det F)^r + (\det F)^{-s} \right) \quad \forall F \in \mathbb{M}_+^3 \quad (3.22)$$

$$and \quad E[\phi] \;\geq\; \gamma E_{\mathrm{dist}}[\phi] \quad \forall \phi \in \mathscr{A}^{\#}. \tag{3.23}$$

*(iii) Continuity condition on $\omega$. Assume that $\omega_0(v, w, A) = \omega(\frac{v}{\|v\|}, \frac{w}{\|w\|}, A)$, for some function $\omega : S^2 \times S^2 \times \mathbb{R}^{3,3} \to \mathbb{R}_0^+$, which is continuous in $\frac{v}{\|v\|}$, $\frac{w}{\|w\|}$, convex in $A$ and for a constant $m < q$ the estimate*

$$\omega(v, w, A) - \omega(u, w, A) \leq C_\omega \, \|v - u\| \, (1 + \|A\|_2^m)$$

*holds for all $u, v, w \in S^2$ and $A \in \mathbb{M}^3$.*

*Then $E$ attains its minimum over all deformations $\phi \in \mathscr{A}^{\#}$ and the mapping is injective in the sense of (3.19).*

*Proof.* The proof combines the techniques of BALL [14], CIARLET&NEČAS [62] and the singularity control of DROSKE&RUMPF [103].

We observe that the total energy is polyconvex. Furthermore the volume of the neighborhood sets $B_\epsilon(\mathscr{D}_T)$ and $B_\epsilon(\mathscr{D}_R)$ of the singularity sets $\mathscr{D}_T$ and $\mathscr{D}_R$ respectively can be controlled. Hence, we can basically confine to a set, where the integrand fulfills Carathéodory's conditions.

Let us first recall the weak continuity results for the principle invariants of the Jacobian. In fact they are the only non linear mappings which are weakly continuous.

> Given a sequence of deformations $(\phi^k)_k$ in $H^{1,p}$, with $\mathrm{Cof}\, D\phi^k \in L^q$ and $\det D\phi^k \in L^r$, then we have the following weak continuity results:
>
> $$\left. \begin{array}{l} \phi^k \rightharpoonup \phi \text{ in } H^{1,p} \\ \mathrm{Cof}\, D\phi^k \rightharpoonup C \text{ in } L^q \\ \det D\phi^k \rightharpoonup D \text{ in } L^r \end{array} \right\} \Rightarrow C = \mathrm{Cof}\, D\phi \text{ and } D = \det D\phi.$$

For the proof we refer to BALL [13] or the book of Ciarlet [61, Section 7.5, 7.6] or Dacorogna [79]. The proof of the theorem proceeds in 5 steps:

*Step 1.* Due to the assumption on the image set $\mathscr{I}(\Omega)$ we have $\mu(\mathscr{D}(u_R)) = \mu(\mathscr{D}(u_T)) = 0$ and hence the energy $E_{\mathscr{M}}[\phi]$ is well defined for all $\phi \in \mathscr{A}^{\#}$. In particular $\omega_0(\nabla u_T \circ \phi, \nabla u_R, \mathrm{Cof}\, D\phi)$ is measurable. Obviously $\mathbb{1} \in \mathscr{A}$ and $E[\mathbb{1}] < \infty$, thus

$$\underline{E} := \inf_{\phi \in \mathscr{A}^{\#}} E[\phi] < \infty$$

and due to (3.22) and the positivity of $\omega_0$ we get $\underline{E} \geq 0$. Let us consider a minimizing sequence $(\phi^k)_{k=0,1,\dots} \subset \mathscr{A}^{\#}$ with $E[\phi^k] \to \inf_{\phi \in \mathscr{A}^{\#}} E[\phi]$. We denote by $\overline{E}$ an upper bound of the energy $E$ on this sequence. Due to the growth condition on $W$ we get that the sequence $\left\{ (D\phi^k, \mathrm{Cof}\, D\phi^k, \det D\phi^k) \right\}_{k=0,1,\dots}$ is uniformly bounded in $L^p(\Omega) \times L^q(\Omega) \times L^r(\Omega)$. Because of the reflexivity of $L^p \times L^q \times L^r$ for $p, q, r > 1$ we can extract a weakly convergent subsequence, again denoted by an index $k$, such that

$$(D\phi^k, \mathrm{Cof}\, D\phi^k, \det D\phi^k) \rightharpoonup (D\phi, C, D)$$

in $L^p \times L^q \times L^r$ with $C : \Omega \to \mathbb{R}^{3 \times 3}$, $D : \Omega \to \mathbb{R}$. Applying the above results on weak convergence we achieve $C = \mathrm{Cof}\, D\phi$ and $D = \det D\phi$. Further by (3.23) we can infer on account of Lemma 3.2.7 we obtain that $\left\{ \phi^k \right\}_{k=0,1,\dots}$ is uniformly bounded in $H^{1,p}(\Omega)$.

In particular the incorporation of the energy $E_{\mathrm{dist}}$ into $E_{\mathrm{total}}$ ensures the boundedness of the $L^p$-norm of the infimizing sequence. For Dirichlet boundary conditions on a subset of $\partial\Omega$, this could be achieved by a simple application of the Poincaré-inequality. Since $\Omega$ has Lipschitz boundary and $p > 3$ the Sobolev space $H^{1,p}(\Omega; \mathbb{R}^3)$ is compactly embedded in $\mathscr{C}^0(\bar\Omega)$ by Kondrašov's Theorem (cf. [165, p. 107]). Hence $\phi^k$ converges uniformly and we obtain $\phi \in \mathscr{C}^0(\bar\Omega)$.

*Step 2*. Next, we control the set where the volume shrinks by a factor of more than $\epsilon$ for the limit deformation. Let us define

$$S_\epsilon = \{ x \in \Omega \,:\, \det D\phi \leq \epsilon \}$$

for $\epsilon \geq 0$. Let as assume without loss of generality that the sequence of energy values $E[\phi^k]$ is monotone decreasing and that for given $\epsilon > 0$ we denote by $k(\epsilon)$ the smallest index such that

$$E[\phi^k] \leq E[\phi^{k(\epsilon)}] \leq \underline{E} + \epsilon \qquad \forall k \geq k(\epsilon).$$

From Step 1 we know that the sequence $\Psi^k := (D\phi^k, \mathrm{Cof}\, D\phi^k, \det D\phi^k)$ converges weakly to $\Psi := (D\phi, \mathrm{Cof}\, D\phi, \det D\phi)$ in $L^p \times L^q \times L^r$. Hence, applying Mazur's Lemma we obtain a sequence of convex combinations of $\Psi^k$ and $\phi^k$ which converges strongly to $\Psi$ and $\phi$ in $L^p \times L^q \times L^r \times L^p$. Thus, there exists a family of weights $((\lambda_i^k)_{k(\epsilon) \leq i \leq k})_{k \geq k(\epsilon)}$ with $\lambda_i^k \geq 0$, $\sum_{k(\epsilon)}^k \lambda_i^k = 1$, such that

$$\lambda_i^k \Psi^i \to \Psi \ \text{ and } \ \lambda_i^k \phi^i \to \phi.$$

Now, taking into account the growth conditions, the convexity of $W$ and Fatou's Lemma we estimate

$$
\begin{aligned}
\beta \epsilon^{-s} \mu(S_\epsilon) \ &\leq \ \beta \int_{S_\epsilon} (\det D\phi)^{-s}\, \mathrm{d}\mu \leq \int_{S_\epsilon} W(\Psi)\, \mathrm{d}\mu \\
&= \ \int_{S_\epsilon} \liminf_{k \to \infty} W(\lambda_i^k \Psi^i)\, \mathrm{d}\mu \leq \int_{S_\epsilon} \liminf_{k \to \infty} \lambda_i^k W(\Psi^i)\, \mathrm{d}\mu \\
&\leq \ \liminf_{k \to \infty} \lambda_i^k \int_{S_\epsilon} W(\Psi^i)\, \mathrm{d}\mu \\
&\leq \ \liminf_{k \to \infty} \lambda_i^k \int_{\Omega} W(\Psi^i) + \omega_0(\nabla u_T \circ \phi^i, \nabla u_R, \mathrm{Cof}\, D\phi^i)\, \mathrm{d}\mu \\
&\leq \ \overline{E}
\end{aligned}
$$

and infer $\mu(S_\epsilon) \leq \frac{\bar{E}\epsilon^s}{\beta}$. As one consequence $\mu(S_0) = 0$ and we know that $\det D\phi > 0$ a. e. on $\Omega$.

*Step 3*. Now, we deal with the singularity set of the image $u_T$. By our assumption on the image set $\mathscr{I}(\Omega)$ we know that for given $\delta > 0$ there exist $\epsilon_T > 0$ such that $\mu(B_{\epsilon_T}(\mathscr{D}_T)) \leq \delta$. From this and the injectivity (cf. [14, Theorem 1 (ii)]) we especially deduce the estimate

$$\mu\left(\phi^{-1}(B_{\epsilon_T}(\mathscr{D}_T)) \setminus S_\epsilon\right) \leq \frac{1}{\epsilon} \int_{\phi^{-1}(B_{\epsilon_T}(\mathscr{D}_T))} \det D\phi\, \mathrm{d}\mu = \frac{1}{\epsilon} \int_{B_{\epsilon_T}(\mathscr{D}_T)} \mathrm{d}\mu \leq \frac{\delta}{\epsilon}.$$

Hence, we can control the pre-image of $B_\epsilon(\mathscr{D}_T)$ with respect to $\phi$ but restricted to $\Omega \setminus S_\epsilon$. Due to the continuous differentiability of both images $u_T$ and $u_R$ we can assume that

$$\|\nabla u_T(x)\| \ \geq \ \gamma(\epsilon) \text{ on } \Omega \setminus B_\epsilon(\mathscr{D}_T) \tag{3.24}$$

where $\gamma : \mathbb{R}_0^+ \to \mathbb{R}$ is a strictly monotone function with $\gamma(0) = 0$.

*Step 4*. Let us now define the set

$$R_{\epsilon,\delta} := \phi^{-1}(B_{\epsilon_T}(\mathscr{D}_T)) \cup S_\epsilon,$$

whose measure can be estimated in terms of $\epsilon$ and $\delta$, i.e.

$$\mu(R_{\epsilon,\delta}) \leq \frac{\delta}{\epsilon} + \frac{\bar{E}\epsilon^s}{\beta}.$$

On account of the uniform convergence of $\phi^k$ the sequence $(\nabla u_T \circ \phi^k)_{k=0,1,\dots}$ converges uniformly to $\nabla u_T \circ \phi$ on $\Omega \setminus R_{\epsilon,\delta}$. Next, from the assumption on $\omega$ and the 0-homogeneous extension property of $\omega_0$ we deduce that

$$|\omega_0(u, w, A) - \omega_0(v, w, A)| \leq C_\gamma \|u - v\| (1 + \|A\|_2^m) \tag{3.25}$$

for $u, v, w \in \mathbb{R}^3$, $A \in \mathbb{M}^3$ and $\|u\|, \|v\|, \|w\| \geq \gamma$. To use this estimate for $u = u_T \circ \phi^k$ and $v = u_T \circ \phi$ below, we assume that $k(\epsilon)$ is large enough, such that $\phi^k(x) \in \Omega \setminus B_{\frac{\epsilon_T}{2}}(\mathscr{D}_T)$ for $x \in \Omega \setminus R_{\epsilon,\delta}$ and

$$C_{\gamma(\frac{\epsilon_T}{2})} \|\nabla u_T \circ \phi^k - \nabla u_T \circ \phi\|_{\infty, \Omega \setminus R_{\epsilon,\delta}} \leq \epsilon$$

for all $k \geq k(\epsilon)$. Now we are able to estimate $E[\phi]$ using especially the convexity of $W$ and $\omega(v, w, \cdot)$, the estimate (3.25), the Hölder inequality and Fatou's Lemma:

$$
\begin{aligned}
E[\phi] &= \int_\Omega W(\Psi) + \omega_0(\nabla u_T \circ \phi, \nabla u_R, \mathrm{Cof}\, D\phi)\, \mathrm{d}\mu \\
&\leq \int_\Omega \liminf_{k\to\infty} \lambda_i^k W(\Psi^i)\, \mathrm{d}\mu + \|n_T \circ \phi - n_R\| C_\omega \int_{R_{\epsilon,\delta}} (1 + \|\mathrm{Cof}\, D\phi\|^m)\, \mathrm{d}\mu \\
&\quad + \int_{\Omega \setminus R_{\epsilon,\delta}} \liminf_{k\to\infty} \lambda_i^k \omega_0(\nabla u_T \circ \phi, \nabla u_R, \mathrm{Cof}\, D\phi^i)\, \mathrm{d}\mu \\
&\leq \liminf_{k\to\infty} \lambda_i^k \int_\Omega W(\Psi^i)\, \mathrm{d}\mu + \underbrace{2 C_\omega \left( \mu(R_{\epsilon,\delta}) + \left( \int_{R_{\epsilon,\delta}} \|\mathrm{Cof}\, D\phi\|^{m \cdot \frac{q}{m}}\, \mathrm{d}\mu \right)^{\frac{m}{q}} \cdot \mu(R_{\epsilon,\delta})^{1-\frac{m}{q}} \right)}_{=b(\mu(R_{\epsilon,\delta}))} \\
&\quad + \liminf_{k\to\infty} \lambda_i^k \int_{\Omega \setminus R_{\epsilon,\delta}} \Big( \omega_0(\nabla u_T \circ \phi, \nabla u_R, \mathrm{Cof}\, D\phi^i) - \omega_0(\nabla u_T \circ \phi^i, \nabla u_R, \mathrm{Cof}\, D\phi^i) \\
&\quad\quad\quad\quad + \omega_0(\nabla u_T \circ \phi^i, \nabla R, \mathrm{Cof}\, D\phi^i) \Big)\, \mathrm{d}\mu
\end{aligned}
$$

where $b(s) := 2\, C_\omega (s + (\frac{\bar{E}}{\beta})^{\frac{m}{q}} s^{1-\frac{m}{q}})$. Here we have in particular used the *a priori* estimate $\|\mathrm{Cof}\, D\phi\|_{q,\Omega} \leq (\frac{\bar{E}}{\beta})^{\frac{1}{q}}$. We estimate further and obtain

$$
\begin{aligned}
E[\phi] &\leq \liminf_{k\to\infty} \lambda_i^k \int_\Omega \Big( W(\Psi^i) + \omega_0(\nabla u_T \circ \phi^i, \nabla u_R, \mathrm{Cof}\, D\phi^i) \Big)\, \mathrm{d}\mu + 2\, b(\mu(R_{\epsilon,\delta})) \\
&\quad + C_{\gamma(\frac{\epsilon_T}{2})} \sup_{k\to\infty} \int_{\Omega \setminus R_{\epsilon,\delta}} \|\nabla u_T \circ \phi - \nabla u_T \circ \phi^k\| \left( 1 + \|\mathrm{Cof}\, D\phi^k\|_2^m \right) \mathrm{d}\mu \\
&\leq \liminf_{k\to\infty} \lambda_i^k E[\phi^i] + 2\, b(\mu(R_{\epsilon,\delta})) + \epsilon\, b(\mu(\Omega)) \\
&\leq \underline{E} + \epsilon + 2\, b(\mu(R_{\epsilon,\delta})) + \epsilon\, b(\mu(\Omega)) .
\end{aligned}
$$

For given $\bar{\epsilon}$ we choose $\epsilon$ and then $\delta$ and the dependent $\epsilon_T$ small enough and $k(\bar{\epsilon})$ large enough to ensure that

$$\epsilon + 2\, b(\mu(R_{\epsilon,\delta})) + \epsilon\, b(\mu(\Omega)) \leq \bar{\epsilon} .$$

and get $E[\phi] \leq \underline{E} + \bar{\epsilon}$. This holds true for an arbitrary choice of $\bar{\epsilon}$. Thus we conclude

$$E[\phi] \leq \underline{E} = \inf_{\phi \in \mathscr{A}^\#} E[\phi] .$$

*Step 5.* We will sketch how to prove $\int_\Omega \det D\phi\, \mathrm{d}\mu \leq \mu(\phi(\Omega))$ to deduce that $\phi \in \mathscr{A}^\#$ and infer that the minimizer is injective almost everywhere, by following the arguments given in [62]. Let $\epsilon > 0$ be arbitrary but fixed. Due to the compactness of $\phi(\bar{\Omega})$, the properties of the Lebesgue measure provide an open set $O_\epsilon$ such that $\phi(\bar{\Omega}) \subset O_\epsilon$ and $\mu(O_\epsilon \setminus \phi(\bar{\Omega})) < \epsilon$. Due to the

compactness of $\phi(\bar{\Omega} \setminus R_\epsilon)$ one can show that there exists $\delta = \delta(\epsilon) > 0$ such that $B_\delta(\phi(\bar{\Omega})) \subset O_\epsilon$ and deduce that there exists $k_0 = k_0(\epsilon)$, such that

$$\phi^k(\bar{\Omega} \setminus R_\epsilon) \subset O_\epsilon \quad \forall k \geq k_0, \tag{3.26}$$

where we used the fact that the sequence $\phi^k$ converges uniformly. The choice of $\mathscr{A}^\#$ and the inclusion (3.26) implies

$$\int_\Omega \det D\phi^k \leq \mu(\phi^k(\bar{\Omega})) \leq \mu(O_\epsilon).$$

Since $\det D\phi^k \rightharpoonup \det D\phi$ in $L^r$ we infer that

$$\int_\Omega \det D\phi \, \mathrm{d}\mu = \lim_{k \to \infty} \int_\Omega \det D\phi^k \, \mathrm{d}\mu \leq \mu(O_\epsilon) = \mu(\phi(\bar{\Omega})) + \epsilon$$

The arguments of *Step 2* or the fact that $\phi \in H^{1,p}(\Omega; \mathbb{R}^3)$, $p > 3$, $d = 3$ imply that $\phi$ maps sets of zero volume onto sets of zero volume. Since $\Omega$ is a Lipschitz domain, we infer $\mu(\partial\Omega) = 0$, and hence $\mu(\phi(\bar{\Omega})) = \mu(\phi(\Omega))$. Since $\epsilon$ was arbitrary we can deduce

$$\int_\Omega \det D\phi \leq \mu(\phi(\Omega)).$$

Since $\phi \in H^{1,p}(\Omega; \mathbb{R}^3)$ and $p > 3$, we can apply a theorem of MARCUS&MIZEL[147] to obtain

$$\int_\Omega \det D\phi = \int_{\phi(\Omega)} \mathrm{card}\,(\phi^{-1}) \, \mathrm{d}\mu$$

and finally deduce

$$\mu(\phi(\Omega)) \leq \int_{\phi(\Omega)} \mathrm{card}\,(\phi^{-1}) \, \mathrm{d}\mu = \int_\Omega \det D\phi \leq \mu(\phi(\Omega))$$

which proves (3.19).

$$\square$$

**Remarks 3.2.11.**

(i) *In Step 1 step a Poincaré type argument for deformations with fixed Dirichlet conditions on a part $\Gamma_D$ of the boundary was replaced by assumption (3.23).*

(ii) *Step 2 to Step 4 are almost identical to the proof of existence with fixed boundary of [103].*

(iii) *Step 5 is necessary to show that the minimizer is in the admissible set. For the details we refer to [62].*

(iv) CIARLET&NEČAS *have given an interpretation for the minimizer of the elastic minimization problem along the boundary, for $x \in \partial\Omega$, we have $\hat{\mathbf{T}}[\phi](x) \cdot \nu = 0$ if there is no contact, and otherwise $\hat{\mathbf{T}}[\phi](x_1) \cdot \nu_1 + \hat{\mathbf{T}}[\phi](x_2) \cdot \nu_2 = 0$, for $\phi(x_1) = \phi(x_2)$ and $x_1 \neq x_2$. Here, the tensor $\hat{\mathbf{T}}$ is given by*

$$\langle E'[\phi]; \psi \rangle = \int_\Omega \hat{\mathbf{T}} : D\psi \, \mathrm{d}\mu.$$

*Furthermore they have also treated the problem with the presence of an obstacle.*

## 3.3  Variation of the energy

In order to applied a regularized gradient descent method as in Chapter 2, let us now address the calculation of the variations of the total energy (3.20). For smooth images, the morphological matching energy does not recognize perturbations of the deformation in normal direction of the template, i. e., in direction $n_T \circ \phi$, hence there exist stationary points which are arbitrary close in the set of minimizers (if they exist) when no regularization is considered. The problem of minimizing the morphological matching energy is hence ill-posed and requires a suitable regularization.

### 3.3.1 The hyperelastic regularization energy $E_{\mathrm{reg}}$

Let us first recall the variation of the *hyperelastic* regularization energy of the form (3.12). Let us consider the contributions

$$E_{\mathrm{len}}[\phi] = \int_\Omega \|D\phi\|^p \, \mathrm{d}\mu, \qquad E_{\mathrm{surf}}[\phi] = \int_\Omega \|\mathrm{Cof}\, D\phi\|^q \, \mathrm{d}\mu \quad \text{and} \quad E_{\mathrm{vol}}[\phi] = \int_\Omega \Gamma(\det D\phi) \, \mathrm{d}\mu.$$

Then the variations of $E_{\mathrm{len}}$ and $E_{\mathrm{surf}}$ can be calculated straightforwardly by the chain rule:

$$\langle E_{\mathrm{len}}[\phi]; \psi \rangle = p \int_\Omega \|D\phi\|^{p-2} D\phi : D\psi \, \mathrm{d}\mu$$

$$\langle E_{\mathrm{surf}}[\phi]; \psi \rangle = q \int_\Omega \|\mathrm{Cof}\, D\phi\|^{p-2} \mathrm{Cof}\, D\phi : \langle \mathrm{Cof}\,' D\phi; D\psi \rangle \, \mathrm{d}\mu.$$

Here, $\mathrm{Cof}\,' A$ denotes the Fréchet-derivative of the mapping $\mathrm{Cof} : \mathbb{R}^{d,d} \to \mathbb{R}^{d,d}$, $A \mapsto \mathrm{Cof}\, A$. For the variation of $E_{\mathrm{vol}}$ we note that for $A \in \mathbb{M}^d$ invertible and $H \in \mathbb{M}^d$, we have $\det(A+H) = \det A \cdot \det(I + A^{-1}H) = \det A \cdot (1 + \mathrm{tr}(A^{-1}H) + o(\|H\|))$, whence, $\langle \det'(A); H \rangle = \det A \cdot \mathrm{tr}(A^{-1}H) = \mathrm{tr}(\mathrm{Cof}\, A^T H)$, so we obtain

$$\langle E_{\mathrm{vol}}[\phi]; \psi \rangle = \int_\Omega \Gamma'(\det D\phi) \mathrm{tr}\big((\mathrm{Cof}\, D\phi)^T D\psi\big) \, \mathrm{d}\mu.$$

### 3.3.2 The morphological matching energy $E_{\mathscr{M}}$

For the specific form of the integrand 3.14, the variation of the energy is given by the following theorem.

**Theorem 3.3.1.** *Let $n_T$, $n_R \in \mathscr{C}^1(\Omega; \mathbb{R}^d)$, and $\omega$ be given by*

$$\omega = \hat{\omega}\left((\mathbb{1} - u \otimes u) Av\right) \quad \text{where } \hat{\omega} : \mathbb{R}^d \to \mathbb{R} \text{ convex}, \tag{3.27}$$

*then the variation of the morphological matching energy is given by*

$$\langle E_{\mathscr{M}}'[\phi]; \psi \rangle = -\int_\Omega D\hat{\omega}\big(P[n_T \circ \phi]\mathrm{Cof}\, D\phi\, n_R\big) \cdot \Big\{ (n_T \circ \phi \cdot \mathrm{Cof}\, D\phi\, n_R) \cdot Dn_T \circ \phi$$

$$+ (n_T \circ \phi) \otimes (Dn_T \circ \phi \cdot \mathrm{Cof}\, D\phi n_R)\Big\} \cdot \psi \, \mathrm{d}\mu$$

$$+ \int_\Omega D\hat{\omega}\big(P[n_T \circ \phi]\mathrm{Cof}\, D\phi\, n_R\big) \cdot \Big\{ P[n_T \circ \phi](\langle \mathrm{Cof}\,' D\phi; D\psi \rangle) \cdot n_R \Big\} \, \mathrm{d}\mu$$

*Proof.* First, recall that for an energy of the form

$$E[\phi] = \int_\Omega f(x, \phi, D\phi) \, \mathrm{d}\mu$$

the variation is given by

$$\langle E'[\phi]; \psi \rangle = \frac{d}{dt} E[\phi + t\psi]\Big|_{t=0}$$

$$= \int_\Omega \left( \frac{d}{dt} f(x, \phi + t\psi, D\phi)\Big|_{t=0} \cdot \psi + \frac{d}{dt} f(x, \phi, D\phi + tD\psi)\Big|_{t=0} : D\psi \right) \mathrm{d}\mu.$$

We first derive w.r.t. $\phi$, setting $f(v, A) := \hat{\omega}((\mathbb{1} - (n_T \circ v) \otimes (n_T \circ v)) \cdot \mathrm{Cof}\, A\, n_R)$:

$$\frac{d}{dt} f(\phi + t\psi, D\phi)\Big|_{t=0} = \frac{d}{dt} \hat{\omega}\big((\mathbb{1} - (n_T \circ (\phi + t\psi)) \otimes (n_T \circ (\phi + t\psi))) \cdot \mathrm{Cof}\, D\phi\, n_R\big)\Big|_{t=0}$$

$$= -D\hat{\omega}\big(P[n_T \circ \phi]\mathrm{Cof}\, D\phi\, n_R\big) \cdot \big[Dn_T \circ \phi \cdot ((n_T \circ \phi) \cdot \mathrm{Cof}\, D\phi\, n_R)\psi$$

$$+ n_T \cdot \frac{d}{dt}(n_T \circ (\phi + t\psi) \cdot n_R)\Big|_{t=0}\big].$$

where we have first applied the chain rule and the product rule. For $n : \mathbb{R}^d \to \mathbb{R}^d$ and $v \in \mathbb{R}^d$, we calculate further

$$(n(z) \cdot (D(n(z) \cdot v)))_{ij} = n_i(z)(n_{k,j}(z) \cdot v_k)_j = (n(z) \otimes ((Dn(z))^T \cdot v))_{ij}$$

and obtain

$$\frac{d}{dt}(n_T \circ (\phi + t\psi) \cdot \operatorname{Cof} D\phi \, n_R)\Big|_{t=0} = (n_T \circ \phi) \otimes (Dn^T \circ \phi \cdot \operatorname{Cof} D\phi \, n_R)$$

which yields the first integral. We continue with the derivation with respect to $D\phi$:

$$\begin{aligned}
\frac{d}{dt}f(\phi, D\phi + tD\psi)\Big|_{t=0} &= \frac{d}{dt}\hat{\omega}\big(P[n_T \circ \phi] \cdot \operatorname{Cof}(D\phi + tD\psi) \, n_R\big)\Big|_{t=0} \\
&= D\hat{\omega}\big(P[n_T \circ \phi] \cdot \operatorname{Cof} D\phi \, n_R\big) \cdot \\
&\qquad P[n_T \circ \phi]\big(D_{D\phi}\operatorname{Cof} D\phi : D\psi\big) \cdot \operatorname{Cof} D\phi \, n_R
\end{aligned}$$

where we again applied the chain rule and used the following formula. For $F : \mathbb{R}^{d,d} \to \mathbb{R}$, $A \mapsto \hat{\omega}(B[A] \cdot v)$, $v \in \mathbb{R}^d$, $B : \mathbb{R}^{d,d} \to \mathbb{R}^{d,d}$, $C \in \mathbb{R}^{d,d}$ we have

$$(\langle F[A]; C \rangle)_i = (F_{i,st}C_{st}) = \bar{\omega}_i(B[A] \cdot v)B_{ij,st}v_j C_{st}.$$

$\square$

### 3.3.3 The feature energy $E_{\text{dist}}$

It is well known that the gradient of the area functional

$$e[\mathcal{M}] = \int_{\mathcal{M}} \mathrm{d}A$$

is given by

$$\langle e'[\mathcal{M}]; v \rangle = \int_{\mathcal{M}} h_{\mathcal{M}}(n \cdot v) \, \mathrm{d}A.$$

Whence for the area functional of the transformed curve $\phi(\Gamma)$

$$e[\phi] := \int_{\phi(\Gamma)} \mathrm{d}A \tag{3.28}$$

we infer—assuming that $\phi$ is invertible by means of the regularization—that

$$\langle e'[\phi]; \psi \rangle = \int_{\phi(\Gamma)} h_{\phi(\Gamma)}(n_{\phi(\Gamma)} \cdot \psi \circ \phi^{-1}) \, \mathrm{d}A = \int_{\Gamma} h_{\phi(\Gamma)} \circ \phi(n_{\phi(\Gamma)} \cdot \psi)\|\operatorname{Cof} D\phi n_\Gamma\| \, \mathrm{d}A. \tag{3.29}$$

Here we have applied the transformation rule

$$\int_{\phi(\Gamma)} g \, \mathrm{d}A = \int_{\Gamma} g \circ \phi\|\operatorname{Cof} D\phi n_\Gamma\| \, \mathrm{d}A. \tag{3.30}$$

On the other hand, the functional in (3.28) is equal to

$$e[\phi] = \int_{\Gamma} \|\operatorname{Cof} D\phi n_\Gamma\| \, \mathrm{d}A,$$

so we obtain,

$$\langle e'[\phi]; \psi \rangle = \int_{\Gamma} D_{D\phi}\|\operatorname{Cof} D\phi n_\Gamma\| : D\psi \, \mathrm{d}A. \tag{3.31}$$
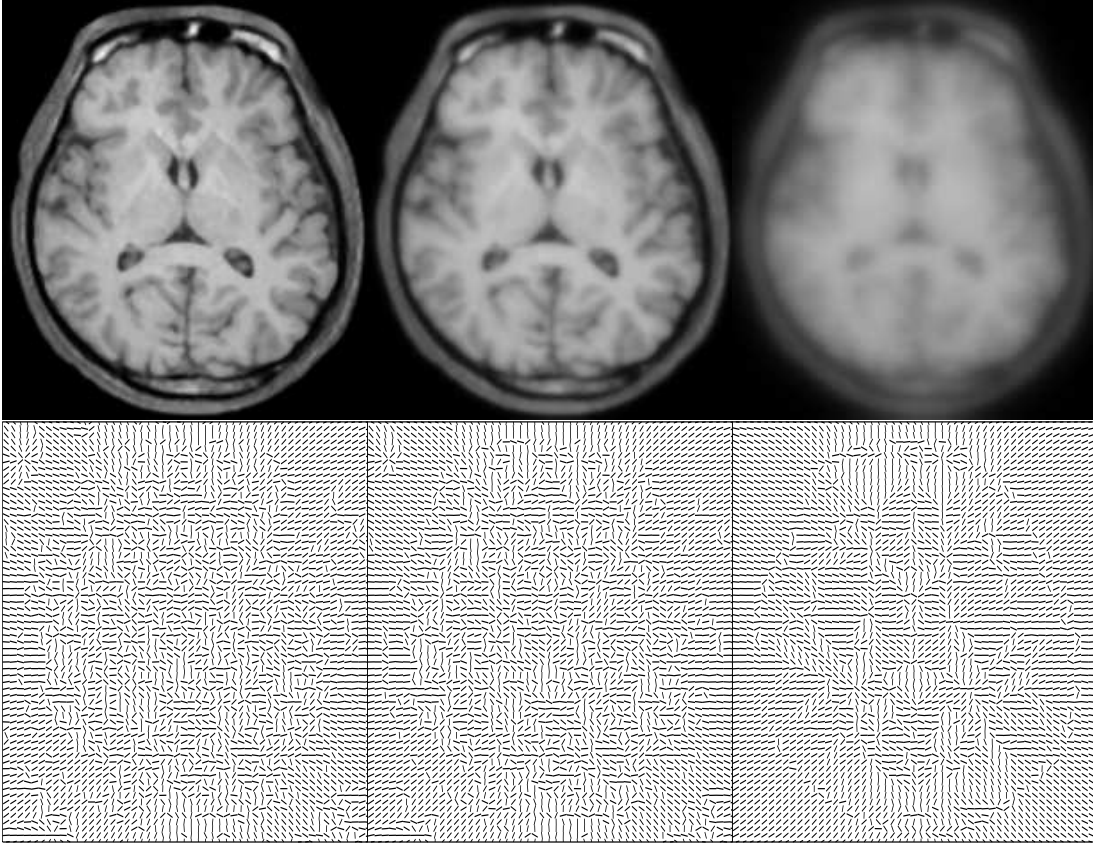
Figure 3.7: *Image and the Gauss map and the corresponding grid for the brain slice at scales* $\sigma = h, 2h, 8h$.

By combining (3.29) and (3.31) and the fact that $\Gamma$ was arbitrary, we deduce that $D_{D\phi}\|\text{Cof}\, D\phi\|$ : $D\psi = h_{\phi(\Gamma)} \circ \phi(n_{\phi(\Gamma)} \cdot \psi)\|\text{Cof}\, D\phi\|$ almost everywhere. Before we proceed with the derivation of $E_{\text{dist}}$, transform the integral to $\Gamma_R$ instead of deriving on $\phi(\Gamma_R)$:

$$E_{\text{dist}}[\phi] = \int_{\phi(\Gamma_R)} \text{dist}(\cdot, \Gamma_T)^2 \, \mathrm{d}A = \int_{\Gamma_R} \text{dist}(\cdot, \Gamma_T)^2 \circ \phi\|\text{Cof}\, D\phi n_\Gamma\| \, \mathrm{d}A,$$

and thus, by using the observation from above, we calculate (setting $d_{\Gamma_T} := \text{dist}(\cdot, \Gamma_T)$)

$$\langle E'_{\text{dist}}[\phi]; \psi \rangle = \int_{\Gamma_R} \left( 2d_{\Gamma_T} \circ \phi \nabla d_{\Gamma_T} \circ \phi\|\text{Cof}\, D\phi n_\Gamma\|\psi + (d_{\Gamma_T} \circ \phi)D_{D\phi}\|\text{Cof}\, D\phi n_\Gamma\| : D\psi \right) \mathrm{d}A$$

$$= \int_{\Gamma_R} \left( 2d_{\Gamma_T} \circ \phi \nabla d_{\Gamma_T} \circ \phi\|\text{Cof}\, D\phi n_\Gamma\|\psi + (d_{\Gamma_T} \circ \phi)h_{\phi(\Gamma)} \circ \phi(n_{\phi(\Gamma)} \cdot \psi)\|\text{Cof}\, D\phi n_\Gamma\| \right) \mathrm{d}A.$$

We want to remark that the derivation can also be obtained by applying the derivation rules in the context of *shape sensitivity analysis*, in particular equation (5.9).

## 3.4   Implementation

The implementation of the minimization of the total energy (3.20) is done exactly the way as described in Section 2.6.7. In order to implement Algorithm 2.6.7, we have to choose a suitable scale space operator on the normals. We induce a such a scale operator, by first considering a scale space operator on the images and computing the normals from the images at a coarser

scale. The natural morphological scale space is given by the mean curvature flow. We define

$$n_u^\sigma := n_{u^\sigma} \quad \text{for } u = u_T, u_R$$

Moreover, the restriction that the measure of flat region of the images is zero cannot be ensured in practice. To avoid, division by zero, whence undefined normals, we consider the following approximation to the normalization:

$$n_u^{\sigma,\epsilon} := \frac{\nabla u_\sigma}{\sqrt{\|\nabla u_\sigma\|^2 + \epsilon^2}} \quad \text{for} \quad u = u_T, u_R \text{ and } \epsilon > 0.$$

As in the unimodal case, the smoothed data induces a coarse scale energy $E_{\mathscr{M}}^\sigma$. Alternatively, one might consider a simple Gaussian filtering by linear diffusion. In fact, the linear smoothing worked well in practice. The homogenous diffusion in all directions had a favorable effect on the overall matching algorithm. The effect of Gaussian filtering on the normals is shown in Figure 3.7. As a regularizing metric we chose $g = (\cdot,\cdot)_{L^2} + \frac{\sigma^2}{2}(\nabla\cdot,\nabla\cdot)_{L^2}$.

## 3.5 Results and Discussion

To test a registration approach, one has to study the resulting deformation. Given an image $u_R$ and an image $u_T$, there usually exists a large set of deformations such that the disparity of $u_R$ and $u_T \circ \phi$ is small with respect to the matching energy, possibly containing entirely meaningless deformations. Thus, a true validation cannot be based on the observation of the deformed template itself. However, in real applications the exact deformation is not known.

Figure 3.3 shows a test example, in which the reference image has been generated by a deformation of a given template $u_T$ (MRT) for a known deformation $\psi \in \mathscr{A}_0$. Furthermore, the grey values of the deformed template $u_T \circ \psi$ have been transformed under a *non-monotone* contrast change $\beta : \mathbb{R} \to \mathbb{R}$ and finally defined $u_R := \beta \circ u_T \circ \psi$. The computed solution $\phi$ now yields a deformed template $u_T \circ \phi$ which is shown on the bottom right. The white circles indicate some regions of interest, we see that visually, the deformed structures are very close to the shapes of $u_R$, even in regions with low contrast. The advantage of the morphological registration approach is the independence of contrast, and thus the only driving factor is given by the geometry. On the other hand, we deduce that dominating edges are neglected entirely. In Chapter 5 we will enhance the registration approach by taking into account the alignment of discontinuities[1]. Finally, Figure 3.4 compares the deformation $\psi$ with the computed result $\phi$. We observe that the deformation

*(i)* is regular and injective, i. e., no over-folding occurred,

*(ii)* captures the structure of the original "exact" deformation $\psi$.

*(iii)* In the regions closer to the boundary, the computed solution is closer to the identity than $\psi$. This is explained by the fact, that in this regions the images themselves to do not show any relevant morphological structures, so here the regularization energy dominates.

Figure 3.8 shows an application on a real, multimodal set of data. The reference image is a section of a CT scan of the human spine, the bone of a particular vertebra is clearly visible and shown as the bright structures in the center of the image. The template image is an MRT scan of the same patient and particularly reveals the tissue structure. Still, the major morphological features are very similar. The white dots mark some dominant visible features in the reference image, which have been selected by hand. These are shown at the *same position* in the template to illustrate the initial misfit.

Due to the complexity of the images, especially the oscillatory textures in the bottom part of the template and the lack of these structures in the reference, the incorporation of a feature energy was necessary. Instead of incorporating the *feature-based energy* into the total energy we

---

[1]This is to be understood in the sense of the model of *Mumford-Shah*.

proceeded in two steps. This allows to validate the additional effect of the morphological energy separately. The two images on the bottom show the result after the *pre-registration* under the minimization of the *feature-energy* and the final result by minimizing the combination of the regularization and the morphological matching energy. Especially in the middle of the image, one can see a significant improvement of the matching result after the second step.

This is further visualized in Figure 3.9, which shows a striped superposition of the reference template in comparison to the initial template and the final deformed template. Figure 3.10 shows the corresponding deformations after the first and the second step respectively. Here, on can see that the pre-registration mainly results in a pure shift, while the final morphological registration locally aligns significant morphological features.

Finally, in Figure 3.12 the result of a registration of two MR images is shown, the reference is T1-weighted, while the template is a FLAIR image. Both images were taken from the same patient. Both images are already geometrically close to each other, so we did not incorporate the feature based energy. The deformed template matches well to the original reference in most parts of the image. Even though the morphology is aligned also in the region marked by the dotted line, the dominant edges are not overlaid well. The registration morphological energy only measures deviations of the Gauss-maps, the alignment of these features however would correspond to a shift in normal direction. In such cases, additional modeling of feature alignment has to be taken into account. This will be the subject of Chapter 5.

Figure 3.8: *Sectional morphological registration on a pair of MR and CT images of a human spine. Dotted lines mark certain features visible in the reference image. There are repeatedly drawn at the same position in the other images.* TOP LEFT: *reference, CT,* TOP RIGHT: *template, MR, with clearly visible misfit of structures marked by the dotted lines.* BOTTOM LEFT: *deformed template after feature based registration $T \circ \phi_f$, where $\phi_f$ is the result of a feature based pre-registration (cf. Figure 3.11 for the feature sets used in this example).* BOTTOM RIGHT: *deformed template $T \circ \phi$ after final registration where the dotted feature lines nicely coincide with the same features in the deformed template MR-image. All images have a resolution of $257^2$.*
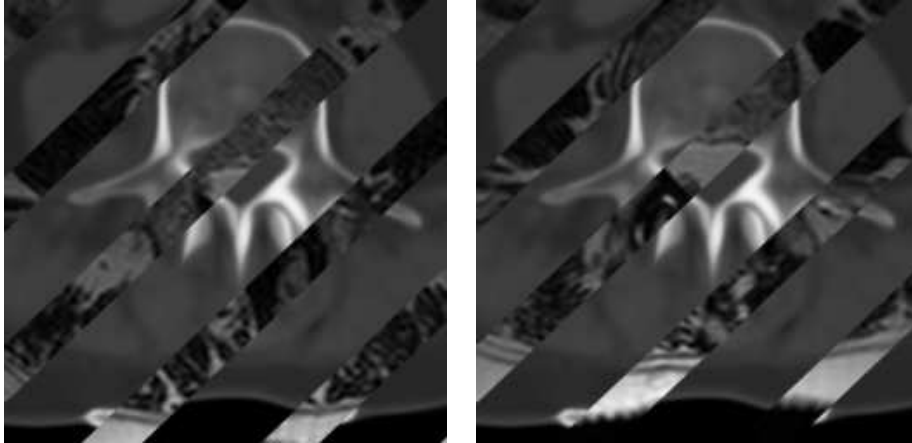
Figure 3.9: *Comparison of superimposed template and reference before* (LEFT) *and after* (RIGHT) *registration.*
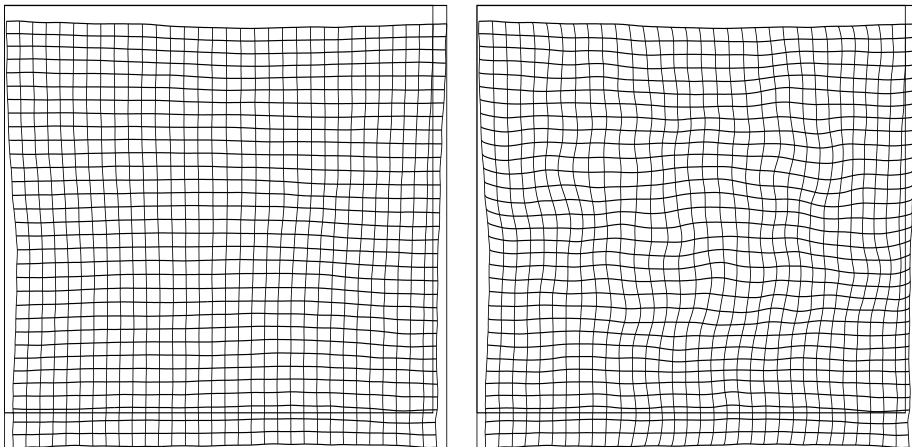


Figure 3.10: LEFT: *deformation after the pre-registration solely based on the feature energy.* RIGHT: *final deformation after the registration including feature and morphological matching energy.*
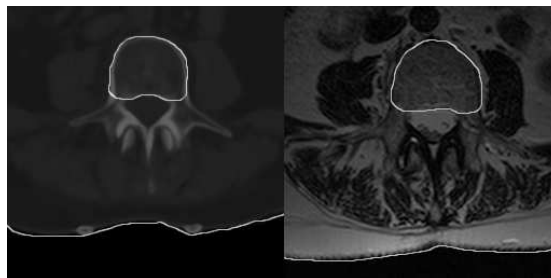


Figure 3.11: Feature sets serving as a rough guidance of the matching process.

Initial misfit

After registration

Figure 3.12: *Registration of a T1-weighted MR-image* (TOP LEFT) *against an MR-image with FLAIR weighting* (TOP RIGHT) *. The initial misfit and the final registration result are shown in the* (BOTTOM LEFT) *and* (BOTTOM RIGHT) *parts respectively.*

# Chapter 4

# Γ-Convergence of perturbed registration energies

WE have considered mainly two kinds of perturbations of the registration energies $E_m$ and $E_{\mathscr{M}}$ in Chapters 2 and 3, namely to instate a *scale-space* on the data and to add an additional regularization energy (*Tikhonov* regularization). So far, these approximations were based on heuristic arguments and their applicability was only confirmed by numerical results. The aim of this chapter is to verify a *variational convergence* of these perturbations, or, more precisely, to study the behavior of the minimizers when the scale parameter and the regularization parameter go to zero.

The convergence of variational functionals is a central interest in many research areas as for example, homogenization, phase transitions, non-smooth analysis and approximation of variational functionals.

Γ-convergence as introduced by DI GIORGI is probably the most general notion of variational convergence and provides a well-developed framework for a large class of problems. In this chapter we will first recall the definition of Γ-convergence and its basic properties, that will be need in the forthcoming sections. For further results and applications, we refer the interested reader to the books of DAL MASO [80] and BRAIDES [33] for comprehensive overviews. In Section 4.2 we will see that it is not difficult to verify, that for a given lower semicontinuous functional $E$ the sequence of *Tikhonov*-regularized functionals $\alpha^{-1}E + E_{\mathrm{reg}}$ converges to a functional whose set of minimizers is *optimal with respect to the regularization* with vanishing energy $E$. This confirms the interpretation of the rôle of the regularization energy to impose a choice criterion. In Section 4.3 we will study the variational convergence of the perturbations given by the coarsened energies by means of the scale-space methodology in case of the unimodal energy.

## 4.1 The notion of Γ-convergence

**Definition 4.1.1 (Γ-convergence).** *Let $(\mathscr{A}, d)$ be a metric space. We say, that a sequence $E_\alpha : \mathscr{A} \to \overline{\mathbb{R}}$ of functionals Γ-converges to $E : \mathscr{A} \to \overline{\mathbb{R}} := \mathbb{R} \cup \{-\infty, \infty\}$, iff for all $\phi \in \mathscr{A}$, the following two conditions hold.*

*(i) (*lim inf *inequality) For every sequence $(\phi_\alpha) \to \phi$ in $\mathscr{A}$*

$$E[\phi] \leq \liminf_{\alpha \to \infty} E_\alpha[\phi_\alpha]. \tag{4.1}$$

*(ii) (*lim sup *inequality) There exists a sequence $(\phi_\alpha) \to \phi$ in $\mathscr{A}$, such that*

$$E[\phi] \geq \limsup_{\alpha \to \infty} E_\alpha[\phi_\alpha]. \tag{4.2}$$

*This sequence is called a recovering sequence of $\phi$.*

*The definition can also be formulated using a continuous index.*

We will need the following results and definitions (cf. Dal Maso [80, Def. 7.6]).

**Definition 4.1.2.** *The sequence $(E_\alpha)$ is equi-coercive on the space $\mathscr{A}$ if for every $t \in \mathbb{R}$ there exists a closed countably compact subset $K_t$ of $\mathscr{A}$, such that $\{E_\alpha \leq t\} \subseteq K_t$ for every $\alpha > 0$.*

**Lemma 4.1.3.** *The Γ-limit is lower semicontinuous.*

**Definition 4.1.4.** *For $\epsilon > 0$ and $E \in \mathscr{A}$ we define*

$$M_\epsilon[E] := \{\, \phi \in \mathscr{A} \mid E[\phi] \leq \inf_{\psi \in \mathscr{A}} E[\psi] + \epsilon \,\} \quad \text{and}$$

$$M[E] := \{\, \phi \in \mathscr{A} \mid E[\phi] = \inf_{\psi \in \mathscr{A}} E[\psi] \,\} = \bigcap_{\epsilon > 0} M_\epsilon(E)\,.$$

An important, fundamental consequence of Γ-convergence along with equi-coercivity is the following theorem (see [80, Th. 7.23]).

**Theorem 4.1.5.** *Suppose that $(E_\alpha)$ is equi-coercive and Γ-converges to a functional $E$ on $\mathscr{A}$. Then for every neighborhood $U$ of $M(E)$ in $\mathscr{A}$ there exists $\epsilon > 0$ and $\alpha > 0$ such that*

$$M(E_\beta) \subseteq M_\epsilon(E_\beta) \subseteq U \tag{4.3}$$

*for every $0 < \beta < \alpha$. If, in addition, $E$ is not identically $+\infty$, then for every $\phi \in M(E)$, for every neighborhood $V$ of $\phi$ and every $\epsilon > 0$ there exists $\alpha > 0$ such that*

$$M_\epsilon(E_\beta) \cap V \neq \emptyset \tag{4.4}$$

*for every $0 < \beta < \alpha$.*

Or analogously

**Theorem 4.1.6.** *Let $(\mathscr{A}, d)$ be a metric space, $(E_\alpha)$ be a sequence of equi-coercive functionals on $\mathscr{A}$, and let $E := \Gamma - \lim_{\alpha \to 0} E_\alpha$, then*

$$\exists \min_{\mathscr{A}} E = \lim_{\alpha \to 0} \inf_{\mathscr{A}} E_\alpha.$$

*Moreover, if $(\phi_\alpha)$ is a precompact sequence such that*

$$\lim_{\alpha \to 0} E_\alpha[\phi_\alpha] = \lim_{\alpha \to 0} \inf_{\mathscr{A}} E_\alpha,$$

*then for every converging subsequence $\phi_\alpha \to \phi$, $\phi$ is a minimum point of $E$, i. e., $\phi \in \arg\min E_\alpha$.*

## 4.2 Tikhonov regularization

In Section 1.4.1 we proposed to use *Tikhonov* regularization for the regularization of registration problems. From the combination (1.10) we see that the matching energy and the regularization are competing against each other:

$$E_{\text{total},\alpha}[\phi] = E_m[\phi] + \alpha E_{\text{reg}}[\phi]$$

In (3.20) we combined the morphological registration energy with the non-quadratic polyconvex regularization energy. A strong regularization energy will hence lead to a very smooth minimizer, but this minimizer may be far from minimizing $E_m$. The regularization parameter $\alpha$ controls the trade-off of these energies, the proper choice of $\alpha$ is however a non-trivial task. In Section 1.4.1 we have also pointed out, that for linear problems, *Tikhonov* regularization corresponds to the computation of the *least-squares* solution (w.r.t. to a specific *norm*) of $E_{\text{match}} = E_m$ (unimodal

matching energy) or $E_{\text{match}} = E_{\mathscr{M}}$ (the morphological matching energy of Chapter 3), i. e., for a norm $\|\cdot\|_A$ on $\mathscr{A}$:

$$\text{find } \phi \in \mathscr{A} \text{ such that } \|\phi\|_A^2 = \inf_{\psi \in M[E_{\text{match}}]} \|\psi\|_A^2.$$

This requires $\mathscr{A}$ to be a *Banach*-space. The framework of $\Gamma$-convergence, however requires $\mathscr{A}$ only to be a *metric space*. One may ask, under which conditions the minimization of $E_{\text{total},\alpha}$ corresponds to the problem

$$\text{Find } \phi \in \mathscr{A} \text{ such that } E_{\text{reg}}[\phi] = \inf_{\psi \in M[E_{\text{match}}]} E_{\text{reg}}[\psi].$$

Let us define $\underline{E} := \inf_{\psi \in \mathscr{A}} E_{\text{match}}[\psi]$. From now on we assume that $E_{\text{match}}$ is *lower-semicontinuous*, and that $E_{\text{reg}}$ is *coercive* and *lower-semicontinuous* with respect to the chosen topology, e. g., the weak topology of $H^{1,p}(\Omega; \mathbb{R}^d)$ as in Section 3.

**Remark 4.2.1.** *As a consequence $\alpha^{-1}(E_{\text{reg}}[\phi] - \underline{E}) + E_{\text{match}}[\phi]$ it is also lower semicontinuous for all $\alpha > 0$.*

**Remark 4.2.2.** *Since $E_\alpha \geq E_{\text{reg}}$, and $E_{\text{reg}}$ is lower semicontinuous and coercive, the equi-coercivity follows by Proposition 7.7 in [79].*

First, we see that the family $E_{\text{total},\alpha}$, $\alpha > 0$ is not equi-coercive since the *coercivity* induced by $E_{\text{reg}}$ is scaled with $\alpha$. However, we obtain an equi-coercive functional by defining

$$E_\alpha[\phi] := \alpha^{-1}(E_{\text{match}}[\phi] - \underline{E}) + E_{\text{reg}}[\phi], \tag{4.5}$$

where we assume $\underline{E} > -\infty$. Furthermore we define

$$E[\phi] := \begin{cases} E_{\text{reg}}[\phi], & E_{\text{match}}[\phi] = \underline{E} \\ \infty, & \text{otherwise}. \end{cases} \tag{4.6}$$

It is then not difficult to verify the following $\Gamma$-convergence result.

**Theorem 4.2.3.** $\Gamma - \lim\limits_{\alpha \to 0} E_\alpha = E$.

*Proof.* We will verify the inequalities of Definition 4.1.1. (i) For the $\liminf$ inequality, we have to show that

$$E[\phi] \leq \liminf_{\alpha \to 0} \alpha^{-1}(E_{\text{match}}[\phi_\alpha] - \underline{E}) + E_{\text{reg}}[\phi_\alpha]$$

for all $\phi \in \mathscr{A}$ and all $\phi_\alpha \to \phi$ in $\mathscr{A}$.

**Case (a)** $E[\phi] < \infty$**:** That follows directly from the remark 4.2.1 and the fact that,

$$\liminf_{\alpha \to 0} \left( \alpha^{-1}(E_{\text{match}}[\phi_\alpha] - \underline{E}) + E_{\text{reg}}[\phi_\alpha] \right)$$
$$\geq \liminf_{\alpha \to 0} \left( E_{\text{match}}[\phi_\alpha] - \underline{E} + E_{\text{reg}}[\phi_\alpha] \right) \geq \liminf_{\alpha \to 0} E_{\text{reg}}[\phi_\alpha] \geq E[\phi].$$

**Case (b)** $E[\phi] = \infty$**:** We observe

$$\liminf_{\alpha \to 0} \left( \alpha^{-1}(E_{\text{match}}[\phi_\alpha] - \underline{E}) + E_{\text{reg}}[\phi_\alpha] \right)$$
$$= \liminf_{\alpha \to 0} \left( \alpha^{-1}\underbrace{(E_{\text{match}}[\phi_\alpha] - E_{\text{match}}[\phi])}_{\geq 0} + \alpha^{-1}\underbrace{(E_{\text{match}}[\phi] - \underline{E})}_{>0} + E_{\text{reg}}[\phi_\alpha] \right)$$
$$= \infty + \liminf_{\alpha \to 0} E_{\text{reg}}[\phi_\alpha] = E.$$

(ii) We have to show that for each $\phi \in \mathscr{A}$, there exists a sequence $(\phi_\alpha)$, $\phi_\alpha \in \mathscr{A}$ with $\phi_\alpha \to \phi$, such that

$$E[\phi] \geq \limsup_{\alpha \to 0} \alpha^{-1}(E_{\text{match}}[\phi_\alpha] - \underline{E}) + E_{\text{reg}}[\phi_\alpha].$$

**Case (a)** $E[\phi] = \infty$: Directly fulfilled.

**Case (b)** $E[\phi] < \infty$: By choosing $\phi_\alpha := \phi$, we obtain $E_{\text{match}}[\phi] = \underline{E}$, and hence

$$\limsup_{\alpha \to 0} \left( \alpha^{-1}(E_{\text{match}}[\phi_\alpha] - \underline{E}) + E_{\text{reg}}[\phi_\alpha] \right) = 0 + E_{\text{reg}}[\phi].$$

$\square$

**Remark 4.2.4.** *This theorem is only interesting if $E_{\text{match}}$ has minimizers in $\mathscr{A}$, since otherwise the limit $E$ is always $+\infty$. Since the Γ-limit is unique, this however allows to deduce that in case $E_{\text{match}}$ does not have a minimizer, $E_\alpha$ will eventually converge to the functional $E \equiv +\infty$, and indicates once more that regularization is absolutely essential.*

By Lemma 4.1.3, $E$ is lower semicontinuous, however the direct minimization of $E$ seems to be impossible in practice since it corresponds to the minimization of $E_{\text{reg}}$ over the set of minimizers of $E_{\text{match}}$. The minimization of $E_\alpha$ for small $\alpha$ renders this problem to be feasible in practice. We conclude that for $\alpha \to 0$ and eventually choosing a converging subsequence of this sequence, it is possible to obtain the optimal minimizer with respect to the regularization, which is can be interpreted as an analogue to the concept of the *Moore-Penrose* inverse.

## 4.3   Multiscale perturbation of the unimodal matching energy

In this section, we want to study the matching functionals $E_m^\sigma$ defined in Eq. (2.16) with respect to Γ-convergence. The smoothing via a scale-space operator $\mathcal{S}^\sigma$ is essential for the matching algorithm, especially when the images have discontinuities (see the detailed treatise of the subject in the work of RUMPF [179]). It would be an intolerable restriction to define matching problems only on smooth images. The smoothed version $\mathcal{S}^\sigma u_T$ renders the gradient flow feasible to computational gradient descent methods. Let us now define a suitable function space of images which allows to have discontinuities, which can be represented by the union of finitely many Lipschitz curves.

**Definition 4.3.1 (Function space of images).**

$$\mathscr{I}^1(\Omega) := \Big\{ u : \Omega \to \mathbb{R} \,\Big|\, u \in L^\infty(\Omega), \exists \alpha \in (0,1], J \subset \Omega, m \in \mathbb{N},$$

$$\mathscr{H}^{n-1}(J) < \infty, J_i \text{ of class } \mathscr{C}^{0,1} \text{ s.t. } \mathscr{H}^{n-1}\Big(J - \bigcup_{i=1}^{m} J_i\Big) = 0, u \in C^{0,\alpha}(\Omega \setminus J) \Big\}.$$

Note that the definition implies $\mathscr{I}^1(\Omega) \subset SBV(\Omega)$ and that $\mu(B_\epsilon(S_u)) \xrightarrow{\epsilon \to 0} 0$.

**Theorem 4.3.2.** *Suppose $d = 3$, $u_T$, $u_R \in \mathscr{I}^1(\Omega)$. Consider the matching energy*

$$E_m[\phi] := \int_\Omega |u_T \circ \phi - u_R|^2 \, d\mu \tag{4.7}$$

*and the regularized matching energy*

$$E_m^\sigma[\phi] := \int_\Omega |\mathcal{S}^\sigma(u_T) \circ \phi - \mathcal{S}^\sigma(u_R)|^2 \quad \sigma > 0, \tag{4.8}$$

*where $\mathcal{S}^\sigma$ denotes a scale operator at scale $\sigma > 0$, fulfilling the following properties*

   *(i) $\|\mathcal{S}^\sigma u - u\|_{L^2(D)} \to 0$ for $\sigma \to 0$, $u \in \mathscr{I}(\Omega)$ and $D \subset \Omega$ Lipschitz domain.*

*(ii) $\exists 0 < \alpha \leq 1$, s. t. for all $u \in \mathscr{C}^{0,\alpha}(D)$ we have a constant $C$ depending on $u$ with*

$$\sup_{\sigma} \|\mathcal{S}^{\sigma} u\|_{\mathscr{C}^{0,\alpha}(D)} \leq C(u).$$

*Furthermore we consider the polyconvex regularization energy*

$$E_{reg}[\phi] := \int_{\Omega} W(D\phi, \operatorname{Cof} D\phi, \det D\phi) \, \mathrm{d}\mu, \qquad (4.9)$$

*and the overall energies*

$$E[\phi] := E_m[\phi] + E_{reg}[\phi] \quad \text{and} \quad E^{\sigma}[\phi] := E_m^{\sigma}[\phi] + E_{\mathrm{reg}}[\phi] \qquad (4.10)$$

*defined for all $\phi$ in*

$$\mathscr{A}_0 = \{\phi : \Omega \to \Omega \mid \phi \in H^{1,p}(\Omega), \operatorname{Cof} D\phi \in L^q(\Omega),$$
$$\det D\phi \in L^r(\Omega), \det D\phi > 0 \text{ a.e. in } \Omega, \phi = \mathbb{1} \text{ on } \partial\Omega\}$$

*where $p, q > 3$ and $r > 1$. Suppose $W : \mathbb{M}^3 \times \mathbb{M}^3 \times \mathbb{R}^+ \to \mathbb{R}$ is convex and there exist constants $\beta, s \in \mathbb{R}$, $\beta > 0$, and $s > \frac{2q}{q-3}$ such that*

$$W(A, C, D) \geq \beta \left( \|A\|_2^p + \|C\|_2^q + D^r + D^{-s} \right) \quad \forall A, C \in \mathbb{M}^3, D \in \mathbb{R}^+. \qquad (4.11)$$

*Then*

$$\Gamma - \lim_{\sigma \to 0} E^{\sigma} = E \text{ in } X := \mathscr{A} \cap E < M.$$

*Proof.* The proof relies on many techniques already used in the existence proof in [179], especially the restriction to the complement of a set whose measure is arbitrary small.

Due to Rellich's embedding theorem $\phi_{\sigma} \rightharpoonup \phi$ in $H^{1,p}(\Omega; \mathbb{R}^d)$ implies the strong convergence of $\phi_{\sigma} \to \phi$ in $L^p(\Omega; \mathbb{R}^d)$. By Sobolev's embedding theorem, we know that $\mathscr{A} \subset \mathscr{C}^0(\bar{\Omega}, \bar{\Omega})$ and hence that $\phi_{\sigma} \rightrightarrows \phi$ (uniform convergence). Now, for $\delta > 0$, we choose $\epsilon_T$, $\epsilon_R$, such that $\mu(B_{\epsilon_T}(S_T)) < \delta$, $\mu(B_{\epsilon_R}(S_R)) < \delta$. Furthermore, we set

$$S_{\epsilon} := \{\det D\phi \leq \epsilon\},$$

Using the change of variables formula for Sobolev functions given $p > n$, the Lebesgue measure of $S_{\epsilon}$ can be estimated (cf. [179]) by $\mu(S_{\epsilon}) \leq \frac{M\epsilon^s}{\beta}$. Similarly the measure of the pre-image of the neighborhood of the singularity set of $u_T$ can be estimated by

$$\mu(\phi^{-1}(B_{\epsilon_T} \setminus S_{\epsilon})) \leq \frac{\delta}{\epsilon}.$$

We define

$$R_{\epsilon,\delta} := \phi^{-1}(B_{\epsilon_T}(S_T)) \cup B_{\epsilon_T}(S_R) \cup S_{\epsilon},$$

whose measure can be estimated by

$$\mu(R_{\epsilon,\delta}) \leq \frac{\delta}{\epsilon} + \delta + \frac{M\epsilon^s}{\beta}$$

and since $\mu$ is a Radon measure, we one can find an open set $U$, such that $R_{\epsilon,\delta} \subset U$, and $\mu(U \setminus R_{\epsilon,\delta})$ arbitrary small, and furthermore, since $\mu$ is the Lebesgue measure, we can approximate $U$ by an overlapping of the union of a countable number of $d$-dimensional cubes, we find an open set $\hat{R}_{\epsilon,\delta}$ with Lipschitz boundary and $U \subset \hat{R}_{\epsilon,\delta}$, such that

$$\mu(\hat{R}_{\epsilon,\delta}) \leq \mu(R_{\epsilon,\delta}) + \epsilon$$

and observe that $(u_T \circ \phi_{\sigma} - u_R)$ converges uniformly to $u_T \circ \phi - u_R$ on the compact set $\bar{\Omega} \setminus \hat{R}_{\epsilon,\delta}$, due to the uniform continuity of $u_T$ and $u_R$ on that set.

(i) We start by showing, the $\liminf$-inequality (4.1), that is

$$E[\phi] \leq \liminf_{\sigma \to 0} E^\sigma[\phi_\sigma] \quad \forall \phi_\sigma \rightharpoonup \phi \text{ in } H^{1,p}$$

and estimate by recalling that $u_T, u_R \in L^\infty$:

$$
\begin{aligned}
(E_m[\phi])^{\frac{1}{2}} &\leq \|u_T \circ \phi - u_R\|_{L^2(\bar{\Omega} \setminus \hat{R}_{\epsilon,\delta})} + C_\infty \eta(\mu(\hat{R}_{\epsilon,\delta})) \\
&\leq C_\infty \eta(\mu(\hat{R}_{\epsilon,\delta})) \\
&\quad + \|u_T \circ \phi - u_R - \mathcal{S}^\sigma(u_T \circ \phi - u_R)\|_{L^2(\bar{\Omega} \setminus \hat{R}_{\epsilon,\delta})} && \text{(I)} \\
&\quad + \|\mathcal{S}^\sigma(u_T \circ \phi) - \mathcal{S}^\sigma(u_T) \circ \phi\|_{L^2(\bar{\Omega} \setminus \hat{R}_{\epsilon,\delta})} && \text{(II)} \\
&\quad + \|\mathcal{S}^\sigma(u_T) \circ \phi - \mathcal{S}^\sigma(u_T) \circ \phi_\sigma\|_{L^2(\bar{\Omega} \setminus \hat{R}_{\epsilon,\delta})} && \text{(III)} \\
&\quad + \|\mathcal{S}^\sigma(u_T) \circ \phi_\sigma - \mathcal{S}^\sigma(u_R)\|_{L^2(\bar{\Omega} \setminus \hat{R}_{\epsilon,\delta})} \\
&\leq C_\infty \eta(\mu(\hat{R}_{\epsilon,\delta})) + \text{(I)} + \text{(II)} + \text{(III)} \\
&\quad + \|\mathcal{S}^\sigma(u_T) \circ \phi_\sigma - \mathcal{S}^\sigma(u_R)\|_{L^2(\Omega)} + C_\infty \eta(\mu(\hat{R}_{\epsilon,\delta}))
\end{aligned}
$$

where $\eta(s) \to 0$ for $s \to 0$. Clearly (I) $\to 0$ for $\sigma \to 0$.

To treat (II), we further estimate

$$\text{(II)} \leq \|\mathcal{S}^\sigma(u_T \circ \phi) - u_T \circ \phi\|_{L^2(\bar{\Omega} \setminus \hat{R}_{\epsilon,\delta})} + \|u_T \circ \phi - \mathcal{S}^\sigma(u_T) \circ \phi\|_{L^2(\bar{\Omega} \setminus \hat{R}_{\epsilon,\delta})}.$$

The first summand clearly goes to 0 for $\sigma \to 0$. Since $\det D\phi > \epsilon$ on $\Omega \setminus \hat{R}_{\epsilon,\delta}$, we get

$$
\begin{aligned}
\int_{\bar{\Omega} \setminus \hat{R}_{\epsilon,\delta}} |u_T \circ \phi - \mathcal{S}^\sigma(u_T) \circ \phi|^2 \, d\mu &= \int_{\phi(\bar{\Omega} \setminus \hat{R}_{\epsilon,\delta})} |u_T - \mathcal{S}^\sigma(u_T)|^2 (\det D\phi)^{-1} \, d\mu \\
&\leq \frac{\mu(\Omega)}{\epsilon} \int_{\Omega \setminus B_{\epsilon_T}(S_T)} (\operatorname{card} \phi^{-1}) |\mathcal{S}^\sigma(u_T) - u_T|^2 \, d\mu \longrightarrow 0 \text{ for } \delta \to 0.
\end{aligned}
$$

To estimate (III) we first observe that $u_T$ restricted to $\overline{\Omega} \setminus \hat{R}_{\epsilon,\delta}$ is in $C^{0,\alpha}(\overline{\Omega} \setminus \hat{R}_{\epsilon,\delta})$, so that the set $\{\mathcal{S}^\sigma(u_T) : \sigma > 0\}$ is bounded in $C^{0,\alpha}(\overline{\Omega} \setminus \hat{R}_{\epsilon,\delta})$ and thus is equi-continuous. We know that $\phi_\sigma$ converges uniformly to $\phi_0$ on $\Omega$, hence

$$\text{(III)} = \|\mathcal{S}^\sigma(u_T) \circ \phi - \mathcal{S}^\sigma(u_T) \circ \phi_\sigma\|_{L^2(\bar{\Omega} \setminus \hat{R}_{\epsilon,\delta})} \longrightarrow 0$$

for $\sigma \to 0$. For given arbitrary $\bar{\epsilon}$, one can choose $\epsilon, \delta, \epsilon_T, \epsilon_R$ such that

$$E_m[\phi] \leq \bar{\epsilon} + E_m^\sigma[\phi_\sigma]$$

for $0 < \sigma < \sigma(\epsilon, \delta, \bar{\epsilon})$ sufficiently small. Due to the weak lower-semicontinuity of $E_{reg}$ and its independence of $\sigma$, we find

$$E_m[\phi] + E_{reg}[\phi] \leq \liminf_{\sigma \to 0} E_m^\sigma[\phi_\sigma] + \liminf_{\sigma \to 0} E_{reg}[\phi_\sigma] \leq \liminf_{\sigma \to 0} E^\sigma[\phi_\sigma] + \bar{\epsilon}$$

for $\bar{\epsilon} > 0$ arbitrary, which is the desired result of the $\liminf$ inequality.

($ii$) To show the $\limsup$-inequality (4.2), we set $\phi_\sigma := \phi$ and obtain:

$$
\begin{aligned}
\left( \int_\Omega |\mathcal{S}^\sigma(u_T) \circ \phi_\sigma - \mathcal{S}^\sigma(u_T \circ \phi)|^2 \right)^{\frac{1}{2}} &\leq \|\mathcal{S}^\sigma(u_T) \circ \phi - \mathcal{S}^\sigma(u_R)\|_{L^2(\bar{\Omega} \setminus \hat{R}_{\epsilon,\delta})} \\
&\quad + \|\mathcal{S}^\sigma(u_T \circ \phi - u_R)\|_{L^2(\bar{\Omega} \setminus \hat{R}_{\epsilon,\delta})} + C_\infty \eta(\mu(\hat{R}_{\epsilon,\delta})) \\
&\leq \sqrt{\frac{\mu(\Omega)}{\epsilon}} \|\mathcal{S}^\sigma(u_T) - u_T\|_{L^2(\bar{\Omega} \setminus \hat{R}_{\epsilon,\delta})} \\
&\quad + \|\mathcal{S}^\sigma(u_R) - u_R\|_{L^2(\Omega)} \\
&\quad + \|u_T \circ \phi - u_R\|_{L^2(\Omega)} + C_\infty \mu(\hat{R}_{\epsilon,\delta}) \\
&\leq \bar{\epsilon} + \|u_T \circ \phi - u_R\|_{L^2(\Omega)}
\end{aligned}
$$

for arbitrary $\bar{\epsilon}$, if $\epsilon$, $\delta$, $\epsilon_T$, $\epsilon_R$ are chosen appropriately small and $0 < \sigma < \sigma(\epsilon, \delta, \bar{\epsilon})$ sufficiently small. Here we used again the estimate for (II) from the first part. Hence, we arrive at the desired $\limsup$-inequality

$$\limsup_{\sigma \to 0} E^\sigma[\phi_\sigma] = \limsup_{\sigma \to 0} E_m^\sigma[\phi] + E_{reg}[\phi] \leq E_m[\phi] + E_{reg}[\phi]$$

and we conclude the desired $\Gamma$-convergence of $E^\sigma$ to $E$. $\qquad\square$

**Remark 4.3.3.** *We have to address the equi-coercivity, in order to apply Theorem 4.1.5. Due to the growth condition of $W$ and its independence on $\sigma$, $E^\sigma$ is equi-coercive. Hence, we know that all the converging subsequences of the sequence $\phi_\sigma$ of minimizers of $E^\sigma$ converge to a minimizer of $E$. Furthermore this process can be regarded as a choice process for the selection of minimizers out of the overall set of minimizers of $E$.*

# Chapter 5

# Mumford-Shah based registration

MORPHOLOGICAL registration aims at aligning the level sets of the reference image with the level sets of the deformed template. Until now we have ignored the fact that dominant edges, that can be mathematically interpreted as discontinuities with a sufficiently "large" jump in the images can also be regarded as belonging to the morphological description of an image, even though this is not reflected by the definition of $\mathcal{M}[I]$. In fact our visual perception is well trained at detecting edges in natural images. In areas of smooth transitions, we are rather sensible to shapes and textures. In this chapter we will enhance the registration model by discontinuity alignment.

## 5.1 A coupled free discontinuity problem of *Mumford-Shah* type

Let us reconsider the functional of MUMFORD & SHAH from (1.4):

$$E_{MS}(u, \Gamma) = \int_{\Omega} (u - u_0)^2 dx + \frac{\mu}{2} \int_{\Omega \setminus \Gamma} \|\nabla u\|^2 \, \mathrm{d}\mu + \nu \mathscr{H}^{n-1}(\Gamma).$$

The mathematical treatment of this energy is subtle. It has to be minimized over the set of admissible curves $\Gamma$ and admissible $u$ simultaneously. However, it is not possible to obtain lower-semicontinuity of the Hausdorff measure within a reasonable topology of subsets of $\Omega$.

Existence theory for (1.4) is established by DE GIORGI, CARRIERO AND LEACI [83] who proposed to consider the minimization of the energy depending on $u$ only, and the set of admissible sets is chosen as $SBV(\Omega)$, the space of functions of bounded variation $u$ for which the measure $Du$ can be written as $Du = \nabla u \mu + (u^+ - u^-) n \mathscr{H}^{d-1} | S(u)$, i. e., the *Cantor* part of the support of the singular part of the measure known from $BV$ functions, is empty [8]. $u^+$ and $u^-$ denote the approximate $\limsup$ resp. $\liminf$ of $u$. The energy is integrated over the entire domain $\Omega$ and $\Gamma$ is now represented by $S_u$ the complement set of Lebesgue points of $u$, i. e. the measure theoretic discontinuity set of $u$. It is well known (cf. AMBROSIO, PALLARA, FUSCO [8]) that using the compactness of $SBV(\Omega)$ and lower-semicontinuity theorems, that under mild conditions there exists a solution $u \in SBV(\Omega)$ with $\mathcal{H}^{n-1}(S_u) < \infty$. Especially due to the complexity of discretizing the singularity set, various approximations $E_\epsilon$ of the Mumford-Shah functional have been introduced for which $\Gamma$-convergence results are known (cf. e. g. [10, 11, 28, 176]). AMBROSIO AND TORTORELLI [11] for example have proposed a phase-field type regularization and introduced an auxiliary variable which itself is regularized by an elliptic functional. We also refer to [197, 76, 77, 115] for further extensions based on the Mumford-Shah functional.

## 5.2 The interdependence of registration and segmentation

From a more general point of view, the proposed approach corresponds to a simultaneous detection of image features which ought to be coupled by a deformation. The subtlety of this

approach is that both the contour in the reference as well as the deformation are unknowns. If no further energy contributions acting on the deformation were present, this would be equivalent to finding the contours in both images separately and a deformation *a-posteriori* which maps the reference contour to the template contour.

However, this would have serious disadvantages: Edge extraction is a very subtle process, it usually relies on indicators derived from differential operators (e. g. gradients or the image Hessian, which is needed for example for DERICHE's filter or CANNY's edge detector) or local integral operators such as moments [74]. Most of those edge detectors act local. The set of detected edges is often disrupted and irregular, and furthermore they are most often given by binary indicators, hence information about *weak* edges is destroyed and often neglected. Let us first assume that we enrich the image space by overlaying several images, which have been registered perfectly in a pre-processing step. Features which are very weak and hardly visible in one of the images might be clear and salient in the other image. A feature detection model may now exploit the complementary information of both images, and only reject possible edges if some statistical or geometrical indicators are weak in all images. Clearly, this approach would make the whole process of feature detection much more stable. If the images are not previously aligned, we have to incorporate the deformation as a further unknown, and the whole process can be described as follows:

> *Given a pair of images, a reference and a template image, we aim to find a deformation and, simultaneously, a set of features, in such a way, that this set describes the features in the reference image well and the transformed feature set corresponds to the template image. Furthermore, the deformation as well the edge set should be as "simple" as possible.*

In this formulation, the deformation is only determined on the set itself. Eventually we aim at a smooth extension of this deformation to the rest of the image domain in order to obtain a mapping of the images also away from the feature sets. Let us emphasize, that this problem can in no way be split equivalently into separate processes of feature extraction and registration, since both processes interdepend on each other.

In the following we will describe in more mathematical detail what is meant by feature extraction, simplicity of the edge set and simplicity of the deformation.

## 5.3   The idea of coupling the free discontinuity sets

By the minimization of the Mumford-Shah functional we will obtain an approximation of the discontinuity sets of $u_0$. Note that $u_0$ is perturbed by noise and only in $L^2(\Omega)$ and may thus have an arbitrarily bad set of discontinuities. On the other hand if $u_0 \in BV$, then for $\mu, \alpha$ small, the discontinuity set of $u$ will be close to that of $u_0$. Apart from the discontinuities, the morphological registration energy may be active, but additionally we want to ensure that the discontinuity set $S(u_{R,0})$ will be mapped onto the discontinuity set of $u_T$, i. e., $\phi(S(u_{R,0})) = S(u_{T,0})$. Here and in the rest of this thesis we denote—with slight abuse of earlier notation—the data by $u_{R,0}$ and $u_{T,0}$ to conform to the usual notation in this framework. Instead of formulating this problem in $SBV(\Omega)$ we will analogously treat the geometric variable $\Gamma$ and the functional variables $u_T$, $u_R$ and $\phi$ independently. See for example the book of AUBERT & KORNPROBST[12] or the book of BRAIDES [32] for a comprehensive overview. Alignment of the singularity set can be achieved by minimization of the following functional [101]:

$$\tilde{E}_{\mathrm{MS}}(\Gamma, \phi, u_R, u_T) = \frac{1}{2} \int_\Omega (u_R - u_{R,0})^2 \, \mathrm{d}\mu + \frac{\mu}{2} \int_{\Omega \backslash \Gamma} \|\nabla u_R\|^2 \, \mathrm{d}\mu + \frac{\nu}{2} \mathscr{H}^{d-1}(\Gamma)$$

$$+ \frac{1}{2} \int_\Omega (u_T - u_{T,0})^2 \, \mathrm{d}\mu + \frac{\mu}{2} \int_{\Omega \backslash \Gamma^\phi} \|\nabla u_T\|^2 \, \mathrm{d}\mu + \frac{\nu}{2} \mathscr{H}^{d-1}(\Gamma^\phi). \quad (5.1)$$

Here $\Omega \subset \mathbb{R}^d$ is the domain of definition of the images with $d = 2, 3$, $u_{T,0}, u_{R,0} \in L^\infty(\Omega)$ are the given template images, $\Gamma \subset \Omega$ is (an approximation of) the edge set of the given image $u_{R,0}$
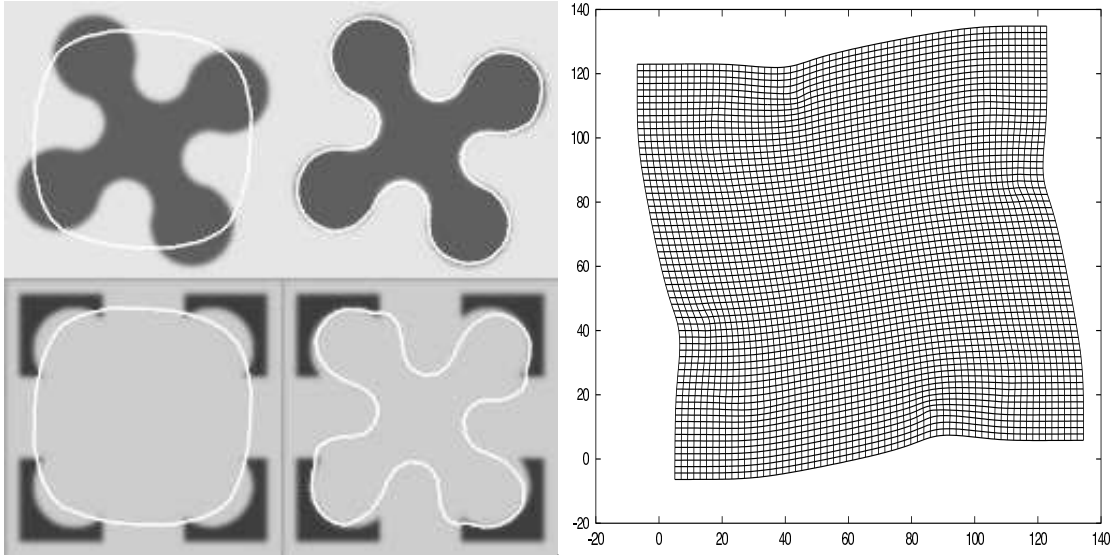
Figure 5.1: *Multimodal complementary registration. The two images on the left show the initial contour $\Gamma$ in the images $u_R$ and $u_T$ where the initial deformation is the identity. On the right of the initial images, the resulting contours, coupled by the deformation (right image) are shown after 75 steps of the regularized gradient descent.*

and $\Gamma^\phi = \phi(\Gamma)$ is the transformed edge-set $\Gamma$ under the transformation $\phi$. In the following we assume that $\Gamma = \partial D$ for an open set $D$ with $\overline{D} \subset \Omega$.

We see, that the deformation is obviously not uniquely determined by this condition, not even on the edge set itself, since reparametrization along the singularity set does not change the energy. Furthermore, the energy does not consider the behavior of $\phi$ away from the edge set. If we do not combine this energy with another registration energy that influences the deformation away from the singularity set, we have to incorporate an additional regularization energy, which ensures that the deformation is suitably extended into $\Omega \setminus \Gamma$. In order to avoid technical difficulties we avoid the length-measurement of $\Gamma^\phi$ and solely measure the length of $\Gamma$:

$$E_{\mathrm{MS}}(\Gamma, \phi, u_R, u_T) = \frac{1}{2} \int_\Omega (u_R - u_{R,0})^2 \, \mathrm{d}\mu + \frac{\mu}{2} \int_{\Omega \setminus \Gamma} \|\nabla u_R\|^2 \, \mathrm{d}\mu + \nu \mathscr{H}^{d-1}(\Gamma)$$
$$+ \frac{1}{2} \int_\Omega (u_T - u_{T,0})^2 \, \mathrm{d}\mu + \frac{\mu}{2} \int_{\Omega \setminus \Gamma^\phi} \|\nabla u_T\|^2 \, \mathrm{d}\mu. \quad (5.2)$$

Let us point out, that the proposed free discontinuity based approach is only a template study which fits into the general formulation of the joint feature extraction and registration problem. Different classes of images may require different models to drive the contour $\Gamma$ towards the significant features of the images, e. g. a geodesic active contour model as proposed by CASELLES, KIMMEL AND SAPIRO [44], which would lead to a coupled energy of the form

$$E_{\mathrm{ac}}(\Gamma, \phi) = \int_\Gamma g_R d\mathscr{H}^{d-1} + \nu \int_\Omega g_R dx + \int_{\Gamma^\phi} g_T d\mathscr{H}^{d-1} + \nu \int_\Omega g_T dx, \quad (5.3)$$

where $g_R$ and $g_T$ correspond to some suitable edge detectors in the images $u_R$ and $u_T$. A common choice is, for example, $g_u(x) = (1 + s|\nabla u(x)|^2)^{-1}$, $s > 0$. The idea of coupling segmentation with registration has also been pointed out by Yezzi, Zöllei and Kapur [134]. They have shown results for the coupling of the geodesic contour model and registration.

In the remainder of this chapter we will present a level set approach by treating the problem as a shape optimization problem, formulate a phase-field approximation of the energy in the spirit of the well-known AMBROSIO & TORTORELLI-approximations, and do a comparison of both methods.

## 5.4 An interface model using level sets

In this section we will describe a level set model for the coupled free discontinuity problem (5.2). We will first restrict ourselves to edge sets which are the union of finitely many Jordan-curves. In this case, the feature set can be viewed as the boundary of detected segments, which are mapped to similar segment boundaries in the second image. For a large class of images, this is a very suitable and convenient approach, since images can often be decomposed into a finite set of independent objects. However this is not always the case. Crack tips might occur not only due to weak edge information but due to the fact that the image contains disrupted discontinuity sets.

For many practical registration problems, we can confine to such simple interface sets, especially if we want to restrict ourselves to dominant feature sets. The complexity of the images may render the aim of mapping all features onto each other unrealistic and inappropriate.

In a shape optimization framework, we would start with an initial feature set and evolve it according to a regularized energy minimization method. The curve may be elegantly described and propagated by the level set approach of OSHER and SETHIAN [169, 170]. In [129] HINTER-MÜLLER & RING have derived a level set based Newton-Type regularized optimization algorithm for minimizing the Mumford-Shah functional. That work is the algorithmical basis for our joint free discontinuity problem for registration. For related approaches we refer to [55, 53, 54, 129].

We consider $\Gamma$ to be given as the zero level set of the level set function $u_\Gamma : \Omega \to \mathbb{R}$, i. e.,

$$\Gamma = \mathcal{M}_0[u] = \{u_\Gamma = 0\}.$$

Furthermore we set $\Omega_1 := \{u < 0\}$ and $\Omega_2 := \{u > 0\}$.

### 5.4.1 Regularization

As pointed out earlier the transformation $\phi$ is not determined by the functional (5.2) on the entire domain $\Omega$. Thus, we incorporate an additional regularization energy $E_{\mathrm{reg}}$ which ensures that the deformation is smoothly extended into $\Omega \setminus \Gamma$.

We write $\phi = \mathbb{1} + \mathbf{d}$ where $u$ is understood as the pure displacement vector field, i. e., the deviation from the identity. Depending on the context we will either use $\mathbf{d}$ or $\phi$ as the optimization variable.

Let us again consider a Tikhonov-type regularization of the form

$$E(\Gamma, \phi, u_R, u_T) = E_{\mathrm{MS}}(\Gamma, \phi, u_R, u_T) + \alpha E_{\mathrm{reg}}(\phi). \tag{5.4}$$

Here, Tikhonov regularization has a prominent rôle in comparison to regularized gradient flows and multiscale methods. Only this type of regularization ensures a meaningful continuation of the deformation on the edge set to the rest of the domain.

If we would—only hypothetically—consider a set of admissible deformations which is fixed along $\Gamma$ then a Dirichlet type regularization would correspond to harmonic interpolation of the deformation within the subregions. Naturally, we also want to regularize the deformation along the edge set itself.

In the context of aligning feature sets we want the transformed contour $\Gamma^\phi$ to have the same topology as $\Gamma$. This means that we have to ensure that the deformation is one-to-one in a neighborhood of $\Gamma$, so the polyconvex registration techniques, which were described in detail in Section 3.2.1 are again a very convenient and suitable regularization.

In the remainder of this chapter, we will focus on the registration energy and for the sake of clarity we will consider the Dirichlet-type regularization energy:

$$E_{\mathrm{reg}}[\phi] = \|D\phi\|_{L^2(\Omega;\mathbb{R}^d)}^2 = \int_\Omega \|D\phi\|^2 \, \mathrm{d}\mu.$$

### 5.4.2 The reduced functional

The functional (5.4) depends on the variables $u_R$, $u_T$, $\phi$ and $\Gamma$. In the process of minimization we may devise different strategies for the different variables. Fortunately the functional is

quadratic in the variables $u_R$ and $u_T$. Hence, we may minimize (5.4) for fixed $\Gamma$ and $\phi$ over image spaces of $u_R$ and $u_T$. Let us now denote by $u_R(\Gamma)$ and $u_T(\Gamma, \phi)$ the minimizers of (5.4) for fixed $\Gamma$ and $\phi$, which are obtained as the solution of a simple quadratic optimization problem. Now we can define the following *reduced* functional

$$\hat{E}(\Gamma, \phi) = E(\Gamma, \phi, u_R(\Gamma), u_T(\Gamma, \phi)). \tag{5.5}$$

It is obvious that the minimizer with respect to $u_R$ depends only on $\Gamma$, whereas the minimizer with respect to $u_T$ depends also on $u$ via the domain of integration $\Omega \setminus \Gamma^\phi$. We specify the functional spaces for the variables $u_R$ and $u_T$ as $u_R \in H^{1,2}(\Omega \setminus \Gamma)$ and $u_T \in H^{1,2}(\Omega \setminus \Gamma^\phi)$. By first variation of the energy with respect to $u_R$ and $u_T$ and the fact that the energy is convex with respect to those variables, we obtain the sufficient conditions of optimality:

$$
\begin{aligned}
0 &= \left\langle \frac{\partial E}{\partial u_R}; \varphi \right\rangle_{H^{-1,2}(\Omega \setminus \Gamma) \times H^{1,2}(\Omega \setminus \Gamma)} \\
&= \mu \int_{\Omega \setminus \Gamma} \nabla u_R \cdot \nabla \varphi \, \mathrm{d}\mu + \int_\Omega (u_R - u_{R,0}) \varphi \, \mathrm{d}\mu \qquad \forall \varphi \in H^{1,2}(\Omega \setminus \Gamma)
\end{aligned} \tag{5.6}
$$

for $u_R = u_R(\Gamma)$ and for $u_T = u_T(\Gamma, u)$ we obtain similarly

$$
\begin{aligned}
0 &= \left\langle \frac{\partial E}{\partial u_T}; \varphi \right\rangle_{H^{-1,2}(\Omega \setminus \Gamma^\phi) \times H^{1,2}(\Omega \setminus \Gamma^\phi)} \\
&= \mu \int_{\Omega \setminus \Gamma^\phi} \nabla u_T \cdot \nabla \varphi \, \mathrm{d}\mu + \int_\Omega (u_T - u_{T,0}) \varphi \, \mathrm{d}\mu \qquad \forall \varphi \in H^{1,2}(\Omega \setminus \Gamma^\phi).
\end{aligned} \tag{5.7}
$$

We obtain the following Euler-Lagrange equations for $u_T$ and $u_R$:

$$
\begin{array}{rclclcrclcl}
-\mu \Delta u_R + u_R &=& u_{R,0} & \text{in} & \Omega \setminus \Gamma, & \qquad & -\mu \Delta u_T + u_T &=& u_{T,0} & \text{in} & \Omega \setminus \Gamma^\phi, \\
\partial_\nu u_R &=& 0 & \text{on} & \Gamma^\phi, & & \partial_\nu u_T &=& 0 & \text{on} & \Gamma.
\end{array}
$$

### 5.4.3 Shape sensitivity calculus

In this section, let us give a brief overview on the calculus of variations for energies which depend on a subdomain of $\Omega$, for instance a "thick" subdomain (with a positive Lebesgue measure) or a hypersurface. Details can be found in the books of SOKOŁOWSKI & ZOLÉSIO [189] or DELFOUR & ZOLÉSIO [92]. Furthermore the Appendix of [129] gives a nice overview.

For a smooth vector field $v : \Omega \to \mathbb{R}^d$ let us first consider the initial value problem

$$
\begin{aligned}
X'(t) &= v(X(t)), \\
X(0) &= X_0,
\end{aligned} \tag{5.8}
$$

for $X_0 \in \Omega$. The flow $T_t : \Omega \to \mathbb{R}^d$ (with respect to $v$ is then defined as $T_t(x) = X(t)$, where is $X(t)$ is the solution of (5.8) with $X_0 = x$. For a functional $E : \mathscr{E} \to \mathbb{R}$, and a fixed perturbation vector field $v$, the *Eulerian derivative* is defined by

$$\langle dE[\Gamma]; v \rangle = \lim_{t \searrow 0} \frac{E[T_t(\Gamma)] - E[\Gamma]}{t}.$$

Here $\mathscr{E}$ denotes a suitable space of interfaces. The functional $E$ is said to be shape-differentiable at $\Gamma$ if the limit exists for all $v \in B$, where $B$ is a Banach space of perturbation vector fields.

We will need the following lemma ( cf. [189]).

**Lemma 5.4.1.** *Let $\Gamma$ be a $\mathscr{C}^1$-hypersurface, and $\theta \in H^2_{\mathrm{loc}}(\mathbb{R}^d)$. Then the functional*

$$E[\Gamma] = \int_\Gamma \theta \, dA$$

*is shape differentiable for any perturbation $v \in \mathscr{C}_0^1(\mathbb{R}^d)$ and the shape derivative is given by*

$$
\begin{aligned}
\langle E'[\Gamma]; v \rangle &= \int_\Gamma \left( \nabla\theta \cdot v + \theta \operatorname{div}_\Gamma v \right) dA \\
&= \int_\Gamma \left( \frac{\partial\theta}{\partial n_\Gamma} + \theta h \right) v \cdot n_\Gamma \, dA
\end{aligned}
\tag{5.9}
$$

*where $n_\Gamma$ denotes the normal to the interface $\Gamma$. Note that the orientation of $\Gamma$ does not influence the value of the integral. $h$ denotes the mean curvature of $\Gamma$.*

**Definition 5.4.2 (material derivative).** *Let $\theta(\Omega) \in B(\Omega)$ for all $\Omega \subset \mathbb{R}^d$ open, $\partial\Omega \in \mathscr{E}$, where $B(\Omega)$ is some Banach space of functions on $\Omega$, furthermore let $v \in \mathscr{C}_0^1(\mathbb{R}^d, \mathbb{R}^d)$ be given. We call the limit*

$$
\frac{D\theta}{dt} := \dot\theta := \lim_{t \searrow 0} \frac{\theta(\Omega_t) \circ T_t - \theta(\Omega)}{t}
$$

*(weak) material derivative, if it exists in the strong (weak) topology of $B(\Omega)$.*

For a function $\theta$ which does not depend on $\Omega$, we have $\dot\theta = \nabla\theta \cdot v$. This gives rise to the following

**Definition 5.4.3 (shape derivative).** *If the weak material derivative and $\nabla\theta(\Omega) \cdot v$ exist in $B(\Omega)$, then we set*

$$
\theta'(\Omega) = \dot\theta(\Omega; v) - \nabla\theta(\Omega) \cdot v
$$

*and call it shape derivative of $\theta$ at $\Omega$ in direction $v$.*

In the next section we will also need the following

**Proposition 5.4.4.** *Let $\theta(\Omega)$ be given such the weak $L^1$-material derivative $\dot\theta(\Omega; v)$ and the shape derivative $\theta'(\Omega; v) \in L^1(\Omega)$ exist. Then, the functional*

$$
E[\Omega] = \int_\Omega \theta(\Omega, x) \, d\mu
$$

*is shape differentiable and the derivative is given by*

$$
\langle dE[\Omega]; v \rangle = \int_\Omega \theta'(\Omega; v) \, d\mu + \int_\Gamma \theta(v \cdot n_\Gamma) \, dA.
\tag{5.10}
$$

### 5.4.4  Sensitivity analysis

With these tools available, we are now able to derive the first variation of $\hat{E}$ with respect to the shape variable $\Gamma$ and with respect to the functional variable $\phi$. It is well known that the shape derivative only depends on the normal component of the perturbation vector field $v \in H_0^{1,2}(\Omega; \mathbb{R}^d)$. Let us first transform the integrals, such that they are defined over the reference configuration via the coordinate transformation $x \mapsto \phi(x)$, $\phi : \Omega \to \Omega$. We then obtain

$$
\begin{aligned}
\hat{E}(\Gamma, \phi) &= \frac{1}{2} \int_\Omega (u_R(\Gamma) - u_{R,0})^2 \, d\mu + \frac{\mu}{2} \int_{\Omega\setminus\Gamma} \|\nabla u_R(\Gamma)\|^2 \, d\mu \\
&\quad + \frac{1}{2} \int_\Omega (u_T(\Gamma, \phi) - u_{T,0})^2 \, d\mu + \frac{\mu}{2} \int_{\Omega\setminus\Gamma^\phi} \|\nabla u_T(\Gamma, \phi)\|^2 \, d\mu \\
&\quad + \nu \mathscr{H}^{d-1}(\Gamma) + \alpha E_{\mathrm{reg}}(\phi) \\
&= \frac{1}{2} \int_\Omega (u_R(\Gamma) - u_{R,0})^2 \, d\mu + \frac{\mu}{2} \int_{\Omega\setminus\Gamma} \|\nabla u_R(\Gamma)\|^2 \, d\mu \\
&\quad + \frac{1}{2} \int_\Omega \left( (u_T(\Gamma, \phi) - u_{T,0})^2 \circ \phi \right) |\det D\phi| \, d\mu \\
&\quad + \frac{\mu}{2} \int_{\Omega\setminus\Gamma} \left( \|\nabla u_T(\Gamma, \phi)\|^2 \circ \phi \right) |\det D\phi| \, d\mu + \nu \mathscr{H}^{d-1}(\Gamma) + \alpha E_{\mathrm{reg}}[\phi].
\end{aligned}
$$

**First variation with respect to $\Gamma$**

Now we can apply (5.9) as well as (5.10), where we have to integrate along the boundaries from both sides of the contour. Furthermore, recall that $v\big|_\Omega \equiv 0$, so we obtain:

$$
d\hat{E}\left((\Gamma,\phi);v\right) = \frac{1}{2}\int_\Gamma [\![(u_R(\Gamma)-u_{R,0})^2]\!]\, v\, \mathrm{d}A + \frac{\mu}{2}\int_\Gamma [\![\|\nabla u_R(\Gamma)\|^2]\!]\, v\, \mathrm{d}A
$$
$$
+ \frac{1}{2}\int_\Gamma [\![(u_T(\Gamma,\phi)-u_{T,0})^2 \circ \phi]\!]\,|\det D\phi|\, v\, \mathrm{d}A + \frac{\mu}{2}\int_\Gamma [\![\|\nabla u_T(\Gamma,\phi)\|^2]\!] \circ \phi\,|\det D\phi|\, v\, \mathrm{d}A
$$
$$
+ \left\langle \frac{\partial E}{\partial u_R}, (u_R')_v \right\rangle + \left\langle \frac{\partial E}{\partial u_T}, (u_T')_v \right\rangle + \nu \int_\Gamma h v\, \mathrm{d}A, \quad (5.11)
$$

where $[\![\cdot]\!]$ denotes the jump of the discontinuity across $\Gamma$ and $\Gamma^\phi$ respectively with respect to the trace onto the interface, i. e., $[\![(u_R(\Gamma)-u_{R,0})^2]\!] = (u_R^{(1)}-u_{R,0})^2 - (u_R^{(2)}-u_{R,0})^2$. $u'_{R,v}$ and $u'_{T,v}$ are the shape derivatives of $u_R$ and $u_T$ in direction to the perturbation given by $v$. $u_R^{(i)}$ denotes the restriction of $u_R$ to $\Omega_i$ (and analogously for $u_T^{(i)}$) for $i=1,2$. Note that the the jumps are well-defined independently of the choice of level set function $u_\Gamma$.

Let us now apply (5.10) for shape integrals of the form $\int_D \theta(\Omega,x)\,\mathrm{d}\mu$ to the weak first order conditions for $u_R$ and $u_T$, (5.6) and (5.7):

$$
\int_{\Omega_i} u_R^{(i)'}\varphi + \mu \nabla u_R^{(i)'}\,\nabla\varphi\,\mathrm{d}\mu + \int_\Gamma \left[(u_R^{(i)}-u_{R,0})\varphi + \mu \nabla u_R^{(i)}\cdot\nabla\varphi\right] v\,\mathrm{d}A = 0,
$$
$$
\int_{\Omega_i^\phi} u_T^{(i)'}\vartheta + \mu \nabla u_T^{(i)'}\,\nabla\vartheta\,\mathrm{d}\mu + \int_\Gamma \left[(u_T^{(i)}-u_{T,0})\vartheta + \mu \nabla u_T^{(i)}\cdot\nabla\vartheta\right] v\,\mathrm{d}A = 0,
$$

for all test functions $\varphi \in H^{1,2}(\Omega_i)$ and $\vartheta \in H^{1,2}(\Omega_i^\phi)$. With a similar reasoning as in [129], we obtain that the shape derivatives $(u_R^{(i)})'$ resp. $(u_T^{(i)})'$ are given as the solution of the above weak formulation of an elliptic problem in $H^{1,2}(\Omega_i)$ resp. $H^{1,2}(\Omega_i^\phi)$ and can thus be used as a test function in (5.6) and (5.7). Hence, the terms $\left\langle \frac{\partial E}{\partial u_R}, (u_R)_v' \right\rangle$ and $\left\langle \frac{\partial E}{\partial u_T}, (u_T)_v' \right\rangle$ in (5.11) vanish if so we can finally summarize:

$$
d\hat{E}\left((\Gamma,\phi);v\right) = \frac{1}{2}\int_\Gamma \left( [\![(u_R(\Gamma)-u_{R,0})^2]\!] + \mu [\![\|\nabla u_R(\Gamma)\|^2]\!] \right) v\,\mathrm{d}A
$$
$$
+ \frac{1}{2}\int_\Gamma \left( [\![(u_T(\Gamma,\phi)-u_{T,0})^2]\!] + \mu [\![\|\nabla u_T(\Gamma,\phi)\|^2]\!] \right) \circ \phi\,|\det D\phi|\, v\,\mathrm{d}A + \nu \int_\Gamma h\, v\,\mathrm{d}A. \quad (5.12)
$$

Recall that $u_R(\Gamma)$ and $u_T(\Gamma,\phi)$ are defined as the solutions of the corresponding Helmholtz problems (5.6) and (5.7).

**First variation with respect to $\phi$**

Let us assume that $\phi$ is invertible and that $\phi^{-1} \in \mathscr{C}^{0,1}(\Omega;\mathbb{R}^d)$ (Recall also Theorem 3.2.5, which suggests that polyconvex regularization would be of benefit also in this case). Then a perturbation $\psi$ of $\phi$ corresponds to a perturbation vector field $\psi \circ \phi^{-1}$ on the transformed curve $\Gamma^\phi$. Thus, the variation with respect to the deformation is given by:

$$
\left\langle \partial_\phi \hat{E}; \psi \right\rangle = \sum_{i=1,2} \int_{D\setminus\Gamma^\phi} \left\{ u_T^{(i)'}(u_T^{(i)}-u_{T,0}) + \mu \nabla u_T^{(i)'}\cdot\nabla u_T^{(i)} \right\}\mathrm{d}\mu
$$
$$
+ \frac{1}{2}\int_{\Gamma^\phi} \left( [\![(u_T(\Gamma,\phi)-u_{T,0})^2]\!] + \mu [\![\|\nabla u_T(\Gamma,\phi)\|^2]\!] \right)(\psi \circ \phi^{-1}\cdot n_{\Gamma^\phi})\,\mathrm{d}A
$$
$$
+ \langle \partial_\phi E_{\mathrm{reg}}; \psi \rangle. \quad (5.13)
$$

By the same arguments as before the first term on the right hand side vanishes. If the regularization term (5.5) is used, the Frèchet derivative of $\hat{E}$ with respect to $\mathbf{d}$ in direction $\psi \in H_0^{1,2}(\Omega;\mathbb{R}^d)$

reads as

$$\left\langle \partial_\phi \hat{E}[\phi]; \psi \right\rangle = \frac{1}{2} \int_{\Gamma\phi} \left( [\![|u_T(\Gamma, \phi) - u_{T,0}|^2]\!] + \mu[\![|\nabla u_T(\Gamma, \mathbf{d})|^2]\!] \right) (\psi \circ \phi^{-1} \cdot n_{\Gamma\mathbf{d}}) \, \mathrm{d}A$$
$$+ \langle \partial_\mathbf{d} E_{\mathrm{reg}}[\phi]; \psi \rangle. \quad (5.14)$$

### 5.4.5   Regularized gradient descent direction

The first variations contain jump terms of $u_T - u_{T,0}$ resp. $u_R - u_{R,0}$, where $u_{R,0}$ and $u_{T,0}$ are the possibly noisy input images. Hence the regularity of the descent direction is at least as low as the regularity of the data, and is thus expected to be very irregular. We will now again incorporate a metric to regularize the descent direction.

**Regularization of the descent direction with respect to $\phi$**

We have considered variations in $H_0^{1,2}(\Omega)$, hence the bilinear form

$$g_0(\phi, \psi) = (\nabla\phi, \nabla\psi)_{L^2}$$

defines a regularizing metric on the space of variations. The regularized descent direction $d_{g_0^\sigma}$ with respect to the metric $g_0^\sigma$ is thus given by

$$g_0(d_{g_0}, \psi) = -\left\langle \hat{E}[\phi]; \psi \right\rangle \qquad \forall \psi \in H_0^{1,2}(\Omega; \mathbb{R}^d)$$

Therefore, the direction of steepest descent is given as the solution to

$$\int_D \langle \nabla d_{g_0}, \nabla\psi \rangle \, \mathrm{d}\mu = -\left( \alpha \int_D \nabla\phi : \nabla\psi \, \mathrm{d}\mu \right.$$
$$\left. + \frac{1}{2} \int_{\Gamma\phi} \left( [\![|u_T(\Gamma, \phi) - u_{T,0}|^2]\!] + \mu[\![|\nabla u_T(\Gamma, \phi)|^2]\!] \right) \langle \psi \circ \phi^{-1}, n_{\Gamma\phi} \rangle \, \mathrm{d}A \right) \quad (5.15)$$

for all $\psi \in H_0^{1,2}(\Omega; \mathbb{R}^d)$.

Alternatively one might want to allow variations in $H^{1,2}$ instead of prescribing homogeneous Dirichlet conditions. This can be particularly important in the case of large translations between the reference and the template image. To this end, let us reconsider the following metric:

$$g^\sigma(\phi, \psi) = (\phi, \psi)_{L^2} + \frac{\sigma^2}{2}(\nabla\phi, \nabla\psi)_{L^2}.$$

Then $d_{g^\sigma} = -\mathrm{grad}_{g^\sigma} \hat{E}(\cdot, \Gamma)$ is given as solution of

$$\int_D \left( d_{g^\sigma} \cdot \psi + \frac{\sigma^2}{2} \nabla d_{g^\sigma} : \nabla\psi \right) \mathrm{d}\mu = -\alpha \int_D \nabla\phi : \nabla\psi \, \mathrm{d}\mu$$
$$- \frac{1}{2} \int_{\Gamma\phi} \left( [\![(u_T(\Gamma, \phi) - u_{T,0})^2]\!] + \mu[\![\|\nabla u_T(\Gamma, \phi)\|^2]\!] \right) (\psi \circ \phi^{-1} \cdot n_{\Gamma\phi}) \, \mathrm{d}A \quad (5.16)$$

for all $\psi \in H^{1,2}(\Omega; \mathbb{R}^d)$. After applying the transformation rule (3.30), the surface integral on the right hand side of (5.15) and (5.16) can be rewritten as

$$\frac{1}{2} \int_\Gamma \left( [\![(u_T(\Gamma, \phi) - u_{T,0})^2]\!] + \mu[\![\|\nabla u_T(\Gamma, \phi)\|^2]\!] \right) (\psi \cdot n_{\Gamma\phi}) \, \|\mathrm{Cof}\, D\phi n_\Gamma\| \, \mathrm{d}A. \quad (5.17)$$

Furthermore the transformed normal $n_{\Gamma\phi}$ is given by

$$n_{\Gamma\phi} = \frac{\mathrm{Cof}\, D\phi n_\Gamma}{\|\mathrm{Cof}\, D\phi n_\Gamma\|}. \quad (5.18)$$

**Regularized descent direction for the geometric variable**

By the same arguments as above, regularization of the shape gradient with respect to the geometric variable is desirable to ensure a stable gradient descent. In this section we aim at finding a metric for the function space of update directions $v$, such that the regularization is balanced with the regularization of the functional variable. The regularized descent direction $v_g$ is determined by

$$v_g = -\mathrm{grad}_{g_\Gamma} \hat{E}(\cdot, \phi) \quad \Rightarrow \quad g_\Gamma(v_g, w) = -d\hat{E}\left((\Gamma, \phi); w\right) \qquad \forall w \in H^{\frac{1}{2}}(\Gamma). \tag{5.19}$$

At this point we have to find a suitable way to define and evaluate the metric $g_\Gamma$. There are several ways to achieve this. An intrinsic approach would consist of defining the scalar product directly on the geometry, i. e.,

$$g_\Gamma^\sigma(v, w) = \int_\Gamma v\, w \,\mathrm{d}A + \frac{\sigma^2}{2} \int_\Gamma \nabla_\Gamma v \cdot \nabla_\Gamma w \,\mathrm{d}A.$$

This would lead to a balance according to the metric $g^\sigma$ for the variations of the deformation, and the regularization of the velocity $v$ would lead to the following geometric elliptic problem on $\Gamma$:

$$-\frac{\sigma^2}{2}\Delta_\Gamma v_d + v_d = v_g \quad \text{on} \quad \Gamma. \tag{5.20}$$

Here, $\Delta_\Gamma$ again denotes the Laplace-Beltrami operator on $\Gamma$. In the other example of the previous section, the update direction $d_g \in H_0^{1,2}(\Omega; \mathbb{R}^d)$ induces a movement of the transformed geometry with a speed in normal direction which is given by

$$v_{d_g} = \langle d \circ \phi^{-1}, n_{\Gamma^\phi} \rangle \in H^{\frac{1}{2}}(\Gamma^\phi)$$

for sufficiently smooth $\phi$. This motivates us to choose the gradient with respect to the $H^{\frac{1}{2}}$-metric on $\Gamma$, i. e., we set

$$g_\Gamma(v, w) := (v, w)_{H^{\frac{1}{2}}(\Gamma)}.$$

By this choice we expect a reasonable balance between the regularization of update directions for the functional variable $\phi$ and the geometric variable $\Gamma$. In order to evaluate the inner product $(\cdot, \cdot)_{H^{\frac{1}{2}}(\Gamma)}$ let us consider the boundary value problem

$$\begin{aligned} -\eta\Delta w + w &= 0 \text{ in } \Omega, \\ \frac{\partial w}{\partial n} &= w_\Gamma \text{ on } \Gamma, \end{aligned} \tag{5.21}$$

for $w_\Gamma \in H^{-\frac{1}{2}}(\Gamma)$. The weak formulation for (5.21) is given by

$$\int_\Omega \left( \eta\nabla w \cdot \nabla\varphi + w\,\varphi \right) \mathrm{d}\mu = \left\langle w_\Gamma, \varphi|_\Gamma \right\rangle_{H^{-\frac{1}{2}}(\Gamma) \times H^{\frac{1}{2}}(\Gamma)} \tag{5.22}$$

for all $\varphi \in H^1(\Omega)$.

Now we define the *Neumann-to-Dirichlet map* for the operator $-\eta\Delta + \mathbb{1}$ on $\Omega$ as the linear operator $\mathcal{N}: H^{-\frac{1}{2}}(\Gamma) \to H^{\frac{1}{2}}(\Gamma)$ which maps $w_\Gamma$ in (5.21) to the Dirichlet trace $w|_\Gamma$ of the solution to (5.21). It is well known (cf.[136]) that $\mathcal{N}$ is an isomorphism and that the inner product on $H^{\frac{1}{2}}(\Gamma)$ can be defined as

$$g_\Gamma(v, w) = (v, w)_{H^{\frac{1}{2}}(\Gamma)} = \left\langle \mathcal{N}^{-1}v, w \right\rangle_{H^{-\frac{1}{2}}(\Gamma) \times H^{\frac{1}{2}}(\Gamma)}$$

Finally the regularized update $v_g$ is determined as the the solution of

$$\left\langle \mathcal{N}^{-1}v_d, w \right\rangle_{H^{-\frac{1}{2}}(\Gamma) \times H^{\frac{1}{2}}(\Gamma)} = -d\hat{E}\left((\Gamma, \phi); w\right) \qquad \forall w \in H^{\frac{1}{2}}(\Gamma)$$

and hence the regularized descent velocity for (5.12), is given by

$$
\begin{aligned}
v_g = \frac{1}{2}\mathcal{N}\Big( & \llbracket |u_R(\Gamma) - u_{R,0}|^2 \rrbracket + \mu \llbracket \|\nabla u_R(\Gamma)\|^2 \rrbracket \\
& + \big( \llbracket (u_T(\Gamma,\phi) - u_{T,0})^2 \circ \phi \rrbracket + \mu \llbracket \|\nabla u_T(\Gamma,\phi)\|^2 \circ \phi \rrbracket \big)\, |\det D\phi| \Big) + \alpha h \quad (5.23)
\end{aligned}
$$

on $\Gamma$.

### 5.4.6   A level set shape gradient descent method

Now that we have derived first order variations of the energy and devised suitable regularizations of the descent directions, we will describe how the optimization, that takes place over a shape and the deformation simultaneously, can be solved numerically. The topology of the solution $\Gamma$ of the optimization problem is not known *a-priori* and furthermore the gradient descent method depends on an initial guess. This should not restrict the class of admissible solutions to shapes of the same homotopy class. Level set methods provide a convenient framework for the representation and numerical evolution of sharp interfaces, especially when topological changes come into play.

**Regularized shape gradient method**

The algorithm consists of the following steps.

**Step 0**  Choose initial level set function $u_{\Gamma,0}$, choose initial deformation $\phi_0$.

**Step 1**  Extract the current shape $\Gamma^k = \{u_\Gamma^k = 0\}$, $\Omega_1^k = \{u_\Gamma^k < 0\}$ and $\Omega_2^k = \{u_\Gamma^k > 0\}$.

**Step 2**  Compute $u_R^k$ and $u_T^k$ by solving (5.6) resp. (5.7) for the current $\Gamma^k$ and $\phi^k$ .

**Step 3**  Compute $v$ according to (5.12).

**Step 4**  Solve the elliptic equation (5.21) with Neumann data $v$ for $w$ and compute $v_g^k$ as the trace of $v$ on $\Gamma^k$.

**Step 5**  Extend $v_g^k$ to a function $v_g^{\mathrm{ext}}$ defined on a neighborhood of $\Gamma^k$ .

**Step 6**  Compute the regularized descent direction $d_g^k$ according to (5.15).

**Step 7**  Solve the level set equation

$$
\frac{u_\Gamma^{k+1,i+1} - u_\Gamma^{k+1,i}}{\tau_u} + v_g^{\mathrm{ext}} \|\nabla u_\Gamma^k\| = 0 \text{ with } u_\Gamma^{k+1,0} = u_\Gamma^k
$$

for the evolution of $\Gamma^k$ for $i = 1, \dots$ as long as the energy is decreasing. $\tau_u$ is chosen to obey the CFL-condition $\tau v_g^{\mathrm{ext}} \leq C_{\mathrm{CFL}} h$. Perform an update $\phi^{k+1} = \phi^k + \tau d_g^k$, where $\tau$ is determined by a line search strategy.

**Step 8**  $k \leftarrow k + 1$.

**Step 9**  check stopping criterion $\|v_g^k\|_{L^2(\Gamma)} + \|d_g^k\| \leq \epsilon$, otherwise go to Step 1 .

**Detailed description of the algorithm**

The Finite Element approximations of the functions $u_R$ and $u_T$ and the auxiliary variable $v$ in (5.22) on the irregular domains $\Omega \setminus \Gamma$, $\Omega \setminus \Gamma^\phi$ and $\Omega$ are done using Composite Finite Elements (cf. [122]). The transformation vector field $\phi$ is discretized using standard Finite Elements. Let us look at some steps of the algorithm in more detail.

**Step 2**

In order to solve (5.6) and (5.7) with standard Finite Elements retriangulation and thus reorganization of the degrees of freedom would be necessary. Composite Finite Elements as introduced by SAUTER & HACKBUSCH [122] are designed to cope with irregular geometries and to allow the application of efficient multigrid solvers. This is of vital importance for the proposed algorithm, since in every iteration, 5 elliptic PDE's have to be solved on domains with moving boundaries. An overview on Composite Finite Elements (CFEs) is given in section 5.4.7.

In order to construct the basis functions of the CFE space, first the contour $\Gamma^k$, which is given as the zero level set of $u_\Gamma^k$, has to be extracted. For the computation of $u_T$ we obtain the contour $\phi(\Gamma^k)$ from the level set function $u_\phi^k := u_\Gamma^k \circ (\phi^k)^{-1}$. To compute $u_\phi^k$ we introduce a simplicial triangulation $\mathscr{T}$ on $D$ and approximate $\phi^k$ as well as $u_\Gamma^k$ by piecewise affine Finite Elements on $\mathscr{T}$. Then we can compute a deformed triangulation $\mathscr{T}^\phi$, which is obtained by $T^\phi = \phi(T)$ for all $T \in \mathscr{T}$, and finally on all of those deformed triangles the nodal values of $u_\phi^k$ are calculated by interpolating the values of $u_\Gamma^k$ which are pushed forward by the deformation $\phi$.

**Step 3**

Before regularizing the descent direction we have to extract the shape gradient on $\Gamma$ by evaluating all the terms which appear in (5.12). This function will then be used as Neumann data in the next step or alternatively be extended to a neighborhood to solve the geometric Helmholtz problem (5.20).

As can be seen from (5.22) the functionals on $\Gamma$ are considered in the form $\int_\Gamma F_g\, \varphi_n \, \mathrm{d}A$, for all Finite Element basis functions $\varphi_n$. Hence the values of $F$ only have to be evaluated in the interior of the edges, which intersect the rectangular Finite Element grid. To this end, the values of $F$ are extended from the discrete contour to all surrounding nodes, which belong to the intersected cells, and are henceforth available for interpolation which is needed for the quadrature rule to compute the line boundary integrals. The calculation of the shape gradient involves the computation of jumps of $u_R - u_{R,0}$ and $\nabla u_R$ along the contour. Here, $u_R$ is the solution to (5.6) on $\Omega$ (and similar jumps depending on $u_T$). Those values are obtained by straightforward interpolation of the discrete Finite Element representations of $u_R$ and $u_T$.

**Step 4**

In order to calculate the regularized descent direction $v_g$ in (5.23), we have to solve

$$(\nabla \hat{\phi}_i, \nabla \hat{\phi}_j)_{L^2(\Omega_1)} \bar{V}_{g,i} + (\hat{\phi}_i, \hat{\phi}_j)_{L^2(\Omega_1)} \bar{V}_{g,i} + (V, \hat{\phi}_i)_{L^2(\partial\Omega_1)} = 0 \qquad \forall \hat{\phi}_j \in \hat{\mathcal{V}},$$

for the discrete representation $V_g$ of $v_g$. Here $\hat{\phi}_i$ denote the basis functions of the composite Finite Elements space (cf. Section 5.4.7), and $\bar{V}_{g,i}$ denotes the $i$-th component of the vector $\bar{V}_g$, standing for the coefficient vector of $V_g$.

**Step 5**

To evolve the level set function with a speed on the contour given by $v_g$, we first have to extend $v_g$ to a function $v_g^{\mathrm{ext}}$ which is defined on a small neighborhood of the contour. A natural extension is given by the following approach. For each point $x$ in a defined neighborhood, the extended velocity is calculated by first projecting $x$ via the projection $\pi_\Gamma$ onto $\Gamma$ and evaluating $v$ at this projected point, i. e., $v_g^{\mathrm{ext}}(x) = v_g(\pi_\Gamma(x))$. This is equivalent to solving the following transport equation:

$$\nabla v_d^{\mathrm{ext}} \cdot \nabla d_\Gamma = 0 \quad \text{on} \quad \Omega \qquad \text{and} \qquad v_d^{\mathrm{ext}} = v_d \quad \text{on} \quad \Gamma, \tag{5.24}$$

where $d_\Gamma$ stands for the distance function $x \mapsto \mathrm{dist}(x, \Gamma)$. $d_\Gamma$ and $v_d^{\mathrm{ext}}$ can be computed simultaneously by a modified fast marching method for solving the *eikonal equation* $\|\nabla d\| = 1$ (cf. [168, 186] for a comprehensive description of the algorithm) or by the method proposed by BORNEMANN & RASCH [29], which computes the viscosity solution of static Hamilton-Jacobi equations by iterated local *Hopf-Lax* updates. Note that if the extension is given by this procedure, distance functions are locally preserved.

**Step 7**

For the evolution of the level set function, via

$$\partial_t u_\Gamma + v_d^{\text{ext}} \|\nabla u_\Gamma\| = 0 \quad \text{on} \quad \Omega \tag{5.25}$$

we have applied a third-order accurate ENO-scheme (cf. [168]).

### 5.4.7  Composite Finite Elements and Multigrid

In this section we will briefly describe the spatial discretization of the function spaces on $\Omega_i$, which are divided by the contour $\Gamma$ given by the level set function $u_\Gamma$. Furthermore we outline a multigrid method for the solution of (5.6), (5.7), (5.15) and (5.22). We use Composite Finite Elements introduced by Hackbusch and Sauter [122]. Let us emphasize, that the advantages of CFEs are twofold. They provide a multilevel framework for the discretization of complicated and moving domains, as well as PDE's with discontinuous coefficients. In our application we have incorporated the CFE for the first reason.

The idea of the CFE approach is the following: Instead of resolving the $\Omega_i$ by a retriangulation or local adaptive refinement, we confine ourselves to a uniform quadrilateral resp. hexahedral grid and define the triangulations $\mathcal{T}_i$ by the following overlap-condition:

$$\Omega_i \subseteq \overline{\bigcup_{T \in \mathcal{T}_i}} \qquad \forall\, T \in \mathcal{T}_i \text{ s. t. } T \cap \Omega_i \neq \emptyset. \tag{5.26}$$

Let us denote by $V_h(\Omega_{\mathcal{T}})$ the usual Finite Element space given by the condition that for $U \in V_h(\Omega_h)$, $U\big|_T$ is a multilinear function for each $T \in \mathcal{T}$. The corresponding Composite Finite Element space is then simply given by the restriction of the functions in $V_h(\Omega_{h,i})$ to the domain $\Omega_i$, i. e.

$$\hat{\mathcal{V}}_h(\Omega_{h,i}) := \{ U|_{\Omega_i} \,|\, U \in \mathcal{V}_h(\Omega_{h,i}) \}. \tag{5.27}$$

Hence, a basis $(\hat\varphi_i)_i$ of $V_h^{CFE}$ is given by $\hat\varphi_i := \varphi_i\big|_{\Omega_{\mathcal{T}_i}}$, where $(\varphi_i)_i$ denotes a basis of the space $\mathcal{V}_h(\Omega_{\mathcal{T}_i})$. For the assembly of the *mass* matrix

$$\hat{M}_{ij}^l = \int_{\Omega_l} \hat\varphi_i \hat\varphi_j \, \mathrm{d}\mu$$

and the *stiffness* matrix

$$\hat{L}_{ij}^l = \int_{\Omega_l} \nabla\hat\varphi_i \nabla\hat\varphi_j \, \mathrm{d}\mu$$

we thus need to apply quadrature rules for functions on $T \cap \Omega_i$. On each cell $T$, which is crossed by the zero level set of $u_\Gamma$ we generate a partition of $T \cap \Omega_i$ into simplices on-the-fly. We can then apply a barycentre quadrature rule on each simplex.
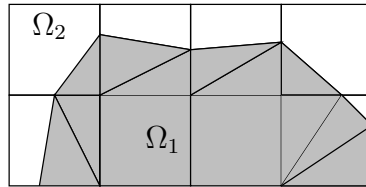


Figure 5.2: *Decompositions of the domains $\Omega_i \cap C$ for a cell $C$ into subtriangles. The type subtriangulation only depends on the signs of the level set function on the vertices of $C$ and can be efficiently generated on-the-fly using lookup-tables.*

So far this procedure is the FE analogue of a *Shortley-Weller* discretization by finite differences. In the iteration of the gradient descent method, the second order elliptic PDE's have to
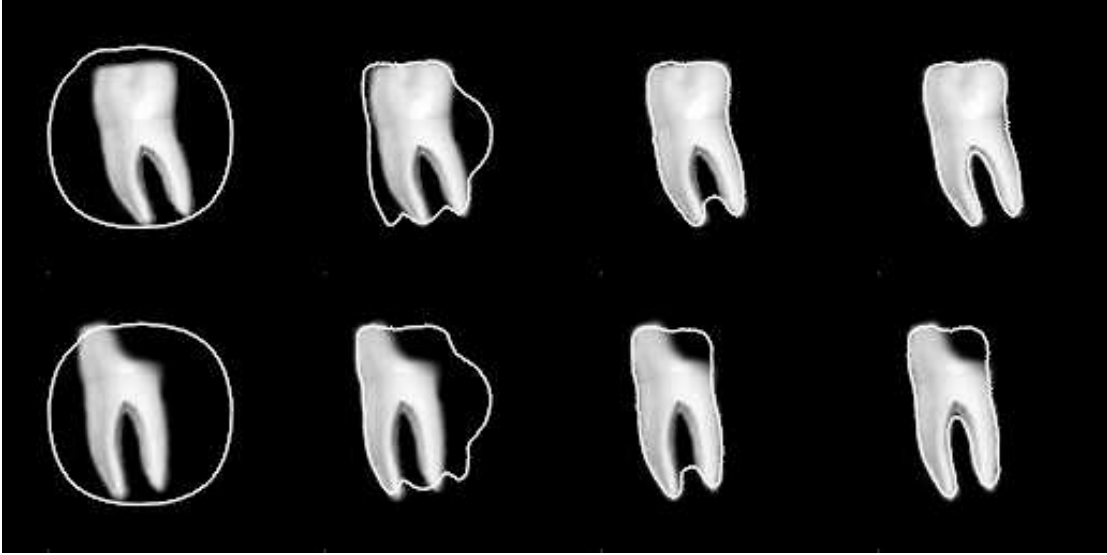
Figure 5.3: *Towards model-based reconstruction. The image at the* TOP LEFT *shows an artificial reference model of a tooth. On the* BOTTOM LEFT *a nonlinearly deformed version of the reference with a large destroyed region is shown. Both images also show the initial contour* Γ. *The sequence shows the evolution of* Γ *and* $\Gamma^\phi$ *for the iteration numbers* $0, 20, 80, 320$, *where the parameters were chosen as* $\mu = 50$, $\alpha = 200$ *and* $\nu = 5000$.

be solved each time the contour changes, i. e., in every iteration. In order to render the descent efficient, it is crucial to solve those equations efficiently and exactly, because an inexact solution would lead to inaccurate velocities. To apply a multigrid method, we first generate a sequence of nested Composite Finite Element spaces by applying an appropriate coarsening process on the CFE triangulation on the finest level $l_{\max}$ ($\Omega_{\mathscr{T}_i}^{l_{\max}} := \Omega_{\mathscr{T}_i}$), i. e.

$$\Omega_i \subset \Omega_{\mathscr{T}_i}^{l_{\max}} \subset \Omega_{\mathscr{T}_i}^{l_{\max}-1} \subset \ldots \subset \Omega_{\mathscr{T}_i}^0 \tag{5.28}$$

leading to correspondingly nested CFE spaces $\hat{\mathcal{V}}_h(\Omega_{\mathscr{T}_i}^l)$, $0 \le l \le l_{\max}$. Prolongations and restrictions naturally have to be defined with respect to the CFE discretization, hence the prolongation onto level $l$ is defined by evaluation of the basis functions $\hat{\varphi}_i^{l-1}$ for Lagrange nodes on level $l$. Convergence analysis for multigrid algorithms using Composite Finite Elements has been investigated by Sauter et al. [122, 202].

### 5.4.8 Numerical experiments

We have tested the approach in different scenarios. Figure 5.2 shows a synthetic image pair, which was designed to test the approach in cases, where only very little common information is contained in the images. The shape on the upper left is supposed to be fitted into the structure on the bottom left, which is hence only determined by the four small objects in the corners of the image. After 75 steps of the gradient descent, a deformation is found which rotates the propeller-like shape, and the resulting push-forward of the contour matches quite well to the rounded corners in the second structure in the bottom. This example shows the capability of a model-based inpainting, where the shape information of the inpainted contour is transformed from a reference image. We assume, that the deviations from the obvious solution of a pure rotation result from the fact, that the rigid transformations are not in the kernel of the regularization energy, and we think that this could be solved by different regularization methods as for example higher order methods [158]. However, we will not focus on the regularization in this context.

In Figure 5.4 we have applied the algorithm to a pair of brain images. The top row shows a positron density (PD) scan, while the bottom row shows a T1-weighted magnetic resonance
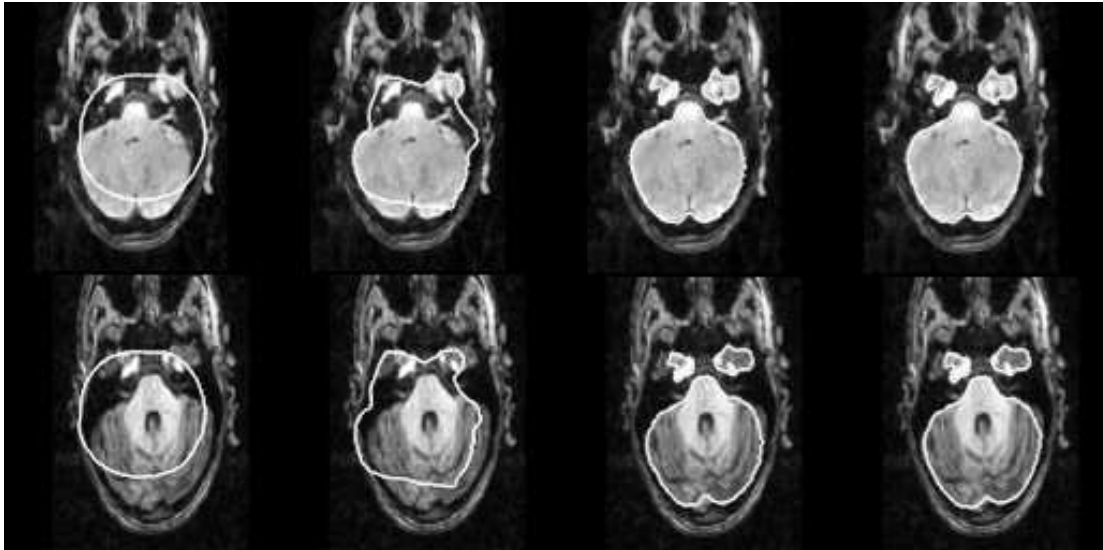
Figure 5.4: TOP ROW: *Reference image $u_R$ (positron density image (PD) of a human brain) and* Γ. BOTTOM ROW: *Template image $u_T$ (T1-weighted MR image). The sequence shows the gradient descent for the iteration numbers $0, 10, 80$ and $180$. The parameters were chosen as $\mu = 50$, $\alpha = 20$, $\nu = 500$.*

image of the same patient. The initial difference of the image pair consists mainly of a translation of about 8-9 pixels. The algorithm finds the brain structure in both images well after about 80 steps, and the resulting deformation consists mainly of a shift enhanced by some minor local deformations. This example underlines the practicability of the level set approach: after a few steps the initial contour splits up into three different components which are henceforth independently mapped onto the corresponding segments in the template.

The last example in Figure 5.3 demonstrates the competing effect of the regularization and the energy contributions which pull the contour towards the edges. We can exploit this in order to map an original reference shape (top row) to a given object, where the shape is partially corrupted (bottom row). Apart from the destroyed region the shapes differ also by a non-rigid deformation plus a translation. This can be well observed in the second column. Here the deformation is still close to the identity and hence the contours are aligning to the edges in the vicinity first until in subsequent iterations the deformation evolves in such a way that the contours map to the true edges in both images apart from the borders of destroyed region. At this stage, the regularization dominates and prohibits the contour in the bottom row to evolve towards the "visible" edge and prefers to adopt the contour from the reference image. This yields a reconstruction of the destroyed shape, which is optimal with respect to the regularization energy.

### 5.4.9   Conclusion

We have presented a level set based algorithm for simultaneous segmentation and registration of images by incorporating a Mumford-Shah type energy on the reference image as well as the template image, where the contour is transformed into the template image by a regularized deformation. The work presented here is motivated by the fact, that, given an exact registration of two images of different modality, edge-extraction and segmentation can be enhanced considerably by combining complementary feature information from both modalities. On the other hand the process of registering a pair of images may rely on segmentations and feature-extractions of both images, which is often a very tedious process, especially if in some areas the feature information is very weak. Due to the coupling of the edge sets by the smooth deformation, the edge is driven to its correct shape.
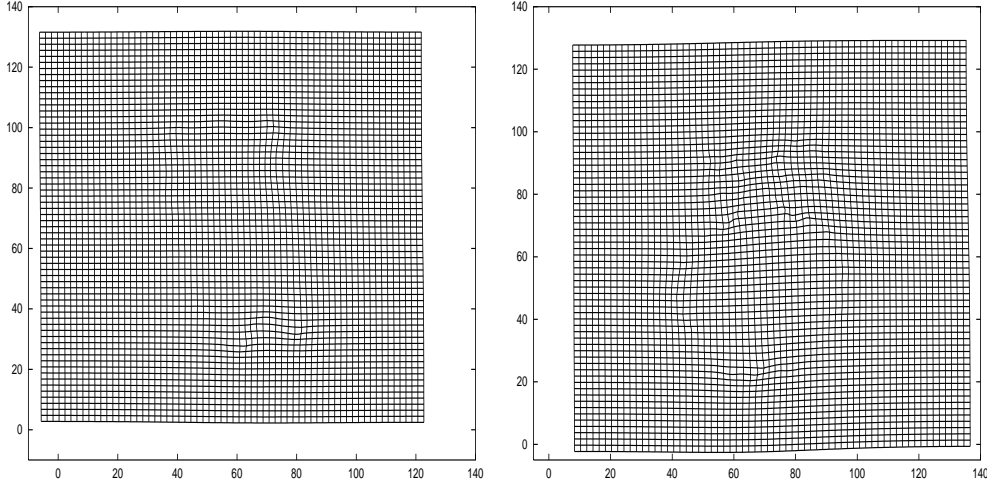
(a) *Deformation plot of the matching result from Figure 5.3.*   (b) *Deformation plot of the matching result from Figure 5.4.*

We have demonstrated a further important application of this method, namely to perform a fully-automatic model-based reconstruction and inpainting of destroyed regions, without having to explicitly mark the region where the object is destroyed as long as there exist no prominently dominating edges.

Due to the regularization of the gradient flow, the minimization process has turned out to be stable and requires only a small number of iterations until convergence. On the other hand, the regularization and necessity of determining the solutions of the Helmholtz equations in the regions $\Omega_1$ and $\Omega_2$ requires the solution of elliptic PDEs. In order to make the method efficient we have applied multigrid techniques which lead to an enormous speed-up of the algorithm.

## 5.5   Phase-field approach to edge-alignment for free discontinuities

In this section we will present an alternative to the previously described sharp interface model. In [11] Ambrosio and Tortorelli proposed a phase field approximation of the *Mumford-Shah* [163] functional

$$E_{\mathrm{MS}}[u, \Gamma] = \int_{\Omega \setminus \Gamma} \|\nabla u\|^2 \, \mathrm{d}\mu + \frac{\mu}{2} \int_{\Omega} (u - u_0)^2 \, \mathrm{d}\mu + \nu \mathscr{H}^{d-1}(\Gamma)$$

where $u_0 \in L^{\infty}(\Omega)$ and $u$ varies in $\mathscr{C}^1(\Omega \setminus \Gamma)$. Theoretical subtleties arise mainly from the fact, that $u$ varies in a space, which depends on $\Gamma$, while the variation of $\Gamma$ results in problems of finding a set of admissible contours with suitable compactness properties. Before we revise the approximation, we rewrite the Mumford-Shah energy [81, 160, 11] to

$$F[u] = \int_{\Omega \setminus \Gamma} \|\nabla u\|^2 \, \mathrm{d}\mu + \frac{\mu}{2} \int_{\Omega} (u - u_0)^2 \, \mathrm{d}\mu + \nu \mathscr{H}^{d-1}(S_u)$$

where the space of admissible functions in $L^{\infty}(\Omega)$ is endowed with the $L^2(\Omega)$ topology, or to be more precise in the space of piecewise $\mathscr{C}^1$ functions

$$PC^1(\Omega) = \left\{ u \in L^{\infty}(\Omega) \, : \, u \in \mathscr{C}^1(\Omega \setminus \overline{S_u}) \text{ and } \mathscr{H}^{d-1}(\overline{S_u} \cap \Omega \setminus S_u) = 0 \right\}.$$

$S_u$ denotes the complement of the set of Lebesgue points of $u$. Since $PC^1$ is not compact with respect to a suitable topology, the common approach is to relax $F$ to $\overline{F}(u) = \inf \left\{ \liminf_{s \to \infty} F(u_s) \, : \, u_s \to u \in L^2(\Omega), \, u_s \right.$

Let us now consider the approximation, that has been proposed by AMBROSIO&TORTORELLI in [11]. Let us suppose $k_\epsilon > 0$ and consider the functional

$$
\begin{aligned}
E_\epsilon[u, v] & = \int_\Omega \left\{ (u - u_0)^2 + \frac{\mu}{2}(v^2 + k_\epsilon) \|\nabla u\|^2 \right\} \mathrm{d}\mu + \nu \int_\Omega \left\{ \epsilon \|\nabla v\|^2 + \frac{(1 - v)^2}{4\epsilon} \right\} \mathrm{d}\mu \\
& =: \ E_{\epsilon,1} + E_{\epsilon,2}. \quad\quad\quad\quad\quad\quad\quad\quad\quad\quad\quad\quad\quad\quad\quad\quad\quad\quad (5.29)
\end{aligned}
$$

They have shown the $\Gamma$-convergence of $E_\epsilon$ to the functional defined by $\overline{E}[u, v] = \overline{F}[u]$, iff $v \equiv 1$, and $\overline{E}[u, v] = +\infty$ otherwise. The $\Gamma$-convergence is respect with to the strong $L^2(\Omega) \times L^2(\Omega; [0, 1])$ topology.

**A remark on anisotropy**

The energy contribution $\int_\Omega \epsilon \|\nabla v\|^2 \, \mathrm{d}\mu$ introduces a homogeneous smoothness energy on the function $v$ which continuously represents the singularity set $S_u$. Even though this $E_\epsilon$ already qualitatively converges to $E$, in practice one aims at minimizing $E_\epsilon$ for a small $\epsilon > 0$. To improve the approximation results for a fixed $\epsilon > 0$, we (for twodimensional problems) propose a modification of the form

$$
\begin{aligned}
E_\epsilon[u, v] = \frac{\beta}{2} \int_\Omega \left\{ (u - u_0)^2 + (v^2 + k_\epsilon) \|\nabla u\|^2 \right\} \mathrm{d}\mu \\
+ \frac{\alpha}{2} \int_\Omega \left\{ \epsilon A(x, \nabla u_0^\sigma) \nabla v \cdot \nabla v + \frac{(1 - v)^2}{4\epsilon} \right\} \mathrm{d}\mu \quad (5.30)
\end{aligned}
$$

where $A : \Omega \times \mathbb{R}^d \to \mathbb{R}^{d,d}$ is a uniformly elliptic and bounded tensor, which we will design in such a way that $v$ is regularized along *estimated edges* and regularization of $v$ is small across such yet to detect edges. Following typical structure-tensor based approaches for the design of such tensors, e. g. WEICKERT [204], NAGEL-ENKELMANN [164], we suggest

$$
A_{2D}(x, \nabla u_0^\sigma) := \frac{(\nabla u_0^\sigma)^\perp}{\|(\nabla u_0^\sigma)^\perp\|} \otimes \frac{(\nabla u_0^\sigma)^\perp}{\|(\nabla u_0^\sigma)^\perp\|} + g(\|\nabla u_0^\sigma\|) \frac{\nabla u_0^\sigma}{\|\nabla u_0^\sigma\|} \otimes \frac{\nabla u_0^\sigma}{\|\nabla u_0^\sigma\|},
$$

where $g : \mathbb{R}_0^+ \to \mathbb{R}_0^+$ is a continuous monotonously decreasing function, and $u_0^\sigma$ denotes a regularized version of $u_0$, obtained by solving the initial value problem of e. g. linear diffusion or mean curvature motion with natural boundary conditions. To generalize the construction of the tensor in more dimensions on can write

$$
A_{2D/3D}(x, \nabla u_0^\sigma) := P[u_0^\sigma] + g(\|\nabla u_0^\sigma\|)(\mathbb{1} - P[u_0^\sigma]).
$$

See Figure 5.5 for improved results obtained with this variant. It has to be mentioned, that it is so far unknown if similar $\Gamma$-results hold in this case. We assume that this will particularly depend on the choice of $g$.

## 5.5.1   Variational model formulation

Let us recall the *Mumford-Shah*-based registration formulation (1.4). Although we have obtained satisfactory results with the sharp interface model in the shape optimization context, it would be interesting to compare the previous approach with the respective phase-field formulation. The reason for this is threefold: First, the sharp interface approach depends on the shape of the initial interface $\Gamma$. Whereas this may be convenient in some cases, for example, when the initialization allows a certain degree of user control to preselect certain features, it may also be ambiguous and tedious in other cases. Secondly, the classical level set framework is restricted to closed curves, and thus it does not allow to represent *crack tips* by a single level set function. Although this could be achieved by combining several level set functions with boolean operations, the phase field approach appears to be more flexible and practicable for the applications discussed here. Thirdly, the phase field model is very easy to implement, if standard numerical toolboxes for the solution of coupled PDE's are available.
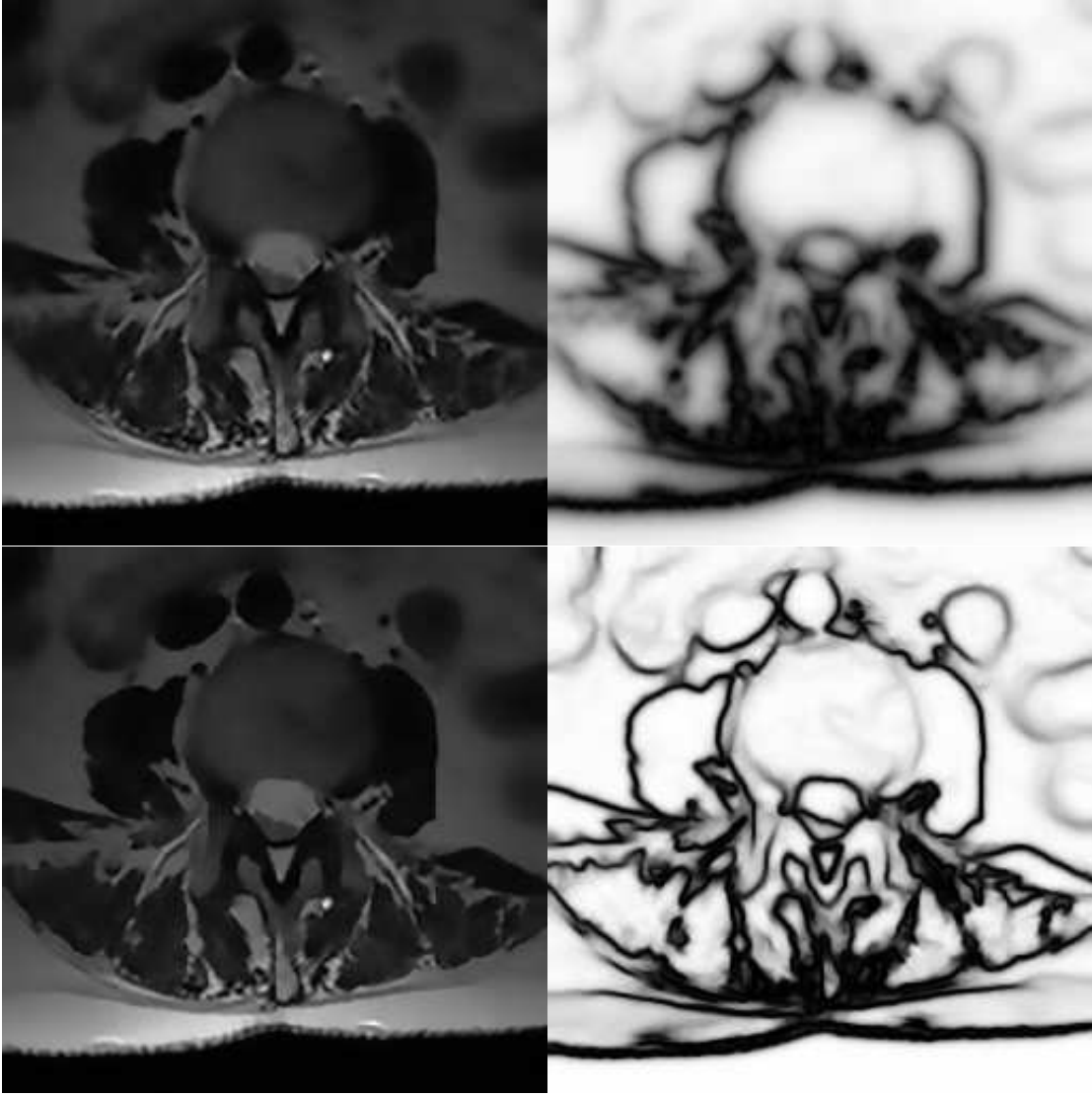
Figure 5.5: Isotropic vs. anisotropic version of the approximation of the Mumford-Shah functional. The parameters were chosen as $\epsilon = 0.01$, $\alpha = 10$ and $\lambda = 0.05$ (for the special choice $g(s) = 1/(1 + \frac{s^2}{\lambda^2})$).

We suggest an analogous coupled phase-field formulation by again introducing an auxiliary variable $v$, describing the singularity set $S_T$ of the image $u_T$, but at the same time $v \circ \phi$ should energetically describe the edge set $S_R$ in the image $u_R$. A corresponding energy formulation is then given by the minimization of

$$E_{\text{ATreg},\epsilon}[u_R, u_T, v, \phi] := \frac{1}{2} \int_\Omega \left\{ (u_R - u_{R,0})^2 + (u_T - u_{T,0})^2 \right\} \mathrm{d}\mu \tag{5.31}$$

$$+ \frac{\mu}{2} \int_\Omega \left\{ (v^2 \circ \phi + k_\epsilon) \|\nabla u_R\|^2 + (v^2 + k_\epsilon) \|\nabla u_T\|^2 \right\} \mathrm{d}\mu \tag{5.32}$$

$$+ \frac{\nu}{2} \int_\Omega \left\{ \epsilon \|\nabla v\|^2 + \frac{1}{4\epsilon} (v - 1)^2 \right\} \mathrm{d}\mu \tag{5.33}$$

with $k_\epsilon = o(\epsilon)$. Now, the signature $v$ corresponds to the contour $\Gamma^\phi$ and the contour $\Gamma$ is described by $v \circ \phi$. The data $u_{R,0}$ and $u_{T,0}$ are given as images in $L^\infty(\Omega)$ and can thus contain very irregular and dense sets of singularities. Again, when we speak of edge sets of $u_{R,0}$

and $u_{T,0}$ this is to be understood in the sense of the Mumford-Shah approximation, where the approximating functions $u_T$ resp. $u_R$ are in $SBV(\Omega)$ with $\mathcal{H}^{n-1}$ measurable discontinuity sets.

Let us now describe this energy in some detail. The first integral measures the deviation of $u_R$ and $u_T$ to the data in the $L^2$-sense. The second integral now forces the signature $v^2$ to be small where $u_T$ has steep gradients and, correspondingly, $v^2 \circ \phi$ to be small where $u_R$ has steep gradients. On the other hand, this determines $\phi$ to align the signature function in the reference domain to line up with the edges of $u_R$, and finally, for fixed signature and deformation, the smoothness of the images $u_R$ and $u_T$ is controlled, i. e., steep gradients of $u_T$ are penalized where $v \not\approx 0$ and analogously for $u_R$.

Again, the deformation $\phi$ will mainly be determined along the discontinuity sets. Away from the contours, the signature $v$ will approximately be identical to $1$, and hence variations of $\phi$ will not change the energy in these regions. Thus, it is essential to further regularize the minimization problem. Let us again consider the nonlinear hyperelastic regularization given by the additional energy contribution (3.12), and consider the minimization problem of finding $(u_R, u_T, v, \phi) \in H^{1,2}(\Omega)^3 \times H_0^{1,2}(\Omega; \mathbb{R}^n) =: \mathscr{A}$, such that

$$E_{\mathrm{ATreg},\epsilon}[u_R, u_T, v, \phi] + \alpha E_{\mathrm{reg}}[\phi] = \inf_{(\tilde{u}_R, \tilde{u}_T, \tilde{v}, \tilde{\phi}) \in \mathscr{A}} E_{\mathrm{ATreg},\epsilon}[\tilde{u}_R, \tilde{u}_T, \tilde{v}, \tilde{\phi}] + \alpha E_{\mathrm{reg}}[\tilde{\phi}] \quad (5.34)$$

The following approaches for the overall registration energy are possible:

- **Pure Edge-based registration**—in order to determine the deformation only by the alignment of features, one might consider the pure Mumford-Shah based approach as described above:

$$E_{\mathrm{ATedge}}[u_R, u_T, v, \phi] \quad = \quad E_{\mathrm{ATreg},\epsilon}[u_R, u_T, v, \phi] + \alpha E_{\mathrm{reg}}[\phi]. \quad (5.35)$$

- **Edge-based registration with weighted regularization**—the signature function $v$ automatically yields information about where the variation of the deformation determines a change in the energy, namely along and in the vicinity of edges, which are given by $v^2 \circ \phi \approx 0$. In order to avoid over-regularization, the integrand of the regularization may be weighted by $v^2 \circ \phi$:

$$E_{\mathrm{ATweight}}[u_R, u_T, v, \phi] = E_{\mathrm{ATreg},\epsilon}[u_R, u_T, v, \phi]$$
$$+ \alpha \int_\Omega (v^2 \circ \phi + k_\epsilon) \mathbb{W}(D\phi, \mathrm{Cof}\, D\phi, \det D\phi)\, \mathrm{d}\mu \quad (5.36)$$

Hence, the regularization dominates away from the edges.

- **Combined Mumford-Shah-Morphological registration**—Here, we add the morphological energy contribution on those areas, weighted such that it gives a stronger contribution in areas away from the singularity sets of $u_R$ and $u_T \circ \phi$. Again this set area is given by $v^2 \circ \phi$.

$$E_{\mathrm{ATmorph}}[u_R, u_T, v, \phi] = E_{\mathrm{ATreg}}[u_R, u_T, v, \phi]$$
$$+ \beta \int_\Omega v^2 \circ \phi \omega_0(\nabla u_T \circ \phi, \nabla u_R, \mathrm{Cof}\, D\phi)\, \mathrm{d}\mu$$
$$+ \alpha \int_\Omega (v^2 \circ \phi + k_\epsilon) \mathbb{W}(D\phi, \mathrm{Cof}\, D\phi, \det D\phi)\, \mathrm{d}\mu \quad (5.37)$$

In this thesis, we have concentrated on the second approach (5.36).

## 5.5.2 Discrete approximation

In contrast to the original approach of [10], where approximating elliptic but non-quadratic functionals have been used, the approximation of (5.29) gives rise to practicable numerical methodologies. We refer for instance to [23, 176]. In order to discretize $E_{\mathrm{ATreg},\epsilon}$, we follow

the approach of BOURDIN [30]. He has shown the $\Gamma$-convergence of the discretized functionals against the functional $\overline{E}$. To this end, we construct the discrete version of the energy $E_{\mathrm{ATreg},\epsilon}$ the following way:

$$E_{\mathrm{ATreg},\epsilon,h}[u_R, u_T, v, \phi] := \frac{1}{2} \int_\Omega \left\{ (u_R - \mathcal{I}_h u_{R,0,\epsilon})^2 + (u_T - \mathcal{I}_h u_{T,0,\epsilon})^2 \right\} \mathrm{d}\mu$$

$$+ \frac{\mu}{2} \int_\Omega \left\{ (v^2 \circ \phi + k_\epsilon) \|\nabla u_R\|^2 + (v^2 + k_\epsilon) \|\nabla u_T\|^2 \right\} \mathrm{d}\mu$$

$$+ \frac{\nu}{2} \int_\Omega \left\{ \epsilon \|\nabla v\|^2 + \frac{1}{4\epsilon}(v-1)^2 \right\} \mathrm{d}\mu$$

where $k_\epsilon = o(\epsilon)$. $\mathcal{I}_h$ stands for the Lagrange interpolation on the usual linear Finite Element space. Moreover, $u_{R,0,\epsilon}$ and $u_{T,0,\epsilon}$ are chosen to be functions in $\mathscr{C}_0^\infty(\Omega)$ approximating $u_{R,0}$ and $u_{T,0}$, in the sense that $u_{R,0,\epsilon} \to u_{R,0}$ strongly in $L^2(\Omega)$, $\|u_{R,0,\epsilon}\|_{L^\infty(\Omega)} \leq \|u_{R,0}\|_{L^\infty(\Omega)}$ and, further, $\|\nabla u_{R,0,\epsilon}\|_{L^\infty(\Omega)} \leq \frac{C}{\epsilon}$ (this can be achieved for instance by mollification with a smooth kernel) and analogously for $u_{T,0,\epsilon}$.

### 5.5.3 First variation of the energy

Let us look at the first variation of the energy. We first calculate the partial variations with respect to the variables $u_R$, $u_T$ and $v$:

$$\langle \partial_{u_R} E_{\mathrm{ATreg},\epsilon,h}[u_R, u_T, v, \phi]; \vartheta \rangle = \int_\Omega (u_R - \mathcal{I}_h u_{R,0,\epsilon}) \cdot \vartheta \, \mathrm{d}\mu + \mu \int_\Omega (v^2 \circ \phi + k_\epsilon) \nabla u_R \cdot \nabla \vartheta \, \mathrm{d}\mu$$

$$\langle \partial_{u_T} E_{\mathrm{ATreg},\epsilon,h}[u_R, u_T, v, \phi]; \xi \rangle = \int_\Omega (u_T - \mathcal{I}_h u_{T,0,\epsilon}) \cdot \xi \, \mathrm{d}\mu + \mu \int_\Omega (v^2 + k_\epsilon) \nabla u_T \cdot \nabla \xi \, \mathrm{d}\mu$$

$$\langle \partial_v E_{\mathrm{ATreg},\epsilon,h}[u_R, u_T, v, \phi]; \zeta \rangle = \mu \int_\Omega \|\nabla u_T\|^2 v \cdot \zeta \, \mathrm{d}\mu + \mu \int_\Omega \|\nabla u_R\|^2 (v \circ \phi) \cdot (\zeta \circ \phi) \, \mathrm{d}\mu$$

$$+ \nu \int_\Omega \epsilon \nabla v \cdot \nabla \zeta \, \mathrm{d}\mu + \nu \int_\Omega \frac{1}{4\epsilon}(v-1)\zeta \, \mathrm{d}\mu \qquad (5.38)$$

for $\vartheta, \xi, \zeta \in H^{1,2}(\Omega)$. On account of the hyperelastic regularization $\phi$ is invertible. Thus we can rewrite (5.38) via the transformation formula.

$$\langle \partial_v E_{\mathrm{ATreg}}[u_R, u_T, v, \phi]; \zeta \rangle = \mu \int_\Omega \|\nabla u_T\|^2 v \cdot \zeta \, \mathrm{d}\mu + \mu \int_\Omega \|\nabla u_R\|^2 \circ \phi^{-1} v \cdot \zeta (\det D\phi)^{-1} \, \mathrm{d}\mu$$

$$+ \nu \int_\Omega \epsilon \nabla v \cdot \nabla \zeta \, \mathrm{d}\mu + \nu \int_\Omega \frac{1}{4\epsilon}(v-1)\zeta \, \mathrm{d}\mu . \qquad (5.39)$$

Hence, for fixed $v$ and $\phi$ the reconstructed images $u_R$ and $u_T$ can be computed by solving the following elliptic Helmholtz-problems:

$$u_R - \mu(v^2 \circ \phi + k_\epsilon)\Delta u_R = \mathcal{I}_h u_{R,0,\epsilon}, \quad u_T - \mu(v^2 + k_\epsilon)\Delta u_T = \mathcal{I}_h u_{T,0,\epsilon} \quad \text{in } \Omega,$$

$$\partial_\nu u_R = 0, \qquad\qquad\qquad \partial_\nu u_T = 0 \qquad\qquad \text{on } \partial\Omega. \qquad (5.40)$$

Since $v \geq 0$ the corresponding bilinear-forms are coercive. Furthermore, we are able to find for each $u_T$, $u_R$ and $\phi$ the optimal $v$ as the solution of the Euler-Lagrange equation with respect to the variation in the variable $v$, i. e.,

$$\mu\|\nabla u_T\|^2 v + \mu\|\nabla u_R\|^2 \circ \phi^{-1} v(\det D\phi^{-1}) + \frac{\nu}{4\epsilon}(v-1) - \nu\epsilon\Delta v = 0 \qquad \text{in } \Omega,$$

$$\partial_\nu v = 0 \qquad\qquad\qquad\qquad\qquad \text{on } \partial\Omega. \qquad (5.41)$$

For $\psi \in H_0^{1,2}(\Omega; \mathbb{R}^n)$ the variation of $E_{\mathrm{ATreg}}$ is given by

$$\langle \partial_\phi E_{\mathrm{ATreg},\epsilon,h}[u_R, u_T, v, \phi]; \psi \rangle = \mu \int_\Omega \|\nabla u_R\|^2 v \circ \phi \, (\nabla v \circ \phi \cdot \psi) \, \mathrm{d}\mu \qquad (5.42)$$

$$= \mu \int_\Omega \|\nabla u_R\|^2 \circ \phi^{-1} v \, (\nabla v \cdot \psi \circ \phi^{-1})(\det D\phi)^{-1} \, \mathrm{d}\mu.$$

### 5.5.4 Description of the algorithm

Again, we consider the Finite Element discretization, which has been described in Section 2.6. The energy is strictly convex, even quadratic in the variables $u_R$, $u_T$ and $v$, which renders the minimization feasible to a Finite Element approach. Analogously to the approach chosen in the sharp interface model, the energy functional can be reduced to depending only on $\phi$, where $u_R^\phi$, $u_T^\phi$ and $v^\phi$ are determined as the unique solutions to the minimization problem for fixed $\phi$:

$$\hat{E}_{\mathrm{ATreg},\epsilon}[\phi] = E_{\mathrm{ATreg},\epsilon}[u_R^\phi, u_T^\phi, v^\phi, \phi]. \tag{5.43}$$

**Multiscale**

We have underlined the importance of a multiscale strategy in Chapter 2. Due to the smoothing of the data, the variation of the energy which results also in the derivation of the input images is significantly more regular. Data is almost always corrupted by some kind of noise. In the derivation this noise is then even amplified further, and hence the gradient would be very irregular, which would limit the step size to be very small. On the other hand, the smoothing of the data introduces globality into the energy formulation, in the sense that the search directions force the deformation towards the stationary point even in regions, where locally the original images match up already.

Due to (5.42) the $L^2$ representation of the partial derivative of $\hat{E}_{\mathrm{ATreg},\epsilon}$ is given by

$$\mathrm{grad}\hat{E}_{\mathrm{ATreg},\epsilon}[\phi] = \|\nabla u_R^\phi\|^2 \circ \phi^{-1} v_\epsilon^\phi (\det D\phi)^{-1} \nabla v. \tag{5.44}$$

Therefore, the smoothness of $\mathrm{grad}E_{\mathrm{ATreg},\epsilon}[\phi]$ is controlled by the smoothness of $\phi^{-1}$, $u_R$ and $v$. On the other hand, the smoothness of $v$ is steered directly by $\epsilon$ on account of the penalty term $\epsilon\|\nabla v\|^2$ in (5.33). Let us now address the smoothness of $u_R$. For larger values of $\epsilon$ the single-well potential in becomes less significant (5.33) and the smoothness term dominates, while for a small $\epsilon$, $v$ is close to $0$ where $\|\nabla u_R\|^2 \circ \phi^{-1}$ or $\|\nabla u_T\|^2$ are large and $v$ is forced to be close to $1$ in the rest of the domain on account of the single well potential. We summarize:

> *The phase field framework comes along with a canonical multiscale strategy, which is controlled by the approximation parameter $\epsilon$. Larger values yield coarse and smooth approximations of the characteristic function $\chi_{S_T}$ and $\chi_{S_R}$.*

Similarly to the multiscale algorithm in Chapter 2, one starts with coarse approximations, to find a stationary point in the simplified energy landscape, iteratively reduces the approximation parameter $\epsilon$ by taking the solution of the previous scale as the new initial guess on the finer scale.

**Regularized gradient flow**

For small values of $\epsilon$, the discrete descent direction may still be perturbed, even though $v$ is smooth. This is due to the approximation property of the finite element space which depends on the $H^{1,2}(\Omega)$ norm. It becomes large in magnitude, once the gradient of $v$ get steep. In practice, the regularization of the gradient flow by a regularizing metric as in Chapter 2 is again significant for a stable descent. In particular, we consider again the metric $g^\sigma$ from (2.5), hence the regularized descent direction $d_g$ becomes

$$d_g[\phi] = -\mathrm{grad}_{g^\sigma}\hat{E}_{\mathrm{ATreg},\epsilon}[\phi] - \alpha\mathrm{grad}_{g^\sigma}E_{\mathrm{reg}}[\phi]. \tag{5.45}$$

Under these considerations, we will now summarize the overall algorithm:

**Algorithm: Phase field Mumford-Shah registration**

The algorithm consists of the following steps.

**Step 0** Choose initial $v$, choose initial deformation $\phi_0$, choose initial $\epsilon > 0$, finest scale $\epsilon_{\mathrm{tol}} = o(h)$.

**Step 1** Compute $u_T$, $u_R$ and $v$ for fixed $\phi$

> **Step 1.1** Solve the elliptic equation in (5.40) for $u_T$.
>
> **Step 1.2** Solve the elliptic equation in (5.40) for $u_R$.
>
> **Step 1.3** Solve the elliptic equation (5.41) for $v$.

**Step 2** Compute the descent direction $d_g$ by (5.45).

**Step 3** Perform an update $\phi \leftarrow \phi + \tau d_g$, where $\tau$ is chosen according to a line-search strategy.

**Step 4** If $\phi$ is not a stationary point, go to Step 1.

**Step 5** If $\epsilon \geq \epsilon_{\mathrm{tol}}$ then geometrically decrease $\epsilon$ and go to Step 1.

The equations in Step 1 as well as the regularization of the descent direction can be solved efficiently by a multigrid method, and here we don't rely on the Composite Finite Element discretization of the sharp interface approach. Due to the smooth transitions of $v$ in the phase-field approach, one is not faced with the numerical problem of solving a PDE with jumping coefficients. However, this holds only true for $\epsilon$ sufficiently large, i. e., the order of the discretization parameter $h$. Otherwise the transition zone cannot be resolved by a Finite Element function. Although again in every time step of the iteration with respect to $\phi$, several PDE's have to be solved until the Jacobi-iteration of Step 1 converges, the algorithm is not slowed down drastically.

### 5.5.5   Results and discussion

In Figure 5.6, we show the result of a registration of a CT and a MR image of a human spine vertebra, computed using the approach described above.

Even though the images reveal very complex structures, the registration could be performed without any pre-registration – no feature extraction was necessary. As can be seen in the overlay of the registered image with the reference, the structures are well aligned onto each other. The method tries to map regions with almost constant intensities, onto their counterparts in the other image.

In contrast to the sharp interface model where an initial guess for the contour $\Gamma$ has to be chosen, the dependence of this model on the initial function $v$ is moderate, and it allows the registration of the entire discontinuity set. By varying the parameter $\epsilon$, a natural multiscale approach can be employed by first starting with a smooth representation of $v$ and henceforth letting $\epsilon \to 0$ to eventually sharpen the edge function in order to match the edges precisely. Since $v$ has to be represented by a Finite Element function, $\epsilon$ has to remain away from $0$ to avoid numerical difficulties. However, $\epsilon$ can be chosen around $h$ [31, 30], and it is more than questionable if a further decrease of $\epsilon$ would further improve the results. We have obtained very promising results and the framework is applicable to a wider class of problems.

$u_R$ reference                  $u_T$ template                  $u_T \circ \phi$ result
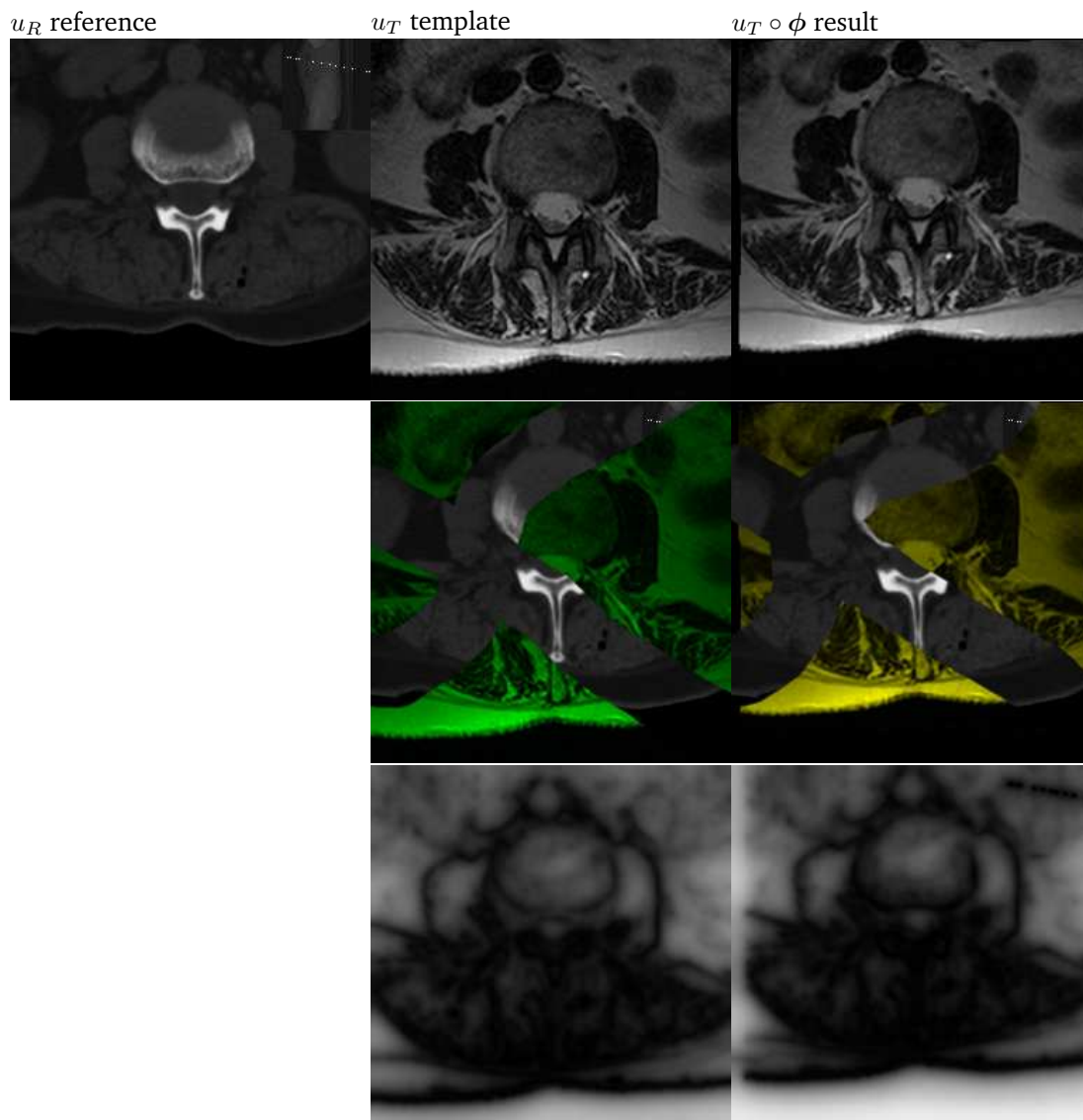


Figure 5.6: *Image registration by the phase field Mumford-Shah approach of CT and MR slices of a human vertebra. The variational formulation aims at finding a signature function $v$ and a deformation $\phi$, such that $v$ describes the edges in the image $u_T$ while $v \circ \phi$ describes the edges in the image $u_R$.* TOP ROW: *Reference image $u_{R,0}$, template image $u_{T,0}$, matched template $u_{T,0} \circ \phi$.* MIDDLE ROW: *The left image shows the initial misfit by overlaying $u_{R,0}$ and $u_{T,0}$ (green), while the image in the right shows the alignment of $u_{T,0} \circ \phi$ (yellow) in comparison with $u_{R,0}$. The initial and final versions of the combined signature function $v$ is shown in the* BOTTOM ROW.

# Chapter 6

# Willmore flow on level sets and graph surfaces

GEOMETRIC methods in image processing are almost always based on the shapes of the the level lines of the intensity function. As discussed in the introduction, the geometric content of an image may be analyzed by considering the union of all submanifolds given as level sets, i. e., to analyze the morphology.

In this chapter we will present a framework, which is based on the following viewpoint: From the geometric functionals defined on the geometric representation of the level sets, we will consider an aggregation by integrating over all level sets, which will yield a functional on the entire morphology. By definition of a suitable metric on the space of level set functions, we will be able to yield the gradient flow of these aggregated energies and obtain directly a weak formulation of the level set flow. It turns out that the variation of the aggregated energies is more convenient than the variation of the differential geometric functionals on the level sets itself.

The geometric viewpoint gives rise to an important prerequisite: level lines, which are initially nested ought to stay nested during the evolution. Otherwise the reconstruction of the new intensity function, treating the motion of the level lines independently is impossible. Similarly, a parabolic level set equation would become ill-posed. In the case of second order methods, the maximum principle gives a positive answer to the nestedness condition, and gives rise to the notion of viscosity solutions [173, 112].

The treatment of fourth order methods is more subtle. Due to the lack of the maximum principle, the framework of viscosity solutions may not be employed, and to the best of our knowledge, the question of a suitable notion of a solution is still open [9, 15] Indeed, fourth order flows may cease to be embedded after arbitrary short times for certain initial configurations. In the case of Willmore flow, which will be described in more details in the subsequent exposition, MAYER & SIMONETT have shown in [151], that self-intersections may occur after short times. The same is true for surface diffusion flow, as well as the volume preserving mean curvature flow [150].

However, in the subsequent considerations, we will establish the relation between regularized level set formulations and the differential geometric evolution of scaled graphs. Existence and uniqueness of the evolution of these graphs can be analyzed by known differential geometric results.

## 6.1 Motivation: continuation of level lines

### 6.1.1 Image and surface inpainting

The problem of image inpainting (also referred to as disocclusion) refers to the reconstruction of hidden domains by taking into account information from the surrounding border.

In the early work [45] CASELLES, MOREL AND SBERT have introduced the absolute minimal Lipschitz extension model (AMLE) derived from fundamental derivation axioms, like translation invariance, rotation invariance, comparison principle, stability and regularity. MASNOU & MOREL [148] have proposed a variational approach based on the geometry on the level lines, by taking into account geometric quantities as length and curvature. This model of *Euler's elastica* has been formulated by treating the level lines parametrically. Later, BERTALMIO, BERTOZZI AND SAPIRO have applied models borrowed from fluid dynamics to inpainting problems [25].

Level set methods allow to evolve all level lines simultaneously, which has been exploited for example by BALLESTER ET. AL. who have coupled the interpolation of normal field to the interpolation of the level lines in [15] or CHAN & SHEN who formulated a level set approach for the Euler's elastica model [52, 49]. However they used a finite difference upwind scheme for the discretization of the resulting fourth order flow. ESEDOGLU & SHEN [109] have combined the Mumford-Shah functional with fourth order inpainting techniques, using a conjecture of De Giorgi to approximate the geometric flow that minimizes the Willmore Euler's elastica energy by a fourth order phase field model. Many of those approaches have in common that they, at least partially, minimize the Willmore energy

$$e[\mathcal{M}] = \frac{1}{2} \int_{\mathcal{M}} h^2 \, \mathrm{d}A.$$

For parameterized surfaces the Willmore energy has been used by CLARENZ, DIEWALD, DZIUK, RUSU & RUMPF for the inpainting of surfaces holes [68]. In [103] we have derived a semi-implicit Finite Element scheme to solve the corresponding fourth order gradient flow in the level set context. Furthermore we refer to [26, 199, 17] for related approaches on inpainting. In addition to inpainting problems, fourth order evolution equations, in combination with locally estimated anisotropies, have also become important in feature-preserving smoothing of surfaces (cf. the work of TASDIZEN ET AL. [191]).

## 6.2   A level set formulation for the Willmore flow

In the following, we will apply the framework of Section 2.2 to define the aggregated Willmore energy on $\mathscr{L}$ (the space of level set ensembles) and to compute its first variation. As described above, the integrand of the Euler's elastica is given by $\alpha + \beta h^2$, since the area functional weighted by $\alpha$ and its gradient flow is well known, the Willmore energy and its corresponding gradient flow allows the incorporation of the full functional.

It is known [207] that the $L^2$ gradient flow for parametric formulations is given by

$$\partial_t x + \Delta_{\mathcal{M}} h(t) + h(t)\Big(\|S(t)\|_2^2 - \frac{1}{2}h(t)\Big)n = 0 \tag{6.1}$$

We will focus on devising a level set formulation. Let us give a short review about theoretical results for the existence of a regular solution of the Willmore flow. For the evolution of closed manifolds under Willmore flow, SIMONETT has shown in [187], that a unique local solution of the Willmore flow exists under the assumption that the initial surface $\mathcal{M}_0$ is a immersed closed compact manifold of regularity $\mathscr{C}^{2,\alpha}$. If the initial surface is sufficiently close to a sphere, a global solution exists. More precisely SIMONETT & MAYER have shown the following existence result

**Theorem 6.2.1.** *For $0 < \alpha < 1$ fixed, there exists a closed embedded surface $\tilde{\mathcal{M}}_0 \in \mathscr{C}^{2,\alpha}$, a constant $u_T$, $0 < t_0 < t_1 \leq T$, and a $\mathscr{C}^{2,\alpha}$ neighborhood $U$ of $\tilde{\mathcal{M}}_0$, such that*

  (i) *there exists a unique classical solution $(\mathcal{M}(t))_{t \geq 0}$ for all $\mathcal{M}_0 \in U$.*

  (ii) *$\mathcal{M}(t)$ is no longer embedded for $t_1 < t < t_2$ and every initial surface $\mathcal{M}_0 \in U$.*

 (iii) *Moreover, each $\mathcal{M}(t)$ is of class $\mathscr{C}^\infty$ for $t \in (0, T]$ and smooth up to $T$.*
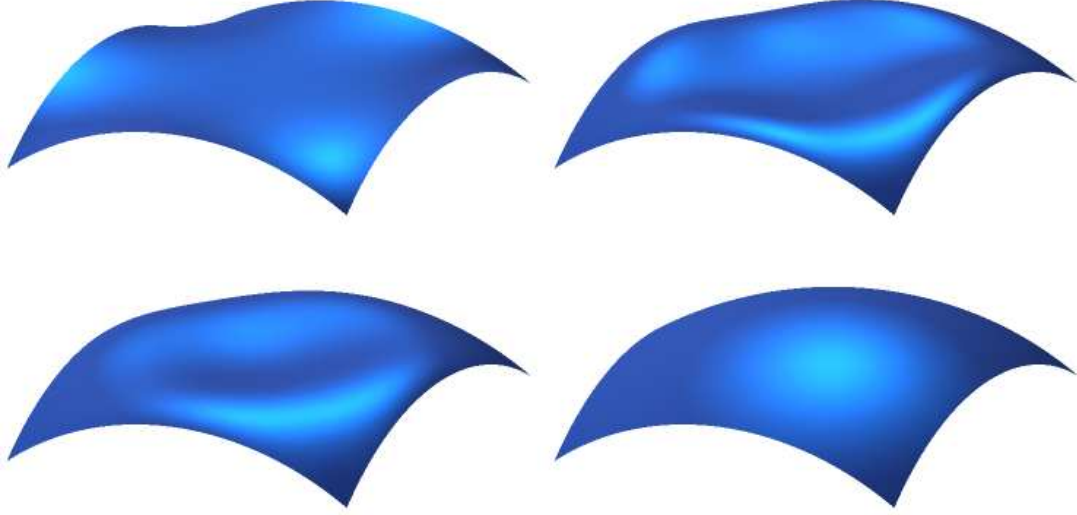
Figure 6.1: *Given an initial graph (left) Willmore flow with prescribed Dirichlet boundary conditions for the position and the normal is applied. Different timesteps of the evolution (from left to right) are displayed. The boundary condition corresponds to a spherical cap over the graph domain which is reflected by the limit surface (right) for $t \to \infty$.*

As a consequence, not all initial configurations may be treated by the level set approach, which is by construction restricted to embedded surfaces. This is also reflected by the work of AMBROSIO & MASNOU [9], who have shown that the level set formulation of the Euler's elastica functional is not lower semicontinuous.

The MAYER&SIMONETT have also shown in [151] that the Willmore energy is non-increasing in the interval of existence, provided that the initial surface is of the class $\mathscr{C}^{2,\alpha}$.

We also refer to the works of KUWERT & SCHÄTZLE [138, 139, 140] who have shown existence of a global solution under the assumption that the Willmore energy of the initial configuration is sufficiently small, in particular $e[\mathcal{M}_0] \leq 16\pi$.

By taking into account (6.1) the corresponding level set formulation is given by

$$\partial_t \phi + \Delta_{\mathcal{M}} h(t) + h(t)\left(\|S(t)\|_2^2 - \frac{1}{2}h(t)\right)\|\nabla\phi\| = 0. \tag{6.2}$$

In Chapter 7 we will propose a narrow band approach to the numerical solution of geometric PDE's of higher order, spatially centered around a particular level set surface $\mathcal{M}_0$. Hence the existence properties are expected to be similar to the existence of the evolution of $\mathcal{M}_0$ under parametric Willmore flow.

### 6.2.1 The metric point of view

In order to obtain the aggregation of the gradient flow $\partial_t x = -\mathrm{grad}_{L^2(\mathcal{M})} e[\mathcal{M}]$ on the independent manifolds, we first apply the co area formula to define

$$E[\phi] = \int_\Omega h^2 \|\nabla\phi\| \, \mathrm{d}\mu \tag{6.3}$$

and again consider the aggregated flow $\partial_t \phi = -\mathrm{grad}_{g_\phi} E[\phi]$ on $\mathscr{L}$.

Further, recall the metric defined on level sets of Section 2.2.2:

$$g_\phi(s_1, s_2) \;=\; \int_\Omega \frac{s_1}{\|\nabla\phi\|} \frac{s_2}{\|\nabla\phi\|} \|\nabla\phi\| \, \mathrm{d}\mu = \int_\Omega s_1 s_2 \, \|\nabla\phi\|^{-1} \, \mathrm{d}\mu \, .$$

**Theorem 6.2.2.** *The first variation of the aggregated Willmore functional* (6.3) *is given by*

$$\langle E'[\phi]; \vartheta \rangle = \int_\Omega \frac{1}{2} h^2 \frac{\nabla \phi}{\|\nabla \phi\|} \cdot \nabla \vartheta - \|\nabla \phi\|^{-1} P \nabla(\|\nabla \phi\| \, h) \cdot \nabla \vartheta \, \mathrm{d}\mu \tag{6.4}$$

*for all* $\forall \vartheta \in C_0^\infty(\Omega)$. *Here,* $P := P[\phi]$ *denotes the projection onto the tangent space defined in Eq.* (1.11).

*Proof.* Let us first recall the variation of the normal from (1.13):

$$\frac{d}{d\epsilon} \frac{v + \epsilon w}{\|v + \epsilon w\|} \bigg|_{\epsilon=0} = \left( \mathbb{1} - \frac{v \otimes v}{\|v\|^2} \right) w.$$

Now we can calculate

$$
\begin{aligned}
\frac{d}{d\epsilon} E[\phi + \epsilon \vartheta] \bigg|_{\epsilon=0} &= \frac{d}{d\epsilon} \frac{1}{2} \int_\Omega \|\nabla(\phi + \epsilon \vartheta)\| \left( \mathrm{div} \left[ \frac{\nabla(\phi + \epsilon \vartheta)}{\|\nabla(\phi + \epsilon \vartheta)\|} \right] \right)^2 \mathrm{d}\mu \bigg|_{\epsilon=0} \\
&= \int_\Omega \frac{1}{2} h^2 \frac{\nabla \phi}{\|\nabla \phi\|} \cdot \nabla \vartheta + \|\nabla \phi\| \, h \, \mathrm{div} \left( \frac{d}{d\epsilon} \left[ \frac{\nabla(\phi + \epsilon \vartheta)}{\|\nabla(\phi + \epsilon \vartheta)\|} \right] \bigg|_{\epsilon=0} \right) \mathrm{d}\mu \\
&= \int_\Omega \frac{1}{2} h^2 \frac{\nabla \phi}{\|\nabla \phi\|} \cdot \nabla \vartheta + \|\nabla \phi\| \, h \, \mathrm{div} \left[ \|\nabla \phi\|^{-1} P \nabla \vartheta \right] \mathrm{d}\mu \\
&= \int_\Omega \frac{1}{2} h^2 \frac{\nabla \phi}{\|\nabla \phi\|} \cdot \nabla \vartheta - \|\nabla \phi\|^{-1} P \nabla(\|\nabla \phi\| \, h) \cdot \nabla \vartheta \, \mathrm{d}\mu
\end{aligned}
$$

which is the desired result. □

By taking into account the metric $g_\phi$ of the manifold of level set ensembles, we obtain

$$\int_\Omega \frac{\partial_t \phi \, \vartheta}{\|\nabla \phi\|} \mathrm{d}\mu = \int_\Omega -\frac{1}{2} h^2 \frac{\nabla \phi}{\|\nabla \phi\|} \cdot \nabla \vartheta + \|\nabla \phi\|^{-1} P \nabla(\|\nabla \phi\| \, h) \cdot \nabla \vartheta \, \mathrm{d}\mu. \tag{6.5}$$

Hence, by integration by parts we obtain the following strong formulation of the Willmore flow in level set form.

$$\partial_t \phi + \mathrm{div} \left( \frac{1}{2} h^2 \frac{\nabla \phi}{\|\nabla \phi\|} - \|\nabla \phi\|^{-1} P \nabla(\|\nabla \phi\| \, h) \right) \|\nabla \phi\| = 0 \tag{6.6}$$

This equation is of fourth order, and is thus not implementable in a straightforward manner with first order Finite Elements. A common approach is to reformulate the fourth order equation into two equations of second order. Previously, in the parametric case RUSU devised a mixed formulation with piecewise affine Finite Elements [181] This gives rise to the question of finding a suitable second variable, which is substituted into the weak formulation and subject to a second possibly geometric equation. An obvious first choice would be the mean curvature $h$, however the last term in (6.4) suggests that the curvature concentration

$$w := -\|\nabla \phi\| \, h$$

is the natural dependent quantity. The variable $w$ is determined by the weak formulation

$$\int_\Omega \|\nabla \phi\|^{-1} w \, \psi \, \mathrm{d}\mu = \int_\Omega \frac{\nabla \phi}{\|\nabla \phi\|} \cdot \nabla \psi \, \mathrm{d}\mu$$

for all $\psi \in \mathscr{C}_0^\infty(\Omega)$. Now, substituting the terms $-\|\nabla \phi\| \, h$ by $w$ we end up with the following coupled problem:

**Problem 6.2.3 (Weak coupled Willmore flow formulation).** *Given an initial function $\phi_0$ on $\Omega$ find a pair of functions $(\phi, w)$ with $\phi(0) = \phi_0$, such that*

$$\int_\Omega \frac{\partial_t \phi}{\|\nabla \phi\|} \vartheta \, \mathrm{d}\mu = \int_\Omega -\frac{1}{2} \frac{w^2}{\|\nabla \phi\|^3} \nabla \phi \cdot \nabla \vartheta - \|\nabla \phi\|^{-1} P \nabla w \cdot \nabla \vartheta \, \mathrm{d}\mu, \tag{6.7}$$

$$\int_\Omega \|\nabla \phi\|^{-1} w \, \psi \, \mathrm{d}\mu = \int_\Omega \frac{\nabla \phi}{\|\nabla \phi\|} \cdot \nabla \psi \, \mathrm{d}\mu \tag{6.8}$$

*for all $t > 0$ and all functions $\vartheta, \psi \in \mathscr{C}_0^\infty(\Omega)$.*

For this level set formulation, one can deduce the decrease of the Willmore energy in same fashion as in the graph case. We follow [89]. Differentiating the second equation in Problem 6.2.3 yields

$$
\begin{aligned}
0 &= \int_\Omega \left( \frac{\partial_t w\,\psi + w\,\partial_t\psi - \nabla\phi_t\cdot\nabla\psi + \nabla\phi\cdot\nabla\partial_t\psi}{\|\nabla\phi\|} - \frac{(w\,\psi - \nabla\phi\cdot\nabla\psi)\frac{\nabla\phi}{\|\nabla\phi\|}\cdot\nabla\phi_t}{\|\nabla\phi\|^2} \right) \mathrm{d}\mu \\
&= \int_\Omega \left( \frac{\partial_t w\,\psi}{\|\nabla\phi\|} - \frac{w\psi\frac{\nabla\phi}{\|\nabla\phi\|}\cdot\nabla\phi_t}{\|\nabla\phi\|^2} - P[\phi]\nabla\phi_t\cdot\nabla\psi \right) \mathrm{d}\mu.
\end{aligned}
\tag{6.9}
$$

After testing (6.9) with $w$, the first equation of 6.2.3 with $\phi_t$, and adding the results one obtains

$$
0 = \int_\Omega \left( \frac{\phi_t^2}{\|\nabla\phi\|} - \frac{1}{2}\frac{w^2\frac{\nabla\phi}{\|\nabla\phi\|}\cdot\nabla\phi_t}{\|\nabla\phi\|^2} + \frac{w\,w_t}{\|\nabla\phi\|} \right) \mathrm{d}\mu = \int_\Omega \frac{\phi_t^2}{\|\nabla\phi\|}\,\mathrm{d}\mu + \frac{1}{2}\frac{\mathrm{d}}{\mathrm{d}t}\int_\Omega h^2\,\mathrm{d}\mu.
$$

### 6.2.2 Derivation from the classical formula

Instead of deriving the level set formulation for Willmore flow from the metric point of view described above, it is alternatively possible to consider the classical parametric gradient flow formulation and to translate it appropriately into the according weak level set formulation. In order to underline that the gradient flow approach is more intuitive, we will proceed by considering the classical formula.

First, we multiply (6.2) with a test function $\vartheta\,\|\nabla\phi(t)\|^{-1}$ for arbitrary $\vartheta \in \mathscr{C}^\infty(\Omega)$. After integrating over $\Omega$ we obtain

$$
\int_\Omega \frac{\partial_t\phi(t)}{\|\nabla\phi(t)\|}\vartheta + \Delta_{\mathcal{M}}h(t)\vartheta + h(t)\left( \|S(t)\|_2^2 - \frac{1}{2}h(t)^2 \right)\vartheta\,\mathrm{d}\mu = 0
$$

for all $\vartheta \in \mathscr{C}^\infty(\Omega)$. At first, we note that $\|S(t)\|^2 = Dn^T : Dn$ and $h = \operatorname{div} n$ [103]. Thus, applying (1.12) we obtain

$$
\begin{aligned}
\int_\Omega \Delta_{\mathcal{M}}h\vartheta\,\mathrm{d}\mu &= \int_\Omega \Delta h\vartheta - h\nabla h\cdot n\vartheta - (D^2 hn\cdot n)\vartheta\,\mathrm{d}\mu \\
&= -\int_\Omega \nabla h\cdot\nabla\vartheta - h\nabla h\cdot n\vartheta - (D^2 hn\cdot n)\vartheta\,\mathrm{d}\mu \\
&= -\int_\Omega \nabla h\cdot\nabla\vartheta - h\nabla h\cdot n\vartheta - \nabla(\nabla h\cdot n)n\vartheta + \nabla h\cdot(Dn\,n)\vartheta\,\mathrm{d}\mu \\
&= -\int_\Omega \nabla h\cdot\nabla\vartheta - h\nabla h\cdot n\vartheta + h\nabla h\cdot n\vartheta + (n\otimes n)\nabla h\cdot\nabla\vartheta + \nabla h\cdot(Dn\,n)\vartheta\,\mathrm{d}\mu \\
&= \int_\Omega -P\nabla h\cdot\nabla\vartheta + \nabla h\cdot(Dn\,n)\,\mathrm{d}\mu.
\end{aligned}
$$

Furthermore, we use the formula

$$
\int_\Omega \nabla v : \nabla w\,\mathrm{d}\mu = -\int_\Omega v\cdot\mathbf{div}w\,\mathrm{d}\mu
$$

and $\mathbf{div}(\nabla v) = \nabla\operatorname{div}(v)$, where $\mathbf{div}$ is the divergence of matrix valued functions, to compute

$$
\begin{aligned}
\int_\Omega h\|S\|^2\vartheta\,\mathrm{d}\mu &= \int_\Omega hDn : Dn\,\mathrm{d}\mu \\
&= -\int_\Omega \left( n\cdot\mathbf{div}(Dn\,h\vartheta) \right)\mathrm{d}\mu \\
&= -\int_\Omega \left( (n\cdot\mathbf{div}(Dn))h\vartheta + (n\cdot Dn\,\nabla h)\vartheta + (n\cdot Dn\,\nabla\vartheta)h \right)\mathrm{d}\mu \\
&= -\int_\Omega \left( h\nabla h\cdot n\vartheta + (n\cdot Dn\,\nabla h)\vartheta + (n\cdot Dn\,\nabla\vartheta)h \right)\mathrm{d}\mu.
\end{aligned}
$$

Moreover, we obtain

$$
\begin{aligned}
-\frac{1}{2}\int_\Omega h h^2 \vartheta \, \mathrm{d}\mu &= -\frac{1}{2}\int_\Omega \operatorname{div}(n) h^2 \vartheta \, \mathrm{d}\mu \\
&= \frac{1}{2}\int_\Omega \nabla(h^2)\cdot n\vartheta + h^2 n\cdot\nabla\vartheta \, \mathrm{d}\mu.
\end{aligned}
$$

By collecting all these terms and taking into account the relation

$$
Dn\cdot n = \frac{1}{\|\nabla\phi\|}PD^2\phi n = \frac{1}{\|\nabla\phi\|}P\nabla\|\nabla\phi\|
$$

we end up with

$$
\begin{aligned}
\int_\Omega \left(\Delta_{\mathcal{M}}h + h(\|S\|^2 - \tfrac{1}{2}h^2)\right)\vartheta \, \mathrm{d}\mu &= \int_\Omega \left( -P\nabla h\nabla\vartheta - (n\cdot(Dn\,\nabla\vartheta))h + \tfrac{1}{2}h^2 n\cdot\nabla\vartheta \right)\mathrm{d}\mu \\
&= \left( -P\nabla h\nabla\vartheta - \frac{h}{\|\nabla\phi\|}\cdot\nabla\vartheta + \tfrac{1}{2}h^2 n\cdot\nabla\vartheta \right)\mathrm{d}\mu \\
= \int_\Omega \left( -P\nabla(\|\nabla\phi\|h)\cdot\nabla\vartheta\|\nabla\phi\|^{-1} \right. &+ \left. \tfrac{1}{2}\|\nabla\phi\|^{-3}(\|\nabla\phi\|h^2)\nabla\phi\cdot\nabla\vartheta \right)\mathrm{d}\mu
\end{aligned}
$$

which is the weak formulation we have derived in the previous section. Hence, we have verified that the aggregated gradient flow perspective yields the same evolution problem as integrating the gradient of the parametric Willmore energy in a straightforward manner.

## 6.3 A level set formulation for surface diffusion

Since, to our knowledge, surface diffusion has no important applications in image processing we refer to [188, 38, 21, 22, 20] and only briefly describe how surface diffusion fits into the above framework. One of its main application is in the modeling of epitaxial growth of crystals [18, 194, 193].

It is well known, that surface diffusion is the gradient flow of the area functional with respect to the $H^{-1}$-metric, which is given by

$$
(v_1, v_2)_{-1,\mathcal{M}} := -\int_{\mathcal{M}} (\Delta_{\mathcal{M}}^{-1} v_1)\cdot v_2 \, \mathrm{d}A
$$

By integrating over all level sets, one obtains the aggregated metric

$$
g_{-1,\mathscr{L}}(s_1, s_2) = -\int_\Omega \frac{(\Delta_{\mathscr{M}}^{-1} s_1)\, s_2}{\|\nabla\phi\|^2}\|\nabla\phi\| \, \mathrm{d}\mu = -\int_\Omega \frac{(\Delta_{\mathscr{M}}^{-1} s_1)\, s_2}{\|\nabla\phi\|} \, \mathrm{d}\mu.
$$

By the Ansatz,

$$
g_{-1,\mathscr{L}}(\partial_t\phi, \vartheta) = -\int_\Omega \frac{\nabla\phi\cdot\nabla\vartheta}{\|\nabla\phi\|} \, \mathrm{d}\mu \qquad \forall\,\vartheta\in\mathscr{C}_0^\infty(\Omega)
$$

one ends up with the

**Problem 6.3.1 (Weak formulation for surface diffusion in level set form).** *For an initial function $\phi_0 \in H^{1,2}(\Omega)$, find a pair of functions $\phi \in L^2(H^{1,2}(\Omega))$ and $w \in L^2(H^{1,2}(\Omega))$, such that for all $t \in \mathbb{R}^+$*

$$
\begin{aligned}
\int_\Omega \frac{\partial_t\phi\vartheta}{\mathrm{d}\mu} + \int_\Omega P[\phi]\nabla w\cdot\nabla\vartheta\|\nabla\phi\| \, \mathrm{d}\mu &= 0 \qquad \forall\,\vartheta\in H_0^{1,2}(\Omega), \\
\int_\Omega w\,\psi \, \mathrm{d}\mu + \int_\Omega \frac{\nabla\phi\cdot\nabla\psi}{\|\nabla\phi\|} \, \mathrm{d}\mu &= 0 \qquad \forall\,\psi\in H_0^{1,2}(\Omega).
\end{aligned}
$$

## 6.4 Regularization

We observe that the evolution problem (6.7), (6.8) reveals terms of the form $\|\nabla\phi\|^{-1}$. It is somewhat expectable that the evolution equation degenerates when the gradient $\|\nabla\phi\|$ of the level set function vanishes. The derivation of the Willmore flow was made under the assumption that the level sets of $\phi$ are manifolds, however, if the level set function is flat in some regions, one can no longer speak of the notion of a hypersurface. These singularities will also cause numerical difficulties, since the speed of evolution becomes arbitrary large, which will be reflected in a high condition number of the coupled system. In practical computations small gradients cannot always be avoided. The Willmore flow is not the only evolution problem, where degenerate gradients cause numerical difficulties. Let us reconsider the weak formulation of the mean curvature flow equation

$$\int_\Omega \frac{\partial_t \phi \vartheta}{\|\nabla\phi\|} \, \mathrm{d}\mu = -\int_\Omega \frac{\nabla\phi}{\|\nabla\phi\|} \cdot \nabla\vartheta \, \mathrm{d}\mu\,.$$

where $\|\nabla\phi\|$ appears in the denominator on both sides of the equation. A common approach is to regularize the Euclidian norm and to define

$$\|v\|_\epsilon := \sqrt{\|v\|^2 + \epsilon},\tag{6.10}$$

and accordingly the regularized evolution equation becomes

$$\int_\Omega \frac{\partial_t \phi \vartheta}{\|\nabla\phi\|_\epsilon} \, \mathrm{d}\mu = -\int_\Omega \frac{\nabla\phi}{\|\nabla\phi\|_\epsilon} \cdot \nabla\vartheta \, \mathrm{d}\mu\,.\tag{6.11}$$

For $\epsilon > 0$ the denominator is bounded away from zero, and hence the elliptic part of the equation remains coercive. This equation has been studied in detail by EVANS & SPRUCK [112], furthermore DECKELNICK & DZIUK have derived a detailed numerical analysis of the corresponding Finite Element scheme [87].

However, it is interesting to observe, that the regularized problem can be interpreted as the evolution of the mean curvature flow equation of a graph which is scaled by $\epsilon^{-1}$. Let us first fix some

**Notation 6.4.1.** *For a given $\phi \in \mathscr{C}^2(\Omega)$ and $\epsilon > 0$ we denote by $\mathcal{G}_\epsilon[\phi] := \left\{(x,\, \epsilon^{-1}\phi(x)) \,:\, x \in \Omega\right\}$ the graph of $\phi$.*

**Notation 6.4.2.** *Let $\epsilon > 0$, in analogy to the level set case we define*

$$P_{\mathcal{G}_\epsilon[\phi]} := \mathbb{1} - \frac{\nabla\phi}{\sqrt{\epsilon^2 + \|\nabla\phi\|^2}} \otimes \frac{\nabla\phi}{\sqrt{\epsilon^2 + \|\nabla\phi\|^2}}.$$

*To avoid confusion, note that $P_{\mathcal{G}_\epsilon[\phi]}$ is not a projection, since $P_{\mathcal{G}[\phi]}v \cdot v \geq \frac{1}{\epsilon^2 + \|\nabla\phi\|^2}\|v\|^2$.*

The upward oriented normal on the graph $\mathcal{G}_\epsilon$ is given by $n^\epsilon := \left\|(-\nabla\phi, \epsilon)^T\right\|^{-1}(-\nabla\phi, \epsilon)^T$. Let us now determine the normal velocities $v^\epsilon$ of the evolving graph in dependence of the normal velocity $v$ of the level set function. This velocity $v^\epsilon$ in normal direction $n^\epsilon$ of the graph corresponds to a velocity $v$ of the corresponding level set in direction of the level set normal $n$. The normal velocity $V^\epsilon$ is given by

$$V^\epsilon = v^\epsilon n^\epsilon = ((vn) \cdot n^\epsilon) n^\epsilon = v\left(\frac{(-\nabla\phi, 1)}{\|(-\nabla\phi, 1)\|} \cdot \frac{(\nabla\phi, 0)}{\|(\nabla\phi)\|}\right) n^\epsilon = -v\frac{\|\nabla\phi\|}{\|\nabla\phi\|_\epsilon}n^\epsilon.$$

and hence, we obtain

$$v^\epsilon = -v\frac{\|\nabla\phi\|}{\|\nabla\phi\|_\epsilon}\,.\tag{6.12}$$

Now let us define the metric of tangent vectors of $\mathscr{L}$ by pulling back the corresponding scalar normal velocities of the scaled graph:

$$
\begin{aligned}
g_{\phi,\epsilon}(s_1, s_2) &= \int_{\mathcal{G}^\epsilon} v_1^\epsilon v_2^\epsilon \,\mathrm{d}A = \int_\Omega \sqrt{1 + \epsilon^{-2} \|\nabla \phi\|^2} \, v_1^\epsilon \, v_2^\epsilon \,\mathrm{d}\mu \\
&= \int_\Omega \frac{\|\nabla \phi\|_\epsilon}{\epsilon} \, v_1 \, v_2 \, \frac{\|\nabla \phi\|^2}{\|\nabla \phi\|_\epsilon^2} \,\mathrm{d}\mu = \frac{1}{\epsilon} \int_\Omega \frac{s_1 \, s_2}{\|\nabla \phi\|_\epsilon} \,\mathrm{d}\mu \,.
\end{aligned}
$$

We are now in the position to define the energies on graph surfaces.

### Regularized mean curvature flow

We consider again the area functional, which now measures the area of the scaled graph.

$$
e[\phi] := e[\mathcal{G}_\epsilon] = \int_{\mathcal{G}_\epsilon} \mathrm{d}A = \int_\Omega \sqrt{\det g} \,\mathrm{d}\mu = \int_\Omega \sqrt{1 + \epsilon^{-2}\|\nabla\phi\|^2} \,\mathrm{d}\mu.
$$

The first variation of $e[\mathcal{G}_\epsilon]$ is given by

$$
\begin{aligned}
\langle e'[\phi]; \vartheta \rangle &= \left. \frac{d}{d\delta} e[\phi + \delta\vartheta] \right|_{\delta=0} \\
&= \int_\Omega \frac{\epsilon^{-2} \nabla\phi \cdot \nabla\vartheta}{\sqrt{1 + \epsilon^{-2}\|\nabla\phi\|^2}} \,\mathrm{d}\mu = \frac{1}{\epsilon} \int_\Omega \frac{\nabla\phi \cdot \nabla\vartheta}{\sqrt{\epsilon^2 + \|\nabla\phi\|^2}} \,\mathrm{d}\mu.
\end{aligned}
$$

Now, the gradient flow with respect to $g_{\phi,\epsilon}$ yields

$$
\frac{1}{\epsilon} \int_\Omega \frac{\partial_t \phi \vartheta}{\|\nabla\phi\|_\epsilon} \,\mathrm{d}\mu = \frac{1}{\epsilon} \int_\Omega \frac{\nabla\phi \cdot \nabla\vartheta}{\|\nabla\phi\|_\epsilon^2} \,\mathrm{d}\mu,
$$

which is the regularized mean curvature flow (6.11).

### Regularized Willmore flow

The Willmore energy $e[\mathcal{G}^\epsilon]$ of the graph surface $\mathcal{G}^\epsilon$ is given by

$$
\begin{aligned}
e[\mathcal{G}^\epsilon] &= \int_{\mathcal{G}^\epsilon} (h^\epsilon)^2 \,\mathrm{d}A \\
&= \int_\Omega \sqrt{1 + \epsilon^{-2}\|\nabla\phi\|^2} \,\mathrm{div}\left( \frac{\epsilon^{-1}\nabla\phi}{\sqrt{1 + \epsilon^{-2}\|\nabla\phi\|^2}} \right) \,\mathrm{d}\mu \\
&= \frac{1}{\epsilon} \int_\Omega \|\nabla\phi\|_\epsilon \,\mathrm{div}\left( \frac{\nabla\phi}{\|\nabla\phi\|_\epsilon} \right) \,\mathrm{d}\mu
\end{aligned}
$$

where $h^\epsilon$ is the mean curvature of the $d + 1$ dimensional graph surface $\mathcal{G}^\epsilon$ and $E[\phi]$ the energy from Section 6.2. Hence, regularization can be understood as an approximation of Willmore flow for implicit surfaces via Willmore flow for graph surfaces with a scaling $\epsilon^{-1}$ for $\epsilon \to \infty$.

For the Willmore flow of graphs we obtain

**Problem 6.4.3 (Weak formulation for the Willmore flow of scaled graphs).** *Given an initial function $\phi_0$ on $\Omega$, $\epsilon > 0$ find a pair of functions $(\phi, w)$ with $\phi(0) = \phi_0$, such that*

$$
\int_\Omega \frac{\partial_t \phi \vartheta}{\|\nabla\phi\|_\epsilon} \,\mathrm{d}\mu = -\int_\Omega \frac{1}{2} \frac{w^2}{\|\nabla\phi\|_\epsilon^3} \nabla\phi \cdot \nabla\vartheta + \|\nabla\phi\|_\epsilon^{-1} P_{\mathcal{G}_\epsilon[\phi]} \nabla w \cdot \nabla\vartheta \,\mathrm{d}\mu, \qquad (6.13)
$$

$$
\int_\Omega \frac{w\,\psi}{\|\nabla\phi\|_\epsilon} \,\mathrm{d}\mu = \int_\Omega \frac{\nabla\phi \cdot \nabla\psi}{\|\nabla\phi\|_\epsilon} \,\mathrm{d}\mu \qquad (6.14)
$$

*for all $t > 0$ and all functions $\vartheta, \psi \in \mathscr{C}_0^\infty(\Omega)$.*

The case $\epsilon = 1$ has been analyzed by Deckelnick and Dziuk [89]. Their main result is the following numerical error estimate:

**Theorem 6.4.4.** *Given that the Willmore flow of graphs with Dirichlet boundary conditions in both variables has a unique solution in the interval $[0, T]$, which fulfills*

$$
\begin{aligned}
\phi &\in L^\infty((0,T); H^{4,\infty}(\Omega)) \cap L^2((0,T); H^5(\Omega)), \\
\phi_t &\in L^\infty((0,T); H^{2,\infty}(\Omega)) \cap L^2((0,T); H^3(\Omega)), \\
\phi_{tt} &\in L^\infty((0,T); L^\infty(\Omega)) \cap L^2((0,T); H^1(\Omega)).
\end{aligned}
$$

*Further let $u_{0h} = \mathcal{I}_h u_0$ be the projection of $u_0 \in H^2(\Omega) \cap H_0^{1,2}(\Omega)$ then*

$$
\begin{aligned}
\sup_{0 \le t \le T} \|\phi(t) - \phi_h(t)\| + \sup_{0 \le t \le T} \|w(t) - w_h(t)\| &\le Ch^2 |\log h|^2, \\
\sup_{0 \le t \le T} \|\nabla\phi(t) - \nabla\phi_h(t)\| &\le Ch, \\
\int_0^T \|u_t - u_{ht}\|^2 \, \mathrm{d}t &\le Ch^4 |\log h|^4, \\
\int_0^T \|\nabla w - \nabla w_h\|^2 \, \mathrm{d}t &\le Ch^2.
\end{aligned}
$$

This result confirms that the proposed weak scheme is appropriate for the straightforward numerical discretization by a semi-implicit Finite Element scheme.

## 6.5 Boundary conditions

In this section we will analyze the boundary conditions, which result directly by the choice of test functions.

**Homogenous Neumann conditions**

Let us allow the test functions $\vartheta, \psi$ to be in $\mathscr{C}^\infty(\Omega)$. We first integrate by parts in equation (6.8) by assuming sufficient regularity for $\phi$:

$$
\int_\Omega \|\nabla\phi\|^{-1} w \, \psi \, \mathrm{d}\mu = \int_\Omega \frac{\nabla\phi}{\|\nabla\phi\|} \cdot \nabla\psi \, \mathrm{d}\mu = -\int_\Omega \operatorname{div}\left(\frac{\nabla\phi}{\|\nabla\phi\|}\right) \mathrm{d}\mu + \int_{\partial\Omega} \frac{\nabla\phi}{\|\nabla\phi\|} \cdot \nu\psi \, \mathrm{d}A
$$

By the fundamental lemma, we obtain $w\|\nabla\phi\| = -h$ in $\Omega$ and $n = \frac{\nabla\phi}{\|\nabla\phi\|} \cdot \nu = 0$, or $n \perp \nu$ a. e., where $\nu$ denotes the outward pointing normal of the boundary $\partial\Omega$. This means that the level sets are orthogonal to the boundary $\partial\Omega$.

Now, let us integrate by parts also in equation (6.7):

$$
\begin{aligned}
\int_\Omega \frac{\partial_t\phi\,\vartheta}{\|\nabla\phi\|_\epsilon} \, \mathrm{d}\mu &= \int_\Omega \operatorname{div}\left(\frac{1}{2}\frac{w^2}{\|\nabla\phi\|^3}\nabla\phi + \|\nabla\phi\|^{-1} P\nabla w\right) \mathrm{d}\mu \\
&\quad - \int_{\partial\Omega} \left(\frac{1}{2}\frac{w^2}{\|\nabla\phi\|^3}\nabla\phi + \|\nabla\phi\|^{-1} P\nabla w\right) \cdot \nu\vartheta \, \mathrm{d}A
\end{aligned}
$$

and again the fundamental lemma yields

$$
\partial_t\phi - \|\nabla\phi\| \operatorname{div}\left(\frac{w^2}{2}\frac{\nabla\phi}{\|\nabla\phi\|^3} + P\nabla w\right) = 0 \text{ in } \Omega
$$

whereas on $\partial\Omega$ we obtain on account of $\frac{\nabla\phi}{\|\nabla\phi\|} \perp \nu$:

$$
\frac{h^2}{2} \underbrace{\frac{\nabla\phi}{\|\nabla\phi\|} \cdot \nu}_{=0} + \underbrace{P\nu \cdot \nabla w}_{\nabla w \cdot \nu} = 0.
$$

Hence, we obtain the second boundary condition $\nabla w \cdot \nu = 0$.

**Dirichlet conditions for $\phi$, Neumann conditions for $w$**

In order to prescribe Dirichlet conditions $\phi = \phi^\partial$ on $\partial\Omega$ we consider $\mathscr{C}_0^\infty(\Omega)$ as the space of test functions for $\vartheta$. This will already determine the normal $n = \frac{\nabla\phi}{\|\nabla\phi\|}$ of the level sets in tangential direction along the boundary:

$$(\mathbb{1} - \nu \otimes \nu)\frac{\nabla\phi}{\|\nabla\phi\|} = \frac{\nabla_{\partial\Omega}\phi^\partial}{\|\nabla_{\partial\Omega}\phi^\partial\|}.$$

In order to prescribe the full normal $n^\partial$, we have to determine the normal component (with respect to the boundary) of the normal of the level lines, i. e., $n^\partial \cdot \nu$.

Now we consider consider test functions $\psi \in \mathscr{C}^\infty(\Omega)$ and enhance the equation by the required boundary integral (6.8)

$$\int_\Omega \|\nabla\phi\|^{-1} w\, \psi\, \mathrm{d}\mu \;\;=\;\; \int_\Omega \frac{\nabla\phi}{\|\nabla\phi\|} \cdot \nabla\psi\, \mathrm{d}\mu - \int_{\partial\Omega} \gamma\vartheta\, \mathrm{d}A\,, \qquad (6.15)$$

for a scalar function $\gamma$ on $\partial\Omega$. We obtain the same equation $w = -h\|\nabla\phi\|$ in $\Omega$, and $\frac{\nabla\phi}{\|\nabla\phi\|} \cdot \nu = n\cdot\nu = \gamma$ on $\partial\Omega$. Hence, the choice of $\gamma$ is restricted to fulfill $|\gamma| \le 1$. Since the normal component of $n^\partial$ is now given by $\gamma$, with this combination of boundary conditions we are able to prescribe the full normal of the level set function:

$$n^\partial = (\mathbb{1} - \nu \otimes \nu)n + \gamma\nu\,.$$

If the tangential gradient of $\phi^\partial$ is zero we have to set $\gamma = 1$ for consistency reasons. Indeed, the boundary condition would result in $n^\partial = \nu$. This will be the boundary condition of choice for inpainting problems to be discussed later, since it allows to prevent the motion of the level sets in tangential direction, while it fixes the angle under which the level set function meets the boundary. In the case of the Willmore flow of scaled graphs one can proceed in a completely analogous way to prescribe the full normal of the graph surface in $\mathbb{R}^{d+1}$.

**General Neumann conditions for both equations**

We might proceed for $w$ as above, choose as test functions for the first equation $\vartheta \in \mathscr{C}^\infty(\Omega)$ and modify (6.7) to

$$\int_\Omega \frac{\partial_t\phi}{\|\nabla\phi\|}\vartheta\, \mathrm{d}\mu \;\;=\;\; \int_\Omega -\frac{1}{2}\frac{w^2}{\|\nabla\phi\|^3}\nabla\phi \cdot \nabla\vartheta - \|\nabla\phi\|^{-1} P\nabla w \cdot \nabla\vartheta\, \mathrm{d}\mu - \int_{\partial\Omega} \eta\psi\, \mathrm{d}A,$$

where the equation within $\Omega$ remains unchanged and we impose

$$\frac{h^2}{2}\frac{\nabla\phi}{\|\nabla\phi\|} \cdot \nu + P\nu \cdot \nabla w = \eta,$$

and finally obtain $P\nu \cdot \nabla w = \eta - \frac{h^2}{2}\gamma$.

## 6.6 Semi implicit Finite Element discretization

We will now describe spatial and temporal discretization of the weak formulation of the regularized Willmore flow and suggest a semi implicit scheme in time. The spatial discretization is again given by the the Finite Element discretization based on uniformly refined quadrilateral resp. hexahedral cells with bi- resp. trilinear elements which has been described in Section 2.6.

Now we proceed with the temporal and spatial discretization of the regularized Willmore flow problem. We discretize the system of partial differential equations (6.7), (6.8) first in time using a semi implicit backward Euler scheme and then in space based on piecewise affine Finite Elements.

## 6.6.1   Spatial discretization

Now, we formulate the semi discrete Finite Element problem, which is only discretized with respect to space and we consider homogeneous Neumann boundary conditions for both variables. Again, capital letters and symbols denote the discrete analogon of the the continuous variables.

**Problem 6.6.1 (Semi discrete problem).** *Find $\Phi : \mathbb{R}_0^+ \to V^h$ with $\Phi(0) = \mathcal{I}_h \phi_0$ and a corresponding curvature concentration function $W : \mathbb{R}^+ \to \mathcal{V}^h$, which fulfill*

$$\int_\Omega \frac{\partial_t \Phi(t)\Theta}{\|\nabla\Phi(t)\|}\,\mathrm{d}\mu + \int_\Omega \left( \frac{W(t)^2}{2\,\|\nabla\Phi(t)\|^3}\nabla\Phi(t)\cdot\nabla\Theta + \frac{P_\epsilon[\Phi(t)]}{\|\nabla\Phi(t)\|}\nabla W(t)\cdot\nabla\Theta \right)\mathrm{d}\mu = 0 \quad (6.16)$$

$$\int_\Omega \frac{W(t)\Psi}{\|\nabla\Phi(t)\|}\,\mathrm{d}\mu - \int_\Omega \frac{\nabla\Phi(t)}{\|\nabla\Phi(t)\|}\cdot\nabla\Psi\,\mathrm{d}\mu = 0 \quad (6.17)$$

*for all $t > 0$ and all test functions $\Theta$, $\Psi \in \mathcal{V}^h$.*

This problem is a system of ordinary differential equations.

## 6.6.2   Semi implicit time discretization

Let us now address the discretization in time. For a fixed time step $\tau$, we want to compute the discrete approximations $\Phi^k$ of the level set function at time $k\tau$, namely $\Phi(k\tau)$. Due to prohibitive time step restrictions of the type $\tau \leq Ch^4$, where $h$ is the spatial grid size (cf. results presented in [211, 52]), we will not consider any explicit schemes. For a backward Euler scheme in time of the discrete system of ODE's which we obtain after the spatial discretization, we consider the backward difference quotient of the time derivative

$$\partial_t\Phi((k+1)\tau) \approx \frac{\Phi^{k+1} - \Phi^k}{\tau}.$$

In Problem 6.6.1 we observe that the terms which are related to the metric, are depending nonlinearly on $\Phi$ and $W$. These are the weight $\|\nabla\Phi\|$ and the projection $P[\Phi]$. If we evaluate these at the previous time step, we obtain a coupled linear system for $\Phi^{k+1}$ and $W^{k+1}$. For the other occurrences of $\Phi$ we have several possibilities to decide, which terms are to be treated explicitly and which terms are to be treated implicitly. The term $\frac{P_\epsilon[\Phi]}{\|\nabla\Phi\|}\nabla W\cdot\nabla\Theta$ is the dominating one. It represents the variation of the energy integrand $h^2$ for fixed metric weight and is primarily of fourth order, since $W$ is already obtained by a differential operator of second order. We will hence always choose this term to be fully implicit.

We will also treat the term $\frac{W(t)^2}{2\|\nabla\Phi(t)\|^3}\nabla\Phi\cdot\nabla\Theta$ explicitly in (6.16) with respect to $\Phi$ apart from the denominator. It represents the discrete variation of the metric weight $\|\nabla\phi\|$ for fixed energy integrand $h^2$ and is of second order. In numerical experiments, it turned out to be of significance to maintain stability.

If we decompose the projection into $P_\epsilon[\Phi^k] = \mathbb{1} + (\mathbb{1} - P_\epsilon[\Phi^k])$ we can treat the second summand either implicitly or explicitly. Note that the eigenvalues of $P_\epsilon$ depend on $\epsilon$, for $\epsilon = 0$, the normal $\frac{\nabla\Phi}{\|\nabla\Phi\|}$ is an eigenvector to the eigenvalue $0$. Let us now summarize these two possibilities and formulate the fully discrete problems.

**Problem 6.6.2 (Fully discrete semi-implicit problem (I)).** *Find a sequence of image intensity functions $(\Phi^k)_{k=0,\cdots} \subset V^h$ with $\phi^0 = \mathcal{I}_h\phi_0$ and a corresponding sequence of weighted mean curvature functions $(W^k)_{k=0,\cdots} \subset \mathcal{V}^h$ such that for all test functions $\Theta$, $\Psi \in \mathcal{V}^h$ we have*

$$\int_\Omega \left( \frac{(\Phi^{k+1} - \Phi^k)\Theta}{\tau\|\nabla\Phi^k\|_\epsilon} + \frac{(W^k)^2}{2\|\nabla\Phi^k\|_\epsilon^3}\nabla\Phi^{k+1}\cdot\nabla\Theta + \frac{P_\epsilon[\Phi^k]}{\|\nabla\Phi^k\|_\epsilon}\nabla W^{k+1}\cdot\nabla\Theta \right)\mathrm{d}\mu = 0$$

$$\int_\Omega \frac{W^{k+1}\Psi}{\|\nabla\Phi^k\|_\epsilon}\,\mathrm{d}\mu - \int_\Omega \frac{\nabla\Phi^{k+1}\cdot\nabla\Psi}{\|\nabla\Phi^k\|_\epsilon}\,\mathrm{d}\mu = 0.$$

After definition of the matrices

$$
\mathbf{M}[\Phi^k] = \left( \int_\Omega \frac{\Psi_\alpha\,\Psi_\beta}{\|\nabla\Phi^k\|_\epsilon}\,\mathrm{d}\mu \right)_{\alpha,\beta}, \qquad
\mathbf{L}_P[\Phi^k] = \left( \int_\Omega \frac{P_\epsilon[\Phi]}{\|\nabla\Phi^k\|_\epsilon}\nabla\Psi_\alpha\cdot\nabla\Psi_\beta\,\mathrm{d}\mu \right)_{\alpha,\beta},
$$

$$
\mathbf{L}[\Phi^k] = \left( \int_\Omega \frac{\nabla\Psi_\alpha\cdot\nabla\Psi_\beta}{\|\nabla\Phi^k\|_\epsilon}\,\mathrm{d}\mu \right)_{\alpha,\beta}, \quad
\mathbf{L}_W[\Phi^k,W^k] = \left( \int_\Omega \frac{(W^k)^2}{2\|\nabla\Phi^k\|_\epsilon^3}\nabla\Psi_\alpha\cdot\nabla\Psi_\beta\,\mathrm{d}\mu \right)_{\alpha,\beta},
$$

where $\alpha$, $\beta$ are iterating over all Lagrange-nodes of the Finite Element space $\mathcal{V}^h$, we—by a Schur-complement approach—end up with the block system

$$
\begin{pmatrix} \frac{1}{\tau}\mathbf{M}+\mathbf{L}_W & \mathbf{L}_P \\ -\mathbf{L} & \mathbf{M} \end{pmatrix}
\begin{pmatrix} \bar\Phi^{k+1} \\ \bar W^{k+1} \end{pmatrix}
= \begin{pmatrix} \frac{1}{\tau}\mathbf{M}\bar\Phi^k \\ 0 \end{pmatrix}
$$

which rewrites after the elimination of $W^{k+1}$ as

$$
(\mathbf{M} + \tau\mathbf{L}_W + \tau\mathbf{L}_P\mathbf{M}^{-1}\mathbf{L})\bar\Phi^{k+1} = \mathbf{M}\bar\Phi^k. \tag{6.18}
$$

This system is non-symmetric. One possibility is to use a BiCG-stab iteration as a solver.

**Problem 6.6.3 (Fully discrete problem (II)).** *Given $\phi_0 \in H^{1,2}(\Omega)$, find a sequence of image intensity functions $(\Phi^k)_{k=0,\dots} \subset \mathcal{V}^h$ with $\Phi^0 = \mathcal{I}_h\phi_0 \in \mathcal{V}^h$ and a corresponding sequence of curvature concentration functions $(W^k)_{k=0,\dots} \subset \mathcal{V}^h$ such that for all test functions $\Theta,\ \Psi \in \mathcal{V}^h$ we have*

$$
\int_\Omega \left( \frac{(\Phi^{k+1}-\Phi^k)\Theta}{\tau\|\nabla\Phi^k\|_\epsilon} + \frac{(W^k)^2}{2\|\nabla\Phi^k\|_\epsilon^3}\nabla\Phi^{k+1}\cdot\nabla\Theta \right.
$$

$$
\left. + \frac{\nabla W^{k+1}\cdot\nabla\Theta}{\|\nabla\Phi^k\|_\epsilon}\nabla W^{k+1}\cdot\nabla\Theta \right)\mathrm{d}\mu = \int_\Omega \frac{(\mathbb{1}-P_\epsilon[\Phi^k])}{\|\nabla\Phi^k\|_\epsilon}\nabla W^k\cdot\nabla\Theta\,\mathrm{d}\mu
$$

$$
\int_\Omega \frac{W^{k+1}\,\Psi}{\|\nabla\Phi^k\|_\epsilon}\,\mathrm{d}\mu - \int_\Omega \frac{\nabla\Phi^{k+1}\cdot\nabla\Psi}{\|\nabla\Phi^k\|_\epsilon}\,\mathrm{d}\mu = 0.
$$

With a similar notation as above, we obtain the following block symmetric block system.

$$
\begin{pmatrix} \frac{1}{\tau}\mathbf{M}+\mathbf{L}_W & \mathbf{L} \\ -\mathbf{L} & \mathbf{M} \end{pmatrix}
\begin{pmatrix} \bar\Phi^{k+1} \\ \bar W^{k+1} \end{pmatrix}
= \begin{pmatrix} \frac{1}{\tau}\mathbf{M}\bar\Phi^k + \mathbf{L}_{(\mathbb{1}-P)}\bar W^k \\ 0 \end{pmatrix}
$$

which again after the elimination of $W^{k+1}$ becomes

$$
(\mathbf{M} + \tau\mathbf{L}_W + \tau\mathbf{L}\mathbf{M}^{-1}\mathbf{L})\bar\Phi^{k+1} = (\mathbf{M} + \tau\mathbf{L}_{(\mathbb{1}-P)})\bar\Phi^k.
$$

The matrix on the left hand side is symmetric and positive definite, so the whole system can be solved with a conjugate gradient solver.

### Numerical Quadrature

For the entries of the matrices no explicit formulas are available to compute the weighted integrals of products of the basis functions. We will apply numerical quadrature schemes for the assembly of the *mass* matrix $\mathbf{M}$ and the the *stiffness* matrices $\mathbf{L}$ and its variants. In particular, we use *mass* lumping (cf. the book of THOMÉE [196]) for the *mass* matrix and we apply Gaussian quadrature rules for the computation of the *stiffness* matrices.

For the *mass* matrix, we will need a generalized variant of lumping, since the products of the basis functions are weighted by $\|\nabla\Phi^k\|_\epsilon^{-1}$. To this end, we introduce a projection $\mathcal{I}_h^0$ to the space of piecewise constant functions with respect to the grid by $\mathcal{I}_h^0\Lambda|_C = \Lambda(s_C)$. Here $s_C$ denotes the center of gravity of an element $C \in \mathcal{C}$. Then we define the general weighted lumped *mass* matrix by

$$
\mathbf{M}_h[\omega]_{ij} := \int_\Omega \mathcal{I}_h^0(\omega)\mathcal{I}_h(\Phi_i\Phi_j)\,\mathrm{d}\mu
$$

which reveals again a diagonal structure, but the diagonal entries are now a weighted sum, of the usual contributions $\int_C \mathcal{I}_h(\Phi_i \Phi_j) \, d\mu$ with respect to the weight $\omega$. Now in the previously described matrix systems (6.18) and (6.19) of the discretized Willmore flow, we will replace all occurrences of $\mathbf{M}[\Phi^k]$ by $\mathbf{M}_h[\|\nabla \Phi^k\|_\epsilon^{-1}]$.

For the local integrals, which make up the entries of the *stiffness* matrices, we will apply Gaussian quadrature. Consider the Lagrangian projection $\mathcal{I}_h^1$ corresponding to the Gaussian quadrature nodes on each element. In our computations we have mainly used 4 point formulas (for 2D) and 8 point formulas in 3D, which ensure an exact integration up to third order tensor product polynomials.

The Gauss quadrature of the weighted second order *stiffness* matrix can be written as

$$\mathbf{L}_h[A] := \int_\Omega \mathcal{I}_h^1 (A \nabla \Phi_i \cdot \nabla \Phi_j) \, d\mu.$$

Now after replacing all occurrences of the *stiffness* matrices, by their approximations due to numerical quadrature, i. e.,

$$\mathbf{L}[\Phi^k] \quad \rightsquigarrow \quad \mathbf{L}_h[\|\nabla \Phi^k\|_\epsilon^{-1}], \qquad \mathbf{L}_W[\Phi^k, W^k] \quad \rightsquigarrow \quad \mathbf{L}_h \left[ \frac{(W^k)^2}{2\|\nabla \Phi^k\|_\epsilon^3} \right],$$

$$\mathbf{L}_P[\Phi^k] \quad \rightsquigarrow \quad \mathbf{L}_h[P[\Phi^k]\|\nabla \Phi^k\|_\epsilon^{-1}], \qquad \mathbf{L}_{(\mathbb{1}-P)}[\Phi^k] \quad \rightsquigarrow \quad \mathbf{L}_h[(\mathbb{1} - P[\Phi^k])\|\nabla \Phi^k\|_\epsilon^{-1}],$$

we end up with a fully practical Finite Element scheme.

Although we did not observe any problem in the numerical simulation, the solvability of the linear system of equation appearing in variant I is still unclear. Furthermore, the linear system matrix $\mathbf{A}$ is not symmetric. Thus, in the implementation we apply BiCGstab as iterative solver. Concerning variant II, the corresponding matrix $\mathbf{A}$ is obviously symmetric and positive definite. Hence, $\mathbf{A}$ is invertible and the linear systems of equations can be solved applying a CG method.

### 6.6.3 Boundary conditions

The discretization described above was with respect to homogeneous Neumann conditions in both variables, i. e.,

$$\frac{\nabla \Phi}{\|\nabla \Phi\|} \cdot \nu = 0 \quad \text{and} \quad \nabla W \cdot \nu = 0.$$

We will now briefly describe the implementation of the boundary conditions which have been described in Section 6.5. In the following, we will, for the sake of simplicity, restrict ourselves to the first variant of the discretization.

**Neumann conditions in both equations**

As described above, we may impose $\frac{\nabla \Phi}{\|\nabla \Phi\|} \cdot \nu = \mathcal{I}_h \gamma$ for $|\gamma| \leq 1$. We consider the test functions $\Psi$ of the second equation to be in $\mathcal{V}^h$ and obtain:

$$\int_\Omega \frac{W^{k+1} \Psi}{\|\nabla \Phi^k\|_\epsilon} \, d\mu = \int_\Omega \frac{\nabla \Phi^{k+1} \cdot \nabla \Psi}{\|\nabla \Phi^k\|_\epsilon} - \int_{\partial \Omega} \mathcal{I}_h \gamma \cdot \Psi \, dA$$

thus by defining $(\mathbf{R}[\gamma])_\alpha := \int_{\partial \Omega} \mathcal{I}_h \gamma_\alpha \cdot \Psi \, dA$ for all $\alpha \in I$, we obtain the coefficient vector of $W^{k+1}$:

$$\bar{W}^{k+1} = \mathbf{M}^{-1}(\mathbf{L}\bar{\Phi}^{k+1} - \mathbf{R}[\gamma]). \tag{6.19}$$

For the first equation we may impose $P\nu \cdot \nabla W = \mathcal{I}_h\eta - \frac{W^2}{\|\nabla\Phi\|}\mathcal{I}_h\gamma$ and by the considerations of Section 6.5 we can write

$$
\begin{aligned}
0 &= \int_\Omega \frac{\Phi^{k+1} - \Phi^k}{\|\nabla\Phi^k\|_\epsilon}\, \mathrm{d}\mu - \int_\Omega \mathrm{div}\left( \frac{(W^{k+1})^2}{2\|\nabla\Phi^k\|_\epsilon^2}\frac{\nabla\Phi^{k+1}}{\|\nabla\Phi^k\|_\epsilon} + \frac{P_\epsilon[\Phi^k]}{\|\nabla\Phi^k\|_\epsilon}\nabla W^{k+1} \right) \cdot \Theta\, \mathrm{d}\mu \\
&= \int_\Omega \frac{\Phi^{k+1} - \Phi^k}{\|\nabla\Phi^k\|_\epsilon}\, \mathrm{d}\mu + \int_\Omega \left( \frac{(W^{k+1})^2}{2\|\nabla\Phi^k\|_\epsilon^3}\nabla\Phi^{k+1}\cdot\nabla\Theta + \frac{P_\epsilon[\Phi^k]}{\|\nabla\Phi^k\|_\epsilon}\nabla W^{k+1}\cdot\nabla\Theta \right) \mathrm{d}\mu \\
&\quad - \underbrace{\int_{\partial\Omega} \frac{W^{k+1}}{2\|\nabla\Phi^k\|_\epsilon}\left( \frac{\nabla\Phi^{k+1}}{\|\nabla\Phi^k\|_\epsilon}\cdot\nu \right)\Theta\, \mathrm{d}A - \int_{\partial\Omega}\left( \frac{P_\epsilon[\Phi^k]}{\|\nabla\Phi^k\|_\epsilon}\nabla W^{k+1}\cdot\nu \right)\Theta\, \mathrm{d}A}_{=\int_{\partial\Omega}\mathcal{I}_h\eta\Theta\, \mathrm{d}A} \qquad (6.20)
\end{aligned}
$$

for test functions $\Theta \in \mathcal{V}^h$. The two boundary integrals in the last part of the equation allow us to conveniently impose the normal and the gradient of the curvature concentration from a different level set function resp. graph function. By inserting $W^{k+1}$ from (6.19) the whole system then reads

$$
\begin{aligned}
\mathbf{M}\bar{\Phi}^{k+1} + \tau\mathbf{L}_W\bar{\Phi}^{k+1} + \tau\mathbf{L}_P\mathbf{M}^{-1}(\mathbf{L}\bar{\Phi}^{k+1} - \mathbf{R}[\gamma]) &= \mathbf{M}\bar{\Phi}^{k+1} + \mathbf{R}[\eta], \\
\Leftrightarrow (\mathbf{M} + \tau\mathbf{L}_W + \tau\mathbf{L}_P\mathbf{M}^{-1}\mathbf{L})\bar{\Phi}^{k+1} &= \mathbf{M}\bar{\Phi}^{k+1} + \mathbf{L}_P\mathbf{M}^{-1}\mathbf{R}[\gamma] + \mathbf{R}[\eta],
\end{aligned}
$$

here $\mathbf{R}[\eta]$ is defined analogously to $\mathbf{R}[\gamma]$.

### Dirichlet condition in the first equation

In order to prescribe Dirichlet conditions for the variable $\phi$, namely $\phi\big|_{\partial\Omega} = g \in L^2(\partial\Omega)$, we introduce the Finite Element space

$$
\mathcal{V}_\partial^h[g_h] = \left\{ \psi \in \mathcal{V}^h \,:\, T\psi = g_h \right\}
$$

as the discrete representation of the space

$$
H_\partial^{1,2}(\Omega)[g] := \left\{ \psi \in H^{1,2}(\Omega) \,:\, T\psi = g \right\}
$$

Here, $g_h$ denotes the $L^2$-projection of $g$ onto the restriction of the Finite Element space $\mathcal{V}^h$ to the boundary and $T$ denotes the trace operator with respect to the space $\mathcal{V}^h \subset H^{1,2}(\Omega)$, i. e., the unique bounded linear mapping $T : H^{1,2}(\Omega) \to L^2(\partial\Omega)$ which fulfills $Tf = f$ on $\partial\Omega$ for all $f \in H^{1,2}(\Omega) \cap \mathscr{C}^0(\overline{\Omega})$ [1, 111]. We denote the interior nodes of $\mathscr{T}^h$ by $\mathcal{N}_0(\mathscr{T}^h)$, corresponding to the Lagrange nodes of $\mathcal{V}^h$ in the interior of $\Omega_h$ and denote the nodes on the boundary $\partial\Omega_h$ by $\mathcal{N}_\partial(\mathscr{T}^h)$.

For Problem 6.6.2 we obtain again, in case of natural Neumann conditions for the curvature concentration, $\bar{W}^{k+1} = \mathbf{M}^{-1}\mathbf{L}\bar{\Phi}^{k+1}$. For the first equation we obtain

$$
\begin{aligned}
0 &= \sum_{\beta\in\mathcal{N}_0} \frac{\bar{\Phi}_\beta^{k+1} - \bar{\Phi}_\beta^k}{\tau}\int_\Omega \frac{\Psi_\beta\Psi_\alpha}{\|\nabla\Phi^k\|_\epsilon}\, \mathrm{d}\mu + \sum_{\beta\in\mathcal{N}_0}\bar{\Phi}_\beta^{k+1}\int_\Omega \frac{(W^k)^2}{2\|\nabla\Phi^k\|_\epsilon^3}\nabla\Psi_\beta\cdot\nabla\Psi_\alpha\, \mathrm{d}\mu \\
&\quad + \int_\Omega \frac{P_\epsilon[\Phi^k]}{\|\nabla\Phi^k\|_\epsilon}\nabla W^{k+1}\cdot\nabla\Psi_\beta + \sum_{\beta\in\mathcal{N}_\partial}\int_\Omega \bar{\Phi}_\beta^{k+1}\int_\Omega \frac{(W^k)^2}{2\|\nabla\Phi^k\|_\epsilon^3}\nabla\Psi_\beta\cdot\nabla\Psi_\alpha\, \mathrm{d}\mu
\end{aligned}
$$

for all $\alpha \in \mathcal{N}_0$. After splitting $W^{k+1}$ into the interior nodes and the exterior nodes, and considering a lumped *mass* matrix we obtain the following system for the restricted set of degrees of freedom:

$$
(\mathbf{M}_0 + \tau\mathbf{L}_{W,0} + \tau\mathbf{L}_{P,0}\mathbf{M}_0^{-1}\mathbf{L}_0)\bar{\Phi}_0^{k+1} = \mathbf{M}_0\bar{\Phi}^k - \tau\mathrm{Restr}[\mathcal{V}_0^h]\mathbf{L}_W\bar{g}_h - \tau\mathrm{Restr}[\mathcal{V}_0^h]\mathbf{L}_P\mathbf{M}^{-1}\mathbf{L}\bar{g}_h.
$$

The matrices with subindex $0$, denote the usual assembly, where now the indices are only running over interior nodes. One can proceed analogously for the second variant. The restriction operator from $\mathcal{V}^h$ to $\mathcal{V}_0^h$ is denoted by $\mathrm{Restr}[\mathcal{V}_0^h]$.
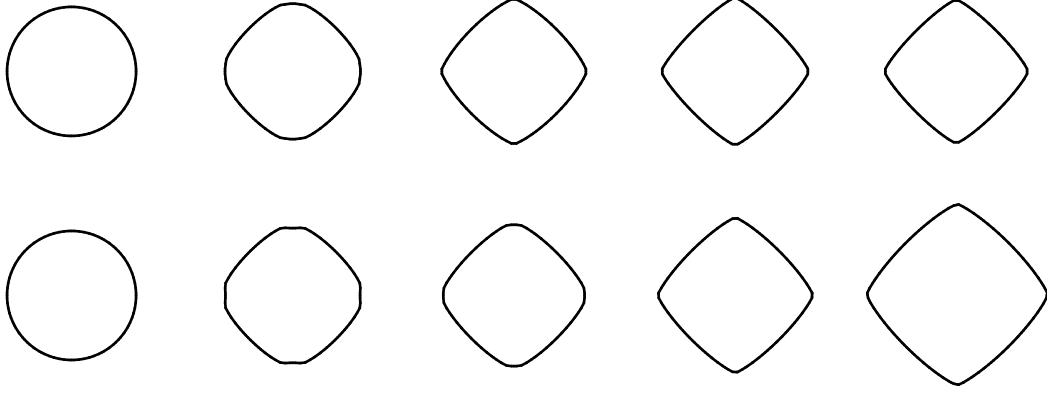
Figure 6.2: *Anisotropic Surface Diffusion (*TOP ROW*) and Willmore flow (*BOTTOM ROW*) evolution. The results for the anisotropy $\gamma(z) = (|z_1|^6 + |z_2|^6)^{\frac{1}{6}}$ are depicted for timesteps $0, 50, 100, 1000, 4000$. The timestep $\tau$ was chosen as $2h^4$ and $\epsilon = 2h$.*

## 6.7 A note on anisotropic variants of geometric flows

In this thesis, our motivation of the Willmore flow was founded on the fact that for fixed boundary conditions, stationary points of the Willmore functional are fitting smoothly to the exterior and furthermore, shapes are preferred for which the curvature is evenly distributed and is hence suitable for inpainting. We have assumed that we have no information whatsoever about the morphology in the inpainting domain, that we might exploit during the inpainting process.

This might not be the case in all applications. Imagine, that at each point of the inpainting domain, we have some kind of prior available that indicates, whether certain orientations are preferred or unlikely. Then we might aim at devising a flow, such that alignment to directions and smoothing is combined.

Furthermore, anisotropic surface energies play an important rôle in material science. Crystal lattices are in general anisotropic. Actually the Wulff-shapes are named after a material scientist who analyzed the growth of crystals [210, 114]. Certain materials are characterized by preferred orientations, which correspond to the molecular structure of the material [193]. A detailed treatise of the anisotropic case with respect to physics and its possible applications in image processing would be beyond the scope of this thesis. Hence, we will only give an overview on how the framework of the aggregated surface energies naturally extend to the anisotropic case, leading the way to future applications, which may then be based on the anisotropic case (see also [192, 48, 91, 87, 85, 208, 209]).

### 6.7.1 Weighting with respect to orientations

Mathematically, the variational modeling of preferred orientations is expressed in terms of a weighting function on the space of normals, i. e.,

$\gamma : S^{d-1} \to \mathbb{R}^+$ which extended 1-homogeneously: $\gamma(\lambda z) = \lambda \gamma(z) \, \forall \lambda > 0, z \in \mathbb{R}^d$.

**Definition 6.7.1.** *Let $\gamma : S^{d-1} \to \mathbb{R}^+$ be positive, convex and 1-homogenous, then we define the Frank-Diagram $\mathscr{F}_\gamma$ and the corresponding Wulff-shape $\mathscr{W}_\gamma$ by*

$$\mathscr{F}_\gamma \quad := \quad \left\{ z \in \mathbb{R}^d \, : \, \gamma(z) = 1 \right\} \tag{6.21}$$

$$\mathscr{W}_\gamma \quad := \quad \left\{ z \in \mathbb{R}^d \, : \, \gamma^*(z) := \sup_{n \in S^{d-1}} \frac{\langle z, n \rangle}{\gamma(n)} = 1 \right\}. \tag{6.22}$$

Let us remark, that this definition is different from the usual definition in the literature, where theses sets are not defined as surfaces, but as the convex bodies, which are enclosed by the sets defined above.

The geometric interpretation is the following. Consider a convex body $K$ with $0 \in K$, and for each $n \in S^{d-1}$ the unique intersection point $x_n := \{tn \,:\, t \in \mathbb{R}^+\} \cap \partial K$ and define $\gamma(n)$ as the distance of $x_n$ to the origin, i. e., $\gamma(n) := \langle x_n, n \rangle$. Then due to the convexity $K$ is characterized by

$$K = \bigcap_{n \in S^{d-1}} \{x \in \mathbb{R}^n \,:\, \langle x - x_n, n \rangle \le 0\} = \bigcap_{n \in S^{d-1}} \{x \in \mathbb{R}^n \,:\, \langle x, n \rangle \le \gamma(n)\}.$$

Hence, for each $n \in S^{d-1}$, we obtain the corresponding intersection on the boundary of $K$ by $\gamma(n)n$. We can now rewrite $\mathscr{W}_\gamma$ as

$$\mathscr{W}_\gamma = \left\{\gamma(n)n \,:\, n \in S^{d-1}\right\}.$$

Moreover, it can be shown that $\mathscr{W}_\gamma = \gamma_z(S^{d-1})$ given that $\gamma$ is differentiable [66].

Now let, us define the weighted area functional

$$e_{\mathrm{a},\gamma}[\mathcal{M}] := \int_{\mathcal{M}} \gamma(n) \, \mathrm{d}A.$$

In analogy to the isotropic case define the $L^2$ representation of the anisotropic mean curvature by the variation of the weighted area functional:

$$(h_\gamma, \vartheta)_{L^2(\mathcal{M})} = \langle e'_\gamma[\mathcal{M}], \vartheta \rangle \qquad \forall \vartheta \in \mathscr{C}^\infty(\mathcal{M})$$

We will from now on call this anisotropic mean curvature call $\gamma$-mean curvature. The anisotropic Willmore functional is defined by

$$e_{\mathrm{W},\gamma}[\mathcal{M}] := \frac{1}{2} \int_{\mathcal{M}} h_\gamma \, \mathrm{d}A.$$

It is shown in [66] that the $L^2$ gradient flow of the anisotropic Willmore functional is given by

$$\partial_t x = \Delta_\gamma h_\gamma + h_\gamma (\mathrm{tr}(\mu_\gamma S^2) - \frac{1}{2} h h_\gamma),$$

where $\Delta_\gamma \cdot = \mathrm{div}_{\mathcal{M}}(\mu_\gamma \nabla_{\mathcal{M}} \cdot)$ and $\mu_\gamma$ denotes the push-forward of $\gamma_{zz}$ onto the tangent bundle $T\mathcal{M}$. By observing that in the level set context the relation $h_\gamma = \mathrm{tr}(\mu_\gamma S) = \mathrm{div}\gamma_z(\nabla\phi)$ (cf. [72] for more details) holds, we obtain the aggregated Willmore energy as

$$E_{\mathrm{W},\gamma}[\phi] = \frac{1}{2} \int_\Omega (\mathrm{div}\gamma_z(\nabla\phi))^2 \|\nabla\phi\| \, \mathrm{d}\mu.$$

By a similar computation as in the proof of Theorem 6.2.2 and by choosing analogously $w_\gamma := -h_\gamma \|\nabla\phi\|$ as the natural second variable one obtains:

**Problem 6.7.2.** *For an initial function $\phi_0 \in H^{1,2}(\Omega)$, find a pair of functions $\phi \in L^2(H^{1,2}(\Omega))$ and $w \in L^2(H^{1,2}(\Omega))$, such that for all $t \in \mathbb{R}^+$*

$$\int_\Omega \frac{\partial_t \phi \, \vartheta}{\|\nabla\phi\|} + \int_\Omega \left(\frac{w_\gamma^2}{2\|\nabla\phi\|}\nabla\phi \cdot \nabla\vartheta + \gamma_{zz}(\nabla\phi)\nabla w \cdot \nabla\vartheta\right) \mathrm{d}\mu \;=\; 0 \qquad \forall \vartheta \in H^{1,2}(\Omega),$$

$$\int_\Omega \frac{w_\gamma \, \psi}{\|\nabla\phi\|} \mathrm{d}\mu - \int_\Omega \gamma_z(\nabla\phi) \cdot \nabla\psi \, \mathrm{d}\mu \;=\; 0 \qquad \forall \psi \in H^{1,2}(\Omega).$$

**Remarks 6.7.3.** *We observe the following.*

 (i) *Keeping the denominator $\|\nabla\phi\|$ fixed in a semi-implicit scheme in the fashion of the isotropic case is not sufficient to make the second equation linear.*

 (ii) *Again, the equation has to be regularized to avoid the degeneration for vanishing gradients. Since $\gamma$ is 1-homogenous, the first derivative $\gamma_z$ is discontinuous in the origin. It is possible to follow again the approach of regularizing with scaled graphs. However, one has to carefully design the extension of the anisotropy to dimension $d + 1$.*

 (iii) *$\gamma$ has to be twice differentiable.*

 (iv) *Anisotropic surface diffusion can be obtained similarly. See [193, 38, 72] for further details.*

 (v) *Anisotropic Total Variation flow has been analyzed by* ESEDOGLU & OHSER *[110].*

### 6.7.2 Outlook: Application scenarios in image processing

In the case of an anisotropic Willmore energy it is then possible to steer the preferred orientations of the minimizer of the Willmore energy. This idea is based on the work of CLARENZ [67], who has shown that the Wulff-shape minimizes the anisotropic Willmore energy. Also for locally varying Wulff-shapes, the anisotropic Willmore flow is expected to drive the surface to facet according to the preferred orientations. The fundamental problem is to find priors of feature directions and subsequently construct the function $\gamma$, such that its corresponding (locally varying) Wulff-shapes reflect the desired feature directions of the image. CLARENZ, RUMPF & TELEA [74] have constructed stable classify surfaces locally.

Let us describe some scenarios where priors about preferred orientations can be obtained. This is to be understood as an outlook.

*(i)* **Partial destruction of the region.** Assume that the image to be reconstructed is only partially destroyed, e. g., corrupted by noise. Then it might still be possible to extract feature directions in a similar way as this is done in anisotropic diffusion [203]. To our knowledge, no stable ways of retrieving Wulff-shapes from corrupted images have been proposed in the literature so far.

*(ii)* **Reconstruction based on matching.** Let us assume that the inpainting region in one image is completely destroyed, but that we have a registration available, such that the morphology can be analyzed in a second reference image. In that case, by the assumption that the morphologies of these images are supposed to be similar, it is possible to extract feature orientations in the known region and transfer it to the second.

## 6.8 Numerical results

**EOC-analysis: convergence to a spherical cap**

For a first validation of the numerical method, we consider the limit behavior for graph surfaces. It is known that 2-dimensional spheres are stationary points of the Willmore functional. We keep the position and the normals of the surface fixed along the boundary by considering boundary conditions of zero$^{th}$ and first order, i. e., Dirichlet conditions in the first equation and Neumann conditions in the second equation, which are choosing according to the surface of the *exact solution*, which is given by $\phi^*(x,y) = \sqrt{1 - x^2 - y^2}$ for $\Omega = (-\frac{1}{2}, \frac{1}{2})^2$. We chose the initial graph function $\phi_0$ as the solution of the *Poisson*-problem

$$\Delta\phi_0 = 0 \quad \text{in } \Omega \qquad \phi_0 = \phi^* \quad \text{on } \partial\Omega.$$

We set $\epsilon = 1$ and compute the evolution of VARIANT I of the gradient flow as in Problem 6.6.2. We observe that $\Phi^k$ is converging to a stationary point of the Willmore functional as shown in Figure 6.1. Moreover, $\Phi^k \xrightarrow{k \to \infty} \Phi \approx \mathcal{I}_h \phi^*$. We study the experimental order of convergence (EOC) for successively refined grids. Discretization parameter $h$ is halved in every refinement step, hence the EOC is given by:

$$\mathrm{EOC}_h := \log_2 \left( \frac{\|\Phi_{2h} - \mathcal{I}_h \phi^*\|_{L^2}}{\|\Phi_h - \mathcal{I}_h \phi^*\|_{L^2}} \right).$$

As expected we verify that $\|\Phi_h - \mathcal{I}_h \phi^*\|_{L^2} \leq Ch^2$, hence the numerical error of the converged solution is in the order of the interpolation error (see Table 6.1).

**Comparison to exact solutions in the level set context**

For radially symmetric evolution of curves under the Willmore flow we see for instance by Eq. (6.2) and taking into account the fact that $h = r^{-1}$ and $\|S\|^2 = r^{-2}$ that the evolution can be described by an ordinary differential equation for the radius $\dot{r}(t) = \frac{1}{2} r(t)^{-3}$. For a positive initial radius $r(0) = r_0$ the evolution in time of the radius must hence be given by

$$r(t) = (2t + r_0^4)^{1/4}. \tag{6.23}$$

| $h$ | $2^{-3}$ | $2^{-4}$ | $2^{-5}$ | $2^{-6}$ | $2^{-7}$ | $2^{-8}$ |
|---|---|---|---|---|---|---|
| $L^2$-error | 1.043e-3 | 2.519e-4 | 6.244e-5 | 1.575e-5 | 4.002e-6 | 1.219e-6 |
| $\mathrm{EOC}_h$ | | 2.05 | 2.01 | 1.99 | 1.98 | 1.71 |

Table 6.1: $L^2$-error and experimental order of convergence for the limit surface of the Willmore flow which is expected to converge to a sphere cap depending on the grid size $h$.

As initial function on the domain $\Omega = (-\frac{1}{2}, \frac{1}{2})^2$ we chose $\phi_0$ to be a radially symmetric level set function with $\|\nabla\phi_0\| = 1$, here the distance to the origin, and compute the Willmore flow for $\epsilon = h/2$ on a grid of size $65 \times 65$, as well as on a grid of size $129 \times 129$. We tracked the evolution of a particular level set $\mathcal{M}_c$ in time and compared it with the exact solution. The time step was chosen as $2h^4$. After every 50 time steps, we have reinitialized the level set function by computing the signed distance function with respect to $\mathcal{M}_c$. This comparison is shown in Figure 6.3. Here, we have to mention, that the error is not only due to the discretization error in the Finite Element scheme for Willmore flow but also due to the interpolation error during the reinitialization of the discrete signed distance function. The latter can influence the evolution of the scheme significantly, it is hence advisable to avoid superfluous re-initializations. To measure the error (cf. Figure 6.4), we define $r(t, \cdot) : \mathcal{M}_c(t) \to \mathbb{R}$ by $r(t, x) = \|x\|$ and compute the $L^\infty$-error $\|r(t) - r(t, \cdot)\|_{L^\infty(\mathcal{M}_c(t))}$.

### Comparison with parametric Willmore flow

For a further validation of the algorithm, we compare the numerical method for the evolution of graphs under Willmore flow with a different parametric Finite Element method for Willmore flow presented in [68]. We define as initial function

$$\phi_0 : [0,1]^2 \to \mathbb{R}, (x,y) \mapsto -\frac{1}{4}\sin(\pi y)(\frac{1}{4}\sin(\pi x) + \frac{1}{2}\sin(3\pi x))$$

and subsequently generate a triangulation of the graph as input for the parametric algorithm. Here, we have a grid of size $65^2$ and time step size $\tau = 10^{-6}$. Different timesteps of the numerical graph and parametric evolution are shown in Figure 6.6. As Dirichlet boundary conditions we set $\phi(t) = 0$ on $\partial\Omega$ and upwards pointing normals. The $L^2$ and $L^\infty$ errors plotted in Figure 6.7 are computed over the domain of the graph by converting the parametric triangulations into their corresponding graph representations.

### A topology-change of an evolving level set

Figure 6.5 demonstrates a topology change of a curve, which evolves under the Willmore flow. As an initial configuration, two square like shapes are placed close to each other. In the early stage of the evolution, the flow is dominated by an evolution which rounds off the corners until the shapes are close to circles. Due to the observation (6.23) that states that circles are growing under the Willmore flow, the two shapes have no other possibility to get closer to each other, until the get in contact, merge and eventually evolve to a single circle. However, we want to emphasize that the notion of a solution is not completely understood in such a situation of a singularity in the moment of contact.

### Simultaneous flow of all level sets

In Figure 6.8 an initial function with ellipse-like level sets attached to the boundary is evolved under Willmore flow for level sets with $\epsilon = h$ using VARIANT II of the fully discrete Problem 6.6.3. The initial function is given by

$$\phi_0 : [0,1]^2 \to \mathbb{R}, (x,y) \mapsto 1 + e^{1 - \frac{1}{1-y^2}} \cos(\pi x) \cos\left((\frac{1}{2} + \frac{3}{2}(3x^2 - 2x^3))\pi y\right). \qquad (6.24)$$

Clearly we observe that the ellipses tend to get rounder. The applied Neumann boundary conditions ensure orthogonality of the level lines at the boundary. We additionally observe a concentration of level sets and a steepening of the gradient as well as a flattening behavior in other regions. This is not very surprising: In a relatively short time-scale ellipses become circles, which then grow outwards. At some later time, these circles have to get in closer and closer to other shapes, which are given as the level sets with respect to a different iso-value. This is reflected by a significant steepening of the level set function. If the shapes were treated independently, they would intersect each other and continue to grow, this intersection, however is prohibited by the fact that the morphology is described by a level set function: the flow of the morphology under Willmore flow stops to have a solution.

**Numerical examples of *anisotropic* flows**

Finally, we will briefly illustrate the results of anisotropic Willmore flow as of Problem 6.7.2 and anisotropic surface diffusion. In all examples we have chosen the weighting function $\gamma$ as a regularized version of $\|\cdot\|_\infty$, namely $\gamma(z) = \|z\|_p$ with $p = 6$. The *Frank diagram* corresponds to a regularized square which is aligned to the axes of the standard coordinate system. Figure 6.7 shows an evolution of a single level set. The initial level set function $\phi_0$ was chosen as the distance to the origin. We observe that during the evolution, the shape evolves in such a way, that the feature directions are similar to those of the *Wulff-shape* which is a diamond-like shape. Furthermore we observe that in the case of surface diffusion, the shape converges. Similarly to the isotropic case, the shapes continue to grow under anisotropic Willmore flow.

In Figure 6.9 a comparison between the graph evolution of these flows is shown. One can see, that the surface diffusion tends to a steepening of the graph surface.

Let us now reconsider the initial level set function of (6.24) and the anisotropic variants of the simultaneous flow of all level sets as shown in Figures 6.10 and 6.11. Again, we observe *steepening* as well as *flattening* of the level set function. Additionally, the geometry locally adjusts to the weighting of the normals as given by $\gamma$: the inexpensive directions of the level sets are preferred.
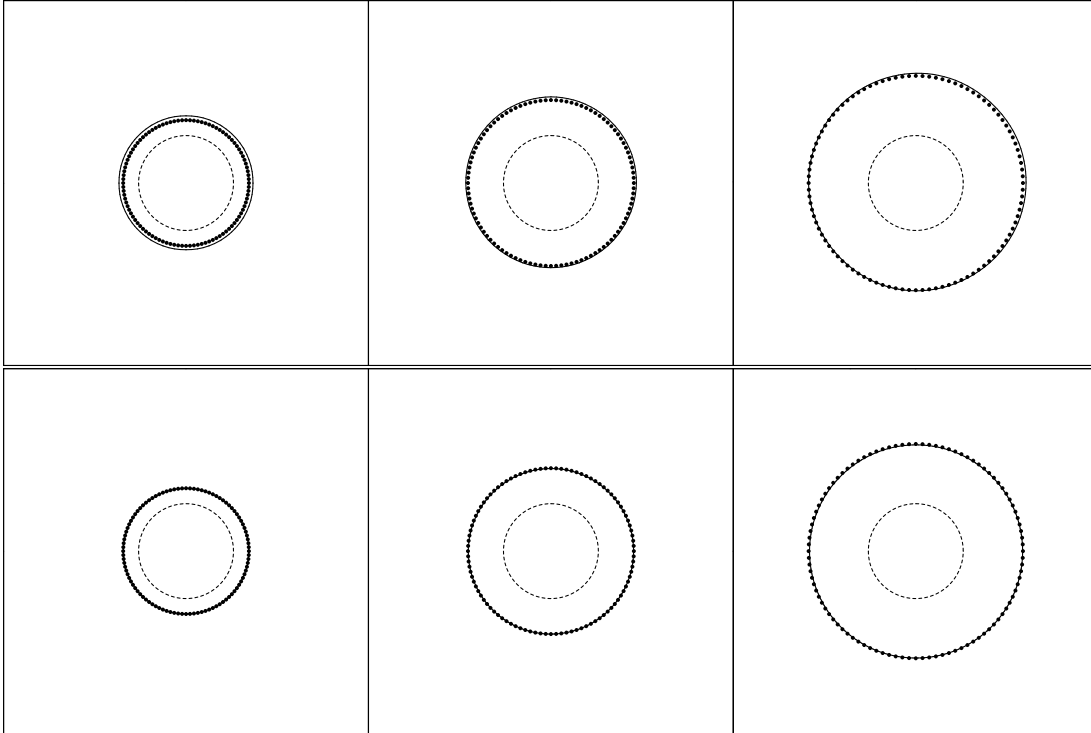
Figure 6.3: *A circle of radius $r_0 = 0.13$ expands due to its propagation via Willmore flow ($h = 64^{-1}$ (*TOP ROW*), and $h = 128^{-1}$ (*BOTTOM ROW*), $\tau = 10h^4$ ). The circle is represented by a level set function. During the evolution by the level set method for Willmore flow a signed distance function is recomputed every $50^{th}$ time step. The exact solution (*DOTTED LINE*) and the corresponding level set (*SOLID LINE*) are plotted for different times $t = 2.99 \cdot 10^{-4}, 1.192 \cdot 10^{-3}$ and $3.576 \cdot 10^{-3}$.*
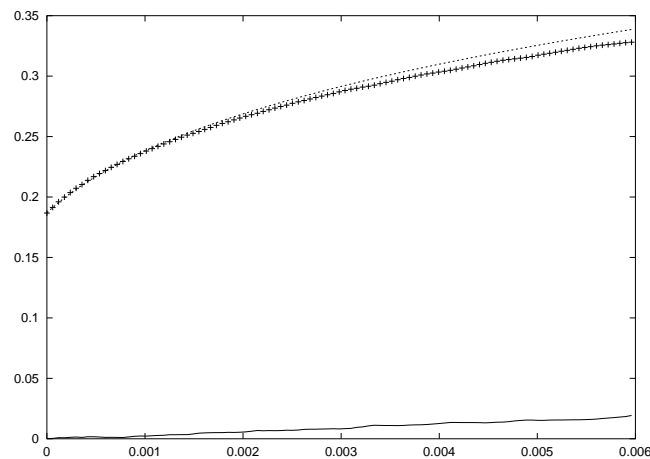


Figure 6.4: *Comparison of the numerical (*CROSSED LINE*) and the exact growth of circles represented as a level set under Willmore flow over $10000$ timesteps ($\tau = 10h^4$, $\epsilon = \frac{1}{2}h$) is shown. Additionally, the $L^\infty$ error for the radius function $r(t, \cdot)$ over the propagating level set is plotted in time at the bottom.*
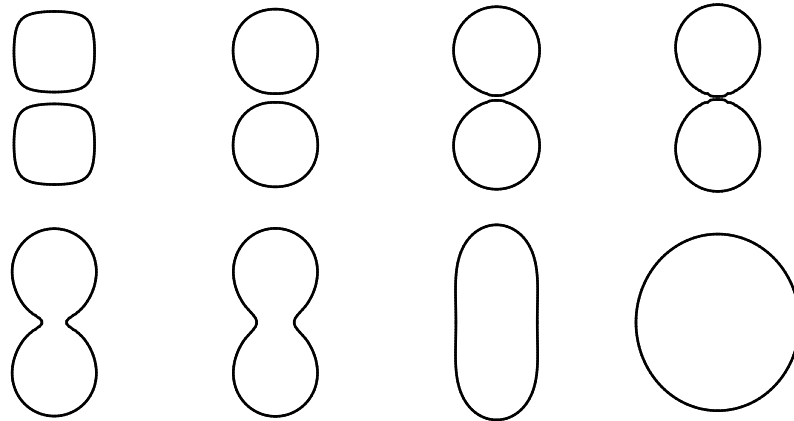
Figure 6.5: Two shapes merge under the level set evolution of Willmore flow. The parameters were chosen as follows: $\epsilon = 5h$, where $h = 128^{-1}$, the time step size $\tau$ was $10h^4$. Timesteps $0, 100, 800, 1600, 1700, 1800, 4000, 40000$ are depicted from top left to bottom right.
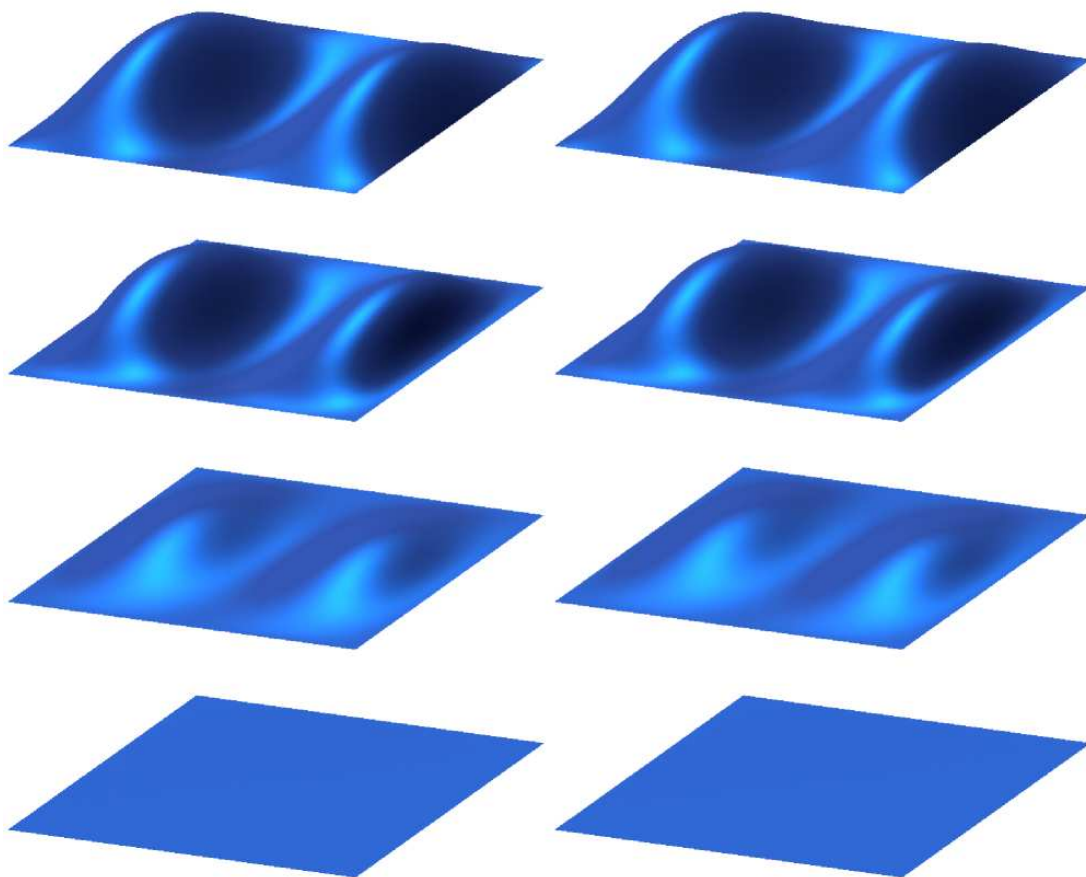


Figure 6.6: *Comparison of numerical time stepping for graph (left) and parametric (right) representation for times $t = n10^{-8}$, $n = 0, 100, 1000, 2500$.*
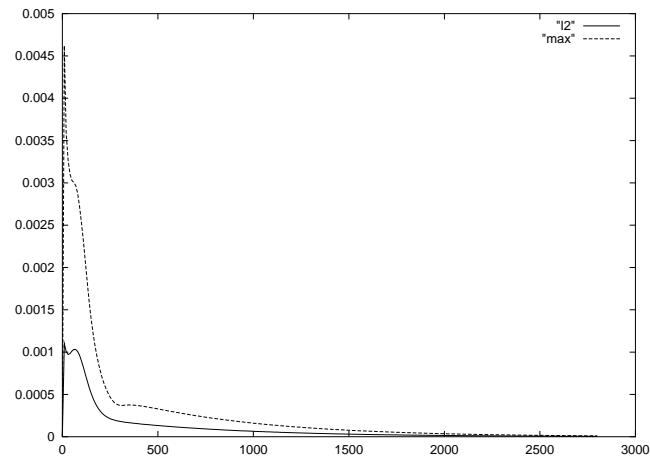
Figure 6.7: $L^2$ and $L^\infty$ difference of graph and parametric Willmore flow plotted over time steps.
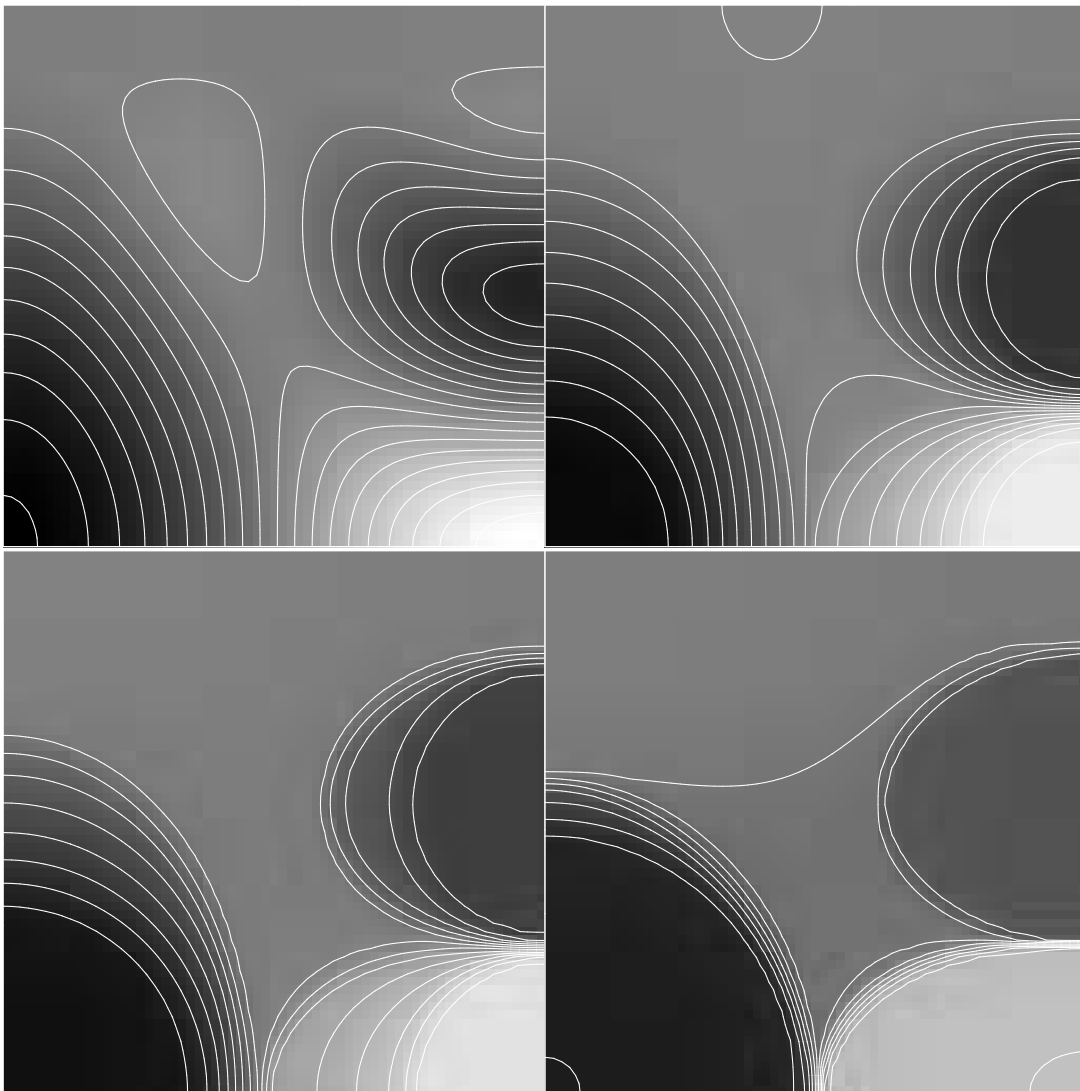


Figure 6.8: Level set evolution of Willmore flow. On the top left, some level sets of the initial configuration are shown. The other images show the result of the evolution after timesteps 1000, 5000 and 25000.
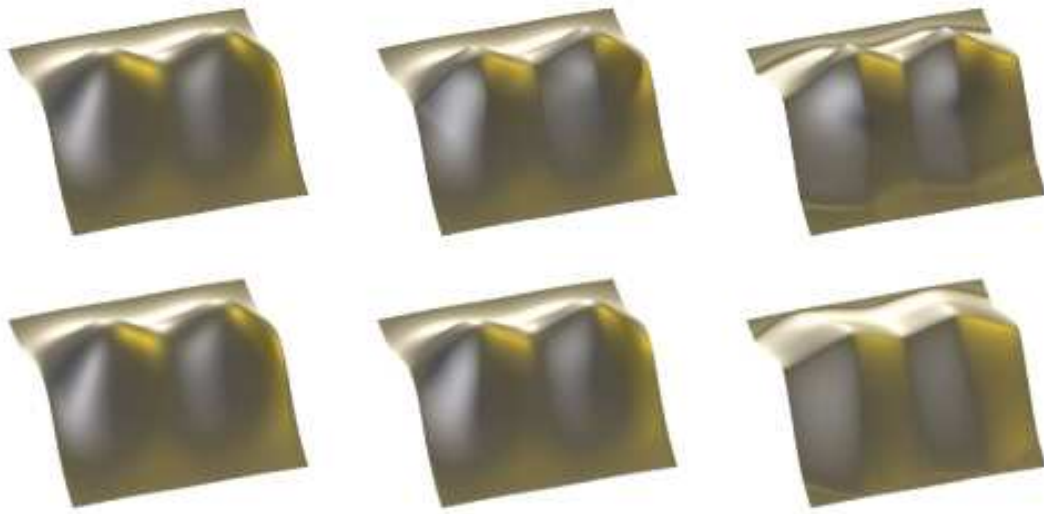
Figure 6.9: *Surface diffusion (*TOP*) and Willmore flow (*BOTTOM*) in the graph case. $p = 6$, $\tau = 2h^4$, $h = 128^{-1}$. Steps $0, 100, 5000$ are shown.*
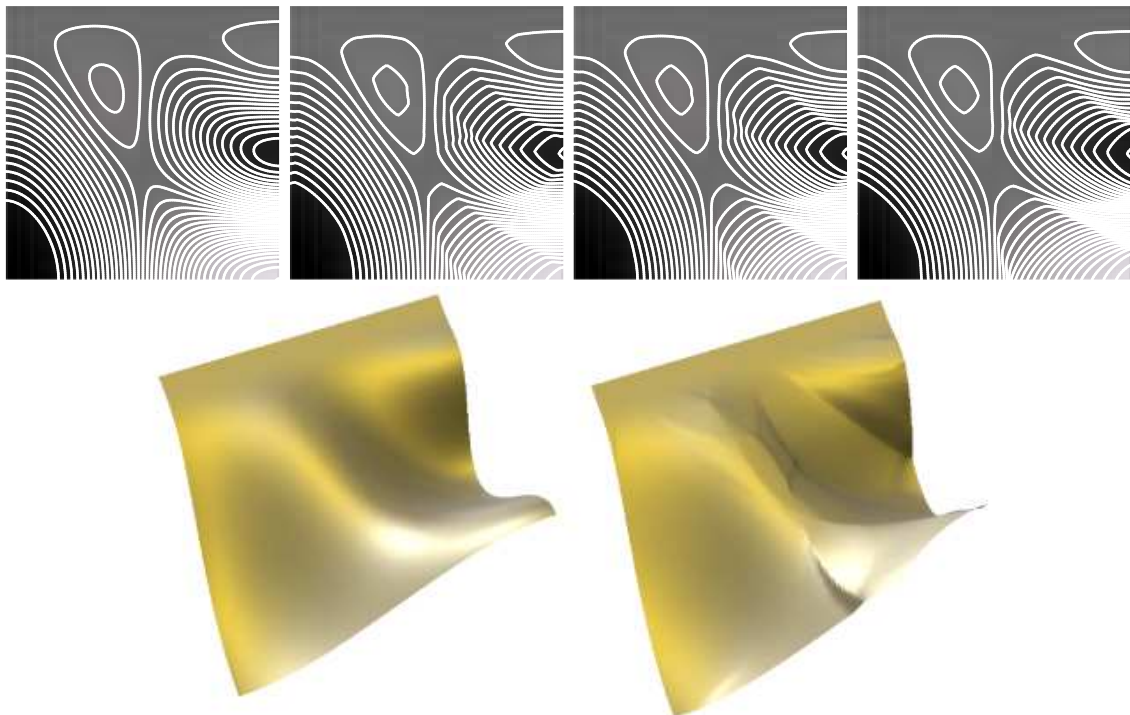


Figure 6.10: Anisotropic Surface Diffusion level set case ($\epsilon = 10h$), $p = 6$, $\tau = h^4$, $h = 128^{-1}$. Steps $0, 500, 1000, 3000$ are shown. The picture at the bottom illustrates the steepening of the level set function.
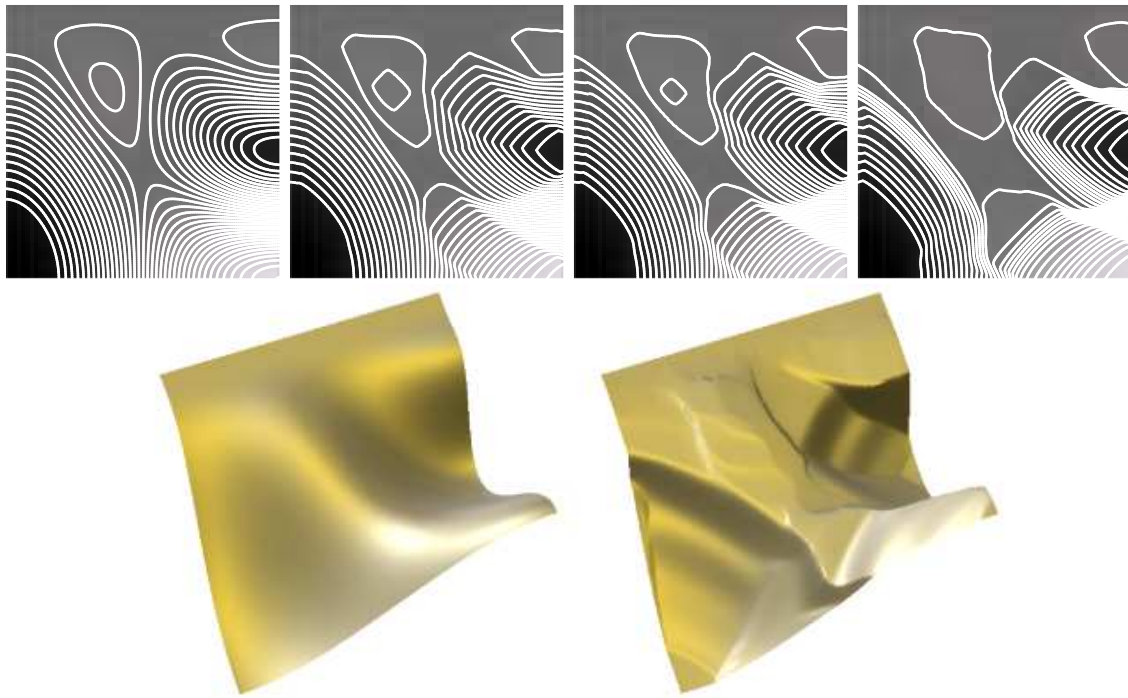
Figure 6.11: Anisotropic Willmore flow level set case ($\epsilon = 10h$), $p = 6$, $\tau = h^4$, $h = 128^{-1}$. Steps $0, 500, 1000, 3000$ are shown. The picture at the bottom illustrates the steepening of the level set function.

# Chapter 7

# Narrow band level set methods for geometric evolution problems

FOURTH-ORDER geometric evolution problems suffer from two major drawbacks in the level set context. First, embedding the evolution into the level set context, involves the fact that the dimension of the whole problem is increased by one. This is justifiable, if one is interested in the simultaneous evolution of the entire morphology $\mathcal{M}$, however if only a single level set surface is of interest, this mean a vast waste of computational efficiency, since further away of the interface, the shapes and densities of the level sets do by construction of the level set equation not affect the evolution of the particular interface of interest. In practice, however, the type of extension is not arbitrary. In order to avoid degeneracies, a level set function with a gradient magnitude close to 1 is desirable.

Secondly, the lack of the maximum principle questions the applicability of the level set approach. As in the exposition of the numerical results in the previous chapter, the existence interval for the evolution of the entire morphology may be arbitrary small for certain initial configurations, even though the evolution of the single particular surfaces would be well defined. As already pointed out by several authors [186, 188], the simultaneous evolution of level sets by fourth order geometric flows, can be ambiguous and lacks a fundamental notion of solution.

The aim of this chapter is to devise narrow band methods especially for fourth order geometric evolution problems in order to cope with these deficiencies. In particular, it is desirable to render these methods applicable to two dimensional surfaces embedded in highly resolved three dimensional data sets and to avoid having a small time interval where the solution exists. This also holds true for narrow band formulations, however, the global effect which characterizes the fourth order flow is ruled out by restricting only to a small subset of the domain $\Omega$, namely an $\epsilon$-neighborhood of the interface of interest. By maintaining a certain choice of extension of the level set function, keeping the level set function close to a signed distance function prevents steepening or flattening and ensures that the velocity is mainly given by the geometry of the interface itself. One might consider also the parametric variant of inspecting and computing the evolution of a single hypersurface. However, let us emphasize that in many applications it is not convenient to leave the level set context, especially when the surfaces are extracted from real three dimensional images, where the structural organization is canonically given by level set functions.

In the following we focus on the evolution of a single level set. The notion of a narrow band corresponds to the idea of only considering a tubular neighborhood of the surface instead of computing the evolution in the entire domain.

## 7.1 Evolution of signed distance functions

The signed distance function with respect to a set $\Omega$ is given by

$$\bar{d}_\Omega(x) := \operatorname{dist}(x, \Omega) - \operatorname{dist}(x, \Omega^c),$$

Figure 7.1: Inpainting of a subdomain of a sphere using a narrow band approach. Within the inpainting domain the initialization was chosen as a minimal surface. Steps 0, 10, 50 and 150 are shown.

and one sees directly that the Lipschitz constant of $\bar{d}_\Omega$ is not greater than 1, and that by Rademacher's Theorem is differentiable a.e. Moreover, $\|\nabla \bar{d}_\Omega\| \leq 1$. Furthermore, it is known that the differentiability of $\bar{d}_\Omega$ at $x$ only depends on the uniqueness of the projection of $x$ onto $\partial\Omega$ [6, Thm. 4.1]. According to the definition of FEDERER, a boundary is said to be *of positive reach*, if there exists a tubular neighborhood, in which the uniqueness of the projection onto the boundary is fulfilled. Note that the projection is given by [92, Ch. 4, Thm 4.4].

$$p_{\mathcal{M}_t}(x) = x - \frac{1}{2}\nabla \bar{d}_{\Omega_t}^2(x) \quad \text{for a.e.} x \in \mathbb{R}^n. \tag{7.1}$$

Consider a domain $\Omega$ with smooth boundary $\mathcal{M} := \partial\Omega$, on which we apply a geometric evolution equation. Then the evolution of the family $(\mathcal{M}_t)$ for $t \in [0, T]$ induces the evolution of the signed distance function $\bar{d}_{\Omega_t}$ and vice versa. In the case of the mean curvature flow, it is clear that $\mathcal{M}_t$ evolves in with the negative mean curvature if and only if

$$\partial_t \bar{d}_{\Omega_t}(x) = \Delta \bar{d}_{\Omega_t}(x) \quad \forall t \in [0, T], \, x \in \mathcal{M}_t$$

since the mean curvature on the interface is given by $\Delta \bar{d}_{\Omega_t}$ and considering the level set equation. This approach is due to SONER [190]. He characterized the mean curvature flow by the inequalities

$$\partial \bar{d}_{\Omega_t} \geq \Delta \bar{d}_{\Omega_t} \in \Omega_t^c \quad \text{and} \quad \partial \bar{d}_{\Omega_t} \geq \Delta \bar{d}_{\Omega_t} \in \Omega_t$$

to be understood in the viscosity sense. In the literature there is a general agreement, that formulations of geometric evolution problems based on signed distance functions is an appropriate Ansatz to analyze the evolution if single interfaces.

In [93] DELFOUR & ZOLÉSIO have studied the evolution of the distance function for a given velocity field $V$ on the interface $\mathcal{M}$. They derive the corresponding nonlinear evolution equation for the signed distance function $\bar{d}$:

$$\partial_t \bar{d}_{\Omega_t} + \nabla \bar{d}_{\Omega_t} \cdot (V(t) \circ p_{\mathcal{M}_t}) = \partial_t \bar{d}_{\Omega_t} + n_{\mathcal{M}_t} \cdot (V(t) \circ p_{\mathcal{M}_t}) = 0 \tag{7.2}$$

and moreover they have given a weak formulation for the evolution of the projection in time

$$\frac{\mathrm{d}}{\mathrm{d}t} \int_{\mathbb{R}^n} p_{\mathcal{M}_t} \cdot \psi \, \mathrm{d}\mu = \int_{\mathbb{R}^n} (p_{\mathcal{M}_t} - \mathbb{1})(V(t) \circ p_{\mathcal{M}_t}) \mathrm{div}\psi \, \mathrm{d}\mu \tag{7.3}$$
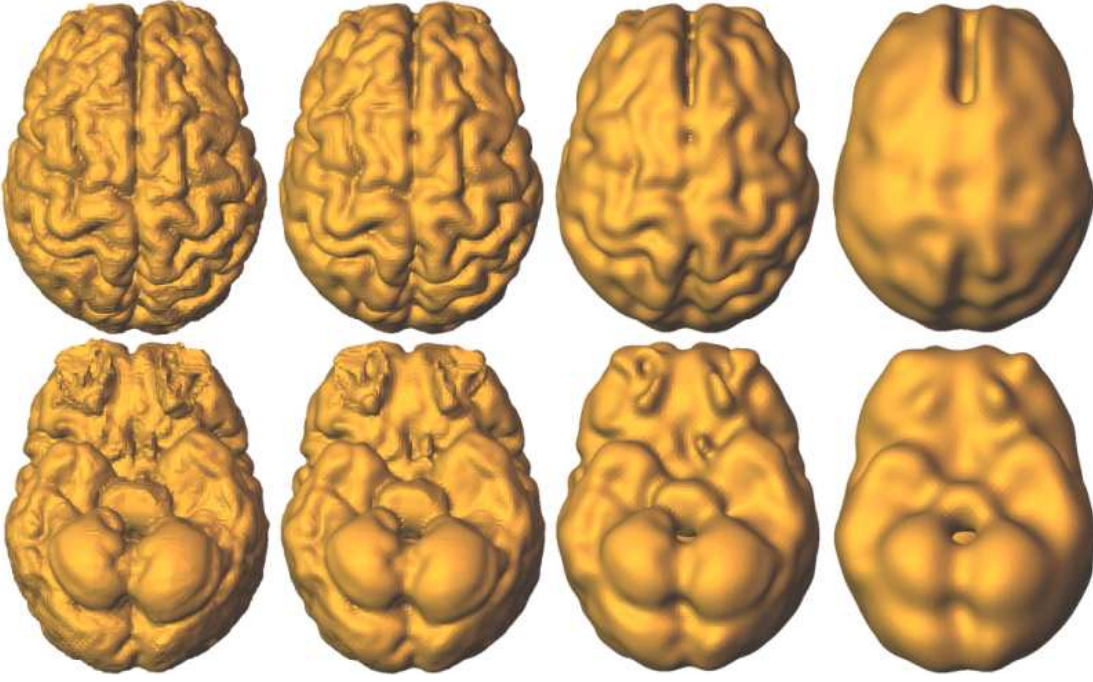
Figure 7.2: Smoothing surfaces via Willmore flow. The sequence shows the evolution starting on a noisy initial surface from the segmentation of a human brain from the top and the bottom. Steps $0$, $1$, $5$ and $30$ are shown. See also Figure 7.7.

for all test functions $\psi \in \mathscr{C}_0^\infty(\mathbb{R}^n; \mathbb{R}^n)$. In the level set context, $p_{\mathcal{M}_t}$ can be determined in a constructive way from the knowledge of $p_{\mathcal{M}_t}$, in fact $V(t) \circ p_{\mathcal{M}_t}$ corresponds to the extension of $V$ in normal direction. This becomes clear by the observation that the characteristics along $\nabla \bar{d}$ are straight lines (from $\|\nabla \bar{d}\|^2 = 1$ we infer $D^2\bar{d} \cdot \nabla \bar{d} = 0$), where $\bar{d}$ is sufficiently smooth and that $\nabla \bar{d}$ is equal to the normal of the interface on $\mathcal{M}$. If $\mathcal{M}_t$ is a smooth surface, then there exists a tubular neighborhood, in which $\bar{d}_{\Omega_t}$ is smooth. Hence, also $V^{\text{ext}}(t) := V \circ p_{\mathcal{M}_t}$ is constant on these trajectories. Note that this formulation only depends on the geometry of $\mathcal{M}_t$, more precisely, the evolution only depends on the velocity $V(t)$ on the surface $\mathcal{M}_t$. In the following, we focus on practical algorithms to evolve the geometry by evolution of its signed distance function in a small neighborhood. In principle, the following approaches to solving the coupled system consisting of equations (7.2) and (7.3) are imaginable.

*(i)* One may first compute the velocity $V(t)$ on the interface $\mathcal{M}_t$, extend it to $V^{\text{ext}}(t)$ defined on a small neighborhood, and finally compute an explicit timestep of the approximate signed-distance function. [119, 168, 186] In practice higher order ENO schemes are advisable, however, due to the fact that his approach is fully explicit, one is restricted to small time steps to be $\tau \leq Ch^k$, where $k$ is the order of the evolution equation.

*(ii)* A different approach would consist in first determining the projection from the knowledge of the interface in a constructive way, e. g., via the computation of the signed distance function and taking into account the relation (7.1). From this one could try to solve (7.2) implicitly. However, the numerical computation of the projection by the relation (7.1) should be avoided due to instabilities.

*(iii)* In order to avoid the prohibitive time step restrictions, one may aim to solve the system (7.2)-(7.3) fully implicitly. Because these equations are nonlinear this system can however not be implemented in a straightforward way.

In the following we will propose practical schemes to approximate the solution of the evolution of the signed distance function. The main idea is to iteratively solve the level set formulation

of the corresponding evolution equation, and enforcing the level set function to remain close to a signed distance function by an appropriate choice of boundary conditions. Furthermore we will describe the efficient implementation of the solution of higher order PDEs on a thin discrete subdomain which surrounds the discrete interface $\mathcal{M}_{t,h}$.

## 7.2 Iterative solution of the nonlinear evolution problem

Before we head onto the fully discrete scheme for narrow band methods we first discretize in time. We consider a tubular neighborhood $B_\delta(\mathcal{M}(t))$ for $\delta > 0$ and distinguish between the level set function $\Phi(t) : B_\delta(\mathcal{M}(t)) \to \mathbb{R}$ and the exact signed distance function $\bar{d}_{\Omega(t)}$, where $\Omega(t) := \{\Phi(t, \cdot) > 0\}$. In fact, since we are in interested in the evolution of $\mathcal{M}(t) = \mathcal{M}_0[\Phi(t)]$. $\Phi$ may differ from $\bar{d}$ as long as the zero level set reflects the true shape.

### 7.2.1 Implicit time discretization and boundary conditions

We consider the following evolution equation for an initial surface $\mathcal{M}_0$ and an initial choice of sign for the signed distance function $\bar{d}$:

$$
\begin{aligned}
\partial_t \phi + V_{\phi(t)}^{\text{ext}} \|\nabla \phi\| &= 0 && \text{in} && B_\delta(\mathcal{M}(t)) \\
\phi(0) &= \bar{d}_{\Omega_0} && \text{in} && B_\delta(\mathcal{M}_0)
\end{aligned}
$$

where we for now have left the boundary condition on $(0, T] \times \partial B_\delta(\mathcal{M}(t))$ unspecified. We now consider a straightforward partition of $[0, T]$ into intervals of length $\tau > 0$ and to approximate the derivative with respect to time we use a forward difference quotient, i. e., $\partial_t \phi \approx \frac{\Phi^{k+1} - \Phi^k}{\tau}$, where again $\Phi^k := \phi(\tau k)$. For the other occurrences of $\Phi$ we have to decide, whether to choose the old value $\Phi^k$ or the unknown function $\Phi^{k+1}$. For obvious reasons, it is not practicable to solve the problem for a varying domain $B_\delta(\mathcal{M}(t))$, so we keep it fixed during one timestep and treat the other terms implicit. We arrive at the following weak formulation

$$
\int_{B_\delta(\mathcal{M}_k)} \frac{(\Phi^{k+1} - \Phi^k)\vartheta}{\tau \|\nabla \Phi^{k+1}\|} \, \mathrm{d}\mu + \int_{B_\delta(\mathcal{M}_k)} V_{\Phi^{k+1}}^{\text{ext}} \vartheta \, \mathrm{d}\mu = 0 \quad \forall \vartheta \in \mathscr{C}_0^\infty(B_\delta(\mathcal{M}_k)). \quad (7.4)
$$

The extended velocity ensures, that $\Phi^{k+1}$ will remain a signed distance function. However, one has to take the following significant subtlety into account: in order to obtain a fully implicit scheme, the extension of the velocity has to be computed with respect to the yet unknown new interface. The computation of $p_\Gamma$ or, directly the extended velocity $V^{\text{ext}}$ should extend the velocity from $\Phi^{k+1}$ otherwise the whole scheme remains explicit. However, this would make the whole problem hardly handable in practice. Our approach is the following. We drop the extension of the velocity and compute the velocity from the neighboring level sets, which vary only slightly in shape and ensure that $\Phi$ remains close to a distance function by suitable boundary conditions. In fact, for mean curvature for example it is known that this scheme converges to the exact solution i. e., the $L^2$ error behaves is estimated by $C(\tau + h^2)$ (cf. DECKELNICK&DZIUK [88]).

**Second order flows**

Let us now consider the mean curvature motion as a prototype problem for second order Cauchy problems to illustrate the different possible choices of boundary conditions. The velocity is given by the negative mean curvature $h = \text{div}(n)$, and hence, we obtain, with non-homogenous *Neumann* boundary conditions

$$
\int_{B_\delta(\mathcal{M}_k)} \frac{(\Phi^{k+1} - \Phi^k)\vartheta}{\tau \|\nabla \Phi^{k+1}\|} \, \mathrm{d}\mu + \int_{B_\delta(\mathcal{M}_k)} \frac{\nabla \Phi^{k+1} \cdot \nabla \vartheta}{\|\nabla \Phi^{k+1}\|} \, \mathrm{d}\mu = \int_{\partial B_\delta(\mathcal{M}_k)} \gamma \vartheta \, \mathrm{d}A \quad (7.5)
$$

for all $\vartheta \in \mathscr{C}^\infty(B_\delta(\mathcal{M}_k))$. The function $\gamma$ (recall the consistency condition $|\gamma| \leq 1$) prescribes the normal component of $\nabla \Phi^{k+1}/\|\nabla \Phi^{k+1}\|$. In order to keep $\Phi^{k+1}$ close to a signed distance function, we postulate:

*A natural choice of boundary conditions is given by the Neumann resp. Dirichlet data induced by the signed distance function.*

Hence, in the case of *Neumann* boundary conditions, we set $\gamma = \nabla \bar{d} \cdot \nu$, which means nothing else than

$$\frac{\mathrm{d}\Phi}{\mathrm{d}\nu} = \frac{\mathrm{d}\bar{d}}{\mathrm{d}\nu} \quad \text{on} \quad \partial B_\delta(\mathcal{M}_k).$$

Here $\nu$ denotes the outer normal of $B_\delta(\mathcal{M}_k)$. The geometric interpretation is that simply the level lines of $\Phi$ are parallel to the level lines of $\bar{d}$ along the boundary. Observe that for the choice of the domain as a tubular neighborhood, we have $\gamma = \nabla \bar{d} \cdot \nu = 1$, however this will change as soon the domain deviates from $B_\delta(\mathcal{M}_k)$ or the fact that $B_\delta(\mathcal{M}(t))$ changes in time and if the problem is discretized in space.

The signed distance function also depends on $\Phi$, in particular the level set $\mathscr{M}_0[\Phi]$. After the solution of (7.4), we obtain a new interface, which induces a new signed distance function. As we aim towards the boundary condition $\frac{\mathrm{d}\Phi^{k+1}}{\mathrm{d}\nu} = \frac{\mathrm{d}\bar{d}^{k+1}}{\mathrm{d}\nu}$, we propose an iterative scheme: for $i = 1, \dots$ solve

$$\int_{B_\delta(\mathcal{M}_k)} \frac{(\Phi_{i+1}^{k+1} - \Phi^k)\vartheta}{\tau\|\nabla\Phi_i^{k+1}\|} \,\mathrm{d}\mu + \int_{B_\delta(\mathcal{M}_k)} \frac{\nabla\Phi_{i+1}^{k+1} \cdot \nabla\vartheta}{\|\nabla\Phi_i^{k+1}\|} \,\mathrm{d}\mu \quad = \quad \int_{\partial B_\delta(\mathcal{M}_k)} (\bar{d}_i^{k+1} \cdot \nu)\vartheta \,\mathrm{d}A \quad (7.6)$$

for all $\vartheta \in \mathscr{C}^\infty(B_\delta(\mathcal{M}_k))$ until convergence. Here, $\bar{d}_i^{k+1}$ denotes the signed distance function for the interface given by $\Phi_i^{k+1}$, and set $\Phi_1^{k+1} := \Phi^k$ (the stationary point of the previous iteration).

A similar scenario can be obtained by prescribing *Dirichlet* boundary data. Here, the natural choice is to use the boundary values given by the signed distance function, i. e.,

$$\Phi = \bar{d} \quad \text{on} \quad \partial B_\delta(\mathcal{M}_k).$$

By the same reasoning as above, it may be useful to iterate over $i$ and successively update the boundary conditions according to the new signed distance function $\bar{d}$.

The difference is fundamental: while the *Neumann* condition allows level sets to move outward or inward as long as they stay *parallel* to the level sets of the signed distance function, the *Dirichlet* condition allows directions of the level sets to vary freely along the boundary as long as the position of the level sets along the boundary are the same as those of the signed distance function.

Let us remark, that in the continuous formulation the boundary conditions should not influence the evolution of the interface in the interior, since in theory the motion of the level sets is decoupled. However, the finite element discretization in space induces some numerical viscosity also in normal direction, which has the effect of a local averaging.

### Fourth order flows

For fourth order flows, we are left to choose two boundary conditions. Here, we will consider the level set formulation of Willmore flow of section 6.2 as a prototype problem. In section 6.5 we have described the boundary conditions in detail.

*(i)* **Neumann conditions**—In the second equation for the weak formulation of the Willmore flow, we can prescribe the normal component (with respect to boundary) of the normal (of the level set) in the same manner as above for the mean curvature flow by choosing $\gamma$ appropriately. In the first equation, we end up with a *Neumann* condition for $w$, depending on the boundary function $\eta$:

$$P\nu \cdot \nabla w = \eta - \frac{h^2}{2}\gamma = \eta - \frac{w^2}{2\|\nabla\Phi\|^2}\gamma.$$

It is more intuitive to recall equation (6.20), which gives a relation between $\eta$ and the normal components of $\Phi$.

$$\int_{\partial\Omega} \frac{W^{k+1}}{2\|\nabla\Phi^k\|_\epsilon} \left( \frac{\nabla\Phi^{k+1}}{\|\nabla\Phi^k\|_\epsilon} \cdot \nu \right) \Theta \,\mathrm{d}A - \int_{\partial\Omega} \left( \frac{P_\epsilon[\Phi^k]}{\|\nabla\Phi^k\|_\epsilon}\nabla W^{k+1} \cdot \nu \right) \Theta \,\mathrm{d}A = \int_{\partial\Omega} \mathcal{I}_h\eta \,\mathrm{d}A$$

By inserting the corresponding normals and curvatures of the distance function, i. e., $\nabla \bar{d}$ resp. $\Delta \bar{d}$ instead of $\nabla \Phi^{k+1}$ resp. $W^{k+1}$ into this integral, we obtain a natural choice for the *Neumann* data, if we aim at keeping $\Phi$ compatible with the signed distance function. These are $1^{st}$ and $3^{rd}$ order conditions for $\Phi$.

*(ii)* **First and second order conditions**—A probably more intuitive pair of boundary conditions is by choosing *Neumann* conditions in the second equation, resulting in $\partial_\nu \Phi = \partial_\nu \bar{h}$ and Dirichlet conditions for $\Phi$. Here, simultaneously the values and the directions of the level set function are kept in accordance with the desired signed distance function. As mentioned in the previous chapter, this pair of boundary conditions is the natural choice on the boundary of the region to be restored in the inpainting problem. In this context, the geometric meaning of this boundary condition can be interpreted by observing that one time step corresponds to a time step of an inpainting problem, such that the level sets are inpainted according to the distance function in the exterior. The boundary conditions are adjusted in every timestep, to ensure that the interface is allowed to move freely and is only driven by the evolution equation itself.

*(iii)* **Dirichlet conditions in both equations**—Alternatively, we may prescribe the exact data $\bar{d}$ and $\Delta d$ along the boundary by considering Dirichlet conditions in both equations. These are boundary conditions of zero$^{th}$ and $2^{nd}$ order.

## 7.2.2  Finite Element discretization in space

We start by defining subgrids of the triangulation $\mathscr{T}_h$ which divides the entire domain $\Omega$ into cells. These subgrids correspond to different regimes of the neighborhood.

For a given $\delta > 0$ and a given surface $\mathcal{M}$, we define

$$\mathscr{T}_{h,\delta} = \{T \in \mathscr{T}_h \,:\, T \cap B_\delta(\mathcal{M}) \neq \emptyset\}$$

and call this set of triangles the *discrete narrow band*. Furthermore we define the *inner narrow band*, as the set of cells which intersects $\mathcal{M}$ by

$$\mathscr{T}_{h,0} := \{T \in \mathscr{T}_h \,:\, T \cap \mathcal{M} \neq \emptyset\} .$$

Moreover, for an arbitrary triangulation $\mathscr{G}$ we define the extension $\mathscr{G}^+$ to a one-neighborhood, by the union of all cells of which at least one vertex is contained in $\mathscr{G}$ by

$$\mathscr{G}^+ := \{T \in \mathscr{T}_h \,:\, \mathcal{N}(T) \cap \mathcal{N}(\mathscr{G}) \neq \emptyset\} \qquad \mathscr{G}^{(L)} = (\mathscr{G}^{(L-1)})^+ \quad \mathscr{G}^{(0)} = \mathscr{G}.$$

We consider two types of choices of the narrow band:

*(i)* The width of the narrow band is determined by $\delta > 0$. We set $\mathscr{T}_{h,\mathrm{nb}} := \mathscr{T}_{h,\delta}$.

*(ii)* Alternatively we consider building the narrow band by a certain number $L \in \mathcal{N}$ of cell layers around $\mathscr{T}_{h,0}$ and set $\mathscr{T}_{h,\mathrm{nb}} := \mathscr{T}_{h,0}^{(L)}$.

Depending on the context, triangulations will also be understood as the interior of the corresponding set $\bigcup_{T \in \mathscr{G}} \bar{T}$. For a triangulation $\mathscr{G}$, we define the finite element subspace

$$\mathcal{V}^h(\mathscr{G}) := \left\{u \in \mathscr{C}^0(\mathscr{G}) \,:\, u\big|_T \text{ piecewise multilinear}\right\} .$$

## 7.2.3  Computation of the distance function and extension in normal direction from a fixed interface

In this section, we will describe a finite element approach to the computation of the signed distance function. The solution approach is based on the iterative solution scheme for Hamilton-Jacobi equations which recently been introduced by Bornemann&Rasch [29].

Here we will solve the Dirichlet problem for the *eikonal equation*

$$\|\nabla\phi\| = 1 \text{ in } \mathscr{T}_{h,\partial}, \quad \phi\big|_{\partial\mathscr{T}_{h,0}} = g \tag{7.7}$$

where $g$ will later be given by the trace of $\phi$ from the solution of the *local interface scheme* in $\mathscr{T}_{h,0}$. The Hopf–Lax update function $\Lambda : \mathcal{V}_{h,0} \to \mathcal{V}_{h,0}$ of the corresponding Hamiltonian $H(x,p) = \|p\| - 1$, is given by

$$(\Lambda_h\phi_h)(x_h) = \min_{y\in\partial\omega_h(x_h)} \left(\phi_h(y) + \|x_h - y\|\right), \qquad x_h \in \mathcal{N}(\mathscr{T}_{h,\partial}), \ \phi \in \mathscr{T}_{h,\partial} \tag{7.8}$$

where $\omega(x_h)$ is given by

$$\omega(x_h) := \{C \in \mathscr{T}_{h,\partial} : x_h \in \mathcal{N}(C)\}. \tag{7.9}$$

In [29] monotone convergence for Jacobi or Gauss-Seidel type fixed point iterations $\phi_h^{k+1} = \Lambda_h\phi_h^k$ has been proved. Similar to simultaneous computation of a distance field and an extension of a function given on the boundary in the *fast marching method* the iteration can be enhanced by an extension update function $\Theta_h : \mathcal{V}_{h,0} \to \mathcal{V}_{h,0}$. The pointwise update for the extension equation

$$\nabla w_k \cdot \nabla\phi \text{ in } \mathscr{T}_{h,\partial}, \quad w_k\big|_{\partial\mathscr{T}_{h,0}} = h \tag{7.10}$$

is then given by

$$\Theta_h w_k(x_h) = w_k(\tilde{y}) \text{ where } \tilde{y} := \arg\min_{y\in\partial\omega_h(x_h)} \left(\phi_h(y) + \|x_h - y\|\right) \tag{7.11}$$

For the computation of a *signed* distance function we slightly change the update function, where the $\phi$ is negative

$$(\Lambda_h\phi_h)(x_h) = \begin{cases} \min_{y\in\partial\omega_h(x_h)} \left(\phi_h(y) + \|x_h - y\|\right), & \phi(x_h) \geq 0 \\ \max_{y\in\partial\omega_h(x_h)} \left(\phi_h(y) - \|x_h - y\|\right), & \phi(x_h) < 0 \end{cases} \tag{7.12}$$

for $x_h \in \mathcal{N}(\mathscr{T}_{h,\partial})$, $\phi \in \mathscr{T}_{h,\partial}$. For linear functions on triangular elements explicit formulas are given in [29], which remain valid unchanged for bilinear quadrilateral elements, since also here minima over line segments on which $\phi_h$ varies linearly is determined. For trilinear elements in 3D, the Hopf–Lax update means to find minima over a face on which the discrete function is bilinear. In this case, the update function is given by

## 7.3 A narrow band algorithm for semi-implicit schemes of geometric evolution equations

In this section we will describe the algorithmical details on how the narrow band method can be implemented efficiently. We will throughout this chapter let the full index set of the finite elements space unchanged and use subsets which correspond to the degrees of freedom within the narrow band. For higher order evolution problems the main restricting factor is given by speed, not by memory requirements. Furthermore, since the discrete narrow band is always built around the moving interface, it has to be reconstructed frequently, which means that the set of active degrees of freedoms has to be adjusted as well. The subsets of indices can be constructed in a very efficient way. On the other hand, it would be very inefficient to reallocate coefficient vectors in each iteration just to maintain a small index set.

The main algorithmical components of the narrow band method are:

*(i)* distance function computation

*(ii)* grid and boundary management

*(iii)* management of the corresponding degrees of freedom and efficient solvers

*(iv)* incorporation of boundary conditions

*(v)* the main iteration

### 7.3.1   Distance function computation

During the startup, in order to construct the initial narrow band grid, we first to have to locate the interface by finding all intersected cells, and construct a discrete neighborhood of cells. Even though we have two possibilities to select the cells which should belong to the grid, namely by extending a discrete sets of grids by layers of cells or, alternatively, to select all cells which intersect the $\delta$-neighborhood $B_\delta(\mathcal{M}_h(t))$, where $\mathcal{M}_h(t)$ denotes the discrete interface, which is given by the zero level set of the finite element function $\Phi(t)$.

In either case we will need the distance function in order to prescribe boundary conditions. A single traversal through the entire grid is necessary to locate $\mathcal{M}_h(0)$ at the beginning of the algorithm in order to locate the set of intersected cells The union of these cells yields the triangulation $\mathscr{T}_{h,0}$, which is algorithmically represented as an explicit storage container. This is done in the fashion of the *Marching Cubes* algorithm proposed by LORENSEN & CLINE [75]. From then on, full traversals are no longer necessary, since the narrow band subgrid can be used from then on. Hence, we can waive on more efficient multilevel techniques, based on hierarchical estimators, which are very efficient for repeated extraction of iso-surfaces for static data [117, 167, 166]. The *Marching Cubes* algorithm generates a triangulation of the interface $\mathcal{M}_h(t)$. During the traversal, the boundary data of the distance function $d_h$ on the nodes $\mathcal{N}(\mathscr{T}_{h,0})$ is initialized by the distance of the corresponding node to the triangulation of the interface of the intersected cell. This triangulation only has to be locally available and is generated on the fly efficiently using lookup tables. We will not expand this in further detail here and refer the reader to []. On these nodes we will now chose the same sign for $\bar{d}$ as the sign of $\phi$. Now, we proceed by iterating over the update procedure of the *Hopf-Lax*-scheme (7.8). Here, we use an Gauss-Seidel update, to chose an efficient ordering in the spirit of the *Fast-Marching-method*. This technique maintains a heap structure which stores the set of "candidate" nodes, which are to be updated and allows instant access on the node with the smallest value (cf. the book of SETHIAN [186] and [29] for further details). Hence, we can safely stop the computation when this value exceeds the threshold $\delta + h$ in order to make sure that all values are computed on the narrow band grid $\mathscr{T}_{\delta,h}$.

If we chose the narrow band by the construction of discrete layers, the threshold has to be adjusted appropriately.

### 7.3.2   Grid and boundary management

Finite elements are always based on triangulations. In order to assemble finite element matrices, the usual procedure is to traverse all elements, and to compute the integral contributions for all possible pairs of local indices locally and add them into the matrix. It suffices to have knowledge about the set of cells, their geometry and the mapping of local indices to global indices to perform this procedure. This means that, algorithmically, the triangulation can be represented as an unstructured set of cells. Since, the triangulation is based on equally shaped elements, the cells are entirely described by their offset position.

Even though for the assembly itself neighborhood information is not required, we store all elements in a `hash_set`, which allows efficient traversal and fast random access. This allows the fast extraction of the boundary by a simple single traversal of all elements in the narrow band. For each cell, we traverse all faces and check if the neighboring element with respect to this face is contained in the triangulation of the narrow band. If this is not the case, this face is obviously a boundary element and is stored in a container which doesn't require any special structure.

### 7.3.3   Degrees of freedom and efficient solvers

The choice of the narrow band grid determines the set of global indices of the finite element space $\mathcal{V}^h(\mathscr{T}_{h,\mathrm{nb}})$. In the case of nodal basis functions, these correspond to the set of nodes $\mathcal{N}(\mathscr{T}_{h,\mathrm{nb}})$. The entire set of global coefficients is stored in a large vector with dimension $\dim \mathcal{V}^h(\mathscr{T})$. However, for the computation on the narrow band the set unknowns is a fragmented subset of this set. Iterative solvers can be written in terms of local operations on the coefficients and matrix rows. For instance, in a conjugate gradient solver, scalar products and
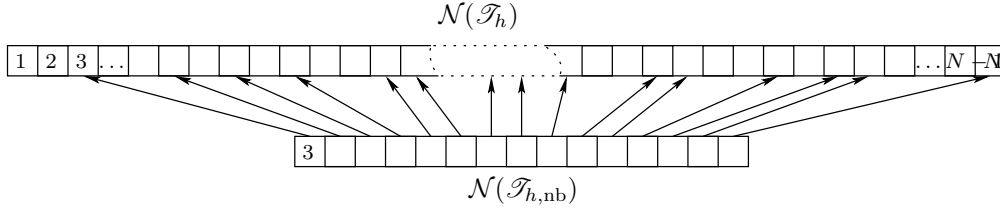
Figure 7.3: *Generation of a small set of coefficients by referencing the required indices from a larger vector.*

multiplications of a matrix row with the vector are computed. In order to ignore the coefficients which are not in $\mathcal{N}(\mathscr{T}_{h,\mathrm{nb}})$, one might set the diagonal entries of the matrix to $1$ and set the right-hand side of the linear system to arbitrary values for coefficients $\alpha \notin \mathcal{N}(\mathscr{T}_{h,\mathrm{nb}})$. However, this would still require scalar products and matrix-vector products to be computed for the entire set of coefficients (see Figure 7.3).

It is by far more efficient to perform the entire computations only on the set coefficients which correspond to the finite element space of the narrow band. Immediately after the construction of $\mathscr{T}_{h,\mathrm{nb}}$, we determine its degrees of freedom and perform a *run length encoding*, which enables us to iterate through $\mathcal{N}(\mathscr{T}_{h,\mathrm{nb}})$ efficiently in $O(\dim \mathcal{N}(\mathscr{T}_{h,\mathrm{nb}}))$. Scalar products and matrix vector products can now be implemented efficiently by iterating over the run length encoded set of coefficients. The matrices are represented by a sparse matrix structure, consisting of sparse rows. These rows only have to be initialized for indices in $\mathcal{N}(\mathscr{T}_{h,\mathrm{nb}})$, the other rows don't require any memory and are ignored during the matrix-vector multiplication.

### 7.3.4 Incorporation of boundary conditions

As described in Section 7.2.1, we have to prescribe boundary conditions in every time step of the iteration.

**General geometric problems of second order**

Again we first consider second order PDEs for level set formulations of geometric flows and assume they are given in the following divergence form

$$\partial_t \phi - \mathrm{div}_{\mathbb{R}^n}\big(A(x,\phi)\nabla\phi\big)\|\nabla\phi\| = 0 \quad \text{in } B_\delta(\mathcal{M}(t))$$

and hence the Neumann conditions are given by $A(x,\phi)\nabla\phi \cdot \nu = \gamma$ on $\partial B_\delta(\mathcal{M}(t))$. The natural choice for $\gamma$ is then determined by the signed distance function, i. e., $\gamma = A(x,\phi)\nabla\bar{d}\cdot\nu$ and so we obtain the corresponding backward Euler scheme in matrix formulation:

$$(\mathbf{M}[\|\nabla\phi\|^{-1}] + \tau\mathbf{L}[A(x,\phi)])\bar{\Phi}^{k+1} = \mathbf{M}[\|\nabla\phi\|^{-1}]\bar{\Phi}^k + \mathbf{R}_\gamma[\bar{d}]$$

where we have set

$$(\mathbf{R}_\gamma[\bar{d}])_\alpha = \int_{\partial B_\delta(\mathcal{M}(t))} \mathcal{I}_h\gamma\,\Psi_\alpha\,\mathrm{d}A \quad \alpha \in I(\mathcal{V}^h).$$

For *Dirichlet* boundary conditions, one proceeds similarly as described in Section 6.6.3.

**General geometric problems of fourth order**

We consider general fourth order problems of the following form, where $q_1$, $q_2$ are either $0$ or $1$:

$$\partial\phi - \mathrm{div}(A_1\nabla\phi - A_2\nabla(\mathrm{div}(B\nabla\phi)\|\nabla\phi\|^{q_2})\|\nabla\phi\|^{q_1} = 0 \quad \text{in } B_\delta(\mathcal{M}(t))$$

which can be written as two coupled second order equations. Here, for *Neumann* boundary conditions, we obtain the weak formulation:

$$\int_{B_\delta(\mathcal{M}(t))} \frac{\partial_t \phi\,\vartheta}{\|\nabla\phi\|^{q_1}}\,\mathrm{d}\mu + \int_{B_\delta(\mathcal{M}(t))} (A_1\nabla\phi\cdot\nabla\vartheta + A_2\nabla w\cdot\nabla\vartheta)\,\mathrm{d}\mu = \int_{\partial B_\delta(\mathcal{M}(t))} \eta\vartheta\,\mathrm{d}A$$

$$\int_{B_\delta(\mathcal{M}(t))} \frac{w\,\psi}{\|\nabla\phi\|^{q_2}}\,\mathrm{d}\mu - \int_{B_\delta(\mathcal{M}(t))} B\nabla\phi\cdot\nabla\psi\,\mathrm{d}\mu = \int_{\partial B_\delta(\mathcal{M}(t))} \gamma\psi\,\mathrm{d}A$$

for test functions $\vartheta,\ \psi \in C^\infty(B_\delta(\mathcal{M}(t)))$. As before, choosing $\gamma$ and $\eta$ means to prescribe the boundary conditions

$$A_1\nabla\phi\cdot\nu + A_2\nabla w\cdot\nu = \eta \quad \text{and } B\nabla\phi\cdot\nu = \gamma.$$

**Remark 7.3.1.** *This formulation covers the geometric flows that we have already described in Chapter 6:*

- **Willmore flow**—*Choose $q_1 = q_2 = 1$ and set $A_1 := \frac{w^2}{2\|\nabla\phi\|^3}$, $A_2 := \frac{P[\phi]}{\|\nabla\phi\|}$ and $B := \frac{1}{\|\nabla\phi\|}$.*

- **Surface diffusion**—*Choose $q_1 = q_2 = 0$ and set $A_1 := 0$, $A_2 = P[\phi]$ and $B := \frac{1}{\|\nabla\phi\|}$.*

As always, *Dirichlet* conditions are incorporated by replacing the set of test functions by $C_0^\infty(B_\delta(\mathcal{M}(t)))$ in one or both of the equations. After the discretization in time by a finite difference approximation of the time derivative, and choosing the nonlinear terms to be explicit one can decompose $\phi$ (or similarly $w$) into $\phi = \phi_0 + \phi_\partial$, where $\phi_\partial$ is an admissible function attaining the desired Dirichlet values on the boundary.

In order to apply the boundary conditions, which we have discussed in Section 7.2.1 the implementation of the Neumann conditions can be performed in a straightforward manner by choosing $\eta := A_1\nabla\bar{d}\cdot\nu + A_2\nabla w_{\bar{d}}\cdot\nu$ and $\gamma := -B\nabla\bar{d}\cdot\nu$, where $w_{\bar{d}}$ corresponds to the solution of

$$\int_{B_\delta(\mathcal{M}(t))} \frac{w_{\bar{d}}\,\psi}{\|\nabla\bar{d}\|^{q_2}}\,\mathrm{d}\mu - \int_{B_\delta(\mathcal{M}(t))} B\nabla\bar{d}\cdot\nabla\psi\,\mathrm{d}\mu = \int_{\partial B_\delta(\mathcal{M}(t))} \gamma\psi\,\mathrm{d}A \qquad (7.13)$$

In order to prescribe the *Dirichlet* conditions in the second equation, or *Neumann* conditions in the first equation, it is required to determine the values of $w_{\bar{d}}$ resp. $\nabla w_{\bar{d}}$ along the boundary. However, this evaluation of $w_{\bar{d}}$ on a surface of co-dimension 1 leads to a loss of consistency , which is even worse, when derivatives of $w_{\bar{d}}$ have to be evaluated.

### Dirichlet conditions in both equations with overlapping domains

We propose an alternative strategy to allow a convenient implicit evaluation of the second variable on the boundary. It is easy to achieve that the signed distance function is also available in a slightly larger domain than $B_\delta(\mathcal{M}(t))$, say for $\delta^+ > \delta$. In this case we may solve (7.13) on $B_{\delta^+}(\mathcal{M}(t))$ with homogeneous *Neumann* conditions to obtain $w_{\bar{d}}^+$, so that we obtain $w_{\bar{d}} = w_{\bar{d}}^+\big|_{B_\delta(\mathcal{M}(t))}$. In order to discretize this approach we are dealing with the three index sets

$$I(\mathcal{V}_0^h) \subset I(\mathcal{V}^h) \subset I(\mathcal{V}^{h,+}).$$

On account of $\|\nabla\bar{d}\| = 1$ a.e., this translates into

$$\bar{w}_{\bar{d}} = \mathrm{Restr}[\mathcal{V}^h](\mathbf{M}^+)^{-1}\mathbf{L}^+[B]\bar{d}^+$$

where notations $\mathbf{M}^+$ and $\mathbf{L}^+$ correspond to assembly of the matrices on the discretization $\mathscr{T}_{\delta^+,h}$ of the enlarged domain $B_{\delta^+}(\mathcal{M}(t))$ and $\mathrm{Restr}[\mathcal{V}^h]$ simply corresponds to the restriction of the coefficient vector by dropping all coefficients, which are not available in the (smaller) index set of the finite element space $\mathcal{V}^h$.
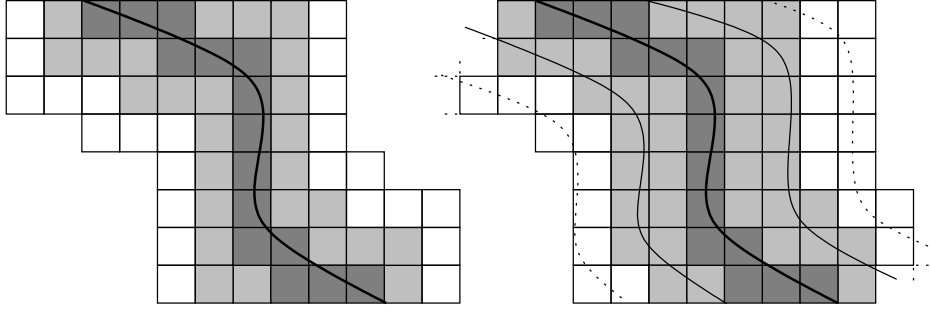
Figure 7.4: $\mathscr{T}_{h,\delta}$ (*Left*) vs. $\mathscr{T}_{h,0}^{(L)}$ (*Right*).

**Full system in matrix formulation**

On account of the decomposition $\Phi^{k+1} = \Phi_0^{k+1} + \Phi_\partial^{k+1}$, where $\Phi_\partial^{k+1} = D$ on $\partial\mathscr{T}_{h,\mathrm{nb}}$ and $\Phi_0^{k+1} \in \mathcal{V}_0^h$ and the notation that $\mathbf{M}_0$ and $\mathbf{L}_0$ correspond to the matrices obtained by pairing all basis functions of $\mathcal{V}_0^h$, we finally obtain the matrix formulation of the full *Dirichlet* problem:

$$\left(\mathbf{M}_0[\|\nabla\Phi\|^{q_1}] + \tau\mathbf{L}_0[A_1] + \tau\mathbf{L}_0[A_2]\mathrm{Restr}[\mathcal{V}_0^h](\mathbf{M}^+[\|\nabla\Phi\|^{q_2}])^{-1}\mathbf{L}^+[A_2]\right)\bar{\Phi}_0^{k+1} = \qquad (7.14)$$
$$\mathbf{M}_0[\|\nabla\Phi\|^{q_1}]\bar{\Phi}_0^k - \tau\mathrm{Restr}[\mathcal{V}_0^h]\left(\mathbf{L}[A_1] + \mathbf{L}[A_2]\mathrm{Restr}[\mathcal{V}^h](\mathbf{M}^+[\|\nabla\Phi\|^{q_2}])^{-1}\mathbf{L}^+[A_2]\right)\bar{\Phi}_\partial^k.$$

Here $D$ denotes the discrete version of $\bar{d}$ as computed by the *Hopf-Lax* update procedure. Finally it has to be mentioned, that $A_1$, $A_2$ and $B$ may explicitly depend on $W$ and $\Phi$ (e.g. in the case of Willmore flow, $A_1 = A_1(w)$ and $A_2 = A_2(\phi)$). To obtain a semi-implicit time stepping scheme, we insert the corresponding discrete functions from the previous time step. Here $W^k$ is computed in the extended finite element space $\mathcal{V}^{h,+}$ and subsequently restricted to $\mathcal{V}^h$.

### 7.3.5 The main loop

Let us now turn to the description of the full algorithm. Hereby, we focus on the variant of the *Dirichlet* conditions that has been described at the end of the previous section for fourth order problems. Second order problems are implemented similarly in a straightforward way, by discretizing the iteration (7.6) or an analogous variant in space with *Dirichlet* or *Neumann* boundary conditions.

In order to consider an inner iteration, let us abbreviate the operators on left and right hand side of the matrix formulation (7.14) by

$$\mathbf{A}[W,\Phi] \quad := \quad \mathbf{L}[A_1] + \tau\mathbf{L}[A_2]\mathrm{Restr}[\mathcal{V}^h](\mathbf{M}^+[\|\nabla\Phi\|^{q_2}])^{-1}\mathbf{L}^+[A_2]$$
$$\mathbf{A}_0[W,\Phi] \quad := \quad \mathbf{L}_0[A_1] + \tau\mathbf{L}_0[A_2]\mathrm{Restr}[\mathcal{V}_0^h](\mathbf{M}^+[\|\nabla\Phi\|^{q_2}])^{-1}\mathbf{L}^+[A_2]$$

so that, hence, a single implicit time step with fixed boundary conditions becomes

$$\left(\mathbf{M}_0[\|\nabla\Phi\|^{q_1}] + \tau\mathbf{A}_0[W^k,\Phi^k]\right)\bar{\Phi}_0^{k+1} = \mathbf{M}_0[\|\nabla\Phi\|^{q_1}]\bar{\Phi}_0^k - \tau\mathrm{Restr}[\mathcal{V}_0^h]\mathbf{A}[W^k,\Phi^k]\bar{\Phi}^k.$$

But, as described before, it is recommendable to successively adjust the boundary conditions according to the changing signed distance function of the evolving geometry. A convenient way to achieve this is to iteratively update the distance function within the narrow band and repeatedly solve the equation

$$\left(\mathbf{M}_0[\|\nabla\Phi_i^{k+1}\|^{q_1}] + \tau\mathbf{A}_0[W_i^{k+1},\Phi_i^{k+1}]\right)\bar{\Phi}_{0,l+1}^{k+1}$$
$$= \mathbf{M}_0[\|\nabla\Phi_i^{k+1}\|^{q_1}]\bar{\Phi}_{0,i}^{k+1} - \tau\mathrm{Restr}[\mathcal{V}_0^h]\mathbf{A}[W_i^{k+1},\Phi_i^{k+1}]\bar{D}_i^{k+1}. \quad (7.15)$$

for $i = 1,\ldots$ until convergence. Here, we have used the convention that for $k \in \mathbb{N}$, we set $\Phi^k$ to the function $\Phi_{i_{\max}}^k$, assuming, that we stopped the inner iteration for the $k^{th}$ time step at iteration number $i_{\max}$, $\Phi_1^{k+1} := \Phi^k$ and $\Phi_0^0 := \Phi_0$. For $W$ we proceed analogously.

This means, that all occurring matrices have to be reassembled in each step of the inner iteration. In order to at least be able to use the same storage structure within the inner iteration, we choose the narrow band to be thick enough to ensure that the interface $\mathcal{M}(\tau(k+1))$ of the new time step is still contained in the same grid. Furthermore, this allows an efficient way to update the distance function in the narrow band: the required process of extracting the distance of the vertices of the intersected cells to the interface prior to the *Hopf-Lax-update* or *Fast-Marching-Method* can be achieved by traversal over the narrow band grid, instead of traversing the cells of the entire domain.

From the $k^{th}$ to the $(k+1)^{th}$ time step, the narrow band grid is adjusted to the new position of the interface; the domain on which the PDE is solved changes. Algorithmically, this requires a discrete extension operator from $\Omega_h^k \to \Omega_h^{k+1}$. Since the approach is based on the idea of keeping $\Phi^{k+1}$ close to a signed distance function, an obvious choice would be to set $\Phi_0^{k+1}$ to $D^k$ (discrete distance function with respect to the discrete interface $\mathcal{M}_{0,h}[\Phi^k]$) after every time step. On the other hand, this "redistancing" always introduces numerical errors. In fact, it is in general impossible to update the finite element space, such that the zero level set remains constant and that at the same time the values at the Lagrange points correspond to the signed distance to the discrete interface. To avoid a significant impact of this numerical error, we extend $\Phi^{k+1}$ by this reinitialization only every $k_{\mathrm{redist}}^{th}$ time step. For the remaining time steps, the *Hopf-Lax*-update is only computed on nodes, which do not belong to interfaced cells.

Let us now summarize these considerations and formulate the main algorithm.

**Iterative narrow band evolution of signed distance functions**

**Step 0** Set the level to $k := 0$, $\Phi^0 = \mathcal{I}_h \phi_0$ and choose $\delta > 2h$, $\mathscr{T}_{h,0} := \emptyset$

**Step 1** For all $C \in \mathscr{T}_h$ check the condition $C \cap \mathcal{M}_h(\Phi^0) \neq \emptyset$ . In this case update $\mathscr{T}_{h,0} \leftarrow \mathscr{T}_{h,0} \cup C$.

**Step 2 (main loop)**

    **Step 2.1 (a)** compute distance function $D^k(\Phi^k)$ by *Gauss-Seidel* iteration of (7.12) within the band $\delta$ and collect swept cells into $\mathscr{T}_{h,\mathrm{nb}}$ on the fly

    **Step 2.1 (b)** **or** alternatively $\mathscr{T}_{h,\mathrm{nb}} := \mathscr{T}_{h,0}^{(L)}$ by a $L$-neighborhoods of cells.

    **Step 2.2** if $k \bmod k_{\mathrm{redist}} = 0$ **then** perform reinitialization: $\Phi^k := D^k$.

    **Step 2.3** determine the index sets $I(\mathcal{V}_0^h)$, $I(\mathcal{V}^h)$ and $I(\mathcal{V}^{h,+})$.

    **Step 2.4** Set $i := 1$, $\Phi_1^{k+1} := \Phi^k$

    **Step 2.5( inner loop)**

        **Step 2.5.1** compute $W_i^{k+1}$ from the knowledge of $\Phi_i^{k+1}$ by solving the second equation, e. g., $\bar{W}_i^{k+1} := \mathrm{Restr}[\mathcal{V}^h](\mathbf{M}^+[\|\nabla\Phi\|^{q_2}])^{-1}\mathbf{L}^+[A_2]\bar{\Phi}_i^{k+1}$

        **Step 2.5.2** assemble the required matrices on the narrow band (depending on $W_i^{k+1}$ and $\Phi_i^{k+1}$)

        **Step 2.5.3** compute the right hand side of the system w.r.t. the choice of boundary conditions

        **Step 2.5.4** solve the linear system (7.15) for $\Phi_{i+1}^{k+1}$ with a direct solver or cg.

        **Step 2.5.5** set $i \leftarrow i + 1$. If convergence has been reached leave loop.

    **Step 2.6** set $\Phi^{k+1} := \Phi_{i-1}^{k+1}$

Let us emphasize that even though we don't reallocate the vectors of coefficients every time the finite elements space changes, the the required storage space is reduced enormously. The dominating storage requirement is dictated by the matrices, which for require 9 or 27 times as much space as a full vector of coefficients in two resp. three dimensions.

It is yet unclear under which conditions the inner iteration (7.15) converges. In some cases, when the geometry lacked a "certain amount" of smoothness, the scheme has actually diverged. This was not the case for *Neumann* boundary conditions in both equations and a sufficiently large narrow band with of $\delta > 6h$.
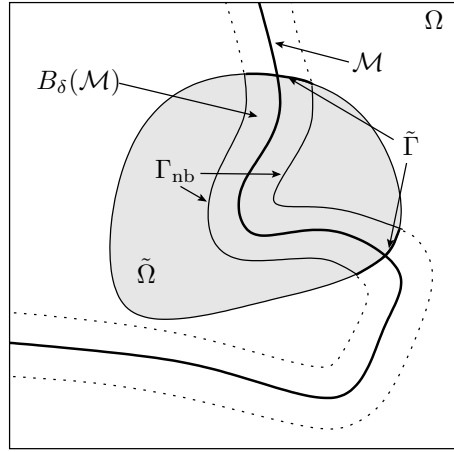
Figure 7.5: Restricting the evolution to a subdomain $\tilde{\Omega}$. Here we consider two types of boundaries: the level set function is kept fixed on $\tilde{\Gamma}$ which is a subset of the boundary of $\tilde{\Gamma}$, while on the remaining boundary ($\Gamma_{\mathrm{nb}}$) the boundary conditions are iteratively adjusted to the signed distance function.

## 7.4 Non-closed surfaces and inpainting

So far, we have based the formulation and the algorithm on the assumption that the surface is closed. In this section we will describe how the evolution of a surface can be implemented, while keeping the boundary fixed. Fortunately this can be achieved by only slight modifications of the above algorithm.

Let us assume that we are only interested in the evolution of $\mathcal{M}(t)$ in $\tilde{\Omega} \subset \Omega = [0,1]^d$, which is described by a level set function $\tilde{\phi}$ such that $\tilde{\Omega} = \{\tilde{\phi} \leq 0\}$, for instance, the signed distance function (see Figure 7.5). We want to deal with the case

$$\partial \mathcal{M}_0 \subset \partial \tilde{\Omega}$$

and keep $\mathcal{M}_0$ fixed along the boundary.

As a consequence, $\tilde{\Gamma} := \partial(B_\delta(\mathcal{M}(t)) \cap \tilde{\Omega}) \cap \partial\tilde{\Omega} \neq \emptyset$. For convenience, we consider the decomposition

$$\overline{\partial(B_\delta(\mathcal{M}(t)) \cap \tilde{\Omega})} = \overline{\tilde{\Gamma}} \cup \overline{\Gamma_{\mathrm{nb}}} \tag{7.16}$$

into the relatively open (w.r.t. $\partial(B_\delta(\mathcal{M}(t)) \cap \tilde{\Omega})$) sets $\tilde{\Gamma}$ and $\Gamma_{\mathrm{nb}}$.

We have described how the various types of boundary conditions can be implemented along the boundary of the narrowband by taking into account the signed distance function. Thus, we have the entire algorithmical components at hand to prescribe different boundary conditions on $\tilde{\Gamma}$ and $\Gamma_{\mathrm{nb}}$ (see Figure 7.5). All of those types have to implemented differently so we will focus only on the most appropriate one in order to use Willmore flow for surface inpainting. If other boundary conditions are desired, one may proceed analogously by taking into account the formulas of Section 7.3.4.

On $\tilde{\Gamma}$ we may want to prescribe fixed boundary conditions, e. g., the variant of *Dirichlet* conditions with different domains as described at the end of Section 7.3.4. However, along $\tilde{\Gamma}$ we do not want to update the boundary conditions according to the distance function. Instead we choose the conditions once at start of the algorithm according to the initial values of $\phi_0$ in $\Omega \setminus \tilde{\Omega}$ or at least a small neighborhood of $\tilde{\Omega}$ and keep it fixed during all time steps. Here we assume that the level set function $\phi_0$ is not only given in $\tilde{\Omega}$ but also in a small neighborhood, which is a reasonable assumption in case of surface inpainting. For the remaining boundary, namely $\Gamma_{\mathrm{nb}}$, we can proceed the same way as for closed surfaces.

Now the sets of cells $\mathscr{T}_{h,\delta}$ and $\mathscr{T}_{h,0}$ are chosen accordingly to ensure that they are fully
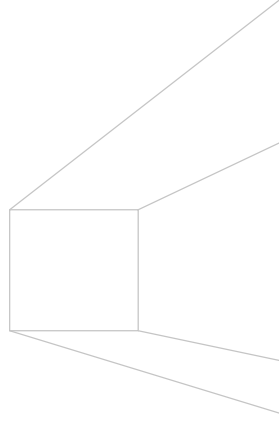
Figure 7.6: Discrete subdomain of computation for an inpainting problem. The blue faces of the cell indicate the boundary $\Gamma_{\mathrm{nb}}$ which is allowed to move and readjust during the computation. The faces marked in cyan mark the Dirichlet boundary $\tilde{\Gamma}$ on which the surface should is kept fixed.

contained in $\tilde{\Omega}$:

$$\tilde{\mathscr{T}}_{h,\delta}(\mathcal{M}) := \left\{ T \in \mathscr{T}_h \,:\, T \subset \tilde{\Omega} \text{ and } T \cap B_\delta(\mathcal{M}) \neq \emptyset \right\},$$

$$\tilde{\mathscr{T}}_{h,0}(\mathcal{M}) := \left\{ T \in \mathscr{T}_h \,:\, T \subset \tilde{\Omega} \text{ and } T \cap \mathcal{M} \neq \emptyset \right\},$$

$$\tilde{\mathscr{G}}^+ := \left\{ T \in \mathscr{T}_h \,:\, T \subset \tilde{\Omega} \text{ and } \mathcal{N}(T) \cap \mathcal{N}(\mathscr{G}) \neq \emptyset \right\}.$$

Furthermore, we will need

$$\hat{\mathscr{G}}^+ := \left\{ T \in \mathscr{T}_h \,:\, T \cap \Omega \setminus \tilde{\Omega} \neq \emptyset \text{ and } \mathcal{N}(T) \cap \mathcal{N}(\mathscr{G}) \neq \emptyset \right\},$$

as well as the analogous finite element spaces $\tilde{\mathcal{V}}_0^h$, $\tilde{\mathcal{V}}_0^h$ and $(\tilde{\mathcal{V}}^h)^+$. As before we chose our narrow band triangulation $\tilde{\mathscr{T}}_{\mathrm{nb}}$ to be either $\tilde{\mathscr{T}}_{h,\delta+}(\mathcal{M})$ or $\tilde{\mathscr{T}}^+_{h,\delta}(\mathcal{M})$.

Here $\mathscr{G}$ stands for an arbitrary subgrid of $\mathscr{T}_h$. The main difference is now the assembly of the matrices on the one-neighborhood of $\mathscr{T}_{h,\mathrm{nb}}$. We define for $\Phi \in \tilde{\mathcal{V}}^h$ the auxiliary extended function $\Phi^+ \in (\tilde{\mathcal{V}}^h)^+$ by

$$\Phi^+\big|_{\mathscr{T}_{h,\mathrm{nb}}} := \Phi \qquad \Phi^+\big|_{\hat{\mathscr{T}}^+_{\mathrm{nb}}} := \Phi_0\big|_{\hat{\mathscr{T}}^+_{\mathrm{nb}}} \qquad \Phi^+\big|_{\tilde{\mathscr{T}}^+_{\mathrm{nb}}} := D(\Phi)\big|_{\tilde{\mathscr{T}}^+_{\mathrm{nb}}}$$

To ensure that $\Phi^+$ is well-defined, we initially set $\Phi_0$ to a signed distance function.

The *stiffness* matrix and the *mass* matrix are now computed with respect to $\Phi^+$, i. e., $\mathbf{L}[\|\nabla\Phi^+\|]$ resp. $\mathbf{M}[\|\nabla\Phi^+\|]$. Now $\Phi^+$ takes the rôle of $\Phi_\partial$ in the linear system 7.14. Furthermore, the *Dirichlet* nodes along the discrete boundary which corresponds to $\tilde{\Gamma}$ namely $\overline{\hat{\mathscr{T}}^+_{\mathrm{nb}}} \cap (\overline{\mathscr{T}_{h,\mathrm{nb}} \cup \tilde{\mathscr{T}}^+_{\mathrm{nb}}})$ are kept fixed to the values of $\Phi_0$.

## 7.5   Numerical Results

**Inpainting of a sphere cap**

As a first test of the narrow band algorithm we consider the reconstruction of a sphere (see Figure 7.1). The inpainting domain was chosen as $\tilde{\Omega} := \left\{ (x,y,z) \in \mathbb{R}^3 \,:\, x \geq 0 \wedge y \geq 0 \wedge z \geq 0 \right\}$. We have obtained an initial surface by running mean curvature on the full sphere with Dirichlet boundary conditions in $\tilde{\Omega}$ until the surface becomes stationary (in which case we obtain a minimal surface). The computations were performed on a grid of resolution $65^3$. The timestep was

chosen as $20h^4$ and a reinitialization of the distance function was performed after every $10^{th}$ timestep of the evolution. Furthermore the narrowband was chosen as $\mathcal{T}_{h,5h}$. Figure 7.1 shows the evolution at time steps $0$, $10$, $50$ and $150$. As expected the Willmore flow drives the surface to the missing part of the sphere.

### Willmore flow for smoothing of surfaces

The use of higher order methods for surface smoothing has already been suggested by TASDIZEN ET AL. [191]. In contrast to the mean curvature flow which reduces noisy perturbations of the surface by a steepest descent of the area, the Willmore flow reduces the bending energy of the surface. A noisy surface naturally reveals a strong local bending due to local oscillations of high frequency. This results in a high magnitude of curvature and is hence measured by the Willmore energy. The steepest descent of the Willmore functional is expected to yield a smooth the surface according to the elimination of high curvature magnitudes. Figure 7.2 shows a top and a bottom view of a surface of a human brain, which is obtained by segmentation of an MRT data set of resolution $129^3$. The timestep was chosen deliberately small ($\tau = h^4$) since for smoothing purposes, one aims to eliminate noise while still remaining close to the initial surface. After one timestep a significant smoothing can be observed. In Figure 7.7 the same results are shown from a side perspective. A part of the surface has been removed to offer a view into the interior structure of the surface which in particular shows the ventricle of the brain. On the right the curvature of the surface is color-coded in order to demonstrate, that the Willmore flow eliminates regions of high curvature quickly and tends to a surface with a uniform distribution of the bending. For these computations we have chosen the width of the narrow band to be $\delta = 5h$ and the level set function has been reinitialized to the distance function after every second timestep.

### Inpainting of a hole in the skull

As a third application we have tested the applicability of the Willmore flow to the inpainting of a real CT data set which reveals a large hole in the skull (see Figure 1.2) for some slices through the initial CT data set. Before one can start with the process of the actual inpainting one first has to extract a surface from the data set as an initialization and to specify an inpainting domain $\tilde{\Omega}$. We have applied a multilevel level set based segmentation algorithm [99] in order to segment the outside region of the skull by a region growing approach. By this procedure we obtain a first guess of the initial surface in the interior of the hole. The tedios part of the inpainting process is to specify the inpainting domain $\tilde{\Omega}$. The choice of $\tilde{\Omega}$ is crucial and has to be selected with care, since on the surface along the boundary of the inpainting domain is used to specify the boundary conditions for the inpainting process (see Figure 7.6). Here we used the Dirichlet conditions in both equations with overlapping domains and in particular solved the semi-implicit scheme 7.14 in every time step. Figure 7.8 shows the final result of the inpainting versus the initial surface. The computations have been performed on a resolution of $129^3$ with a timestep of $\tau = 2h^4$. The overall duration was about 6 hours on an desktop PC with a AMD XP 2.5Ghz CPU with 1Gb of RAM. The resulting surface gives a seamless reconstruction of the hole.

### Growth of circles in 2D

Finally, as a further validation on the numerical accuracy of the narrowband approach, we have compared the numerical growth of radially symmetric solutions of the Willmore flow to the exact solution (see Figure 7.9). Here we again take into account the ODE which describes the evolution of the radius (cf. Eq. 6.23). The regularization parameter $\epsilon$ was chosen as $h$ and a reinitialization has been performed after every $50$ time steps. Furthermore the width of band was chosen as $\delta = 4h$ and $\tau = 10h^4$. We observe a very high degree of accuracy even for long times of execution. The dotted line shows the exact solution while the normal line shows the numerical computation after $0$, $100$, $400$ and $1200$ iterations.
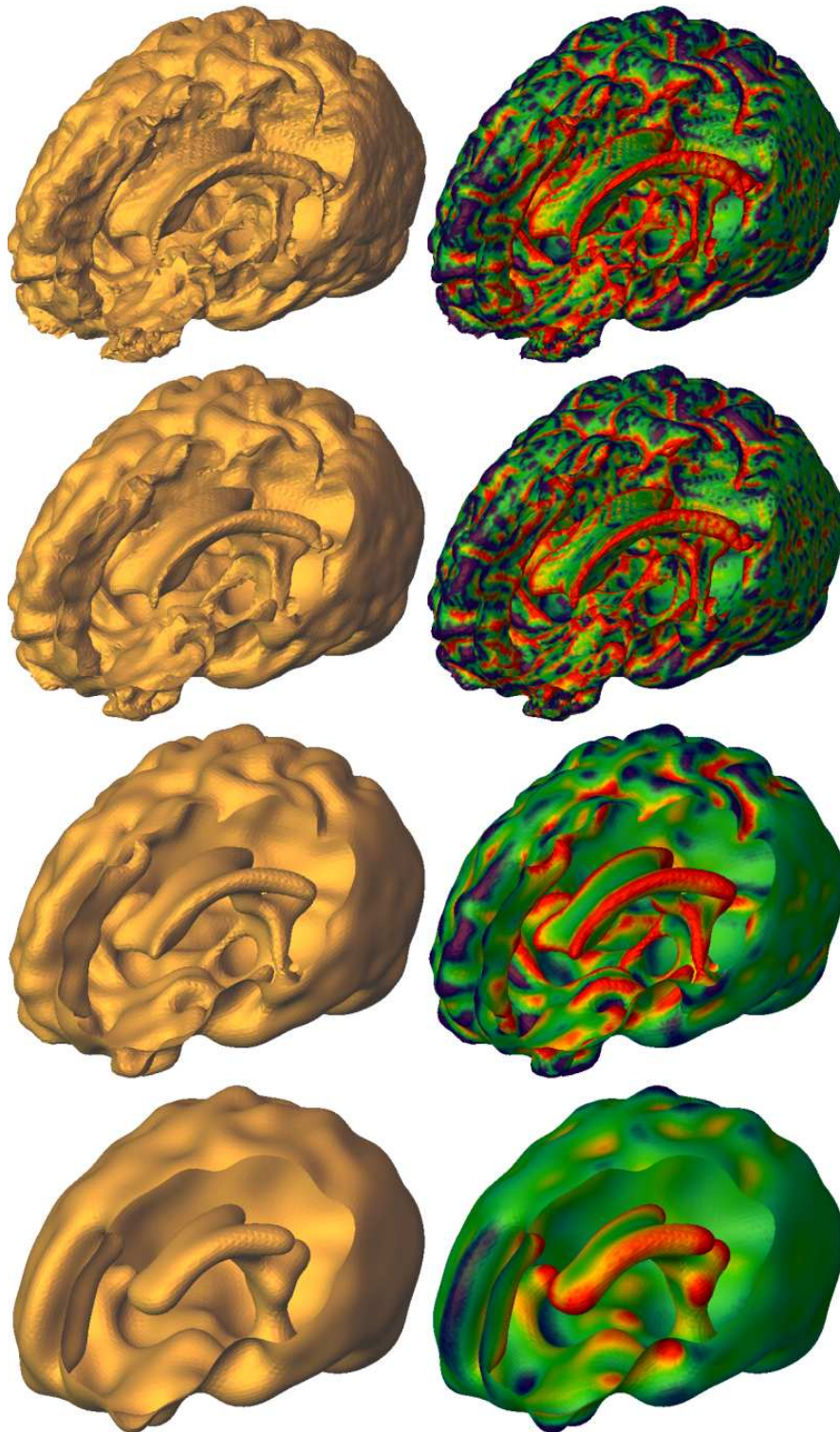
Figure 7.7: A detailed view of the smoothing of Figure 7.2. Again, steps $0, 1, 5$ and $30$ are shown. To offer a view into the interior the surface has been opened. On the right the curvature is color coded during the evolution (blue means negative curvature, read stands for positive curvature while colors close to green indicate a low magnitude.

(a) initial surface (top view)

(b) initial surface (side view)

(c) inpainted surface (top view)

(d) inpainted surface (side view)
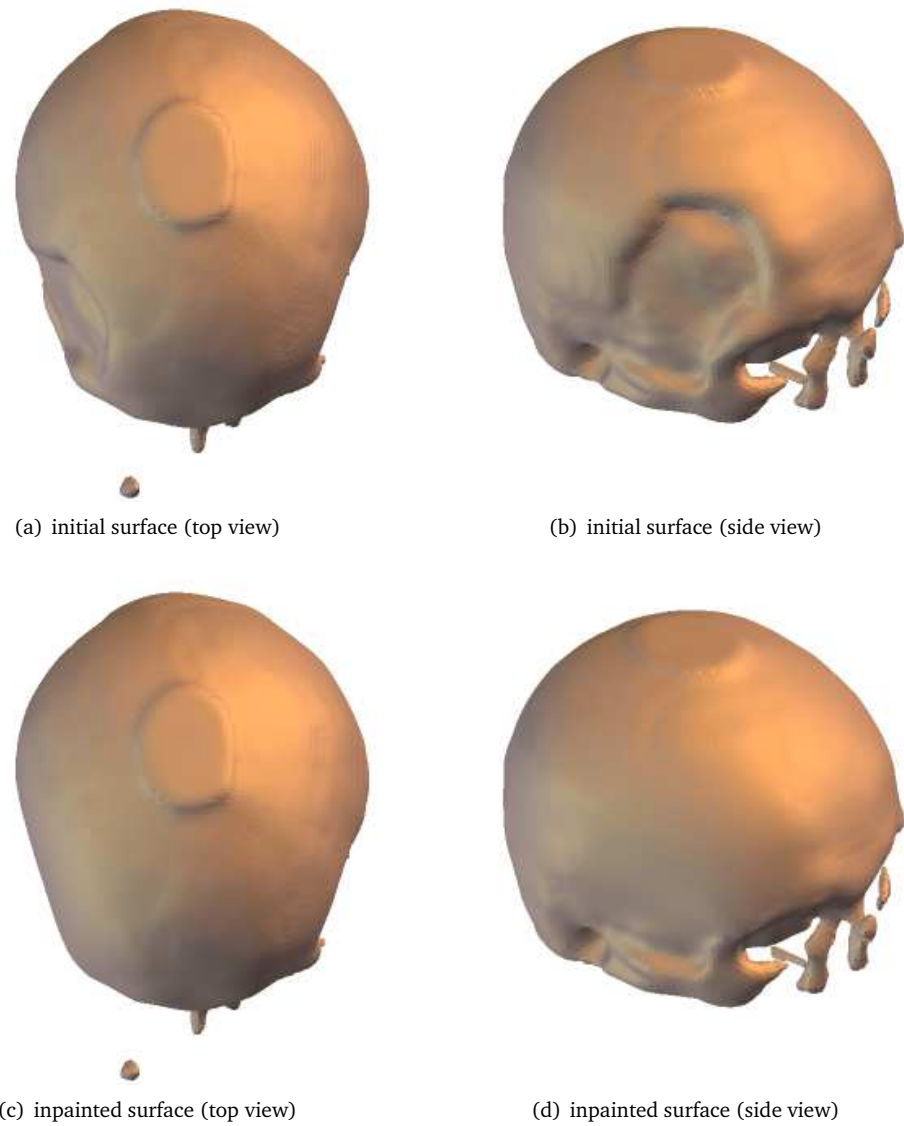
Figure 7.8: Inpainting of a large surface hole in the skull of a patient using the narrow band approach.
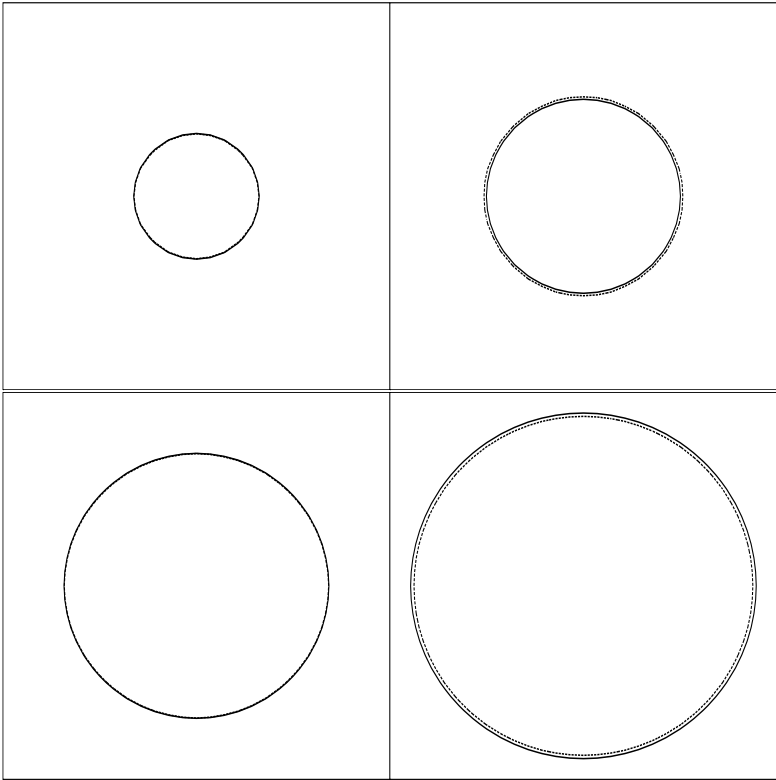
Figure 7.9: Validation of the growth of circles under 2D narrow band Willmore flow.

# Acknowledgment

# List of Figures

# Bibliography

[1] H.W. Alt. *Lineare Funktionalanalysis*. Springer, 1999.

[2] L. Alvarez, J. Esclarin, M. Lefébure, and J. Sánchez. A PDE model for computing the optical flow. Proc. XVI congreso de ecuaciones diferenciales y aplicaciones (C.E.D.Y.A. XVI, Las Palmas de Gran Canaria, Sept. 21–24, 1999).

[3] L. Alvarez, F. Guichard, P. L. Lions, and J. M. Morel. Axioms and fundamental equations of image processing. *Arch. Ration. Mech. Anal.*, 123(3):199–257, 1993.

[4] L. Alvarez, J. Sánchez, R. Deriche, and J. Weickert. Dense disparity map estimation respecting image discontinuities: A pde and scale-space based approach. *IAPR Workshop on Machine Vision*, No. 28-30:423–427, 2000.

[5] L. Alvarez, J. Weickert, and J. Sánchez. A scale–space approach to nonlocal optical flow calculations. In M. Nielsen, P. Johansen, O. F. Olsen, and J. Weickert, editors, *Scale-Space Theories in Computer Vision. Second International Conference, Scale-Space '99, Corfu, Greece, September 1999*, Lecture Notes in Computer Science; 1682, pages 235–246. Springer, 1999.

[6] L. Ambrosio. *Geometric evolution problems, distance function and viscosity solutions*, chapter 1, pages 5–93. Calculus of Variations and Partial Differential Equations, Topics on Geometrical Evolution Problems and Degree Theory. Springer, New York, 2000.

[7] L. Ambrosio, L. Faina, and R. March. Variational approximation of a second order free discontinuity problem in computer vision. *SIAM J. Math. Anal.*, 32(6):1171–1197, 2001.

[8] L. Ambrosio, N. Fusco, and D. Pallara. *Functions of bounded variation and free discontinuity problems*. Oxford University Press, 2000.

[9] L. Ambrosio and S. Masnou. A direct variational approach to a problem arising in image reconstruction. *Interfaces Free Bound.*, 5(1):63–81, 2003.

[10] L. Ambrosio and V. M. Tortorelli. Approximation of functionals depending on jumps by elliptic functionals via $\Gamma$-convergence. *Comm. Pure Appl. Math.*, 43:999–1036, 1990.

[11] L. Ambrosio and V. M. Tortorelli. On the approximation of free discontinuity problems. *Boll. Un. Mat. Ital. B*, 6(7):105–123, 1992.

[12] Gilles Aubert and Pierre Kornprobst. *Mathematical problems in image processing*. Springer-Verlag, New York, 2002. Partial differential equations and the calculus of variations, With a foreword by Olivier Faugeras.

[13] J.M. Ball. Convexity conditions and existence theorems in nonlinear elasiticity. *Arch. Rat. Mech. Anal.*, 63:337–403, 1977.

[14] J.M. Ball. Global invertibility of Sobolev functions and the interpenetration of matter. *Proc. Roy. Soc. Edinburgh*, 88A:315–328, 1988.

[15] C. Ballester, M. Bertalmio, V. Caselles, G. Sapiro, and J. Verdera. Filling-in by joint inter-
polation of vector fields and grey levels. *IEEE Transactions on Image Processing,* 10:1200–
1211, 2001.

[16] C. Ballester, V. Caselles, B. Rougé, and J. Verdera. Une méthode geometrique de fusion
des images p+xs. *Revue de la Societé Française de Photogrammetrie et Teledetection*, 2003.
to appear.

[17] C. Ballester, V. Caselles, and J. Verdera. Disocclusion by joint interpolation of vector fields
and gray levels. preprint.

[18] E. Bänsch, F. Haußer, O. Lakkis, B. Li, and A. Voigt. Finite element method for epitaxial
growth with attachment-detachement kinetics. *J. Comput. Phys.*, 194:409–434, 2004.

[19] E. Bänsch and K. Mikula. A coarsening finite element strategy in image selective smooth-
ing. *Computing and Visualization in Science*, 1:53–63, 1997.

[20] E. Bänsch, P. Morin, and R. H. Nochetto. Finite element methods for surface diffusion. In
*proceedings of the International Conference on Free Boundary Problems, Theory and Appli-
cations, Trento, Italy*, 2002.

[21] E. Bänsch, P. Morin, and R. H. Nochetto. Surface diffusion of graphs: Variational formu-
lation, error analysis and simulation. *SIAM Num. Anal.*, 42(2):773–799, 2002.

[22] E. Bänsch, P. Morin, and R.H. Nochetto. Finite element methods for surface diffusion.
*Preprint No. 805, WIAS, Berlin*, 2003.

[23] G. Belletini and A. Coscia. Discrete approximation of a free discontinuity problem. *Num.
Funct. Anal. Optim.*, 15:201–224, 1994.

[24] A. Berlis, C. Schaller, B. Meyer, J. Frings, K. Möller, C. Pavlidis, J. Schramm, and H. Schild.
Neuroradiological aspects in computerized simulation and individualization of pressure
and flow within the rabbit aorta. *Neuroradiology 41*, page S107, 1999.

[25] M. Bertalmio, A.L. Bertozzi, and G. Sapiro. Navier-Stokes, fluid dynamics, and image
and video inpainting. *Proceedings of the International Conference on Computer Vision and
Pattern Recognition, IEEE*, I:355–362, 2001.

[26] M. Bertalmio, G. Sapiro, V. Caselles, and C. Ballester. Image inpainting. In Kurt Akeley,
editor, *Computer Graphics (SIGGRAPH '00 Proceedings)*, pages 417–424, 2000.

[27] Martin Boehme, Rainer Hagenau, Jan Modersitzki, and Bodo Siebert. Non-linear image
registration on PC-clusters using parallel FFT techniques. *SIIM Technical Report*, A-02-08,
2002.

[28] A. Bonnet. On the regularity of the edge set of Mumford-Shah minimizers. *Prog. in
Nonlinear Differential Equations and Their Applications*, 25:93–103, 1996.

[29] F. Bornemann and C. Rasch. Finite-Element discretization of static Hamilton-Jacobi equa-
tions based on a local variation principle. *to appear in*, 2004.

[30] B. Bourdin. Image segmentation with a Finite Element method. *ESIAM: Mathematical
Modelling and Numerical Analysis*, 33(2):229–244, 1999.

[31] B. Bourdin and A. Chambolle. Implementation of a Finite-Element approximation of the
Mumford-Shah functional. *Numer. Math.*, 85(4):609–646, 2000.

[32] A. Braides. *Approximation of Free Discontinuity Problems*, volume 1694 of *Lecture Notes
in Mathematics*. Springer-Verlag, 1998.

[33] A. Braides. Γ-*convergence for beginners*. Oxford Lecture Series in Mathematics and Its
Applications. Claredon Press, 2002.

[34] A. Brook, R. Kimmel, and N. A. Sochen. Variation restoration and edge detection for color images. *J. Math. Imag. and Vis.*, 18:247–268, 2003.

[35] L. Gottesfeld Brown. A survey of image registration techniques. *ACM Computing Surveys*, 24(4):325–376, 1992.

[36] M. Burger. A framework for the construction of level set methods for shape optimization and reconstruction. *Interfaces and Free Boundaries*, 5:301–329, 2003.

[37] M. Burger. Levenberg-Marquardt level set methods for inverse obstacle problems. *Inverse Problems*, 20:259–282, 2004.

[38] M. Burger. Surface diffusion including free adatoms. Technical report, Industrial Mathematics Institute, Johannes-Kepler-University Linz, 2005.

[39] M. Burger, B. Hackl, and W. Ring. Incorporating topological derivatives into level set methods. *J. Comp. Phys.*, 194:344–362, 2004.

[40] F. Cao. *Geometric Curve Evolution and Image Processing*. Number 1805 in Lecture Notes in Mathematics. Springer, 2003.

[41] V. Caselles, F. Catté, T. Coll, and F. Dibos. A geometric model for active contours in image processing. *Numer. Math.*, 66:1–31, 1993.

[42] V. Caselles and B. Coll. Snakes in movement. *SIAM J. Numer. Analy.*, 33(6):2445–2456, 1996.

[43] V. Caselles, B. Coll, and J. M. Morel. Topographics maps and local contrast invariance in natural images. *Int. J. Comp. Vision*, 33:5–27, 1999.

[44] V. Caselles, R. Kimmel, and G. Sapiro. Geodesic active contours. *International Journal of Computer Vision*, 22(1):61–79, 1997.

[45] V. Caselles, J.-M. Morel, and C. Sbert. An axiomatic approch to image interpolation. *IEEE Trans. Image Processing*, 7(3):376–386, 1998.

[46] F. Catté, P. L. Lions, J. M. Morel, and T. Coll. Image selective smoothing and edge detection by nonlinear diffusion. *SIAM J. Numer. Anal.*, 29:182–193, 1992.

[47] A. Chambolle. Image segmentation by variatonal methods: Mumford-Shah functional and the discrete approximations. *SIAM J. Appl. Math.*, 55(3):827–863, 1995.

[48] A. Chambolle. An algorithm for mean curvature motion. Technical Report 0319, Ceremade Paris, 2003.

[49] T. Chan and J. Shen. Non-texture inpainting by curvature-driven diffusions (ccd). *J. Visual Comm. Image Rep.*, 12:436–449, 2001.

[50] T. Chan and J. Shen. Variational restoration of non-flat image features: models and algorithms. *SIAM J. Appl. Math.*, 61(4):1338–1361, 2001.

[51] T. Chan and L. Vese. An active contour model without edges. In M. Nielsen, P. Johansen, O. F. Olsen, and J. Weickert, editors, *Scale-Space Theories in Computer Vision. Second International Conference, Scale-Space '99, Corfu, Greece, September 1999*, Lecture Notes in Computer Science; 1682, pages 141–151. Springer, 1999.

[52] T. F. Chan, S. H. Kang, and J. Shen. Euler's elastica and curvature-based inpainting. *SIAM Appl. Math.*, 63(2):564–592, 2002.

[53] T. F. Chan and L. A. Vese. Image segmentation using level sets and the piecewise constant Mumford-Shah model. UCLA CAM Report 00-14, University of California , Los Angeles, 2000.

[54] T. F. Chan and L. A. Vese. A level set algorithm for minimizing the Mumford-Shah functional in image processing. UCLA CAM Report 00-13, University of California , Los Angeles, 2000.

[55] T. F. Chan and L. A. Vese. Active contours without edges. *IEEE Trans. Image Processing*, 10(2):266–277, 2001.

[56] T.F. Chan and J. Shen. On the role of the bv image model in image restoration. *AMS Contemporary Mathematics.* to appear.

[57] G. Christensen, R. D. Rabbitt, and M. I. Miller. Deformable templates using large deformation kinematics. *IEEE Transactions on Image Processing*, 5(10):1435–1447, October 1996.

[58] G. E. Christensen, S. C. Joshi, and M. I. Miller. Volumetric transformations of brain anatomy. *IEEE Trans. Medical Imaging*, 16, no. 6:864–877, 1997.

[59] G. E. Christensen, R. D. Rabbitt, and M. I. Miller. Deformable templates using large deformation kinematics. *IEEE Trans. Medical Imaging*, 5, no. 10:1435–1447, 1996.

[60] P. G. Ciarlet. *Mathematical Elasticity,* volume 1. North-Holland, Amsterdam, 1987.

[61] P. G. Ciarlet. *Three-Dimensional Elasticity*. Elsevier, New York, 1988.

[62] P. G. Ciarlet and J. Nečas. Injectivity and self-contact in nonlinear elasticity. *Arch. Rational Mech. Anal.*, 97:171–188, 1987.

[63] Ph. G. Ciarlet. *The finite element method for elliptic problems*. North Holland, Amsterdam, 1978.

[64] U. Clarenz. Injectivity and adjoint extremals. *Calc. Var.*, 8(3):279–292, 1999.

[65] U. Clarenz. *S"atze "uber Extremalen zu parametrischen Funktionalen*. Dissertation, Rheinische Friedrich-Wilhelms-Universit"at Bonn, 1999.

[66] U. Clarenz. *Sätze über Extremalen zu parametrischen Funktionalen*. PhD thesis, Rheinische Friedrich-Wilhelms Univerität Bonn, 1999.

[67] U. Clarenz. The wulff-shape minimizes an anisotropic willmore functional. *Interfaces and Free Boundaries*, 6(3):351–359, 2004.

[68] U. Clarenz, U. Diewald, G. Dziuk, M. Rumpf, and R. Rusu. A finite element method for surface restoration with smooth boundary conditions. *Computer Aided Geometric Design*, 21(5):427–445, 2004.

[69] U. Clarenz, U. Diewald, and M. Rumpf. Nonlinear anisotropic diffusion in surface processing. In T. Ertl, B. Hamann, and A. Varshney, editors, *Proceedings of IEEE Visualization 2000*, pages 397–405, 2000.

[70] U. Clarenz, M. Droske, S. Henn, M. Rumpf, and K. Witsch. Computational methods for nonlinear image registration. 2005. to appear.

[71] U. Clarenz, M. Droske, and M. Rumpf. Towards fast non–rigid registration. In *Inverse Problems, Image Analysis and Medical Imaging, AMS Special Session Interaction of Inverse Problems and Image Analysis*, volume 313, pages 67–84. AMS, 2002.

[72] U. Clarenz, G. Dziuk, M. Droske, and M. Rumpf. On level set formulations of anisotropic geometric gradient flows. in prepration.

[73] U. Clarenz, S. Henn, and K. Rumpf, M. Witsch. Relations between optimization and gradient flow methods with applications to image registration. In *Proceedings of the 18th GAMM Seminar Leipzig on Multigrid and Related Methods for Optimisation Problems*, pages 11–30, 2002.

[74] U. Clarenz, M. Rumpf, and A. Telea. Robust feature detection and local classification for surfaces based on moment analysis. *IEEE Transactions on Visualization and Computer Graphics*, 10(5):516–524, 2004.

[75] Harvey E. Cline and William E. Lorensen. Marching cubes: A high resolution 3d surface construction algorithm. In *SIGGRAPH '87: Proceedings of the 14th annual conference on Computer graphics and interactive techniques*, pages 163–169. ACM Press, 1987.

[76] D. Cremers, T. Kohlberger, and C. Schnörr. Nonlinear shape statistics in mumford-shah based segmentation. In A. Heyden et al., editor, *7th European Conference on Computer Vision, Copenhagen, Springer LNCS*, volume 2351, pages 93–108, 2002.

[77] D. Cremers, F. Tischhäuser, J. Weickert, and C. Schnörr. Diffusion snakes: Introducing statistical shape knowledge into the mumford-shah functional. *International Journal of Computer Vision*, 50(3):1364–1379, 2002.

[78] J.A. Sethian D. Adalsteinsson. The fast construction of extension velocities in level set methods. *Journal of Computational Physics*, 148(1):2–22, 1999.

[79] B. Dacorogna. *Direct Methods in the Calculus of Variations*. Appl. Math. Sciences 78. Springer–Verlag, Berlin, 1989.

[80] G. Dal Maso. *An introduction to Γ-convergence*. Birkhäuser, Bostion, 1993.

[81] G. Dal Maso, J.M. Morel, and S. Solimini. A variational method in image segmentation: existence and approximation results. *Acta Math.*, 168:89–151, 1996.

[82] C. A. Davatzikos, R. N. Bryan, and J. L. Prince. Image registration based on boundary mapping. *IEEE Trans. Medical Imaging*, 15, no. 1:112–115, 1996.

[83] E. De Giorgi, M. Carriero, and A. Leaci. Existence theorem for a minimum problem with free discontinuity set. *Arch. Rat. Mech. and Anal.*, 108:195–218, 1989.

[84] K. Deckelnick and G. Dziuk. Convergence of a finite element method for non-parametric mean curvature flow. *Numer. Math.*, 72:197–222, 1995.

[85] K. Deckelnick and G. Dziuk. Discrete anisotropic curvature flow of graphs. *Math. Modelling Numer. Anal.*, 33:1203–1222, 1999.

[86] K. Deckelnick and G. Dziuk. Error estimates for a semi implicit fully discrete finite element scheme for mean curvature flow of graphs. *Interfaces and Free Boundaries*, 2:341–359, 2000.

[87] K. Deckelnick and G. Dziuk. A fully discrete numerical scheme for weighted mean curvature flow. *Numer. Math.*, (91):423–452, 2002.

[88] K. Deckelnick and G. Dziuk. Numerical approximation of mean curvature flow of graphs and level sets. In P. Colli and J. F. Rodrigues, editors, *Mathematical Aspects of Evolving Interfaces, Madeira, Funchal, Portugal, 2000. Lecture Notes in Mathematics*, volume 1812, pages 53–87. Springer-Verlag Berlin Heidelberg, 2003.

[89] K. Deckelnick and G. Dziuk. Error estimates for the Willmore flow of graphs. *Preprint Nr. 28/2004, University of Magdeburg*, 2004.

[90] K. Deckelnick, G. Dziuk, and C. M. Elliott. Error analysis of a semidiscrete numerical scheme for diffusion in axially symmetric surfaces. CMAIA Research Report 2002/05, University of Sussex, 2002. to appear in SIAM J. Numer. Anal.

[91] K. Deckelnick, G. Dziuk, and C. M. Elliott. Fully discrete simi-implicit second order splitting for anisotropic surface diffusion of graphs. Technical Report 33, Universität Magdeburg, 2003.

[92] M. C. Delfour and J.P Zolésio. *Geometries and Shapes: Analysis, Differential Calculus and Optimization*. Adv. Des. Control 4. SIAM, Philadelphia, 2001.

[93] M. C. Delfour and J.P. Zolésio. Oriented distance function and its evolution equation for initial sets with thin boundary. *SIAM J. Control Optim.*, 42(6):2286–2304, 2004.

[94] R. Deriche, P. Kornobst, and G. Aubert. Optical–flow estimation while preserving its discontinuities: A variational approach. In *Proc. Second Asian Conf. Computer Vision (ACCV '95, Singapore, December 5–8, 1995)*, volume 2, pages 290–295, 1995.

[95] A. Desolneux, L. Moisan, and J. M. Morel. Meaningful alignments. *Int. J. Comp. Vision*, 40(1):7–23, 2000.

[96] F. Dibos and Séré. An approximation result for the minimizers of the Mumford-Shah functional. *Boll. Un. Math. Ital.*, 11A(1), 1997.

[97] M. P. do Carmo. *Riemannian Geometry*. Birkhäuser, Boston, 1992.

[98] M. Droske, B. Meyer, M. Rumpf, and C. Schaller. An adaptive level set method for medical image segmentation. In R. Leahy and M. Insana, editors, *Proc. of the Annual Symposium on Information Processing in Medical Imaging*. Springer, Lecture Notes Computer Science, 2001.

[99] M. Droske, M. Meyer, M. Rumpf, and C. Schaller. An adaptive level set method for interactive segmentation of intracranial tumors. *Neurosurgical Research*, 27, 2005.

[100] M. Droske, T. Preusser, and M. Rumpf. A multilevel segmentation method. In B. Girod, G. Greiner, H. Niemann, and H.-P. Seidel, editors, *Proc. Vision, Modeling and Visualization, MPI Informatik, Saarbrücken, Germany*, pages 327–336, 2000.

[101] M. Droske and W. Ring. A Mumford-Shah level-set approach for geometric image registration. Technical report, Universität Duisburg-Essen, Universität Graz, 2004. in preparation.

[102] M. Droske and M. Rumpf. A level set formulation for willmore flow. *Interfaces and Free Boundaries*, 6(3):361–378, 2004.

[103] M. Droske and M. Rumpf. A variational approach to non-rigid morphological registration. *SIAM Appl. Math.*, 64(2):668–687, 2004.

[104] M. Droske, M. Rumpf, and R. Strzodka. Fast image registration in DX9 graphics hardware. *Journal of Medical Informatics and Technologies*, 6:43–49, Nov 2003.

[105] M. Droske, M. Rumpf, and R. Strzodka. Image registration by a regularized gradient flow - a streaming implementation in DX9 graphics hardware. *Computing*, 2004. to appear.

[106] U. Dupuis, P. Grenander and M. I. Miller. Variational problems on flows of diffeomorphisms for image matching. *Quarterly J. Applied Math. (ed. D. Mumford and W. Freiberger)*, pages 587–600, November 1998.

[107] G. Dziuk. An algorithm for evolutionary surfaces. *Numer. Math.*, 58:603–611, 1991.

[108] H. E. Engl, M. Hanke, and A. Neubauer. *Regularization of Inverse Problems*. Kluwer Academic Publishers, 2000.

[109] S. Esedoglu and S. Jianhong. Digital inpainting based on the Mumford-Shah-Euler image model. *Euro. Jnl. Appl. Math.*, 2002.

[110] S. Esedoglu and S.J. Osher. Decomposition of images by the anisotropic Rudin-Osher-Fatemi model. *Comm. Pure Appl. Math.*, 57:1609–1626, 2004.

[111] L. C. Evans and R. F. Gariepy. *Measure Theory and Fine Properties of Functions*. CRC Press, 1992.

[112] L.C. Evans and J. Spruck. Motion of level sets by mean curvature I. *J. Diff. Geom.*, 33(3):635–681, 1991.

[113] X. Feng and A. Prohl. Analysis of gradient flow of a regularized Mumford-Shah functional for image segmentation and image inpainting. *Mathematical Modelling and Numerical Analysis*, 1999.

[114] M. Fried. A level set based finite element algorithm for the simulation of dendritic growth. *Preprint, University of Freiburg, Germany*, 2001.

[115] M. Fried. Image segmentation using adaptive finite elements. Technical report, University of Canberra, Australia, 2003.

[116] D. Gabor. Theory of communication. *J. IEE*, 93:429–457, 1946.

[117] T. Gerstner, M. Rumpf, and U. Weikard. Error indicators for multilevel visualization and computing on nested grids. *Computers & Graphics*, 24(3):363–373, 2000.

[118] D. Gilbarg and N.S. Trudinger. *Elliptic partial differential equations of second order*. Grundlehren der Mathematischen Wissenschaften. 224. Berlin-Heidelberg-New York: Springer- Verlag, 1992.

[119] J. Gomes and O. Faugeras. Reconciling distance functions and level sets. In M. Nielsen, P. Johansen, O. F. Olsen, and J. Weickert, editors, *Scale-Space Theories in Computer Vision. Second International Conference, Scale-Space '99, Corfu, Greece, September 1999*, Lecture Notes in Computer Science; 1682, pages 70–81. Springer, 1999.

[120] U. Grenander and M. I. Miller. Computational anatomy: An emerging discipline. *Quarterly Appl. Math.*, LVI, no. 4:617–694, 1998.

[121] W. Hackbusch. *Multigrid Methods and Applications*. Springer, Berlin/Heidelberg, 1985.

[122] W. Hackbusch and S. Sauter. Composite finite elements for the approximation of pdes on domains with complicated micro-structures. *Numerische Mathematik*, 75:447–472, 1997.

[123] M. Hanke. A regularizing levenberg-marquardt scheme, with applications to inverse problems. *Inverse Problems*, 3:79–95.

[124] S. Henn. A Levenberg-Marquardt scheme for nonlinear image registration. *BIT Numerical Mathematics*, 43(4):743–759, 2003.

[125] S. Henn and K. Witsch. A multigrid approach for minimizing a nonlinear functional for digital image matching. *Computing*, 64(4):339–348, 2000.

[126] St. Henn and K. Witsch. Iterative multigrid regularization techniques for image matching. *SIAM J. Sci. Comput.*, 23 No 4:1077–1093, 2001.

[127] W. Hinterberger, O. Scherzer, C. Schnörr, and J. Weickert. Analysis of optical flow models in the framework of calculus of variations. Technical report, Numerical Functional Analysis and Optimization, Revised version of Technical Report No. 8/2001, Computer Science Series, University of Mannheim, Germany,, 2001.

[128] M. Hintermüller and W. Ring. A second order shape optimization approach for image segmentation. 2003. submitted.

[129] M. Hintermüller and W. Ring. An inexact newton-cg-type active contour approach for the minimization of the mumford-shah functional. *J. Math. Imag. Vision*, 20:19–42, 2004.

[130] B.K.P. Horn and B.G. Schunk. Determining optical flow. *Artificial Intelligence*, 17:185–204, 1981.

[131] S. C. Joshi and M. I. Miller. Landmark matching via large deformation diffeomorphisms. *IEEE Trans. Medical Imaging*, 9, no. 8:1357–1370, 2000.

[132] J. Jost. *Riemannian Geometry and Geometric Analysis*. Springer, 1998.

[133] G. Dziuk K. Deckelnick. Mean curvature flow and related topics. Technical Report 33, Mathematische Fakultät der Albert-Ludwigs-Universität Freiburg, Oktober 2002 2002.

[134] T. Kapur, L. Yezzi, and L. Zöllei. A variational framework for joint segmentation and registration. *IEEE CVPR - MMBIA*, 2001.

[135] M. Kass, A. Witkin, and D. Terzopoulos. Snakes: Active contour models. *International Journal of Computer Vision*, 1:321–331, 1988.

[136] A Kirsch. *An Introduction to the Mathematical Theory of Inverse Problems*, volume 120 of *applied mathematical sciences*. Springer Verlag, New York, 1996.

[137] J. J. Koenderink. The structure of images. *Biological Cybernetics*, 50:363–370, 1984.

[138] E. Kuwert and R. Schätzle. The Willmore flow with small initial energy. *J. Differential Geom.*, 57(3):409–441, 2001.

[139] E. Kuwert and R. Schätzle. Gradient flow for the Willmore functional. *Comm. Anal. Geom.*, 10(5):1228–1245 (electronic), 2002.

[140] E. Kuwert and R. Schätzle. Removability of Point Singularities of Willmore Surfaces. *Preprint SFB 611, Bonn*, No. 47, 2002.

[141] A. E. Lefohn, J.E. Cates, and R.T. Whitaker. Interactive, gpu-based level sets for 3d brain tumor segmentation. *Medical Image Computing and Computer Assited Intervention*, 2003.

[142] F. Maes, A. Collignon, D. Vandermeulen, G. Marchal, and P. Suetens. Multi–modal volume registration by maximization of mutual information. *IEEE Trans. Medical Imaging*, 16, no. 7:187–198, 1997.

[143] R. Malladi, J. A. Sethian, and B. C. Vemuri. Shape modeling with front propagation: A level set approach. *IEEE Transactions on Pattern Analysis and Machine Intelligence*, 17(2):158–175, 1995.

[144] P. Maragos. A representation theory for morphological image and signal processing. *IEEE Transactions Pat. Anal. and Mach. Int.*, 11(6):586–589, 1989.

[145] P. Maragos. Differential morphology and image processing. *IEEE Trans. Image Processing*, 78:922–937, 1996.

[146] P. Maragos and M. A. Butt. Advances in differential morphology: Image segmentation via Eikonal PDE and curve evolution and reconstruction via constrained dilation flow. In H. Heijmans and J. Roerdink, editors, *Mathematical Morphology and Its Applications to Image and Signal Processing*, pages 167–174. Kluwer Acad. Publ., 1998.

[147] M. Marcus and V.J. Mizel. Transformations by functions in sobolev spaces and lower semicontinuity for parametric variational problems. *Bulletin of the American Mathematical Society*, 79, 1973.

[148] S. Masnou and J.-M. Morel. Level lines based disocclusion. In *5th IEEE International Conference on Image Processing (ICIP), Chicago*, volume 3, pages 259–263, 1998.

[149] G. Matheron. *Random Sets and Integral Geometry*. John Wiley N.Y., 1975.

[150] U. F. Mayer and G. Simonett. Self-intersections for the surface diffusion flow and the volume preserving mean curvature flow. *Differential and Integral equations*, 1999.

[151] U. F. Mayer and G. Simonett. Self-intersections for the willmore flow. In *Evolution Equations: Applications to Physics, Industry, Life Sciences and Economics. EVEQ 2000 Conference in Levico Terme (Trento, Italy)*, pages 341–348. Birkhäuser, Basel, 2003.

[152] Yves Meyer. *Oscillating Patterns in Image Processing and Nonlinear Evolution Equations*, volume 22 of *University Lecture Series*. AMS, 2001.

[153] K. Mikula, T. Preusser, and M. Rumpf. Morphological image sequence processing. *Computing and Visualization in Science*, 6(4):197–209, 2003.

[154] M. I. Miller, S. C. Joshi, and G. E. Christensen. *Brain Warping*, chapter Large Deformation Fluid Diffeomorphisms for Landmark and Image Matching. Academic Press, San Diego, CA, 1999.

[155] M. I. Miller and L. Younes. Group actions, homeomorphisms and matching: a general framework. Technical report, John Hopkins University, Maryland, 1999.

[156] M.I. Miller, A. Trouve, and L. Younes. On the metrics and Euler-Lagrange equations of computational anatomy. *Annual Review of biomedical Engineering*, 4:375–405, 2002. in print.

[157] J. Modersitzki and B. Fischer. Fast diffusion registration. *Special Issue of Contemporary Mathematics, AMS*, 2000.

[158] J. Modersitzki and B. Fischer. Curvature based image registration. *JMIV*, 18(1), 2003.

[159] P. Monasse. Contrast invariant registration of images. In *Proceedings of the International Conference on Acoustics, Speech and Signal Processing, Phoenix, Arizona*, volume 6, pages 3221–3224, 1999.

[160] J.M. Morel and S. Solimini. *Variational models in image segmentation*. Birkäuser, 1994.

[161] Ch. Morrey. *Multiple Integrals in the Calculus of Variations*. Springer–Verlag, New-York, 1966.

[162] D. Mumford. Elastica and computer vision. *Algebraic geometry and its applications, Springer Verlag*, pages 491–506, 1994.

[163] D. Mumford and J. Shah. Optimal approximation by piecewise smooth functions and associated variational problems. *Comm. Pure Appl. Math.*, 42:577–685, 1989.

[164] H. H. Nagel and W. Enkelmann. An investigation of smoothness constraints for the estimation of displacement vector fields from image sequences. *IEEE Trans. Pattern Anal. Mach. Intell.*, 8:565–593, 1986.

[165] J. Nečas. *Les Méthodes Directes en Théorie des Equations Elliptiques*. Masson, Paris, 1967.

[166] M. Ohlberger and M. Rumpf. Hierarchical and adaptive visualization on nested grids. *Computing*, 59 (4):269–285, 1997.

[167] M. Ohlberger and M. Rumpf. Adaptive projection operators in multiresolutional scientific visualization. *IEEE Transactions on Visualization and Computer Graphics*, 4(4), 1998.

[168] S. J. Osher and R. P. Fedkiw. *Level Set Methods and Dynamic Implicit Surfaces*. Springer-Verlag, 2002.

[169] S. J. Osher and N. Paragios. *Geometric Level Set Methods in Imaging, Vision and Graphics*. Springer, 2003.

[170] S. J. Osher and J. A. Sethian. Fronts propagating with curvature dependent speed: Algorithms based on Hamilton–Jacobi formulations. *J. of Comp. Physics*, 79:12–49, 1988.

[171] E. Pauwels, P. Fiddelaers, and L. van Gool. Enhancement of planar shape through optimization of functionals for curves. *IEEE Trans. Pat. Anal. Mach. Int.*, 17(1):1101–1105, 1995.

[172] P. Perona and J. Malik. Scale space and edge detection using anisotropic diffusion. In *IEEE Computer Society Workshop on Computer Vision*, 1987.

[173] Preußer. *Anisotropic Geometric Diffusion in Image and Image Sequence Processing*. PhD thesis, University of Duisburg-Essen, 2003.

[174] T. Preußer and M. Rumpf. A level set method for anisotropic geometric diffusion in 3d image processing. *SIAM J. Appl. Math.*, to appear, 2001.

[175] T. Preusser and M. Rumpf. Extracting motion velocities from 3D image sequences. In *SPIE Conference on Visualization and Data Analysis*, 2003.

[176] T. J. Richardson and S. K. Mitter. A variational formulation based edge focussing algorithm. *Sadhana Acad. P. Eng. S.*, 22(4):553–574, 1997.

[177] L. Rudin and E. Osher, S. ad Fatemi. Nonlinear total variation based noise-removal. *Physica D*, 60:259–268, 1992.

[178] L. Rudin and S. Osher. Total variation based image restoration with free local constraints. In *Proc. IEEE ICIP*, volume I, 1994. Austin, TX.

[179] M. Rumpf. On the matching of images with discontinuities. in preparation, 2005.

[180] M. Rumpf and R. Strzodka. Nonlinear diffusion in graphics hardware. In *Proceedings of EG/IEEE TCVG Symposium on Visualization VisSym '01*, pages 75–84. Springer, 2001.

[181] R. Rusu. An algorithm for the elastic flow of surfaces. *Preprint Mathematische Fakultät Freiburg*, 01-35:, 2001.

[182] G. Sapiro. Vector (self) snakes: a geometric framework for color, texture and multi-scale image segmentation. In *Proc. IEEE Int. Conf. Image Proc. (ICIP), Lausanne*, 1996.

[183] G. Sapiro. *Geometric Partial Differential Equations and Image Analysis*. Cambridge University Press, 2001.

[184] S. Sauter and N. Stahn. Composite finite elements and multi-grid. part i: Convergence theory in 1-d. Technical Report Preprint, 11-01, University of Zürich, 2001.

[185] O. Scherzer and J. Weickert. Relations between regularization and diffusion filtering. *Journal of Mathematical Imaging and Vision*, 12:43–63, 2000.

[186] J. A. Sethian. *Level Set Methods: Evolving Interfaces in Geometry, Fluid Mechanics, Computer Vision and Materials Sciences*. Cambridge Univ. Press, 1996.

[187] G. Simonett. The Willmore Flow near spheres. *Diff. and Integral Eq.*, 14(8):1005–1014, 2001.

[188] P. Smereka. Semi-implicit level set methods for curvature and surface diffusion motion. *Journal of Scientific Computing*, 19(1-3):439–456, 2003.

[189] J. Sokołowski and J-P. Zolésio. *Introduction to shape optimization*. Springer-Verlag, Berlin, 1992. Shape sensitivity analysis.

[190] H. M. Soner. Motion of a set by the curvature of its boundary. *J. Differential Equations*, 101:313–372, 1993.

[191] T. Tasdizen, R. Whitaker, P. Burchard, and S.J. Osher. Geometric surface smoothing via anisotropic diffusion of normals. In *Proceedings Visualisazion 2002*, pages 125–132, 2002.

[192] J.E. Taylor. Anisotropic interface motion. *Mathematics of Microstructure Evolution, Edited by Long-Qing Chen et al, TMS/SIAM, Warrendale, PA, EMPMD Monograph Series*, 4:135–148, 1996.

[193] J.E. Taylor and J.W. Cahn. Linking anisotropic sharp and diffuse surface motion laws vie gradient flows. *J. Stat. Phys.*, 77:183–197, 1994.

[194] J.E. Taylor, J.W. Cahn, and W.C. Carter. Variational methods for microstructural evolution. *JOM*, 49(12):30–36, 1998.

[195] J. P. Thirion. Image matching as a diffusion process: An analogy with maxwell's demon. *Medical Imag. Analysis*, 2:243–260, 1998.

[196] V. Thomée. *Galerkin - Finite Element Methods for Parabolic Problems*. Springer, 1984.

[197] A. Tsai, A. Yezzi, and A. Willsky. Curve evolution implementation of the Mumford-Shah functional for image segmentation, denoising, interpolation, and magnification. *IEEE Transactions on Image Processing*, 10(8):1169–1186, 2001.

[198] B.C. Vemuri, J. Ye, Y. Chen, and C.M. Leonard. Image registration via level-set motion: Applications to atlas-based segmentation. *Medical Image Analysis*, 7:1–20, 2003.

[199] J. Verdera, V. Caselles, M. Bertalmio, and G. Sapiro. Inpainting surface holes. *Preprint no. 1905, IMA, University of Minnesota, 2003*.

[200] P. Viola and W.M. Wells. Alignment by maximization of mutual information. *International Journal of Computer Vision*, 24(2):137–154, 1997.

[201] Paul A. Viola. Alignment by maximization of mutual information. Technical Report AITR-1548, 1995.

[202] R. Warnke. Schnelle Löser für elliptische Randwertprobleme mit springenden Koeffizienten. *Dissertation, Zürich*, 2003.

[203] J. Weickert. *Anisotropic diffusion in image processing*. Teubner, 1998.

[204] J. Weickert. On discontinuity–preserving optic flow. In S. Orphanoudakis, P. Trahanias, J. Crowley, and N. Katevas, editors, *Proc. Computer Vision and Mobile Robotics Workshop (CVMR'98, Santorini, Sept. 17–18, 1998)*, pages 115–122, 1998.

[205] J. Weickert and Ch. Schnoer. A theoretical framework for convex regularizers in pde-based computation of image motion. Technical Report Reine Informatik 13/2000, Uni Mannheim, 2000.

[206] W. Wells, P. Viola, H. Atsumi, S. Nakajima, and R. Kikinis. Multi-modal volume registration by maximization of mutual information, 1996.

[207] T.J. Willmore. *Riemannian Geometry*. Claredon Press, Oxford, 1993.

[208] S. Winklmann. Isoperimetric inequalities involving generalized mean curvature. *Analysis*, 22:393–403, 2002.

[209] S. Winklmann. Enclosure theorems for generalized mean curvature flows. *Calc. Var.*, 16:439–447, 2003.

[210] G. Wulff. Zur Frage der Geschwindigkeit des Wachsthums und der Auflösung der Kristallflächen. *Zeitschrift der Kristallographie*, 34:449–530, 1901.

[211] S. Yoshizawa and A.G. Belyaev. Fair Triangle Mesh Generation with Discrete Elastica. In *Geometric Modeling and Processing, RIKEN, Saitama, Japan*, pages 119–123, 2002.

[212] H.K. Zhao, T. Chan, B. Merriman, and S.J. Osher. A variational level set approach to multiphase motion. *J. Comput. Phys.*, 127:179–195, 1996.